Abstract Volume

International Union of Theoretical and Applied Mechanics (IUTAM)

Symposium on *Aerothermodynamics in Combustors*

Institute of Applied Mechanics
National Taiwan University
Taipei, Taiwan, R. O. C.

June 3 - 5, 1991

Edited by
Richard S. L. Lee (S. L. Lee), J. H. Whitelaw and T.-S. Wung

International Union
of
Theoretical and
Applied Mechanics
(IUTAM)

Symposium on *Aerothermodynamics in Combustors*

Institute of Applied Mechanics
National Taiwan University
Taipei, Taiwan, R. O. C.
June 3 – 5, 1991

PREFACE

The subject of aerothermodynamics is playing an ever increasingly critical role in a variety of important industrial and technical problems in the design of combustors. In recent years, it has become the focus of attention among investigations from research laboratories and industries around the world resulting in a large number of meetings on its various aspects every year. However, most of these meetings deal with a certain problem area, for instance that of the global combustion of fuel droplets in a flow. Because of the inherent complexities involved in such flows, the analytical effort has been mostly confined to over-simplified and over-idealized flow systems while the experimental effort has been mostly directed towards global measurements of flows found in industrial applications. The eminent need for a comprehensive review of the subject matter from an overall point of view over much of the whole field seems belatedly in order.

With the rapid and phenomenal developments of key research tools mostly in the last two decades, in particular those of modern digital computers, laser optics, and electronics, many of the previously unthinkable, rigorous investigations in real-life flows have gradually become feasible. It is against this background that this international conference on the aerothermodynamics in combustors is being held at this point in time.

This International Symposium involves the presentation of papers concerned with Flow and Thermodynamic Characteristics of Combustors, with emphasis on gas-turbine combustors and including information relevant to rocket motors, internal combustion engines and furnaces. It is expected to involve descriptions of experimental and numerical work which has been performed to aid understanding of physical processes including chemical kinetics, turbulent mixing, droplet dispersion, coalescence and evaporation, scalar transport, premixed and non-premixed combustion and radiation.

The area of the Pacific Basin is rapidly becoming one of the economic, scientific and technological centers of the world. This area meets successfully the changes in two key elements: the drastically diminishing cost of computer memory units and a fundamental renewal of production processes. The Republic of China on Taiwan is a small country in area (the size of the Netherlands) with a sizable population (20 million), making it one of the most densely populated areas in the world at 550 persons per square kilometer. It has practically no natural resources but abundant educated manpower as a result of the centuries' old Chinese tradition of deep respect for education. It is this abundance of trained manpower, in particular in science and engineering, that has contributed in a major way to the country's rapid economic development making it a generally regarded shining example for the developing countries in the world. The per capita income has risen sharply from a mere US$60 in the early 1950s to the current level of about US$8,000—a rise of over ten thousand percent in a little over 30 years.

In face of the expected challenges of the 1990s, efforts are being made to restrain the growth of energy-intensive industries and spur the development of technology-intensive industries. Production technology and management will be upgraded to offset rising labor costs, while labor-intensive industries will be encouraged to automate their production processes and to develop more modern and efficient managerial skills. In the meantime, in order to provide the highly trained manpower needed for this restructuring of industry, institutions of higher education will place even greater emphasis on science and engineering. The Institute of Applied Mechanics of National Taiwan University, one the national centers of excellence in engineering, is proud to be the host of his important international conference.

Richard S. L. Lee (S. L. Lee)*
Institute of Applied Mechanics
National Taiwan University
Taipei, Taiwan, R. O. C.

J. H. Whitelaw
Dept. Mechanical Engineering
Emperial College
London, U. K.

T.-S. Wung
Inst. of Appl. Mech.
Nat'l Taiwan Univ.
Taipei, Taiwan, R. O. C.

*Department of Mechanical Engineering
State University of New York at Stony Brook
Stony Brook, New York 11794, U. S. A.

SYMPOSIUM TOPICS

The following topics have been chosen for the various sessions of the symposium:

- Calculations of combusting flows
- Experiments with combustion
- Instrumentation
- Cold-flow simulation
- Gas-turbine combustion
- Unsteady combustion
- Non-reacting two-phase flows
- Reacting two-phase flows
- Miscellaneous topics

SPONSORING AND SUPPORTING ORGANIZATIONS:

The symposium is sponsored and supported by the following organizations:

- International Union of Theoretical and Applied Mechanics
- National Science Council, Republic of China
- Ministry of Education, Republic of China
- Society of Theoretical and Applied Mechanics, Republic of China
- Chinese Society of Mechanical Engineers, Republic of China
- Chinese Society of Engineers, Republic of China
- Chinese Society of Chemical Engineers, Republic of China
- Chinese Society of Aeronautics and Astronautics, Republic of China
- National Taiwan University, Republic of China
- U. S. Army Research European Office

For any further information, please contact:

Prof. Richard S. L. Lee
Institute of Applied Mechanics
National Taiwan University
Taipei 10764, Taiwan
REPUBLIC OF CHINA
TEL: [886]-(2)-363-0979
FAX: [886]-(2)-363-9290
BITNET NO.: NTUIAM@TWNMOE10

SYMPOSIUM SCIENTIFIC COMMITTEE:

Chairman: Prof. R. S. L. Lee, National Taiwan University, Taipei, Taiwan, Republic of China.

Secretary: Prof. J. H. Whitelaw, Imperial College of Science, Technology and Medicine, London, U. K.

Prof. M. Barrere, ONERA, P. O. Box 72, F-92322 Chatilion sous Bagneux, France.

Prof. D. Bradley, Dept. of Mechanical Engineering, University of Leeds, LS29JT, U.K.

Prof. G. Chernyi, Institute of Mechanics, Moscow University, Mos-cow 117192, U. S. S. R.

Prof. F. Durst, Friedrich-Alexander-Universität Erlangen-Nünberg, Erlangen, Federal Republic of Germany.

Prof. G. J. Hwang, National Tsing Hua University, Hsinchu, Taiwan, Republic of China.

Prof. K. K. Kuo, Pennsylvania State University, University Park, PA 16802, U. S. A.

Prof. A. H. Lefebvre, Purdue University, West Lafayette, Indiana 47906, U. S. A.

Prof. Y. Mizutani, Osaka University, Osaka, 565 Japan.

Prof. N. Peters, RWTH Aachen, Tempergraben 55, D-5100 Aachen, Federal Republic of Germany.

LOCAL ARRANGEMENTS COMMITTEE:

Chairman: Prof. H. H. Chiu, National Cheng Kung University, Tainan.

Prof. K. C. Chang, National Cheng-Kung University, Tainan.

Prof. C.-H. Chen, National Chiao Tung University, Hsinchu.

Prof. S.-F. Chou, Prof. H. J. Sheen, Prof. T. S. Wung, National Taiwan University, Taipei.

Prof. J.-J. Hwang, National Sun Yat-sen University, Kaohsiung.

Dr. W.-B. Lee, Power Research Institute, Taipei.

Dr. C.-K. Lin, Aero-Industrial Development Center, Taichung.

Prof. T. M. Liou, Chung Hua Institute of Technology, Tsinchu.

Dr. B. Y.-P. Su, Chung Shan Institute of Science and Technology, Lungtain.

Prof. J.-T. Yang, National Tsing Hua University, Hsinchu.

Dr. S.-C. Yang, Industrial Technology Research Institute, Hsinchu.

TECHNICAL PROGRAM AND CONTENTS

Sunday, June 2, 1991

18:30–21:00 Registration and Reception

Monday, June 3, 1991

8:00–9:00 Registration.

9:00–9:30 Introductory Remarks.

- Prof. Richard S. L. Lee, Symposium Chairman, R.O.C.
- Prof. C. Sun, President, National Taiwan University, R.O.C.
- Prof. K. Z. Li, Chairman, Society of Theoretical and Applied Mechanics of Republic of China, R.O.C.

13:00–14:00 *Lunch Break*

IUTAM Symposium on
Aerothermodynamics in Combustors
June 3-5, 1991, Taipei

ADVANCED LASER DIAGNOSTICS: IMPLICATIONS OF RECENT RESULTS FOR ADVANCED COMBUSTOR MODELS

R.W. Bilger

Department of Mechanical Engineering
The University of Sydney, NSW 2006
Australia

INTRODUCTION

In association with colleagues at Sandia National Laboratories, Livermore, California, USA the combustion group at the University of Sydney has carried out a series of campaigns using the advanced laser diagnostics at Sandia in turbulent flames designed to have finite kinetic rates of the same order as the turbulent mixing rates. Masri et al [1] used laser Rayleigh scattering (LRS) and spontaneous Raman scattering (SRS) to make measurements of temperature and concentrations of CH_4, O_2, CO_2, H_2O, CO and H_2 in piloted–diffusion flames of methane near extinction. These measurements showed a strongly bimodal structure for the reactedness of species and temperature in stoichiometric and lean mixtures. On the other hand, flames with $CO/H_2/N_2$ mixtures as fuel [2,3] show this bimodality to a much lesser extent. These findings have given rise to questions of whether the bimodality (which is commonly found in premixed flames) is associated with fluid dynamic aspects of the flame or with chemical kinetic effects. The stoichiometric mixture fraction, ξ_s, is small (0.055) for undiluted methane/air and higher (~0.3) for $CO/H_2/N_2$ mixtures so that the stoichiometric isopleth surface for the latter will lie much more in the centre of the layer and seldom in the turbulent/non–turbulent superlayer. Measurements in flames using N_2– and air–diluted methane as fuel showed [4] bimodality that is much less pronounced than for undiluted methane, but is more pronounced than for $CO/H_2/N_2$ mixtures. The later results [3,4] include measurement of OH by laser induced fluorescence (LIF).

Two–dimensional (2D) imaging of flame chemi–luminescence and imaging of planar Rayleigh scattering (PLRS) and laser induced fluorescence (PLIF) of CH and OH have also been carried out [5,6] to give some elucidation of the spatial structure of these flames. For undiluted methane, reaction zones are flamelet–like and local extinctions in the flame sheet occur. For fuels with higher values of ξ_s, reacting and extinguished zones appear to be associated with the large eddy structures that are in the flow. In these latter flames and in the downstream regions of air–diluted methane flames, zones of OH are broad compared with the fine scales of the turbulence but the CH appears in narrow, highly contorted sheet–like structures.

This quest for the elucidation of flame structure has been given new impetus and direction by the development of a new conditional moment approach [7] to the analysis and modelling of turbulent reacting flow. This powerful new approach is considered to have great potential for analysing chemical kinetic effects in combustors and turbulent flames. As this work has only recently been submitted for publication it is appropriate to review it briefly before discussing the implications of the laser diagnostic results for modelling.

CONDITIONAL MOMENTS

Figure 1 shows scatter plots of temperature and OH mass fraction in a piloted diffusion flame of methanol [8] at $x/D_j = 20$ and $u_j = 66$ m/s where u_j and D_j are the velocity and diameter of the methanol vapour jet. The data points are for data at all three radii, $r/D_j = 1.1$, 1.4 and 1.7. The full curves are for a laminar counterflow diffusion flame calculation using Smooke's code [9] and for a strain rate parameter $a = 5\ s^{-1}$. At this jet velocity the flame is far from extinguishment and the data at any given mixture fraction are grouped over a narrow range about the conditional means Q_T, Q_{OH} where

$$Q_T(\eta,\underline{x}) \equiv < T(\underline{x},t) \,|\, \xi(\underline{x},t) = \eta > , \qquad (1)$$

$$Q_i(\eta,\underline{x}) = < Y_i(\underline{x},t) \,|\, \xi(\underline{x},t) = \eta > . \qquad (2)$$

Here $\xi(\underline{x},t)$ is the mixture fraction at the spatial point $\underline{x}$, at the time t, Y_i is the mass fraction of species i, η is a sample space variable corresponding to ξ, and the angle brackets and the vertical bar denote averaging conditional on the conditions to the right of the bar, it here being assumed that the flow is statistically stationary. More general definitions of conditional moments are given in Bilger [7] including those suitable for density–weighted averaging. Conditional higher moments such as the variance may be defined in a similar manner and even conditional probability density functions [1].

Figure 2 shows the conditional averages Q_T Q_{OH} for the data of Fig. 1 separated out for the three radii at which it was taken. It is seen that the data of Fig. 1 does, in general, lie close to these conditional means, and the conditional means are not a strong function of radial position in the flame. These two observations lie at the basis for the conditional moment closure method proposed for this type of flow. Of course, piloted turbulent diffusion flames which are close to extinction show much larger variance about the conditional mean. A doubly conditional moment closure is proposed for such flames.

CONDITIONAL MOMENT CLOSURE

Bilger [7] derives equations for the variation of Q_i defined as in Eqn (1) and Q_H defined as in Eqn (1) but for the standardized enthalpy H. The derived equations involve several terms which are difficult to evaluate at this stage, but which are hypothesized to be negligible. Furthermore, the assumption of negligible variation of Q_i with radius yields

$$\langle \rho u | \eta \rangle \frac{\partial Q_i}{\partial x} = \langle w_i | \eta \rangle + \frac{\mathcal{D}_i}{2\,\mathcal{D}} \langle \rho \chi | \eta \rangle \frac{\partial^2 Q_i}{\partial \eta^2} \qquad (3)$$

where ρ is the mass density, u the velocity component in the x (streamwise) cartesian coordinate direction, w_i the net mass rate of formation of species i per unit volume, χ the instantaneous scalar dissipation

$$\chi \equiv 2\mathcal{D}\nabla\xi\cdot\nabla\xi\,, \qquad (4)$$

$\mathcal{D}$ the species diffusivity associated with ξ, and $\mathcal{D}_i$ the diffusivity of species i. The equation for the standardized enthalpy conditional moment Q_H has no chemical source term but, instead, a radiation loss term. Methods for evaluating the conditional mass flux $\langle \rho u | \eta \rangle$ and scalar dissipation $\langle \rho \chi | \eta \rangle$ are given [7].

Closure of the set of Eqns (3) for all the species i requires evaluation of the conditional average reaction rate $\langle w_i | \eta \rangle$. It is proposed that this be done using the conditional averages Q_i in the usual rate expressions together with a representative conditional temperature T_η deduced from Q_i and Q_H. The errors involved will be much less than using the conventional mean values $\tilde{Y}_i$ and $\tilde{T}$ in determining the conventional mean reaction rate $\bar{w}$. From Figs. 1 and 2 it can be seen that most of the variation of T and Y_{OH} can be associated with variation in the mixture fraction.

Equations (3) together with appropriate boundary conditions [7] represent a set of parabolic partial differential equations in x, η space and as such are relatively straight forward to solve. A similar transformation may be made for laminar flames [10] and an analogous form has been obtained for transient flamelets [11]. Solutions will be different from those of the counterflow diffusion flame due to the term on the LHS of Eqn (3), particularly in the near nozzle region of the flame where axial variations have been obtained. At this stage codes are being written for solution of Eqn (3) for turbulent jet diffusion flames and solutions are yet to be obtained. It is expected that predictions will be close to the conditional averages shown in Fig. 2. Solutions have been obtained for the case of an isothermal reacting scalar mixing layer [7], and agree quite well with measurements [12].

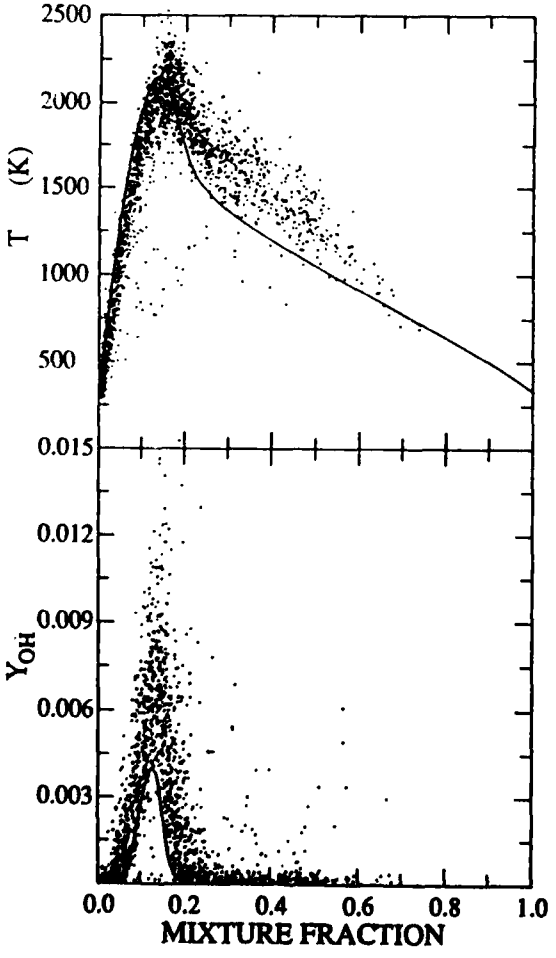

Fig. 1 Laser Raman/Rayleigh/fluorescence measurements in a piloted diffusion flame of methanol [8].

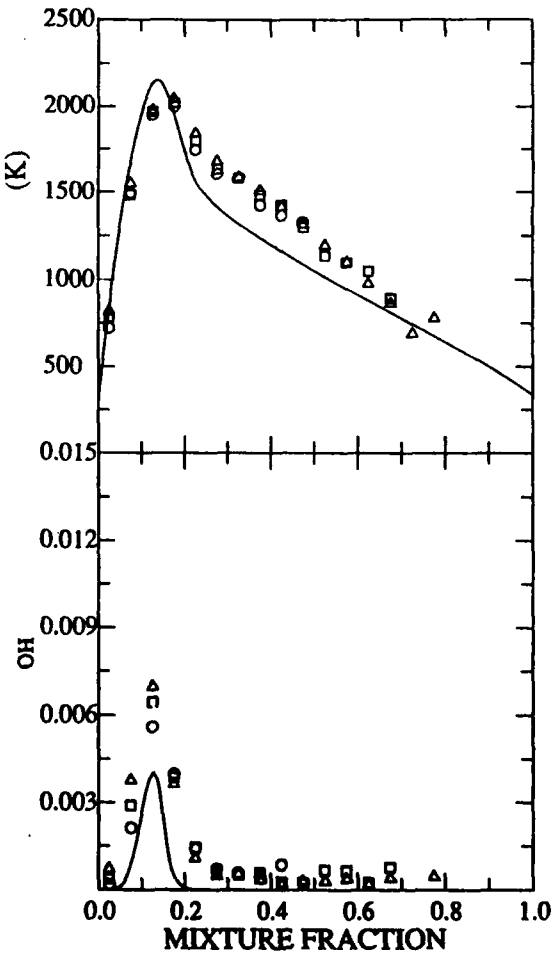

Fig. 2 Conditional averages Q_T of temperature and Q_{OH} of OH mass fraction for data of Fig. 1 separated for the three radii: r/D_j = 1.1 Δ, 1.4 □, 1.7 ○.

In the methanol flame the stoichiometric value of the mixture fraction, $\xi_s = 0.13$, and the reaction zone is not in the flamelet regime [13] since the width of the reaction zone in mixture fraction terms, $\Delta\xi_r \sim 0.16$ is much larger than the Kolmogoroff scalar scale $\Sigma_\xi \approx 1.4\xi' Re_t^{-\frac{1}{4}} \sim 0.06$. Here Re_t is the turbulence Reynolds number, which for this flame is of order 10^3, and ξ' is the rms mixture fraction fluctuation, which, in the shear layer near the nozzle is about 0.25. The conditional moment method, as in Eqn (3) for the first moment, does not distinguish between flamelet or turbulent reaction zones. This explains why data in the form of Fig. 1 has the same appearance at low values of jet velocity (low compared with those for extinction) whether the reaction zone is flamelet like or turbulent. The structure of the reaction zone will, however, enter into the equation for the conditional variance, as is discussed later.

Closer to extinction, the conditional variance of the data becomes large and the conditional data are sometimes distributed bimodally [1]. Here the conditional moment closure outlined above becomes inadequate and a doubly conditional moment approach becomes necessary. Before considering this, however, we can note in passing that the method of Eqn (3) using singly conditional moments will be very useful for predicting pollutants such as NO, CO and even soot in turbulent flames and combustors.

DOUBLY CONDITIONAL MOMENTS

Figure 3 shows conditional scatter plots of species mass fractions and temperature in a piloted turbulent diffusion flame of air–diluted methane. The data shown are for that fraction of the total data which lies close to stoichiometric. It is apparent that there would be a large scatter of the data about the singly conditional mean values and the closure of Eqn (3) will not be satisfactory. It is seen, however, that the data for the major species, CH_4, O_2, H_2O and CO_2 lie close to a mean line that could be drawn as a function of temperature. This line would be that through the doubly conditional averages

$$Q_i(\eta,\zeta,\underline{x}) \equiv < Y_i(\underline{x},t) | \xi(\underline{x},t) = \eta,\ c(\underline{x},t) = \zeta > \qquad (5)$$

where c is a reaction progress variable, such as temperature is in the present case, and ζ is its associated sample–space variable. The correlation for CO, H_2 and OH is not quite so good but this may be due to experimental error [7].

An equation is derived [7] for the doubly conditional averages, $Q_i(\eta,\zeta,x)$, which for statistically stationary flow, becomes, after neglecting terms hypothesized to be small,

$$< \rho u | \eta,\zeta > \frac{\partial Q_i}{\partial x} = < w_i | \eta,\zeta > + < w_c | \eta,\zeta > \frac{\partial Q_i}{\partial \zeta}$$
$$+ < \rho \mathscr{D}_i \nabla\xi\cdot\nabla\xi | \eta,\zeta > \frac{\partial^2 Q_i}{\partial \eta^2}$$
$$+ < \rho \mathscr{D}_i \nabla c\cdot\nabla c | \eta,\zeta > \frac{\partial^2 Q_i}{\partial \zeta^2}$$
$$+ < 2\,2\rho \mathscr{D}_i \nabla\xi\cdot\nabla c | \eta,\zeta > \frac{\partial^2 Q_i}{\partial\eta\partial\zeta}. \qquad (6)$$

Here it is assumed, again, that only variations in the direction of the streamwise coordinate, x, are significant. Closure for the conditional average reaction rates $< w_i | \eta,\zeta >$ and $< w_c | \eta,\zeta >$ is made at the order of $Q_i(\eta,\zeta,x)$ neglecting higher order terms. The modelling of the conditional dissipation–like terms $< \rho \mathscr{D}_i \nabla c\cdot\nabla c | \eta,\zeta >$ and $< 2\rho \mathscr{D}_i \nabla\xi\cdot\nabla\xi | \eta,\zeta >$ presents a challenge. Using appropriate boundary conditions [7] the modelled form of Eqn (6) may be solved to provide predictions of $Q_i(\eta,\zeta,x)$. It can be expected that these predictions will depend on the nature of the flow and other factors such as the amount of premixing. Thus $Q_i(\eta,\zeta,x)$ could be quite different in a lifted diffusion flame than in a piloted diffusion flame of the same fuel at jet velocities producing local extinction. The $Q_i(\eta,\zeta,x)$, while interesting in themselves and important for determining $< w_i | \eta,\zeta >$ and $< w_c | \eta,\zeta >$, will tell us nothing about the joint pdf of ξ and c which is needed to complete the modelling of the combustion process. The essential features of this joint pdf are embodied, however, in the conditional mean of c, $Q_c = <c|\eta>$, and its conditional variance, $V_c = <c'^2|\eta>$, where the prime here denotes fluctuation from the conditional mean. Equation (3) written for Q_c can be solved to provide predictions of Q_c, except that now $< w_c | \eta >$ is obtained by presumed form pdf closure

$$<w_c|\eta> = \int_\zeta < w_c | \eta,\zeta > p_{c|\eta}(\zeta) d\zeta \qquad (7)$$

where $p_{c|\eta}(\zeta)$ is the conditional pdf of c conditional on $\xi = \eta$. This conditional pdf will be evaluated using a presumed form and its predicted moments Q_c and V_c. In Eq. (7) $<w_c|\eta,\zeta>$ is evaluated using the doubly conditional first moment closure as in Eqn (6).

A balance equation for $V_c = V_c(\eta,x)$ has yet to be rigorously derived. It is apparent, however, that the major terms will include

$$<\rho u|\eta> \frac{\partial V_c}{\partial x} + \frac{\partial}{\partial x}\{<\rho u' c'^2|\eta>\}$$
$$+ 2< \rho u' c' | \eta > \frac{\partial Q_c}{\partial x} = 2 <w_c' c' | \eta>$$
$$-2<\rho \mathscr{D}\nabla c'\nabla c' | \eta > + < \rho(\mathscr{D}_c' \mathscr{D})\chi' c' | \eta > \frac{\partial^2 Q_c}{\partial \eta^2}. \qquad (8)$$

In this equation primes on w_c and χ denote fluctuation from their conditional mean value. Gradient modelling of the second and third terms on the LHS of Eq. (8) presents problems due to the well–known existence of countergradient fluxes in premixed flames [14]. The reaction rate correlation term $2<w'c'|\eta>$ can be evaluated by presumed form pdf closure as in Eq. (7). The second term on the RHS is the now familar conditional scalar dissipation of the reactive scalar which poses some challenge to model correctly so that it is valid, both at the flamelet and at distributed reaction zone limits.

The last term on the RHS embodies some interesting physics of the reaction zone structure. With c defined to be zero for unreacted mixing and positive when the mixture is reacted, $\partial^2 Q_c/\partial\eta^2$ is negative. Also the correlation between χ and c will be negative, since high values of χ will lead to mixing being faster than reaction locally and c being less than its conditional mean. This term is thus positive and a source contributing to the increase of V_c. The correlation between χ and c can be expected to be higher at the flamelet limit. When there is turbulence within the reaction zone local diffusion will smoooth out c′ to lower absolute values than if it followed the peaks and valleys of χ throughout the reaction zone.

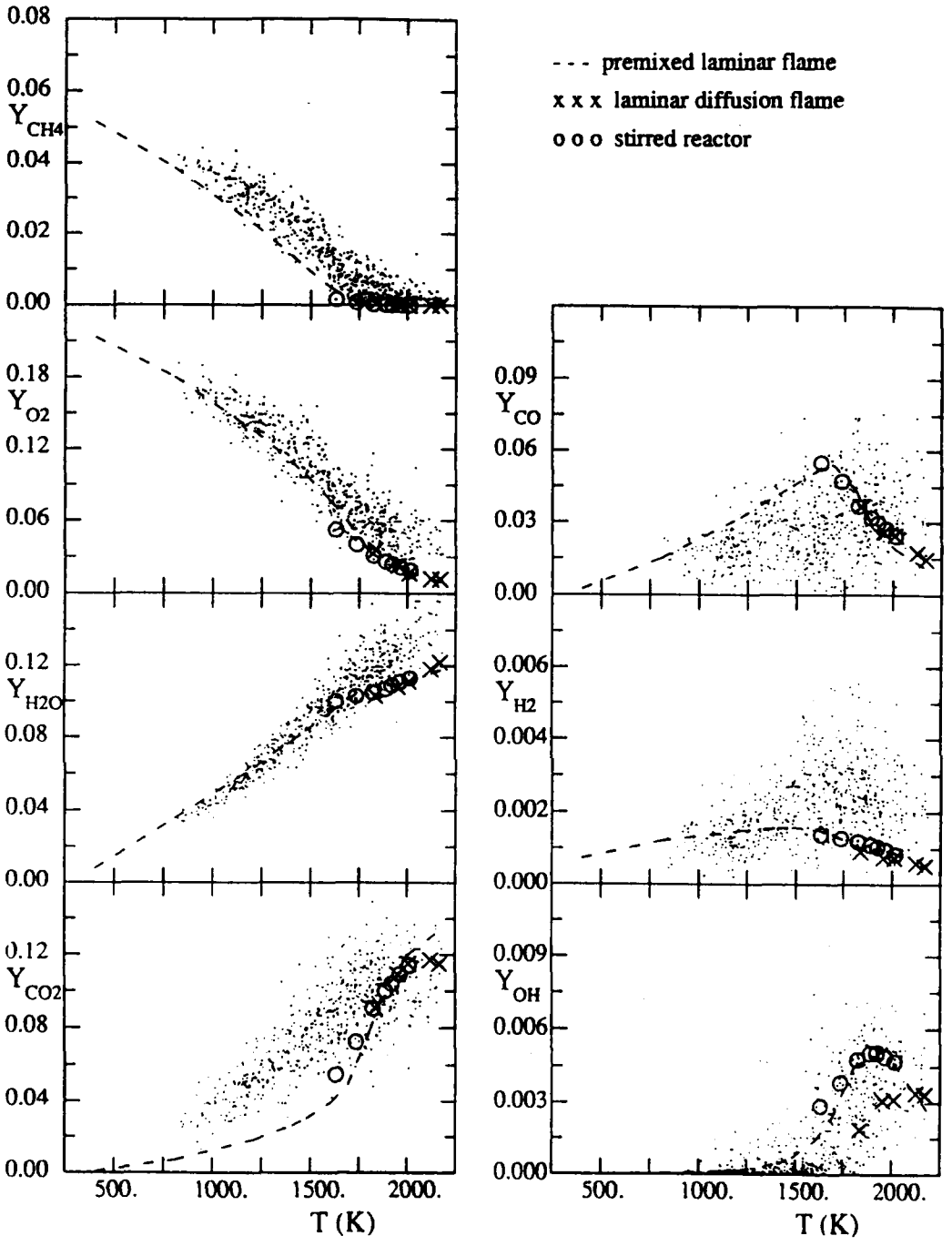

Fig 3. Correlation scatter plots of species mass fraction with temperature conditional on mixture fraction being close to stoichiometric for a piloted diffusion flame of methane diluted with air [4]. Correlations for laminar premixed and diffusion flames and for stirred reactors are also shown.

FLAME STRUCTURE AND MODELLING

The conditional moment theory gives us, then, insights into the interplay between flame structure and modelling and between the different aspects of flame structure. In nonpremixed flames the basic parameter is the ratio $\Omega \equiv \Delta\xi_r/\Sigma_\xi$. For $\Omega << 1$ the reaction zones are flamelet–like and the last term on the RHS of Eq (8) becomes large and the tendency for bimodal structure is strong. When $\Omega >> 1$ this term is much smaller and the tendency to bimodality is reduced. For hydrocarbon fuels the tendency to bimodality is also increased by the reaction rate correlation term, which is the first term on the RHS of Eq (8). For this to be positive Q_c must be less than the value $c_p(\eta)$ where $\langle w_c|\eta,\zeta\rangle$ peaks along the ζ coordinate. For hydrocarbon fuels this lies close to the maximum value of c possible at that η, whereas for $CO/H_2/N_2$ mixtures $c_p(\eta)$ is much more toward the middle of the range. Bimodal flame structure is thus a result of several factors operating through Eq. (8) rather than having a simple parametric dependence.

The thin reaction–sheet structures for CH found in hydrocarbon flames can be explained in terms of Ω for the inner reaction zone where CH is produced and consumed. This inner zone is much narrower in mixture fraction space, $\Delta\xi$, than for the OH reaction zone. Furthermore, laminar flame calculations indicate that $\Delta\xi_r$ decreases with χ while $\Delta\xi_r$ for OH is much less sensitive to χ.

ACKNOWLEDGEMENTS

This work is supported by the Australian Research Council. The contributions of S.B. Pope, S.H. Stårner, A.R. Masri, R.W. Dibble, R.S. Barlow and J.–Y. Chen to this work are gratefully acknowledged.

REFERENCES

1. Masri, A.R., Dibble, R.W. and Bilger, R.W. Combust. Flame, 74, 267–284 (1988)
2. Masri A.R. and Dibble, R.W. Twenty–second Symposium (International) on Combustion, The Combustion Institute, 1989, pp 607–618.
3. Stårner, S.H., Bilger, R.W., Dibble, R.W. and Barlow, R.S. "Piloted Diffusion Flames of CO, CH_4, N_2 and CO, H_2, N_2 Near Extinction" Combust. Flame (in press).
4. Stårner, S.H., Bilger, R.W., Dibble, R.W. and Barlow R.S. Combust. Sci. Technol. 72, 255–269, 1990.
5. Barlow, R.S., Dibble, R.W., Stårner, S.H., Bilger R.W., Fourguette, D.C. and Long, M.B. AIAA Paper 90–0732, January 1990.
6. Stårner, S.H., Bilger, R.W., Dibble, R.W., Barlow, R.S., Fourguette, D.C. and Long, M.B. "Joint Planar Rayleigh/LIF Imaging in Piloted Turbulent Jet Diffusion Flames Near Extinction" Combust Sci Technol (in preparation).
7. Bilger, R.W. "Conditional Moment Methods for Turbulent Reacting Flow Using Crocco Variable Conditions" Phys. Fluids A (submitted).
8. Masri, A.R. Personal Communication.
9. Smooke, M.D., Puri, I.K. and Seshadri, K. Twenty–first Symposium (International) on Combustion, The Combustion Institute, Pittsburgh, PA, 1987 pp 1783–1792.
10. Bilger, R.W. and Stårner, S.H. Combust. Flame 51, 155–176 (1983).
11. Haworth, D.C., Drake, M.C., Pope, S.B. and Blint, R.J. Twenty–Second Symposium (International) on Combustion, The Combustion Inst., Pittsburgh PA 1989, pp. 589–597.
12. Bilger, R.W., Saetran, L.R. and Krishnamoorthy, L.V. "Reaction in a Scalar Mixing Layer" J. Fluid Mech (to appear).
13. Bilger, R.W. Twenty–second Symposium (International) on Combustion, The Combustion Institute, Pittsburgh PA, 1989, pp. 475–488.
14. Moss, J.B. Combust. Sci. Technol, 22, 119–129 (1980).

IUTAM Symposium on
Aerothermodynamics in Combustors
June 3-5, 1991, Taipei

COMBUSTION RESEARCH FOR THE 21ST CENTURY - SOME SPECULATIVE EXTRAPOLATIONS

Felix Weinberg

Department of Chemical Engineering
Imperial College
London SW7 2BY

ABSTRACT

Seventeen years ago, at the Tokyo International Combustion Symposium, I was asked to give a personal overview of the past and future of combustion research in a plenary lecture[1]. Since then many remarkable changes which affect our subject have occurred. Having again been offered the opportunity, I cannot resist the occasion not only to survey the achievements of my former forecast but, more particularly, to assess the effects of developments and constraints which have arisen since then on projections for the future of combustion research.

As regards external constraints, we are, at the time of writing, in the throes of the fifth oil crisis in the last half-century (the emphasis on "the time of writing" is prompted by the surprising intermittency of this phenomenon, which is such that the prevailing state of euphoria may have reasserted itself by the time the Symposium is held), we have ushered in public environmental consciousness, we have discovered a hole in our ozone layer, and we are in the process of adding a relatively inert product of all fossil fuel combustion - carbon dioxide - to our list of potentially hazardous pollutants. As regards research developments, there has been quite a remarkable and continuing escalation in available computing power, as well as great strides forward in optical diagnostics - both of which have had the effect of prompting a substantial growth in our knowledge of fundamental kinetics On the other hand, some of the tools of this trade are very expensive, so much so as to place them almost beyond the means of researchers financed entirely by universities, a situation which has given rise to new kinds of research organisations. Affluent industrial research laboratories are well equiped to deal with these challenges but their studies tend to be largely "misson - oriented". On the political side also, the research pattern has been affected in disparate ways in different countries. In many of the Western democracies, governments have resolved that state - supported research should be motivated by profit rather than by curiosity and the rest of the world may be heading towards the same ideology. While some avenues of research have been attenuating, other new opportunities are emerging; combustion in microgravity, for example, has recently attracted much interest. Whilst the lecture will explore research strategies in response to such constraints, in the absence of a reliable crystal ball, the aim will be to provoke discussion rather than to offer any infallible insights - to which the speaker has no claim whatsoever.

Insecurity in oil supplies as well as recognition of carbon dioxide as a pollutant emphasises the need for research on combustor efficiency. Indeed energy conservation has become an anti - pollution measure. In addition to research on highly efficient, fuel saving, combustion methods generally, the combustion of hydrogen, and hydrogenation of fossil fuels (subject to hydrogen production methods which do not make large energy demands) are seen as important topics for research. Moreover, there is renewed interest in burning hydrocarbons, such as methane at very lean equivalence ratios because leakage into the atmosphere of such species increases the greenhouse effect disproportionately more than the equivalent amount of carbon dioxide. Great strides have been made in heat - recirculating burner systems[2] generally, but

their use has largely been confined to fuel saving and to incineration; their favourable thermodynamic efficiency remains largely unexploited.

More intricate questions arise as a result of government legislation: Research on lean-burn internal combustion engines involving, for example, ignition by radical - rich plasma or combustion driven jets has been attenuated in recent years consequent upon regulations favouring catalytic clean up of combustion generated pollutants. The new recognition of carbon dioxide as one of them ought to reverse this trend.

The remarkable and continuing rapid progress in computer modelling raises the question of whether we may eventually reach the state of being able to predict combustor performance without recourse to experimentation (and whether it might be less costly to do so). Although the computation time is proportional to the cube of the Reynold's Number of the flow system[3], even without taking chemical kinetics into account, the growth in speed has been exponential hitherto.

The concentration of expensive equipment in corporate research establishments has not led, and shows no sign that it is going to lead, to the greater availability of unaffordable research tools and computing facilities. The research aspirations of the guardians of these assets themselves ensure that they are fully employed. However, innovative and fundamental research is both necessary and often relatively inexpensive. Modern tools sometimes offer a choice between solving problems and trampling them to death. Thus verifying particular steps in proposed reaction mechanisms by fitting computer predictions to complex combustor behaviour is likely to be much less efficient and reliable than studying them individually. Great strides have been made in advanced combustion methods[2] but much more remains to be done. Science can only advise technology - practical innovations generally arise not from inventions but out of needs. However, our needs appear to be escalating by the day. The lecture will offer a personal view of various promising lines of development.

References

1. Weinberg, F.J., "The First Half-Million Years of Combustion Research and Today's Burning Problems", 15th Symposium (Int.) on Combustion, The Combustion Institute, Pittsburgh (1975).

2. "Advanced Combustion Methods", Weinberg, F.J. (Ed), Academic Press, London and New York (1986).

3. Jones, W.P. Private communication, (1990).

IUTAM Symposium on
Aerothermodynamics in Combustors
June 3-5, 1991, Taipei

Combustor Modeling Using a Flame Sheet Model

Ming-Chia Lai, Tsan-Hai Chue

Mechanical Engineering Dept.
Wayne State University
Detroit, MI 48202, USA

Wai K. Cheng

Mechanical Engineering Dept.
M. I. T.
Cambridge, MA 02139, USA

ABSTRACT

A flame sheet model for heat release is implemented into KIVA-II (Amsden et al., 1989) program for three dimensional (3D) simulation of spray combustion. The sensitivity of the model is first studied in a non-swirling test case; the simulation is then applied to a swirl can combustor and compared with experimental data. The performance of the scheme is generally good, but limited by the capability of k-ϵ model to predict swirling flows. The model is structured so that the fluid mechanics is decoupled from the reaction chemistry which is calculated off-line and incorporated into the 3D numerical simulation via a look-up table. This approach provides a structure for implementation of kinetically based as well as phenomenologically based emission models.

SUMMARY

A major difficulty in the 3D modelling of turbulent combustion processes such as those found in gas-turbine and diesel engine combustors is in the calculation of the chemical reaction terms. This difficulty arises because in all practical cases, the computational cell size used in the calculation could not resolve the composition and temperature non-uniformity. The flow variables used in the calculation are often interpreted as averaged quantities. The chemical reaction rates, however, are usually nonlinear functions of compositions and temperature so that even if the kinetics are well known, the use of the averaged quantities in the kinetic expression will give an incorrect rate. Empirically based "pseudo-kinetics" were often used, but the results were far from satisfactory. Typically, if an Arrhenius rate expression is used, the calculation would erroneously predict temperature and burn rate because a "homogeneously" burning computation cell could not describe, for example, a mixing controlled burning process where the actual burning occurs only at a thin interface between the fuel and air. Therefore there is a need to develop a flame structure based model to connect the chemistry to the 3D computation for both the premixed and diffusion combustion.

A second difficulty lies in the computation intensity required in implementing kinetic schemes in 3D calculations. The rate equations are usually stiff and sensitive to temperature. Any moderately complicated scheme (say ten reaction) would require a tremendous amount of computation time if an engineering parametric study matrix is to be done. Therefore a flame structure based model which can use a pre-determined rate of, say heat release or pollutants (such as NOx or soot) production per flame structure would be computationally attractive.

A flame sheet model has been applied to both premixed and diffusion engine combustion to alleviate the above difficulties (Cheng et al. 1991). The concept was first proposed by Marble and Broadwell (1977), a more detail discussion may be found in references (Cheng, 1983; Peters, 1986). The present study is limited to the application to spray (diffusion) combustor. The model relies on the fact that in mixing controlled combustion in practical engines, the chemical reaction rate is fast compared to the mixing rate. The actual burning process therefore takes place locally as thin laminar flames surfaces between fuel and oxidizer pockets which have length scales similar to the turbulent eddies. This locally laminar flame is kept in quasi-equilibrium by the turbulent stretching of the fluid elements. The combustion process could then be modelled as a collection of flame surfaces embedded in the strain field of the turbulent eddies. The separation of scales (that the flame surface is thin compared to the eddy size) allows the chemistry and the fluid mechanics to be decoupled. Therefore the 3D calculation needs only to calculate the density of the flame surfaces (flame surface area per unit volume) and the heat release rate and production rates of NOx emission per unit flame surface area are pre-calculated in a separate calculation using the proper kinetic expressions and heat release rates for an one-dimensional stretched flame.

The above scheme explicitly models the spatial non-uniformity within a computational cell by the use of the flame sheets. The computational effort required is quite modest - it requires only to keep tract of the flame surface area per unit volume which is calculated as if this quantity is an extra " species". The 3D computation time is thus independent of the complexity of the chemical kinetics because the chemistry is calculated in a one dimensional stretched flame model separately and the results are to be used in the 3D calculation as stored look-up tables.

Following the formulation of Cheng, Lai and Chue (1991), the transport equation of flame sheet density Σ is:

$$\frac{\partial \Sigma}{\partial t} + \nabla\cdot(u\Sigma) = s\Sigma - \frac{\beta}{\rho}\left(\frac{J_1}{Y_1} + \frac{J_2}{Y_2}\right)\Sigma^2 + \frac{1}{\rho}\nabla\cdot(\rho D_t \nabla \Sigma)$$

where $\quad s = +\alpha e \quad$ *for* $\quad e < e_*$

$$s = -\gamma(e - e_*) \quad \text{for} \quad e > e_*$$

is the source term of Σ due to turbulent stretching of the flame area by the mean strain rate $e = c_e\epsilon/k$, or the sink term due to flame extinction when a critical strain rate e_c (on the order of 10^{-3}/s at atmospheric pressure) is reached. The second term on the RHS is the flame sheet consumption due to the fuel and oxidizer consumption fluxes J_1 and J_2. A simple analytical expression for J_1 (under the assumptions of constant density and diffusivity, and unity Lewis number) can be used if one-dimensional stretched flame calculation is bypassed:

$$J_1 = \frac{\rho(\phi Y_2 + Y_1)}{\sqrt{2\pi}}\sqrt{De}\cdot\exp\{[-erf^{-1}(\xi)]^2\}$$

where $\xi = (\phi Y_2 - Y_1)/(\phi Y_2 + Y_1)$, and ϕ is the stoichiometric air/fuel ratio. As in $k-\epsilon$ model, the turbulent diffusivity of D_t, is taken as $c_\mu k^2/(\rho\epsilon)$. The model constants α, β, C_e were all taken to be 5, and γ was taken to be 1.

As a test case, the model was used to simulate an axi-symmetric spray flame in a duct of 5 cm radius. The computational domain consists of 10 radial by 20 axial cells covering an axial distance of 20 cm. The downstream pressure was atmospheric, and the upstream air velocity and mass flow rate were 3 m/s and 0.028 kg/s. The upstream turbulence level was 10 percent. The fuel was diesel fuel and was injected at 1.38 g/s (air/fuel ratio 20). The fuel jet was a hollow cone distributed evenly from half cone angle of 17.5 to 32.5 degrees. For simplicity, the fuel drops were represented with an Sauter Mean Radius of 30μm, and with an injection velocity of 50 m/s.

Figure 1 shows the velocity vectors of droplet parcels; substantial droplet impingement on the wall is evident. As a result, the converged global energy release rate (takes about 40 seconds Cray 2 CPU time) is only about 77% of the injected rate of fuel energy. The temperature map and flame sheet density Σ are plotted in figures 2 and 3. The most intense burning occurs at the outer edge of the fuel jet where the shear rate generated by the jet is highest. The flame density density distribution is higher at the outer edge than the inner edge, because there is more air available at the outer edge. The sensitivity of the model prediction to the constants α and β was studied by varying their values from the baseline values of 5, and observing their effects on the burned fuel mass fraction, which is defined as the ratio of the total release rate of sensible internal energy over the computational domain to the injection rate of fuel energy. Figure 4 shows that burned fraction collapses to a single curve, indicating that the flame sheet density in mostly in equilibrium.

The experiment of Khalil and Whitelaw (1976) was chosen for comparison to the model predictions, similar to the works of El-Banhawy and Whitelaw (1980), and Shuen (1986). The test geometry of the swirl combustor is shown in Figure 5, and comparison for is shown in Figure 6 for the 0.72 swirl number case. The agreement is generally good, but limited by the capability of the baseline $k-\epsilon$ model to predict swirling flows (similar to finding of Shuen, 1986).

This approach provides a structure for implementation of kinetically based as well as phenomenologically based emission models. The calculation of 1D stretched flame calculation and its application to NOx formation in methane flame has been discussed by Cheng (1983). Further applications to practical combustor will also be discussed.

REFERENCES

Amsden, A. A., O'Rourke, P. J. and Butler, T. D., (1989), "KIVA-II, A Computer Program for Chemically Reactive Flows with Sprays," Report LA-11560-MS, Los Alamos National Laboratory, Los Alamos, New Mexico 87545.

Cheng, W. K., (1983), "Calculation of Turbulent Diffusion Flame Using the Coherent Flame Sheet Model," AIAA Paper 83-1322.

Cheng, W. K. and Diringer, J.A. (1991), "Numerical Modelling of SI Engine Combustion with a Flame Sheet Model," SAE paper 910268, 1991 SAE International Congress.

Cheng, W. K., Lai, M.-C., and Chue, T.-H. (1991), "Multi-Dimensional Modelling of Gas Turbine Combustion using a Flame Sheet Model," AIAA paper 91-0414.

El-Banhawy, Y. and Whitelaw, J. H., (1980), "Calculation of the Flow Properties of a Confined Kerosene-Spray Flame," AIAA J. , Vol. 18(12), pp. 1503-1510.

Khalil, E. E., and Whitelaw, J. H., (1977), "Aerodynamic and Thermodynamic Characteristics of Kerosene-Spray Flame," 16th symp. (Int.) on Combust. pp. 569-576.

Marble, F. E., and Broadwell, J. E., (1977) "The Coherent Flame Model for Turbulent Chemical Reactions," Project SQUID, Technical Report TRW-9-PU.

Peters, N. (1986) "Laminar Flamelet Concepts in Turbulent Combustion," 21st Symp. (Int'l) on Combustion, pp. 1231-1250.

Shuen, J.-S., (1987), "Prediction of the Structure of Fuel Sprays in Cylindrical Combustion Chambers," J. Propulsion & Power, Vol. 3(2), pp. 105-113.

Veynante, D., Lacas, F., and Candel, S., (1989), "A New Flamelet Combustion Model Combining Premixed and Non-Premixed Turbulent Flames," AIAA paper 89-0487.

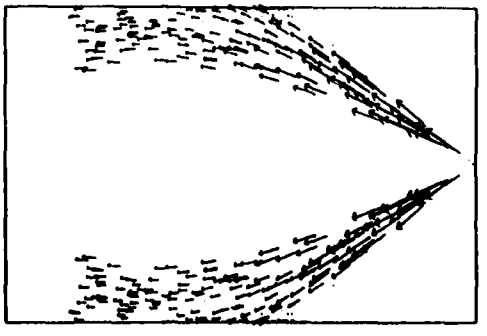

Fig. 1 Velocity vectors of droplet parcels. The maximum velocity is 48 m/s.

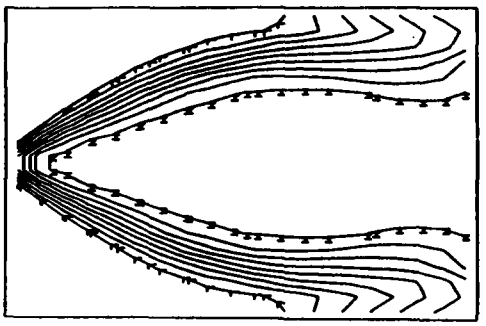

Fig. 2 Contours of temperature. The labels H and L denote 2100 ^{o}K, and 500 ^{o}K; the contours are plotted at intervals of 200 ^{o}K.

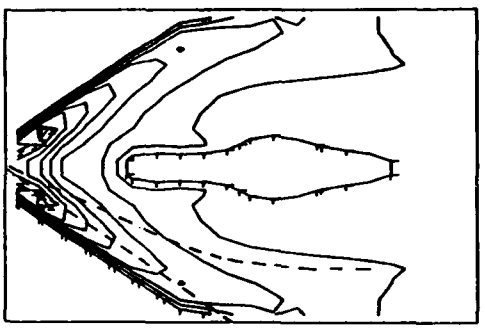

Fig. 3 Contours of flame sheet density. The labels H and L denote 36 cm^{-1} and 4 cm^{-1}; the contours are plotted in intervals of 4 cm^{-1}. The dotted lines represented the spray outline on the right half plane.

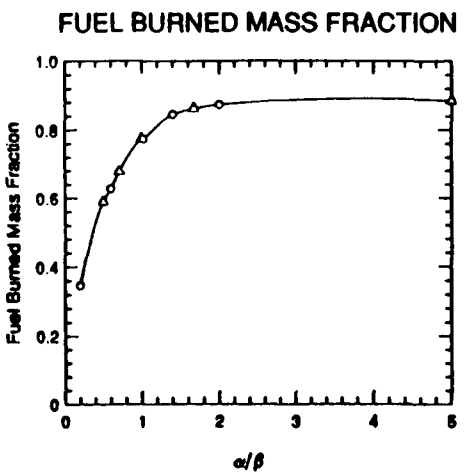

Fig. 4 Fuel burned mass fraction as a function of α/β. The circles are for cases of fixing β at 5, and the triangles for cases of fixing α at 5.

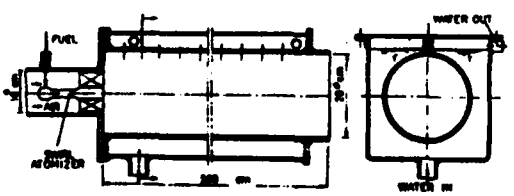

Fig. 5 Geometry of the swirl combustor experiment of Khalil and Whitelaw (1976).

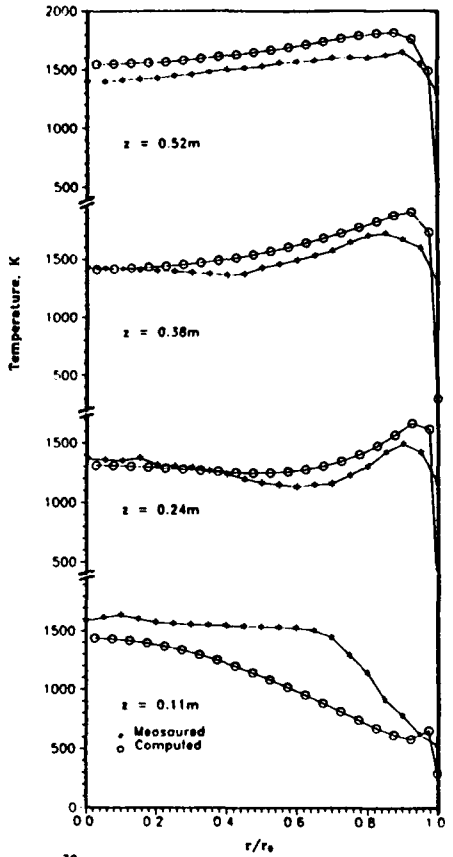

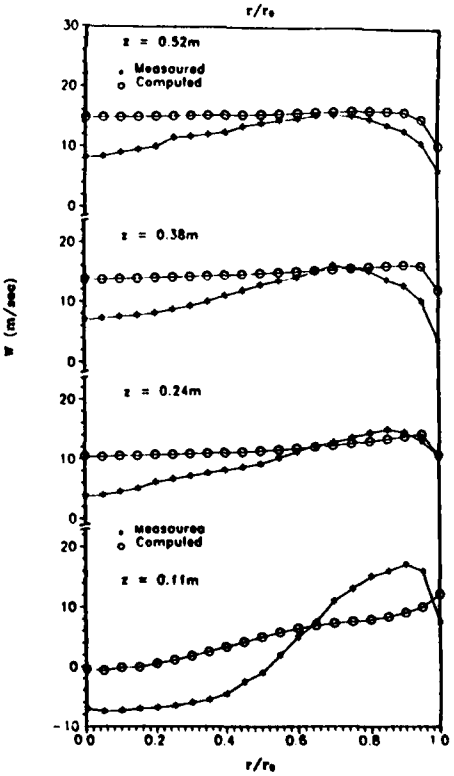

Fig. 6 Comparsion of model predictions of axial velocity and temperature profiles with measurements at different downstream locations.

IUTAM Symposium on
Aerothermodynamics in Combustors
June 3-5, 1991, Taipei

A UNIFIED MODEL OF MEAN REACTION RATE IN TURBULENT PREMIXED FLAMES

M. KATSUKI, Y. MIZUTANI, T. YOSHIDA and T. YASUDA

OSAKA UNIVERSITY
DEPARTMENT OF MECHANICAL ENGINEERING
2-1 YAMADA-OKA, SUITA, OSAKA 565 JAPAN

INTRODUCTION

Recent progress in numerical fluid dynamics has been expanding into the direct simulation of three-dimensional, time-dependent turbulent reacting flows. Nevertheless, the simulation of this kind for practical combustors and furnaces of complex geometry seems yet unrealistic due to the insufficient capacity of existing computers. To satisfy the practical requirements in combustion engineering, therefore, we are obliged to restrict ourselves at present to solving the time-averaged balance equations for fluctuating properties associated with proper boundary conditions. In order to close the time-averaged conservation equations of the first moment for turbulent reacting flows, not only a turbulence model but also a *turbulent reaction* model which gives a mean reaction rate in turbulence is necessary.

The reaction models based on Bray-Moss-Libby's concept are widely accepted recently [1,2]. They should be applied to the flames, the thickness of which is far thinner than the scale of dissipating eddies. In extremely intense turbulence, however, the eddy motion breaks a flame-sheet into reacting gas particles of comparable to the laminar flame thickness. Thus, we need a new reaction model widely applicable to the flames in intense turbulence of small scale as well as laminar flamelets.

Some basic concepts of the fine structure of turbulent premixed flames are roughly classified into two kinds in terms of the Damköhler number, Da, defined as the ratio of the characteristic time for turbulent mixing τ_m to that for chemical reaction τ_c. The so-called "wrinkled laminar flame" or "laminar flamelets" appears when Da is large and the dissipating eddy-scale is larger than the laminar flame thickness, whereas the "distributed reaction zone" appears when Da is small and the scale of dissipating eddies is smaller than the laminar flame thickness. The reaction rates at these two extremes are dominated by chemistry and mixing, respectively. The objective of the present study is to develop a unified model of mean reaction rate in turbulent premixed flames applicable over a wide range of Damköhler number.

EXPERIMENTS

In our previous study [3,4], we observed confined turbulent premixed flames stabilized by a pilot flame in a 50 x 50 mm^2 square duct to elucidate the local fine structure of flames and its influence on mixing processes.

Figure 1 shows the schlieren photographs of the observed flames. Mixtures of natural gas, which was 88% methane, and air having the same equivalence ratio, ϕ_m, with nominal velocities U_1 and U_2, respectively, flowed on either side of the centered pilot burner. The pilot flame was a hydrogen-air premixed flame with an equivalence ratio, ϕ_p, of 0.6. The initial turbulence intensities, u_1' and u_2' were varied by inserting a turbulence generating grid 30 mm upstream of the pilot port. More details are found in Ref.[3].

We classified local fine flame structures based on the measured turbulence *characteristics, and examined the probability* density functions (PDF's) of fluctuating properties in detail [4]. Figure 2 shows PDF's of temperature fluctuations observed at the positions pointed in Fig.1.

Because the fast-chemistry makes a PDF bimodal, such a distribution observed at point B, corresponding to the structure of a "laminar flamelets", appears in many turbulent flames. In contrast, a plateaulike distribution observed at point C is resulted by the interference of reaction by the mixing in extremely intense turbulence with the smaller scale less than the laminar flame thickness, which may correspond to the structure of "distributed reaction zone".

We concluded that the shape of PDF varies with the degree of the interaction between reaction and turbulence, hence the local Damköhler number in flames.

GOVERNING EQUATIONS

The present model has been developed to predict time-averaged profiles of velocities, temperature and species concentrations in combustors, and to be incorporated into the time-averaged version of conservation equations for mass, momentum, enthalpy, and species mass fractions. Additional equations for turbulence energy k and its dissipation rate ϵ are solved in the present model to express turbulent transport.

The Favre-averaging (density weighted averaging) is adopted to take the effect of variable density into account. For a steady two-dimensional flow, the governing equations for the above variables can be cast into the following general form using the general

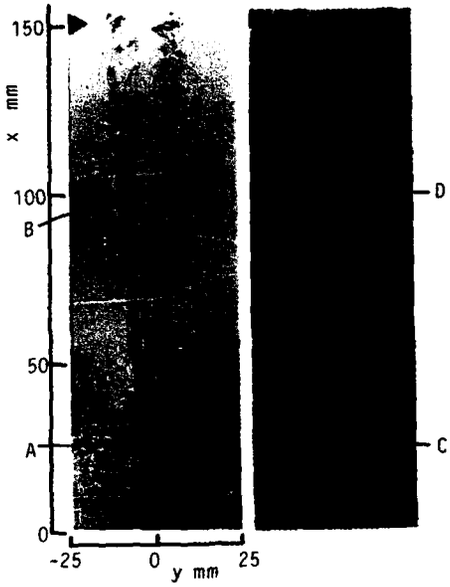

(a) Flame I (b) Flame II

Fig.1 Schlieren images of flames

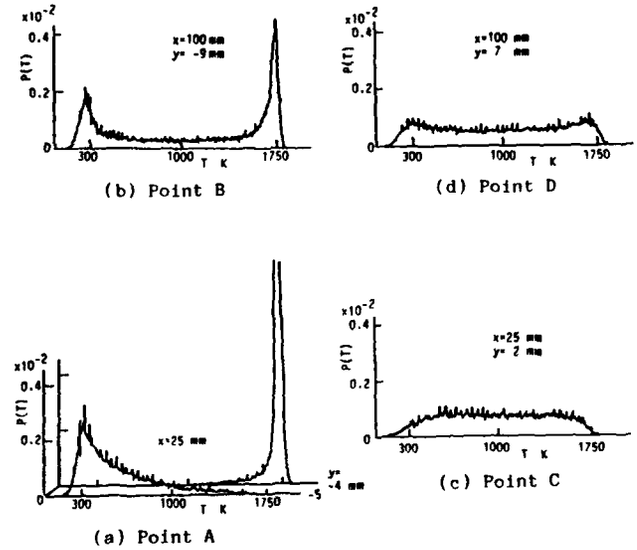

Fig.2 PDF's of temperature fluctuations

Table 1 Exchange coefficient and source term in the general conservation equation (1)

ϕ	Γ	S
1	0	0
u	μ_{eff}	$\frac{\partial}{\partial x}(\mu_{eff}\frac{\partial u}{\partial x})+\frac{\partial}{\partial y}(\mu_{eff}\frac{\partial v}{\partial x})-\frac{\partial}{\partial x}\{p+\frac{2}{3}(\rho k+\mu_{eff}\,\mathrm{div}\,\vec{U})\}$
v	μ_{eff}	$\frac{\partial}{\partial x}(\mu_{eff}\frac{\partial u}{\partial y})+\frac{\partial}{\partial y}(\mu_{eff}\frac{\partial v}{\partial y})-\frac{\partial}{\partial y}\{p+\frac{2}{3}(\rho k+\mu_{eff}\,\mathrm{div}\,\vec{U})\}$
k	μ_{eff}/σ_k	$G_t^*-\rho\varepsilon$
ε	$\mu_{eff}/\sigma_\varepsilon$	$c_1 G_t^*\varepsilon/k-c_2\rho\varepsilon^2/k$
h	μ_{eff}/σ_h	0
m_{fu}	μ_{eff}/σ_α	R_{fu}

$$G_t=\mu_{eff}[2\{(\frac{\partial u}{\partial x})^2+(\frac{\partial v}{\partial y})^2\}+(\frac{\partial u}{\partial y}+\frac{\partial v}{\partial x})^2]$$

$$G_t^*=G_t-\frac{2}{3}\,\mathrm{div}\,\vec{U}(\mu_t\,\mathrm{div}\,\vec{U}+\rho k)-\frac{\mu_t}{\rho^2}(\frac{\partial\rho}{\partial x}\frac{\partial p}{\partial x}+\frac{\partial\rho}{\partial y}\frac{\partial p}{\partial y})-\frac{9}{55}\rho k\,\mathrm{div}\,\vec{U}$$

$$\mathrm{div}\,\vec{U}=\frac{\partial u}{\partial x}+\frac{\partial v}{\partial y}$$

Table 2 Empirical constants and turbulent Prandtl numbers

c_μ	c_1	c_2	σ_k
0.09	1.44	1.92	1.0

σ_ε	σ_h	σ_α
1.3	0.7	0.7

dependent variable ϕ:

$$\frac{\partial}{\partial x}(\rho u\phi)+\frac{\partial}{\partial y}(\rho v\phi)$$

$$-\frac{\partial}{\partial x}(\Gamma\frac{\partial\phi}{\partial x})-\frac{\partial}{\partial y}(\Gamma\frac{\partial\phi}{\partial y})=S \qquad (1)$$

The dependent variable, the exchange coefficient and the source term for each conservation equation are tabulated in Table 1 [5]. The empirical constants appearing in the k - ε turbulence model and turbulent Prandtl numbers for the dependent variables are shown in Table 2 [6]. Because the governing equations are discretized in the numerical procedure, the source term, R_{fu}, of fuel mass fraction should represent the spatially- and temporally-integrated reaction rate over the finite volume of a computational grid.

COMBUSTION MODEL

Visual length of flames and mixing processes in a combustor are primarily governed by the large scale motions of turbulence, but combustion reaction is believed to be closely related to the fine structure of turbulence. The turbulent combustion model, therefore, cannot be embodied without taking the fine structure of turbulence into account.

As described previously, a local mean reaction rate depends on the interaction of chemistry with turbulence. We assume that the reaction rate is the sum of chemistry-controlled and mixing-controlled rates. Thus, the local mean reaction rate, R_{fu}, appears in the conservation equation of fuel is expressed as

$$R_{fu}=R_c\{1-\exp(-k_1 Da)\}+R_m\exp(-k_1 Da) \qquad (2)$$

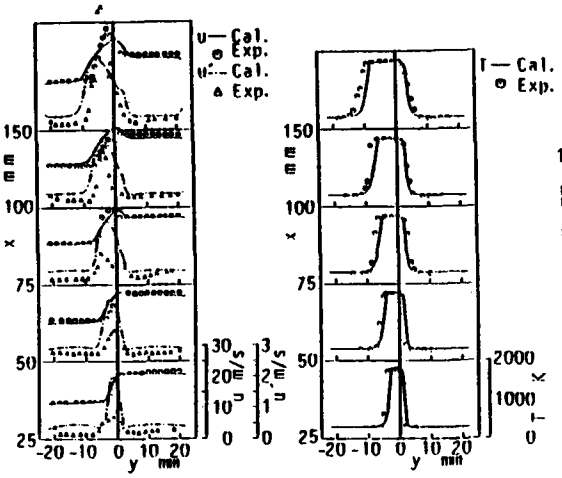

Fig.3 Comparison of predicted profiles with experiments (Flame I)

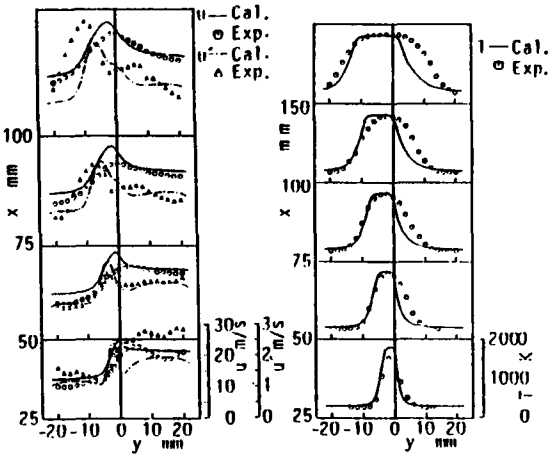

Fig.4 Comparison of predicted profiles with experiments (Flame II)

where k_1 is an empirical constant, R_c and R_m are the chemistry-controlled and the mixing-controlled reaction rates, respectively. The local Damköhler number, Da, is expressed as

$$Da = \tau_m/\tau_c = (\ell/u')/(\delta_L/S_L) \qquad (3)$$

where δ_L and S_L are the laminar flame thickness and the laminar burning velocity, respectively. The length scale ℓ and the turbulence intensity u' are evaluated from the local turbulent quantities, k and ε.

The chemistry-controlled reaction rate is evaluated by Arrhenius law taking account of the influence of fluctuations in temperature and concentrations as follows.

$$R_c = -F\rho^2 m_{fu} m_{ox} \exp(-E/RT)\{1 + X\} \qquad (4)$$

where X denotes the expansion terms of fluctuating components [7].

Following the eddy-break-up concept [8,9], the mixing-controlled reaction rate is related to the dissipation rate of turbulence and the probability of contact of burned gas with unburned reactants as follows.

$$R_m = -A\rho\{V_b(1 - V_b)\}^{1/2}\,\varepsilon/k \qquad (5)$$

where A denotes an empirical constant including a shape factor, and V_b is the volume fraction of burnt gas, which is estimated from the reactedness, ζ. The local reactedness ζ is defined as follows using the local mass fraction of fuel m_{fu}.

$$\zeta = (m_{fu} - m_{fu,b})/(m_{fu,u} - m_{fu,b}) \qquad (6)$$

where $m_{fu,b}$ and $m_{fu,u}$ are the fuel mass fractions in the fully burnt gas and unburned reactants, respectively.

In order to examine the validity of the proposed model, some numerical calculations were carried out with the inlet conditions equivalent to those of flames observed in the experiment.

The predicted profiles of mean axial velocity component, turbulence intensity and mean temperature for Flame I are shown in Fig.3 accompanying the measured data. The global agreement is excellent when the wrinkle laminar flame structure dominates the whole flame. In contrast, the agreement between prediction and experiment for Flame II in Fig.4, which is the case of strongly-turbulent, is deteriorated probably due to the fact that the actual anisotropy of turbulence cannot be well predicted by k - ε turbulence model.

CONCLUSION

In formulating the time-averaged conservation equations for turbulent reacting flows, we have discussed the expression of the time-mean reaction rate applicable to various flames over a wide range of Damköhler number. The rate was expressed by the contributions of chemistry and mixing which depends upon the local flame structure, hence the local Damköhler number.

Due to our limited knowledge of the interaction between reaction and turbulence, some modifications of the present model may be needed later. In the present study, however, the numerical predictions have demonstrated the capability of the concept and its applicability to premixed flames.

REFERENCES

[1] Liew, S.K., Bray, K.N.C. and Moss, J.B., Combustion Flame, 56(1984), 199.

[2] Peters, N., Progress in Energy and Combustion Science, 10(1984), 319.

[3] Katsuki, M., Mizutani, Y., Yasuda, T., Kurosawa, Y., Kobayashi, K. and Takahashi, T., Combustion Flame, 79(1988), 9.

[4] Katsuki, M., Mizutani, Y., Yasuda, T., Kurosawa, Y., Kobayashi, K. and Takahashi, T., Combustion Flame, 82(1990), 93.

[5] Bradley, D., Kwa, L.K., Lau, A.K.C. Missaghi, M. and Chin, S.B., Combustion Flame, 71(1988), 109.

[6] Khalil, E.E., Spalding, D.B., Whitelaw, J.H., Int. J. Heat Mass Transfer, 18(1975), 775.

[7] Borghi, R., Adv. Geophys., 18B(1974), 349.

[8] Spalding, D.B., 13th Symp. (Int.) on Combust., (1971), p.649, The Combustion Institute.

[9] Lockwood, F.C., Combustion Flame, 29(1977), 111.

IUTAM Symposium on
Aerothermodynamics in Combustors
June 3-5, 1991, Taipei

The Influence of Upstream Prevaporization on Flame Extinction of One-Dimensional Dilute Sprays

Chi-Chang Liu and Ta-Hui Lin

Department of Mechanical Engineering
National Cheng-Kung University
Tainan, Taiwan 70101 R.O.C.

INTRODUCTION

The flame extinction of a dilute spray burning in a steady, one-dimensional, low-speed, sufficiently off-stoichiometric, two-phase flow was initially reported by Huang et al. [1]. The mathematical technique was based on the large activation-energy asymptotics introduced to spray studies by Lin et al. [2] and Lin and Sheu [3]. Results showed that a continuous increase of the liquid fuel loading, or decrease of the initial droplet size, results in flame extinction for a rich spray, while no flame extinction occurs for a lean spray. The S-shaped extinction curve (a triple-valued function) for a rich spray was in agreement with Mitani's analysis [4] on the heterogeneous inhibition of premixed flames by chemical inert dust or spray. By introducing the external heat loss represented by the buck heat conduction from the system to the surrounding, to compete with the internal heat loss associated with the droplet gasification process, Liu and Lin [5] found that there only exists C-shaped extinction curves (double-valued functions) for both lean and rich sprays. Furthermore, the flame flux at extinction for a lean spray was first increased, then decreased, and finally approached to $exp(-0.5)$ with increasing the droplet radius; but the correspondingly asymptotic value of the external heat loss was slightly larger than $exp(-1.0)$. For a rich spray, the flame flux at extinction was monotonically increased with increasing the initial droplet radius or decreasing the liquid fuel loading.

From the previous study [5], it is clear that the influence of the internal heat loss on flame extinction is weakened by the introduction of the external heat loss to the system. To understand the whole spectrum on the upstream interaction between external and internal heat losses, we now try to enhance the upstream prevaporization of liquid fuel by varying the surrounding temperature in this study. The detailed discussion will be focussed on the flame extinction curve, the flame flux at extinction, and the critical condition of liquid fuel at extinction.

CONFIGURATION AND ASSUMPTIONS

We consider a one-dimensional system in which a plane flame sits at the origin ($x = 0$), the two-phase combustible mixture comes from $x = -\infty$ and equilibrium reaction products move away toward $x = +\infty$, as shown in Fig.1. The combustible mixture consists of various concentrations of oxidizer, inert, fuel vapor, and fuel droplets of a certain radius. To achieve the asymptotic analysis, we assumed that the spray is monodisperse and dilute, with the amount of liquid loading being $O(\varepsilon)$ of the total spray mass. The small parameter of expansion ε is the ratio of thermal energy to activation energy in the combustion process.

In the problem, the critical initial droplet radius (r_c') for the droplet to achieve complete vaporization at the premixed flame front can be identified. Thus for the cases of $r_{-\infty}' \le r_c'$ and $r_{-\infty}' > r_c'$, we have respectively the completely prevaporized burning and the partially prevaporized burning, as shown in Fig.1a and 1b, respectively. Depending on the availability of the oxidizer in the downstream region, the downstream mixture has either droplet burning for lean sprays or droplet vaporization for rich sprays in the partially prevaporized burning model (Fig.1b). We further assume that the droplet temperature is constant, and its motion is in phase with that of the gas. Therefore, the droplets will start to vaporize, at $x = x_v$, only when the gas temperature has reached the boiling point of the liquid. Droplets then ignite upon crossing the flame, and will extinguish at $x = x_e$ upon complete depletion of the oxygen in the gas mixture. In the case of rich sprays only droplet vaporization is possible.

We shall assume the external heat loss is proportional to $(T - T_u)$, representing loss through heat conduction from the spray to a tube wall maintained at the constant temperature, T_u. For simplicity, we shall also assume that external heat loss being of $O(\varepsilon)$ occurs only in the upstream region of x_v to 0. In the previous study, Liu and Lin [5], the wall temperature (T_u) is assigned to be equal to the upstream temperature ($T_{-\infty}$). However, the selected values of T_u in this analysis will be higher than $T_{-\infty}$ to allow for the simultaneous existence of the external heat gain and loss in upstream. It obviously results in the enhancement of upstream prevaporization for the spray.

Finally, we assume that the fuel and oxidizer reaction for the bulk premixed flame is one-step overall, that

the fuel droplets burn in the flame-sheet limit, and that constant property simplification apply. The comments on the assumptions were generally discussed in Lin et al.[2].

FORMULATION AND RESULTS

The dimensional conservation equations for heat and mass are referred to Lin et al.[2] following Williams [6]. We designated the extent of gas-phase heterogeneity by the parameter $Z = \rho'_G/\rho$ such that $Z = 1$ represents the completely vaporized state. Then the non-dimensional equations for gas-phase continuity, and conservations of fuel, oxidizer and energy are respectively given by

$$Z\dot{m}\frac{dZ}{dx} = \frac{A}{T}(1 - Z_{-\infty})^{\frac{1}{2}}(1 - Z)^{\frac{1}{2}}F(T, Y_0) \tag{1}$$

$$\frac{d}{dx}(Z\dot{m}Y_F - \frac{d}{dx}Y_F) = \dot{\xi} + f_F\dot{m}\frac{dZ}{dx} \tag{2}$$

$$\frac{d}{dx}(Z\dot{m}Y_0 - \frac{d}{dx}Y_0) = \dot{\xi} + f_0\dot{m}\frac{dZ}{dx} \tag{3}$$

$$\frac{d}{dx}(Z\dot{m}T - \frac{d}{dx}T) = -\dot{\xi} + f_T\dot{m}\frac{dZ}{dx} - \varepsilon K(T - T_u)H(O) \tag{4}$$

where

$$A = 3\left(\frac{\lambda'}{r'_{-\infty}\dot{m}'_p}\right)^2\left(\frac{P'\tilde{M}'}{\tilde{R}c'_{PG}Q'\rho'_L}\right) \tag{5}$$

$$\dot{\xi} = -\left(\frac{B'\sigma}{\tilde{M}'_O}\right)\left(\frac{P'\tilde{M}'}{\tilde{R}}\right)^2\left(\frac{\lambda'}{c'_{PG}\dot{m}'^2_p}\right)Y_OY_F exp\left(-\frac{T_a}{T}\right) \tag{6}$$

and the function

$$H(0) = \begin{cases} 1 & \text{for } x_v \le x \le 0 \\ 0 & \text{for } x > 0 \end{cases} \tag{7}$$

while x is the nondimensional distance expressed in units of the preheat zone thickness. In equations (1) – (4), the function $F(T, Y_0)$ and the constant parameters f_F, F_0 and f_T are respectively $\ln[1 + (T - T_b)/h_{LG}], 1, 0, -h_{LG}$ for the vaporizing droplet and $\ln[1 + (T - T_b - Y_0)/h_{LG}], 0, -1$ and $(1 - h_{LG})$ for the burning droplet. K and $\dot{m}$ denote the heat transfer coefficient for the external heat loss, and the flame propagation flux normalized by the premixed value, $\dot{m}'_p$.

For the present problem it is more expedient to use an alternate density parameter,

$$\varsigma = \frac{1 - Z}{1 - Z_{-\infty}}$$

instead of Z. Thus in a dilute spray we can expand $Z_{-\infty} = 1 - \varepsilon\gamma$ such that $Z = 1 - \varepsilon\gamma\varsigma$ where $\varepsilon = T_\infty/T_a$.

Performing the inner and outer expansions, and following the detailed matching procedure of ref.[5] to match the inner and outer solutions, we have te final results as follows

$$\dot{m}^2 = exp[T_1^+(0)] \tag{8}$$

indicating that the flame propagation flux is exponentially affected by the first order temperature downstream near the flame, $T_1^+(0)$. The amount of $T_1^+(0)$ is governed by the combined influence of internal and external heat losses. Setting $Z = 1$ to approach the condition of a homogeneous premixture, we obtain

$$\dot{m}^2\ln(\dot{m}^2) = -Q_L \tag{9}$$

where the parameter,

$$Q_L = K\left[\frac{(T_\infty - T_b)}{T_\infty} - \frac{(T_{-\infty} - T_u)}{T_\infty}\ln\left(\frac{T_b - T_{-\infty}}{T_\infty - T_{-\infty}}\right)\right] \tag{10}$$

shows the combined effect of the external heat loss and gain for the case of $T_u > T_{-\infty}$. It is noted that the upstream spray experiences the external heat gain and loss when $T_u > T_0^-$, and $T_u < T_0^-$ respectively. Therefore, Q_L represents the net influence of external heat transfer on flame extinction, and will be discussed with the other two parameters of the internal heat loss such as the initial droplet radius ($r'_{-\infty}$) and the liquid fuel loading (γ) in the following calculations.

DISCUSSIONS

Sample calculations for n-octane (C_8H_{18}) burning in air are now considered to illustrate the interaction between external and internal heat losses on the flame extinction of dilute sprays by using equations (8) and (9). In addition to three parameters of $\gamma, r'_{-\infty}$ and Q_L used before, Liu and Lin [5], we vary the wall temperature T_u in the analysis. As mentioned earlier, choosing a higher value of T_u will result in a region near x_v and a region ahead of the plane flame having external heat gain and loss, respectively. However, the higher value of T_u will accompany with a larger value of K to provide enough Q_L for flame extinction. To avoid the participant of the learning effect in the gas-phase mixture, discussed by Lin et al. [2], we perform calculations in a non-conserved manner which maintains the initial gas-phase composition the same but varies the liquid fuel loading systematically. In this text, results of lean sprays are presented only.

The responses of flame flux ($\dot{m}$) on the external heat loss (Q_L) are presented in Figs. 2 and 3 with various values of the initial droplet size ($r'_{-\infty}$) and the wall temperature (T_u) for a lean spray of $\phi_G = 0.8$ and $\gamma = 0.02$. The C-shaped extinction curves of the homogeneous premixtures and the completely prevaporized sprays are shown by dot-dash lines and solid lines, respectively. For the completely prevaporized sprays, the critical value of $\dot{m}$ at extinction ($\dot{m}_E$) and the corresponding asymptotic value of the external heat loss are higher than exp(-0.5) and exp(-1.0), respectively. This is caused by the additional heat gain through burning the secondary gasified fuel from the droplet gasification process for a lean spray. It is further found that extinction curves of the homogeneous premixture and the completely prevaporized spray are independent of the wall temperature. A spray having a given burning strength requires a fixed amount of external heat loss to achieve flame extinction. Therefore, the additional heat gain associated with a higher value of T_u will be suppressed by the following heat loss enhanced by a larger value of K, resulting in the same amount of Q_L for extinction.

Fig.2a is basically adopted from the previous study, Liu and Lin [5], for comparison. Results show that the upper branch of $\dot{m}$ curve corresponding to the partially

prevaporized spray, shown by dotted lines in Fig.2a, is initially lower than that of the completely prevaporized spray, and has a cross-over value of Q_L, across which the partially prevaporized spray becomes stronger than the completely prevaporized one. Considering the same value of $r'_{-\infty}$ in Fig.2, the heat transfer coefficient K for the case of T_u = 550K is larger than that of for the case of T_u = 348.6K at the same Q_L. It is noted that a larger value of K promotes the upstream prevaporization when the spray experiences the external heat gain, enhances the following heat loss near the plane flame, and suppresses the possibility of droplet burning in downstream. Therefore, the extinction curve of the partially prevaporized spray with a certain droplet radius shifts inside that of the completely prevaporized spray. The flame extinction then occurs at the condition of the completely prevaporized burning accompanying with a relatively small Q_L, e.g. $r'_{-\infty} = 31\mu m$ in Fig.2b.

In Fig.2b, the flame flux at extinction moves along the lower branch of the extinction curve for the completely prevaporized spray, as we increase the initial droplet size. A spray having large droplets has a small propagation flux, i.e. a large preheating thickness and a shallow temperature gradient at the plane flame. Thus the spray has weak burning intensity, and can be extinguished under a small value of Q_L. Increasing $r'_{-\infty}$ up to $33\mu m$ in Fig.2b, the flame extinction occurs at the condition of the partially prevaporized burning instead of that of the completely prevaporized burning. By assigning $r'^{*}_{-\infty} = 33\mu m$, it is suggested that flame extinction of a lean spray is controlled by the completely and partially prevaporized spray for the case of $r'_{-\infty} < r'^{*}_{-\infty}$ and $r'_{-\infty} \geq r'^{*}_{-\infty}$, respectively. It is worth to emphasize that as $r'_{-\infty} < r'^{*}_{-\infty}$, the spray may have partially prevaporized burning under a certain amount of Q_L, but must be identified by completely prevaporized burning on extinction. As we increase $r'_{-\infty}$ further in Fig.2b, the extinction curve of the lean spray moves toward that of the homogeneous premixture because the liquid fuel in the spray loses its identify.

The above discussion is further explored in Fig.3. For a very large value of T_u, e.g. 650K in Fig.3b, the $\dot{m}_g$ line has a large jump from the completely prevaporized burning to the partially prevaporized burning at the condition of $r'^{*}_{-\infty}(49.4\mu m)$. The S-shaped extinction curve is now reproduced and inserted into the C-shaped extinction curve as $r'_{-\infty} = 60\mu m$ in Fig.3b. It is therefore understood that under the influence of the external heat loss, the characteristics of flame extinction by the internal heat loss (or gain) can be emphasized by the enhancement of upstream prevaporisation. In Fig.3a, it is of interest to note that the flame flux on extinction ($\dot{m}_g$) is almost independent of the initial droplet size and the external heat loss, and closely equal to exp(-0.5) as T_u = 570K.

The flame flux on extinction as a function of Q_L is shown in Fig.4 for various values of $r'^{*}_{-\infty}$ and T_u in a lean spray. It is shown that with increasing the initial droplet size, the $\dot{m}_g$ and its associated Q_L on flame extinction are first increased, then decreased, and finally approaches to exp(-0.5) and exp(-1.0) respectively for small values of T_u. Increasing the wall temperature T_u, the $\dot{m}_g$ line will shift inside the envelope of the extinction curve for the completely prevaporized spray. At the critical condition of $T_u = 510.5K$, the $\dot{m}_g$ is monotonically decreased with increasing the initial droplet size. As $T_u > 510.5K$, the $\dot{m}_g$ curve is broken by a jump from the completely prevaporized burning to the partially prevaporized burning at $r'^{*}_{-\infty}$. In Fig.4, it is generally concluded that the unstable branch of the C-shaped extinction curve for the completely prevaporized spray may be realistically approached by considering a partially prevaporized spray having a higher value of T_u; and that lean sprays having larger droplet size or experiencing larger T_u will be extinguished under a smaller Q_L.

The variation of $r'^{*}_{-\infty}$ for a lean spray $\phi = 0.8$ is presented in Fig.5 with various values of γ, T_u and Q_L. According to Fig.5, the value of $r'^{*}_{-\infty}$ is increased with increasing T_u for a given amount of γ. This points out that the external heat gain enhancing the upstream prevaporization, allows the spray having larger droplets to undergo completely prevaporized burning. Increasing the liquid fuel loading, the $r'^{*}_{-\infty}$ curve moves to experience higher Q_L because of the additional burning of the secondary gasified fuel for a lean spray. It is further found that the minimum value of T_u and the corresponding $r'^{*}_{-\infty}$, allowing a jump from the completely prevaporized burning to the partially prevaporized burning on extinction, are decreased with increasing the liquid fuel loading. Finally, it seems that all curves of $r'^{*}_{-\infty}$ have a tendency to converge together at a very high T_u, as shown in Fig.5.

REFERENCES

1. Huang, C.L., Chiu, C.P., and Lin, T.H., J. of Chinese Soc. of Mech. Engr., Vol.10, No.5, 333-343 (1989).
2. Lin, T. H., Law, C. K., and Chung, S. H., Int. J. of Heat and Mass Transfer, Vol.31, No.5, 1023-1034 (1988).
3. Lin, T. H. and Sheu, Y. Y., Combust. and Flame, accepted and to appear (1991).
4. Mitani, T., Combust. and Flame, Vo.43, 243-253 (1981).
5. Liu, C.C., and Lin, T.H. Combust. and Flame, accepted and to appear (1991).
6. Williams, F.A. Combustion Theory, 2nd Ed., Benjamin/ Cummings, Menlo Park, CA, 446-484 (1985).

ACKNOWLEDGEMENT

This work was supported by the National Science Council, Taiwan, R.O.C. under the contract NSC79-0401-E006-20.

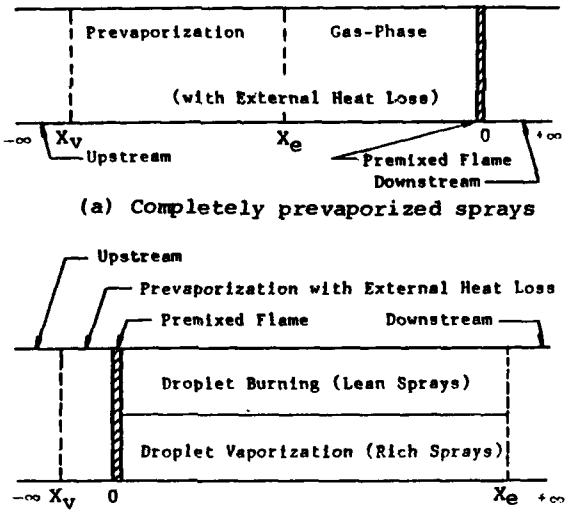

Fig. 1 Schematic diagram of burning sprays.

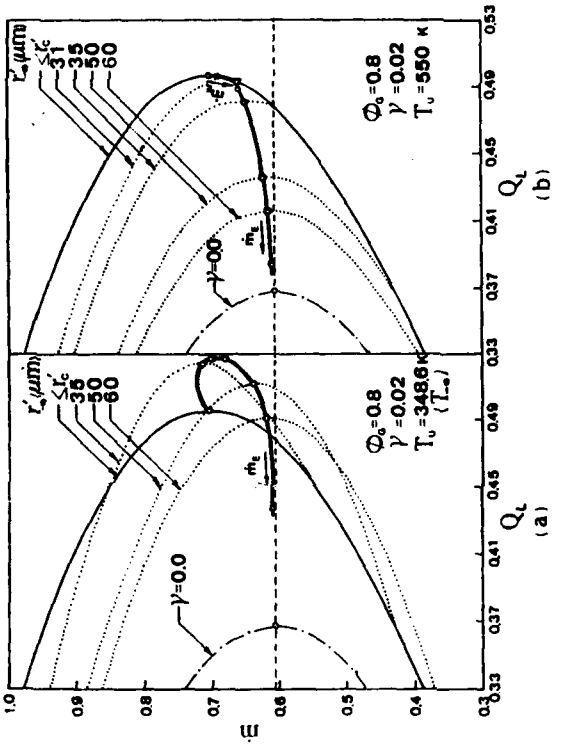

Fig. 2 Extinction curves of partially prevaporized sprays with Q_L for various values of $r'_{-\infty}$ and T_u for a lean spray.

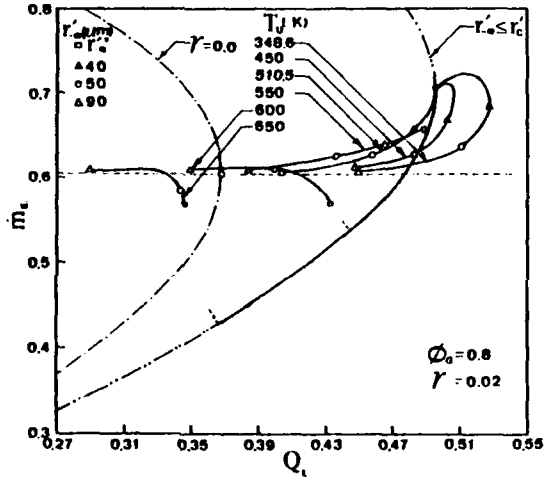

Fig. 4 The $\dot{m}_E$ as functions of Q_L, $r'_{-\infty}$ and T_u for a lean spray.

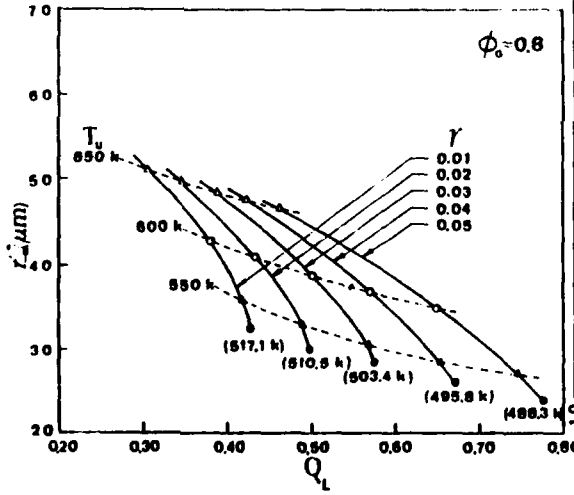

Fig. 5 The $r'^*_{-\infty}$ as functions of γ and T_u for a lean spray.

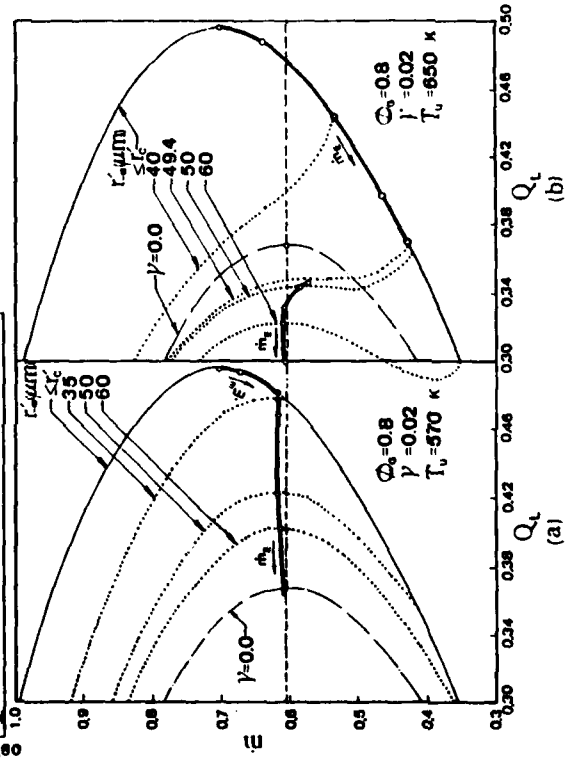

Fig. 3 Extinction curves of partially prevaporized sprays with Q_L for various values of $r'_{-\infty}$ and T_u for a lean spray.

IUTAM Symposium on
Aerothermodynamics in Combustors
June 3-5, 1991, Taipei

NUMERICAL STUDY OF A SWIRLING TURBULENT DIFFUSION FLAME

DANIELE GARRETON, LUC VERVISCH

DIRECTION DES ETUDES ET RECHERCHES - ELECTRICITE DE FRANCE

LNH - 6, Quai Watier - 78400 CHATOU, FRANCE.

INTRODUCTION

In order to assess the numerical developments concerning the modeling of the turbulent reactive flows, an axisymmetric swirling turbulent diffusion flame of methane in air is studied and the comparison between measurements and computed results is performed. With this 20 kW burner, (fig. 1), the methane is introduced axially and the air tangentially, so that a large recirculation zone takes place at the center of the flame and allows for its stabilization. To restore the temperatures, the thermocouple and CARS techniques are used : a companion paper describes these investigations. The LDA is run to measure the velocity field and Gaz de France performs concentrations measurements of CH_4, O_2, CO and CO_2 with a gas sampling probe. The whole set of experimental data enables an inestimable comparison with the model predictions.[1]

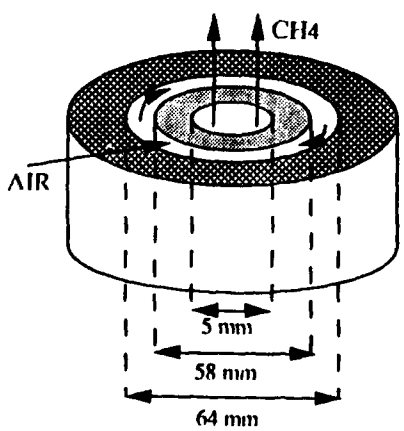

Fig. 1 : The burner geometry

NUMERICAL MODELING

The numerical program, called HADES, describes, with the finite difference technique, the two-dimensional or axisymmetric turbulent flows with a k-ε model for the turbulent correlations. A Reynolds stress model is developped in our lab [2] but its extension to density varying turbulent flows is still under study. Two combustion models are used :
The first one, named "complex chemical equilibrium model", assumes fast kinetics and chemical equilibrium of the instantaneous mixture. An averaging operator is then required to determine the mean concentrations of species. As the equilibrium instantaneous concentrations are function of the non-dimensional carbon atoms mass fraction, f, a probability density function for f is described as a beta function whose coefficients depend on the mean value and the fluctuations of f. The transport equations have to be solved for these two last quantities. If the radiative transfer is not neglected, as it is in this flame, the mean enthalphy is also computed with a transport equation and the instantaneous enthalphy is assumed to be locally a quadratic function of f to enable the averaging step with the pdf of f.
The second one, named "PEUL" "Probabilistic EUlerian Lagrangian" model, is developped in collaboration with Pr Borghi of Rouen and takes into account one finite chemical reaction rate. (The approach with a reduced kinetics scheme is still under study). Each mesh cell is assumed to be an homogenous chemical reactor which is caracterized by a mixing time and the reference mean concentrations of reactive species. The species transport equations in the reactor are written is a lagrangian form with the IEM (Interaction by exchange with the Mean) model for the diffusion term. Three possible behaviours are allowed : pure and inert mixing, chemical equilibrium and mixing-kinetics

competition. As mean values of concentrations and reaction rates can be determined in the reactor with the help of the pdf of f, like previously, these three behaviours are combined so that the mean concentrations in the reactor are the same as the reference values. The mean reaction rates are then taken into account in the eulerian transport equations of species, which lead to a new reference state for the reactor at the next time step.
The reaction is :
$CH_4 + 7/4\ O_2 \rightarrow 1/2\ (CO + CO_2) + 2\ H_2O$
(Methane and oxygen are computed with a transport equation ; their mean reaction rates are proportional.)
The fractional step algorithm, following Chorin, is retained for the numerical method. The advection step is solved with the method of the characteristics, the diffusion step, including source terms, with a splitting between the two space directions and a semi-implication. A very classical SOR method is used for the Poisson equation. [3]

RESULTS

The input velocities are about 30 m/s both axially and tangentially. The first LDA measurements show that the computed velocities (fig. 2 and 5) in the recirculation zone, between the two jets of methane and air and above the methane jet, are too weak and the computed turbulent energy is in general too weak : the mixing is not efficient enough and the temperature remains cold at the bottom of the flame : the radial profiles present a too narrow peak ; at the top of the flame, the products are not cooled enough and the flame is too hot. The comparison between the measured and computed temperatures indicates that the computation reproduces qualitatively the general structures of the flame at the bottom, while the gases are too hot at the top of the flame. (fig. 3)

With the PEUL model, (fig.4), this trend can be balanced with the mixing time, which is proportional to k/ε, but some important discrepancies remain. The temperatures are more realistic at the bottom of the flame, in the recirculation zone ; the problem of too hot gases at the top is reduced but not completely solved.
As the PEUL model gives good results for methane jet flames, such as the Lockwood or Masri-Bilger flames [4], we can infer that this problem is probably more related to the modeling of the swirling flow : the use of the k-ε model is questionnable, particularly in the central recirculation region of the flow.

Another weak point in the simulation is the beta assumed shape for the probability density function of the passive scalar. This assumption was verified in nearly all the flame, for jet flames, except at the jet boundaries ; but again for swirling flames, it may not be the case. The CARS technique shows double peak distribution of temperatures at the edge of the reciculation zone. This result has a physical meanning because, in this region, hot burnt pockets of fluid and cold air pockets of fluid cross the probe volume.

CONCLUSION

As this swirling flame is very similar to many industrial burners, this study is very promising to qualify the capability of our program to predict the good interaction between the turbulent flow and the combustion phenomena.

[1] : Bachmann M., Bellaïche P., Cahen C., Garréton D., Vervisch L. : Modeling and thermometric study of a swirl stabilized turbulent diffusion flame, 23rd Combustion Institute Symposium, Orléans, 1990.

[2] : Kanniche M., Baron F., Viollet P.L. : The 7th Symposium on Turbulent Shear Flows, p. 12.3, Stanford University, 1989.

[3] : Garréton D., Méchitoua N., Viollet P.L. : Third International Conference on Numerical Combustion, p. 433, Antibes, France, INRIA, 1989.

[4] : Vervisch L., Garréton D. : "Modélisation de flammes de diffusion turbulentes avec prise en compte de l'interaction entre les effets thermochimiques et turbulents", rapport EDF-LNH E44 91.04.

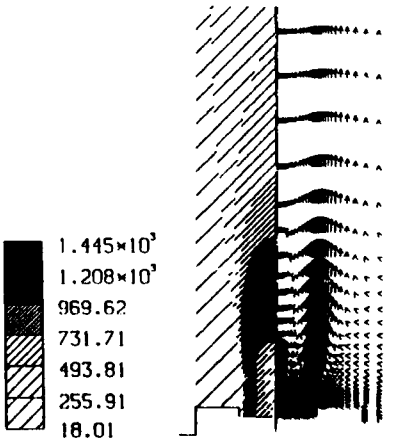

Fig. 2 : The computed temperature and velocity fields

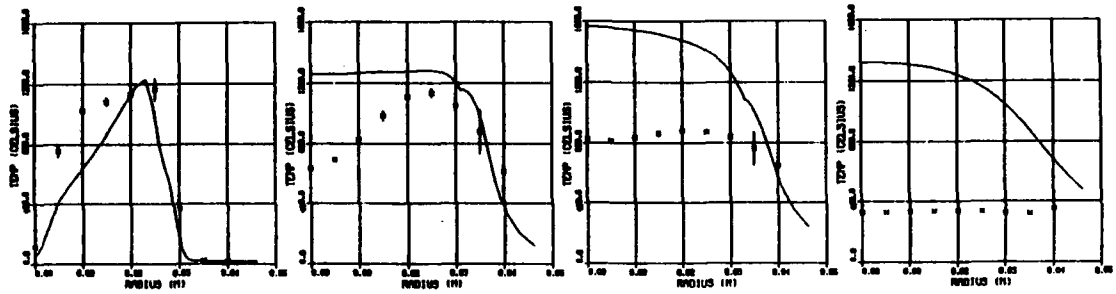

Fig. 3 : Radial profiles of temperature with the equilibrium model (— : computed ; * : measured) at 18 mm, 74 mm, 97 mm and 167 mm from the left side.

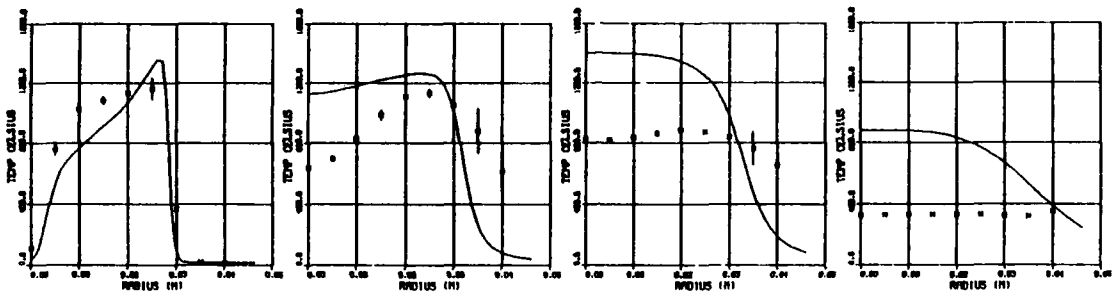

Fig. 4 : Radial profiles of temperature with the PEUL model (— : computed ; * : measured) at 18 mm, 74 mm, 97 mm and 167 mm from the left side.

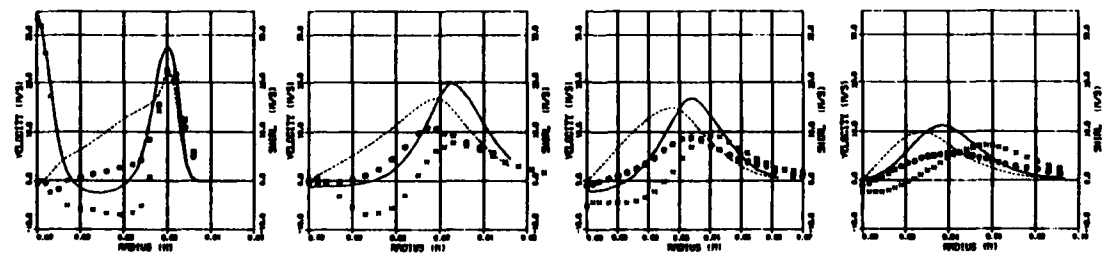

Fig. 5 : Radial profiles of axial (—: computed ; * : measured) and tangential (- - -: computed ; • : measured) velocities with the PEUL model at 18 mm, 74 mm, 97 mm and 167 mm from the left side.

IUTAM Symposium on
Aerothermodynamics in Combustors
June 3-5, 1991, Taipei

A Reaction Mechanism for Soot Formation in Non-Premixed Flames

R. Peter Lindstedt

Fluids Section, Department of Mechanical Engineering, Imperial College, London SW7 2BX

INTRODUCTION

Accurate prediction of soot formation in laminar and turbulent combustion is a formidable problem. However, the solution is of great practical importance particularly in non-premixed combustion applications ranging from turbulent jet flames to internal combustion engines and gas turbine combustion chambers. While most practical applications are strongly turbulent in nature a most basic requirement of any model is the successful prediction of soot characteristics under a wide range of laminar conditions. Unfortunately, even this problem is one of great complexity in particular as any deduced reaction mechanism must be sufficiently compact to be implemented into turbulent flame predictions for example via an extended laminar flamelet presumed *pdf* approach or via a transported *pdf* approach.

The present paper outlines a global reaction mechanism for the formation, growth and combustion of soot particles in laminar non-premixed flames. The model is combined with detailed and global chemistry descriptions for the gas phase. The reaction mechanism [1] involves nucleation, surface growth, particle coagulation and combustion steps and has been created with the intention of being applicable to the prediction of turbulent flames. The soot nucleation and surface growth reactions are linked to the gas phase by making the presumption that soot formation is dependent upon the breakdown path of the fuel and that the presence of pyrolysis products such as acetylene and poly-unsaturated cyclical hydrocarbons are of primary importance in the soot formation process. In the present work acetylene is used as the indicative critical specie of the soot formation process. The deduced reaction mechanism is applied to the coflow methane-air flame measured by Garo et al [2] and to counterflow propane/O_2/N_2 flames measured by Vandsburger et al [3]. For the methane flame a global reaction mechanism [4] with added reaction steps for acetylene has been used to minimize computational effort. For the propane flames a carefully constructed detailed mechanism with 36 species and 111 forward reaction steps applying the latest available rate constant data has been used [5].

SOOT FORMATION MECHANISM

The soot formation mechanism used in the present paper is based on the presumption that the fuel breakdown path is critical in determining sooting characteristics. Specifically it is assumed that the amount of soot formed is proportional to the amount of acetylene generated during the breakdown of the fuel. The model involves the solution of two additional conservation equations for the soot mass fraction and the particle number density and is closed by the assumption of a spherical particle shape. The formation of soot mass is assumed to occur in two parts. Firstly, the formation of incipient soot particles or 'nucleation'. In the present model these particles are assumed to be formed from acetylene as,

$$C_2H_2 \;\text{-->}\; 2\,C(s) + H_2 \qquad (1)$$

The reaction rate constant for this step has been determined by Leung et al [1] by the use of counterflow ethylene-air flames. It has been formulated to account for the formation of incipient particles as well as early surface growth. The latter is important since experimental studies [3] indicate that newly formed particles are significantly (up to an order of magnitude) more reactive than older particles. The rate expression derived from these computations was,

$$R_1 = 0.5\,10^6\, e^{-21100/T}\,[C_2H_2] \quad (kmol/m^3/s)$$

The second reaction responsible for the increase in soot mass is assumed to be surface growth due to adsorption of C_2H_2 on the surface of the particles,

$$C_2H_2 + n\,C(s) \;\text{-->}\; (n+2)\,C(s) + H_2 \qquad (2)$$

The reaction rate of this step must be a function of the surface area (S), or more specifically, the number of active sites of the particle and the concentration of acetylene. It is assumed that the rate dependence upon the latter is essentially linear to a first approximation giving,

$$R_2 = k_2(T)\, f(S)\, [C_2H_2] \qquad (kmol/m^3/s)$$

It can further [1] be shown that a preliminary expression for the function f(S) can be found if it is assumed that to a first approximation the reactivity of a particle is inversely proportional to its size resulting in,

$$R_2 = k_2(T)\,[C_2H_2]\,[C(s)]^{1/3}\,[\rho N]^{1/6}$$

$$k_2(T) = 0.65\,10^4 \sqrt{\pi}\left[\frac{6M_{C(s)}}{\pi\rho_{C(s)}}\right]^{\frac{2}{3}} e^{-12100/T}$$

Where N is particles/kg, $M_{C(s)}$ molecular weight of carbon (12.011 kg/kmol) and $\rho_{C(s)}$ the soot density (2000 Kg/m^3).

The soot oxidation step used in the present work is based on the work by Lee, Thring and Beer [6]. However, the pre-exponential factor has been adjusted by a factor 10 to give a similar peak burnout rate to that observed by Garo et al [2] in their experiments on coflow methane-air flames. Given the present uncertainties in determining an appropriate rate constant or even the major oxidizing specie (O_2 or OH) the current arrangement is viewed as sufficiently accurate for the present purpose. It is further assumed that at flame temperatures soot is oxidised to carbon monoxide as,

$$C(s) + 1/2\,O_2 \rightarrow CO \qquad (3)$$

The resulting rate expression can be written as

$$R_3 = k_3(T)\frac{\pi}{M_{C(s)}}\left[\frac{6M_{C(s)}}{\pi\rho_{C(s)}}\right]^{\frac{2}{3}}[O_2]\,[C(s)]^{2/3}\,[\rho N]^{1/3}$$

$$k_3(T) = 0.125\,10^6\,T^{1/2}\,e^{-19680/T}$$

The soot nucleation step outlined above also gives rise to the source term in the number density equation. The decrease in particle numbers is simply assumed to correspond to agglomeration given by the normal square dependence. The reaction may be written schematically as,

$$n\,C(s) \rightarrow C_n(s) \qquad (4)$$

with the resulting rate expression [1] given by,

$$R_4 = 2N_A R_1/C_{min} - k_4(T)\,[C(s)]^{1/6}\,[\rho N]^{11/6}$$

$$k_4(T) = 2\,C_a\left[\frac{6M_{C(s)}}{\pi\rho_{C(s)}}\right]^{\frac{1}{6}}\left[\frac{6\kappa T}{\rho_{C(s)}}\right]^{\frac{1}{2}}$$

where N_A is Avogadros number 6.022 10^{26} particles/kmol, C_{min} is the number of carbon atoms in the incipient soot particle (10000), κ the Boltzmann constant (1.38 10^{-23} J/K), and C_a the agglomeration constant, assigned the value 9.

GAS PHASE REACTION MECHANISM

The gas phase reaction mechanism used for the propane flames is based on the work of the CEC data evaluation group [7] and further developed to improve prediction of diffusion flames [1,5]. Of particular relevance to the present study is the accuracy of the prediction of pyrolysis products which can be shown to be excellent with the deduced mechanism.

For the coflow methane-air flame [2] an extended version of the global reaction mechanism by Jones and Lindstedt [4] was used. The modifications amounted to including steps for the formation and destruction of acetylene,

$$CH_4 + CH_4 \rightarrow C_2H_2 + 3H_2 \qquad (5)$$

$$C_2H_2 + 3/2\,O_2 \rightarrow CO + CO_2 + H_2 \qquad (6)$$

$$C_2H_2 + 2H_2O \rightarrow 2CO + 3H_2 \qquad (7)$$

with reaction rates (in kmol/m^3/s),

$$R_5 = 0.12\,10^{13}\,e^{-42778/T}\,[CH_4]$$

$$R_6 = 0.15\,10^{12}\,e^{-15098/T}\,[C_2H_2]^{1/2}\,[O_2]^{5/4}$$

$$R_7 = 0.30\,10^{9}\,e^{-15098/T}\,[C_2H_2]\,[H_2O]$$

While the underlying global reaction mechanism [4] is valid for a wide range of flames the additional reactions are valid only for unstrained and weakly strained diffusion flames with a strain rate 'a' < 50 /s. However, for such flames the agreement between the global and detailed mechanisms is very acceptable with typical errors less then 20%.

RESULTS AND DISCUSSION

The first set of computations were of two counterflow propane-air flames burning against oxygen enriched air streams investigated by Vandsburger et al [3], who determined soot volume fractions, particle number densities and particle sizes. The velocity gradient estimated from the experiments was 63/s which was applied in the numerical computations along with a fuel injection velocity of 0.10 m/s and 109 distributed nodes. The oxidant streams consisted of 24% O_2/76% N_2 and 28% O_2/72% N_2 respectively. The comparison of measured and predicted soot volume fractions can be seen from Figure 1 below.

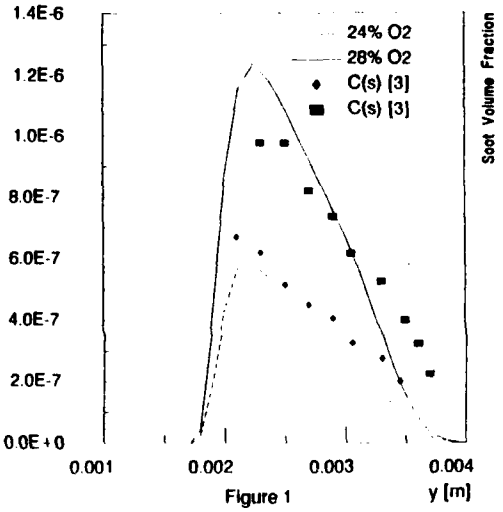

Figure 1

The agreement between predicted and measured soot volume fractions is generally very satisfactory. The predictions of particle number densities are also satisfactory (Figure 2) but young particles close to the main reaction zone appears to agglomerate more quickly than older particles residing in colder parts of the flame.

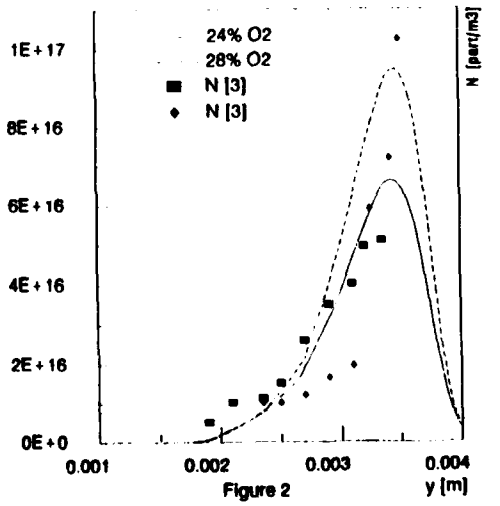

Figure 2

The area of the region of particle formation can also influence the particle number density and size in the early part of the flame. However, the predicted width of this region is around 1 mm or less which appears in good agreement with that observed experimentally [3]. An interesting feature of these flames is that the location in mixture fraction space of the peak growth rates of soot particles is shifted from 0.138 to 0.158 for the 28% oxygen enriched case.

The axi-symmetric coflow methane-air flame measured by Garo et al [2] was computed with 197 distributed nodes and the soot model unchanged from the oxygen enriched counterflow propane flames. This flame provides an interesting comparison as not only are the fuel and oxidant streams changed, but also the flame structure is significantly different. The prediction of the gas phase using the global reaction mechanism for this flame is excellent [4] provided that computations begin at the first measuring station (12.5 mm downstream) and not at the burner exit. This poses a problem as soot nuclei start to form early in the flame and as no soot profiles were available at the first measuring station. Consequently, a preliminary solution was obtained from the burner exit to the first measuring station where the soot data were re-mapped according to the location in mixture fraction space. This procedure is approximate but considered more realistic than assigning zero values to soot volume fractions and particle numbers.

The predicted soot volume fractions and particle sizes along the radius (r) at various distances downstream can be seen in Figures 3 and 4 respectively, where the measurements are from the radial profile at 47 mm downstream.

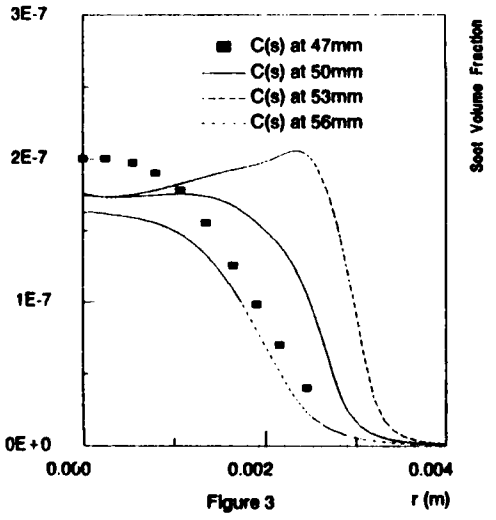

Figure 3

The discrepancy between computed and measured profiles is probably to a large extent due to the approximate nature of the boundary conditions imposed at the first measuring station. This would appear to be given further weight by consideration of the soot volume fraction along the centreline of the flame which displays a similar shift with peak concentrations obtained at 47 mm downstream in experiments compared to 51.5 mm in the computations. It can, however, not be ruled out that further improvements in predictions may be conditional upon the introduction of an oxidation step dependent on OH radicals.

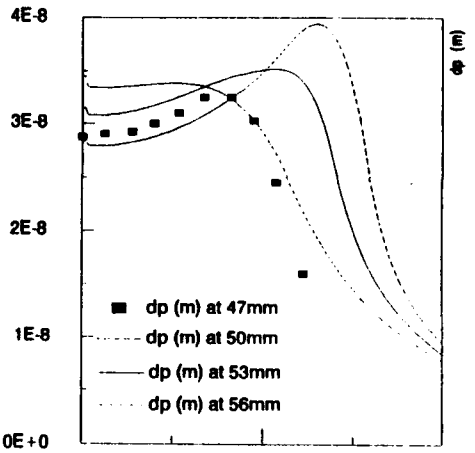

Figure 4

CONCLUSIONS

The results obtained by the soot model presented here show very promising qualitative and quantitative agreement with measured data for a range of flames. In particular, predictions of soot volume fractions using the model appear to be close the uncertainties associated with the detailed and global reaction mechanisms used for the predictions of the gas phase. The predictions of other properties such as particle number densities and aggregate sizes are also satisfactory particularly if the uncertainties in the measurements of these properties are considered. However, further development work is required particularly with respect to oxidation steps and the evolution of particle number densities.

Acknowledgement

The financial support of the Ministry of Defence at RAE Pyestock and the efforts of Mr. K.M. Leung in the modelling of the gas phase chemistry are gratefully acknowledged.

REFERENCES

[1] Leung, K.M., Lindstedt, R.P. and Jones, W.P., 'A Simplified Reaction Mechanism for Soot Formation in Non Premixed Flames', To appear Comb. and Flame

[2] Garo, A., Prado, G. and Lahaye, J., Comb. and Flame 79, pp 226-233 (1990)

[3] Vandsburger, U, Kennedy, I. and Glassman, I. Comb. Science and Tech. 39, pp. 263-285 (1984)

[4] Jones, W.P. and Lindstedt, R.P. Comb. and Flame 73, p. 233 (1988)

[5] Leung, K.M. and Lindstedt, R.P. 'Detailed Kinetic Modelling of Non-Premixed C_1 to C_3 Hydrocarbon Combustion', Imperial College Fluid Section Rept. FS/90/21, December 1990.

[6] Lee, K.B., Thring, M.W. and Beer, J.M., Comb. and Flame 6, p137 (1962)

[7] Baulch, D.L. and Co-workers in the CEC Kinetic Data Evaluation Group, 'Summary of Preferred Rate Data for Combustion Modeling', Final Rept. Sept. 1990

IUTAM Symposium on
Aerothermodynamics in Combustors
June 3-5, 1991, Taipei

TRANSITION OF TURBULENT PREMIXED FLAME STRUCTURE WITH TURBULENCE REYNOLDS NUMBER AND DAMKOHLER NUMBER

Akira Yoshida, Yoshihiko Ando, Michinori Narisawa
and
Hiroshi Tsuji

Tokyo Denki University
2-2 Kanda-Nishikicho, Chiyoda-ku, Tokyo 101, Japan

1. INTRODUCTION

The structure of the turbulent premixed flame depends on the turbulence Reynolds number defined by $R_\lambda = (u'\lambda)/\nu$ or $R_l = (u'l)/\nu$ and the Damkohler number, $D_a = (l/u')/(\delta_L/S_L)$, where u' is the turbulence intensity, ν the kinematic viscosity, λ the Taylor microscale, l the integral scale of turbulence, δ_L is the laminar flame thickness and S_L the laminar burning velocity. When the Damkohler number is large, combustion reactions are rapid compared with the turbulent processes, so that the combustion tends to occur in a thin laminar flame. For small Damkohler numbers, the turbulent mixing is augmented by the small vortices and is rapid compared with the chemistry, so that the combustion reactions are distributed throughout the volume occupied by the turbulent flame zone. In the present study, the transition of the flame structure between these extremes were studied by using the Bunsen burner flames and the opposed jet burner flames.

2. EXPERIMENTAL APPARATUS

A conical turbulent premixed flame with wrinkled laminar flame structure was produced by a conventional cylindrical burner of 30 mm in I.D. Turbulence producing grid was installed at 55 mm upstream from the exit. The flame was stabilized on the exit by a small annular diffusion flame. The average velocity of mixture at the burner exit ranged from 2.68 m/s to 5.37 m/s. The turbulence intensity was changed from 0.04 m/s to 0.57 m/s. The turbulence Reynolds number based on the Taylor microscale ranged from 4.9 to 74.4. A typical Damkohler number is of the order of 20.

Extremely high intensity turbulence with small scale was found to be achieved by an opposed jet burner[1]. The burner used in the present study is shown in Fig. 1. This burner consists of two mixture supply tubes of 10 mm in I.D. which are placed oppositely. The distance between two mixture supply tubes is variable from 5 to 30 mm. Dilution by the surrounding atmosphere is eliminated by two water-cooled square plates of 130 mm X 130 mm. Equal flows of a premixed propane-air mixture were supplied to these tubes. A typical value of R_λ is of the order 300 and that of D_a of the order of 5. An annular turbulent flame is stabilized in the diverging mixture flow in the range of equivalence ratio greater than 0.90, and the stability was found to be almost independent of the flow velocity.

Figure 2 shows the laser tomography and the data processing system. An Ar ion laser of 0.8 W operating at 514.5 nm was expanded to a two-dimensional laser sheet by a cylindrical lens and then focused by a condenser lens. The nominal thickness of the resulting sheet was about 0.2 mm across the measuring area. The unburned mixture was seeded by fine TiO_2 particles. Since the effective scattering cross section of particles is greatly reduced at high temperature[2], only the unburned mixture region is visualized by Mie scattering of these particles. The effect of seeding on the flame process was found negligible. The scattered

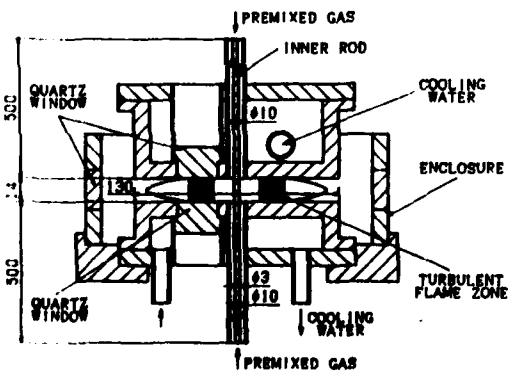

Fig.1 Opposed jet burner

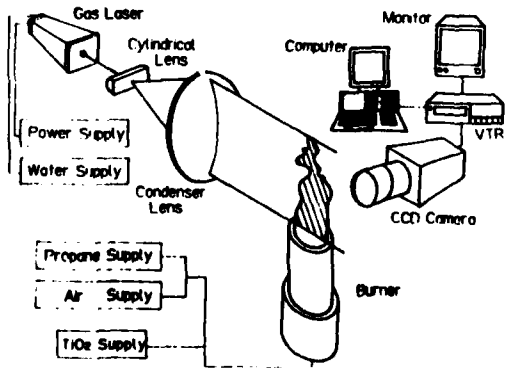

Fig.2 Laser tomography and data processing system

light was collected at the right angle to the sheet and was recorded on the video tape through a CCD camera with an electronic shutter of 1/2000 s duration. The image recorded on the video tape was sent through an interface to the frame memory(512 X 512 pixels) of a computer. The overall spatial resolution was estimated as around 1.5 mm.

The instantaneous temperature was measured by a compensated fine-wire thermocouple as in Ref. 1. An LDV was applied to measure the radial velocity distributions.

3. EXPERIMENTAL RESULTS

3.1 FRACTAL ANALYSIS OF WRINKLED LAMINAR FLAME

The flame image recorded on the video tape was processed to afford the instantaneous shape of wrinkled laminar flame. The algorithm used in the fractal analysis is the one used in Ref. 3, in which the length of flame boundary is obtained by covering the boundary with circles of different diameters. The processed image is shown in Fig. 3 with the procedure for obtaining the length. Successive 10-100 images were analyzed to obtain the fractal dimension and the inner and outer cutoffs.

The logarithm of the length of flame boundary is plotted against the logarithm of the radius of circle. An example of such plots is shown in Fig. 4. It was found that there exist three regions, in each of which data are expressed by a straight line segment. The first and third line segments are nearly horizontal and the second is diagonal in this log-log plot. The intersection point of the first and second line segments represents the inner cutoff and that of second and third line segments represents the outer cutoff. In the vicinity of each cutoffs, a smooth transition between the straight line segments is observed.

From the slope of the second line segment,

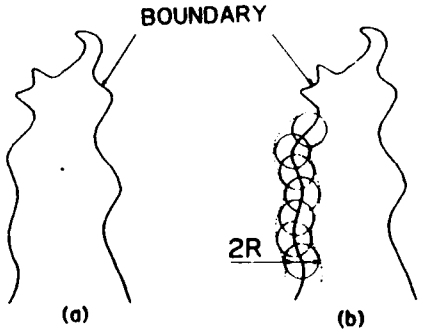

Fig.3 Instantaneous flame shape

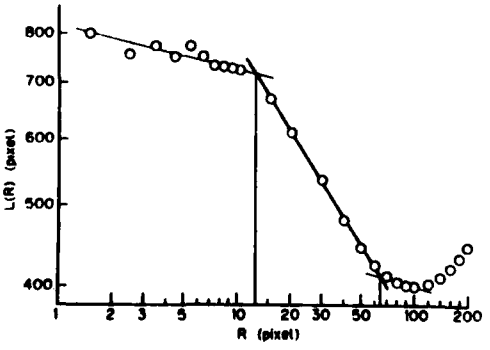

Fig.4 Typical length plot for fractal analysis

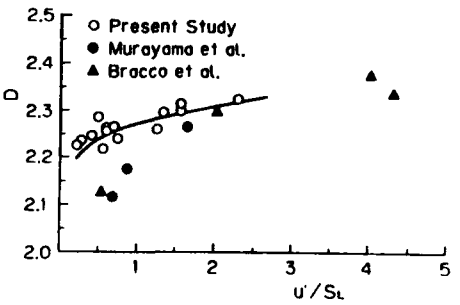

Fig.5 Fractal dimension versus u'/S_L

the fractal dimension D was determined. Since the wrinkled laminar flame geometry changed every instance, we used arithmetic means of the values for 10-100 instances. Fig. 5 shows that the fractal dimension measured in the present study ranges from 2.21 to 2.32 depending on the characteristics of the unburned mixture turbulence. It was found that the fractal dimension depends solely on the turbulence intensity normalized by the laminar burning velocity and that the dimension is almost independent of the turbulence Reynolds number. The fractal dimension increases with the turbulence intensity and the value of 2.36 obtained in a internal combustion engine is approached at high intensity turbulence[4]. Recent measurements in turbulent shear flows indicate that constant property surfaces in these flows are fractal with a D between 2.35 and about 2.60 [5] which is larger than the fractal dimension of the wrinkled laminar flame. Therefore, the wrinkled laminar flame does not act as a constant-property scalar surface, especially for low intensity turbulence.

3.2 INNER AND OUTER CUTOFFS OF FRACTAL BEHAVIOR

For turbulent shear flows, the inner and outer cutoffs appear at scales approximately equal to the orders of the Kolmogorov microscale and the integral scale respectively [5]. In general the laminar flame front is expected to be smoother than that implied by the unperturbed turbulent flow field. The smoothing of the flame surface is predominant in the small scales whereas the larger scales tend to remain unaffected. This suggests that the inner cutoff tends to shift to higher values than the Kolmogorov microscale. The inner cutoff obtained in the present study is significantly larger than the Taylor microscale which is larger than the Kolmogorov microscale and decreases with the turbulence intensity. This fact suggests that the inner cutoff decreases with the roughness of wrinkled laminar flame surface.

The outer cutoff is much larger than the integral scale of the unburned mixture turbulence and is about 2/3 of the burner diameter independently of the characteristics of the unburned mixture turbulence. The burner diameter represents the possible maximum scale in the system. Therefore, the outer cutoff is affected by the maximum scale of the system.

3.3 STRUCTURE OF OPPOSED JET PREMIXED FLAMES

With increasing the turbulence Reynolds number and decreasing the Damkohler number, the local structure of the wrinkled laminar flame is destroyed by small dissipative eddies and

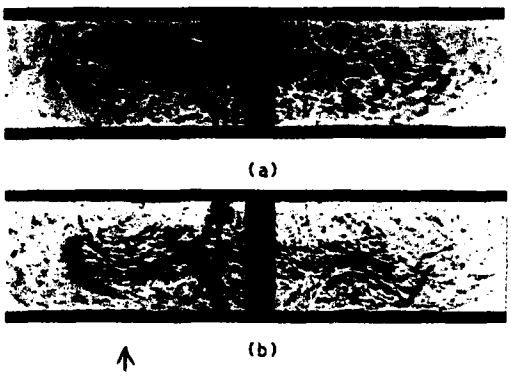

Fig.6 Schlieren photographs of opposed jet flames

(a) V = 18.8 m/s, (b) V = 30.0 m/s

the distributed reaction zone is produced. Figure 6 shows the schlieren photographs of the opposed jet premixed flames in the transition regime to the distributed reaction zone. The distance between two plates was 14 mm. Boundaries between unburned mixture jets and recirculation zones are clearly shown. Figure 6(a) shows that on the unburned gas side, the flame zone includes many large scale wrinkles which are shown as a lot of knob-like [illegible]s. Thin horizontal stringy microstructure appears on the burned gas side. As shown in Fig. 6 (b), with increasing the mixture velocity, wrinkles on the unburned gas side disappears and the whole combustion flow field is filled with the bundles of the stringy microstructure.

Figures 7 shows the mean temperature contours for the mean velocity of 18.8 m/s. The turbulent flame zone extends from R = 10 mm to 30 mm. On the unburned gas side of the flame zone, the isotherms of the mean temperature are nearly parallel except for the regions in the vicinity of the plate, where the recirculation regions are produced. On the burned gas side, an almost uniform temperature region is produced.

The fluctuating temperature contours are shown in Fig. 8. The fluctuating temperature is high on the unburned gas side, suggesting that the instantaneous temperature changes from the nearly unburned gas temperature to that of fully burned products. On the other hand, on the burned gas side, the fluctuating temperature decreases. As suggested in Ref. 6, small temperature fluctuation is a typical feature of the distributed reaction zone.

3.4 TRANSITION OF TURBULENT FLAME STRUCTURE

From the experimental results obtained with the conical turbulent flame, it can be said that the so-called wrinkled laminar flame is produced within the range of R_λ below 100 and D_a above 10.

When R_λ is about 100 and D_a about 10 in the opposed jet burner flame, a large temperature fluctuation was observed on the unburned gas side of the opposed jet burner flame. The large temperature fluctuation is a typical feature of the wrinkled flame, because the discontinuity surface of temperature fluctuates in the flame zone. Therefore, the wrinkled flame feature remains on the unburned gas side. On the burned gas side, the fluctuating temperature decreases and also the mean temperature becomes uniform throughout the reaction zone. In this region, the discontinuity surface does not exits and the fractal analysis cannot be applied to this flame structure.

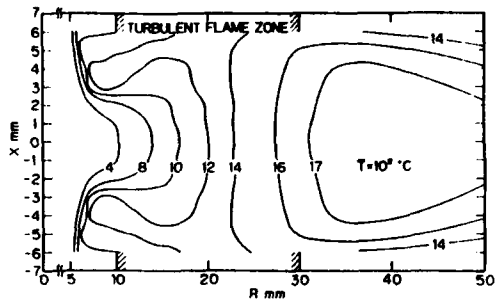

Fig.7 Mean temperature contours

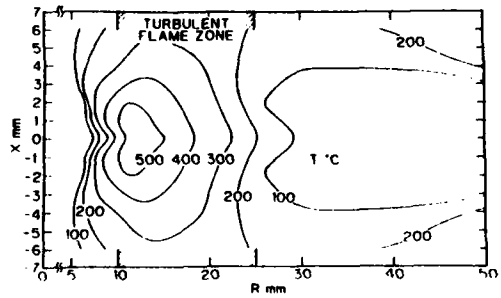

Fig.8 Fluctuating temperature contours

With further increase in R_λ to about 300 and decrease in D_a to about 5, the whole combustion flowfield consists of the folded and tangled vortex tubes. Through the cascade of turbulent energy transfer, the vortex stretching enhances the small scale turbulent mixing and eradicates the non-uniformity of the temperature field.

4. CONCLUSIONS

(1) The transition from wrinkled laminar flames to distributed reaction zone is caused by the increase in R_λ or decrease in D_a.
(2) The wrinkled laminar flames stabilized on the cylindrical burner can be represented by fractal surfaces with a fractal dimension and inner and outer cutoffs to fractal behavior.
(3) In the distributed reaction zone, vortex stretching eradicates the non-uniformity of mean flow and creates a uniform turbulent flow field of isotropy through the cascade of turbulent energy transfer.

REFERENCES

1. Yoshida, A.:Twenty-Second Symposium (Int.) on Combustion, The Combustion Institute, pp. 1471-1478, 1989.
2. Kennedy, I. M.:Comb. Sci. Tech. 27, 247 (1982).
3. Murayama, M. and Takeno. T.:Twenty-Second Symposium (Int.) on Combustion, The Combustion Institute, pp. 551-559, 1988.
4. Mantzaras, J., Felton, P. G., and Bracco, F. V.:Comb. Flame 77, 295(1989).
5. Sreenivasan, K. R. and Meneveau, C.:J. Fluid Mech. 173, 356(1986).
6. Summerfield, M., Reiter, S. H., Kebely, V. and Mascola, R. W.:Jet Propul. 25, 377(1955).

IUTAM Symposium on
Aerothermodynamics in Combustors
June 3-5, 1991, Taipei

Blue Flame Combustion in a Jet-Mixing-Type Spray Combustor

Hiroyuki HIROYASU*, Masataka ARAI**, Kaoru NAKAMORI***
and Shinji NAKASO***

* Dept. of Mechanical Engineering, University of Hiroshima
** Dept. of Mechanical Engineering, Gunma University
*** Mitsubishi Heavy Industries, Ltd.

1. Introduction

Turbulent diffusion combustion systems in which sprays of liquid fuels are burned have been widely utilized in many industries as heating equipment. However, owing to a characteristic of the diffusion flame [1], these conventional combustion systems have been exposed to the danger of an exhausted soot emission which is one of the most undesirable of combustion products [2) 3)] for users. In order to avoid the soot emission, a lot of fundamental and application studies on soot emission control have been undertaken in recent years.

To be free from this soot emission problem, a blue flame burner system has been desired, and a few small burner systems which produce a blue flame have been successfully developed [4) 5) 6)]. Also there has been some minimal experimental work [7) 8) 9)] concerning the relation of the soot emission and the visual appearance of the flame, such as yellow and blue flames or luminous and nonluminous flames. While a soot-free combustion system has been strongly demanded, there is no blue flame system which can allow the use of the conventional spray system.

A new combustion system called a jet-mixing-type combustor has been developed by the authors according to the demand for a nonluminous blue flame combustion system to attain a soot-free combustion. In this combustion system, high speed air jets were impinging to a kerosene spray to make the high turbulence field in the kerosene spray. In this report, the principle mechanism of the combustor and exhaust emission characteristics are discussed.

2. Combustor and Experimental Set-up

Experimental set-up and outline of the combustor are shown in Fig. 1. The combustor was made of stainless steel pipe with an inner diameter of 134mm and a length of 560mm. The combustion air and fuel spray were supplied from the one end of the combustor. The combustion air supplied from a blower was introduced into the combustion chamber as air jets through a baffle plate with 16 air holes. Kerosene fuel was supplied from an accumulator. The fuel nozzle used in this study was a swirl atomizer of a hollow cone type. Its cone angle was 60 deg. and the Sauter mean diameter of its spray was about 25 μm.

In this study, combustion characteristics of nonluminous blue flame, flow field of air jets and fuel spray, temperature distribution in the combustor and exhaust gas emissions were investigated to understand the mechanism and combustion characteristics of the blue flame combustor.

The baffle plate and relative position of fuel spray and air jets are shown in Fig. 1 (a). This baffle plate was one of the most important elements in this nonluminous blue flame combustion system. The air holes of the baffle plate were specified by a hole position D, hole diameter d, number of holes n and a relative impinging angle θ between the air jet and the spray sheath. After many trials, these specifications of the air holes were finalized as D = 50 mm, d = 5 mm and n = 16 to obtain a blue flame under wide flow rates of fuel and air. In order to investigate the effect of a rapid mixing process of fuel and air on the combustion process, the relative impingement angle θ was varied from 0 deg. to 90 deg., because the mixing process was strongly affected by the location of

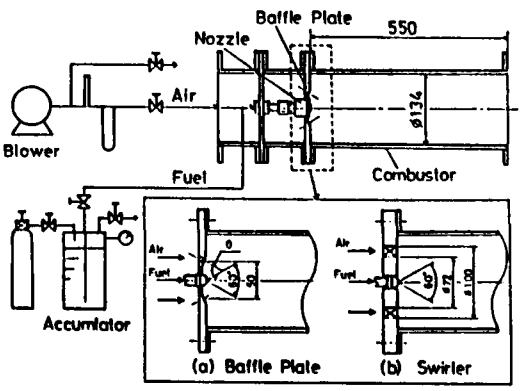

Fig.1 Experimental set up and combustor

the impingement point and the angle between the air jets and the fuel spray. Two kinds of swirlers, of which swirl number S were 0.5 and 0.87, were also used to obtain reference data for this jet-mixing-type combustor. The size of the swirler and its relative position to the nozzle are shown in Fig. 1 (b).

3. Results and Discussion

3.1 Combustion characteristics

The combustion characteristics of this jet-mixing type combustor were thoroughly investigated by changing the relative impinging angle. It was found that the blue flame combustion state appeared under an impinging angle in the range of 30deg. to 90deg. The combustion characteristics obtained by the combustor with the baffle plate of with a relative impinging angle of 60deg. is shown in Fig. 2, where Mf is the fuel flow rate and Ma is the air flow rate. The combustion state in the diagram was divided into three zones according to the visual appearance of the flame. In this figure, zone (1) shows the partially blue and partially yellow luminous flame. Both zones (2) and (3) show a kind of blue flame. The blue flame shown in zone (2) was a stable nonluminous flame that was followed by a violet-blue flame at the exhaust end of the combustor, and zone (3) shows a relatively unstable blue flame owing to a lean mixture ratio of fuel and air. With a further increase of the air fuel ratio, a blow off limit was suddenly reached.

3.2 Mechanism of the blue flame combustion

The range of the equivalence ratio that allows the blue flame state was obtained as a function of the relative impinging angle to investigate the role of a flow field. The range of the stable blue flame was widest at the relative impinging angle of 60 deg., as shown in Fig. 3. The flow field made by the air jets with the impinging angle 60 deg. was considered to be suitable in promoting the better mixing that caused the blue flame. To confirm the role of the flow field, the air jets and spray motions in a cold state were made visible using MgO powder as a tracer. Direct photographs using slit-light illumination method were taken for this purpose. From an image analysis of the Photograph, it was revealed that the air jets flowing through the 16 air holes impinged to the spray sheath and were concentrated together around the combustor axis. It became a single convergent and divergent flow around the axis, and the spray that met each air jet, moved to the center axis and was thoroughly mixed with the combustion air.

In order to compare the luminous yellow and nonluminous blue flames, both flames obtained from the combustors which had the relative impinging angles 20deg. and 60deg. respectively were looked at under the same flow condition. The fuel flow rate of 0.74 g/s and equivalence ratio of 1.4 were set as the flow condition where the stable blue and yellow flames appeared in each combustor.

The axial temperature distributions along the center axis of the combustors are shown in Fig.4. The temperature rise of the blue flame combustor (60deg.) was retarded compared with the yellow flame's temperature rise obtained in the yellow flame combustor (20deg.). This retarded temperature rise was considered to be caused by the convergent and divergent flow field in the blue flame combustor, and, moreover, this was regarded as a characteristic feature of this blue flame mechanism.

The axial distributions of THC are also shown in Fig. 4. The THC level in the yellow combustor shows a very high concentration near the nozzle but it decreased quickly. However, in the blue flame combustor, the THC concentration was not so high near the nozzle. While the THC increased slightly in the main flame zone, it finally decreased to a lower level than that in the yellow combustor at the combustor end. The double marked symbols at Z = 500 mm represent the radial

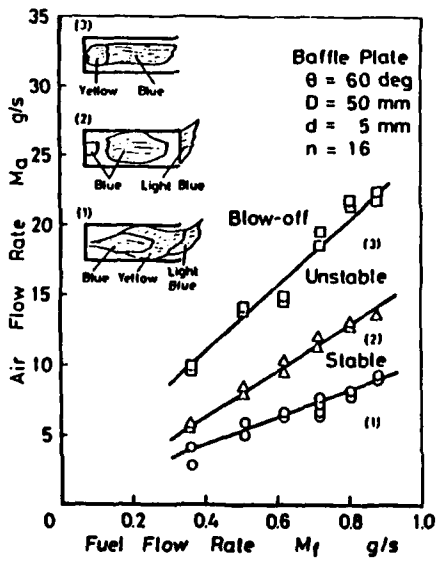

Fig.2 Combustion characteristics of the blue flame combustor with the 60 deg. baffle plate

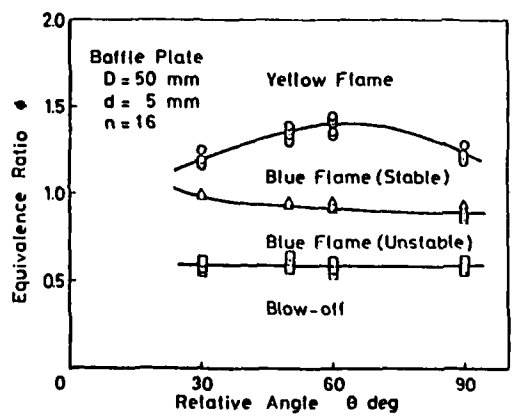

Fig.3 Effect of relative angle of a baffle plate on a blue flame combustion state ; Ma = 10 g/s

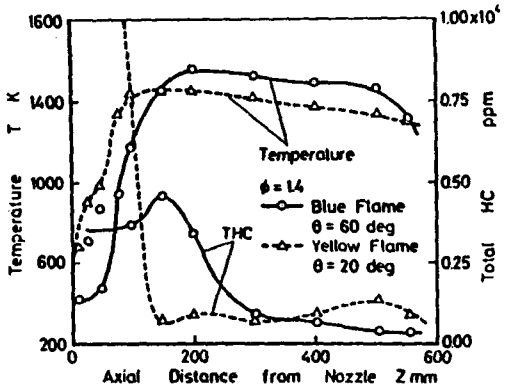

Fig.4 Effects of the relative angle of the baffle plate on the temperature and THC concentration along the combustor axis ;
M_a = 12.7 g/s, M_f = 0.74 g/s, ϕ = 1.4

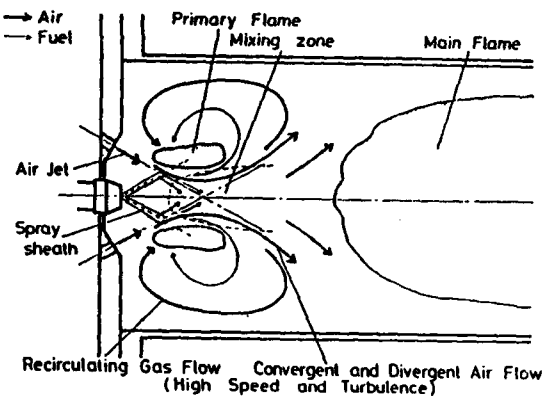

Fig.5 Blue flame combustion mechanism

averaged values of the THC concentration. The average for the blue flame combustor also shows a lower value than that of the yellow combustor.

From the temperature and the THC distributions, it was found that in the yellow flame combustor vaporized over-rich mixture was created and it burned as a turbulent diffusion flame. On the other hand, there was no vaporized over-rich mixture in the blue flame combustor; the evaporation of the fuel and thorough mixing with sufficient combustion air occurred rapidly at the impinging area of the fuel and air. Furthermore, the ignition was retarded owing to the high velocity of the convergent and divergent flow of the mixture.

According to these investigations and flow visualization using the MgO tracer, the mechanism of this blue flame combustor is summarized in Fig. 5 as follows.

(1) From the nozzle to the convergent flow section of the air jets: The impingement of the air jets and the fuel spray induced their rapid mixing. In the same instance, a hot lean burned gas supplied from the blue flame around the air jets was entrained into the mixture and promoted the evaporation of the spray.

(2) From the divergent flow section of the air jets to the flame front: Mixing and evaporating processes occurred in the highly turbulent divergent flow. However there was no flame propagation from the main flame, because the axial flow velocity of the mixture in this zone was higher than the flame propagation velocity.

(3) The main flame zone: The main combustion took place here as a blue nonluminous flame.

(4) Out side of the combustor: When the over-rich mixture was burned inside the combustor, the supplemental violet-blue flame appeared outside of the combustor.

4. Conclusion

A new combustion system called a jet-mixing-type combustor was developed to obtain a blue flame combustion system. The combustion characteristics such as combustion stability, temperature distribution, and emission characteristics were investigated in this new combustion system. It was revealed that the combustion mechanism of prompt mixing and retarded ignition was caused by the convergent and divergent air flow in this combustor. This combustion system showed a high potential for attaining soot-free high efficiency combustion with low NO and THC emissions.

References

1) GAYDON, A. G. : The Spectroscopy of Flames 2nd Ed. p.41, Chapman and Hall, 1974.

2) LEFEBVRE, A. H.: Gas Turbine Combustion, p.473, Hemisphere Pub. Co.,1983.

3) LEVY, A., Nineteenth Symposium (International) on Combustion, p.1223, The Combustion Institute, 1982.

4) TANASAWA,Y., Eighth Symposium(International) on Combustion, p.1003 The Combustion Institute, 1960.

5) NAKAYAMA, M., Trans. of JSME, 39-318, 704 (1973).

6) NAKAYAMA, M. and SUZUKI, T.,Trans. of JSME (B), 48-434, 2116(1982).

7) HIROYASU, H.,KADOTA, T. and ARAI, M., Proceeding of the 3rd World Hydrogen Energy Conference, Tokyo Japan, p.1199 (1980).

8) RICHARD, G. A.,SOJKA, P. E. and LEFEBVRE, A. H., J. of Engineering for Gas Turbines and Power, (Trans. of ASME), 111, 84 (1989).

9) SIVATHANU, Y. R., KOUNALAKIS, M. E., GORE, J. P. and FAETH, G. M.: Radiation from Turbulent Nonluminous and Luminous Diffusion Flames. NIST-GCR-88-553 (1988).

IUTAM Symposium on
Aerothermodynamics in Combustors
June 3-5, 1991, Taipei

High Speed Hydrogen Combustion Phenomena

M. Haibel, F. Mayinger, G. Strube

Lehrstuhl A für Thermodynamik
Technical University of Munich
Arcisstr. 21, D-8000 München 2, FRG

Hydrogen is regarded as one of the most promising energy carriers of the future. It shows a high specific energy density and the exhaust gases from a combustion with air, with H_2O as the main reaction product, contain nearly no toxic parts and do not contribute to the greenhouse effect. Furthermore hydrogen can be generated simply by the electrolytical dissoziation of water. However, the complex interactions of fluid mechanics, gasdynamics and reaction kinetics involved in the combustion process are not yet understood. Therefore the authors' institute is involved in hydrogen combustion research for nearly a decade with two major aspects. For one there are safety considerations with regard to accidental combustion in hydrogen facilities with storage tanks and distribution systems or in nuclear power plants in the course of a loss-of-coolant-accident. The other aspect is the optimization of combustion chambers.

The major safety problem in hydrogen facilities in case of an unintentional ignition of hydrogen/air mixtures beside the release of large amounts of thermal energy are possible strong deflagrations or even detonations. The propagation rate of an initially slow deflagration can be increased by turbulent flame acceleration up to supersonic speeds or even undergo transition to detonation [1, 2]. Since fast flame fronts are connected with strong overpressures, reaching values of more than thirty times the initial pressure in the case of a detonation, they are capable of damaging inventory parts of a facility. Therefore detailed knowledge of the mechanisms of turbulent flame acceleration and the transition from deflagration to detonation is necessaray for safety analysis.

While for unintentional ignitions of large hydrogen/air mixtures the resulting combustion rate should stay as low as possible, the aims pursued in the design of optimized combustion chambers are quite contrary: high energy release, small geometrical dimensions and high efficiency of the reaction. To reach those goals, one basic questions is, how the reaction rate and the stability of a flame can be influenced by means of induced turbulence. The degree of turbulence can both increase the reaction rate at lower degrees but also decrease the reaction rate due to quenching effects at high degrees of turbulence [3, 4]. Therefore the combustion process in a combustion chamber should be organized so that the degree of turbulence is as high as possible but below the level at which quenching effects reduce the reaction rate. The mechanisms involved are similar to the ones responsible for turbulent flame acceleration.

For the investigation of turbulent combustion behaviour of various hydrogen/air mixtures an explosion tube (6 m long, 66 mm inner diameter) equipped with opto electronical sensors to detect the flame front velocity was used. Arrays of orifices with different blockage ratios and distances between two successive orifices were placed inside the explosion tube to study the effect of turbulence on the general combustion behaviour. *Fig 1* shows typical flame front velocities recorded along the axis of the explosion tube when an array of orifices with a blockage ratio of 69% and a spacing value of 490 mm, representing a multichamber geometry, is installed [5]. The blockage ratio is defined as the ratio of the area blocked by the orifices in the detonation tube to the area of the unblocked tube. Flame acceleration is mainly caused by a turbulent jet of hot gases emerging through the opening of the orifice into the next chamber. Depending on the hydrogen concentration different maximum burning velocities connected with different combustion modes are reached. In the mixture with 11% hydrogen the flame propagates as a normal deflagration. Its velocity increases rapidly at the beginning of the obstacle array, but quenching effects cause the velocity to drop after a distance of about 1.5 m and the flame is finally quenched completely before it reaches the end of the tube. At 14% hydrogen the flame is accelerated strongly to proceed as a supersonic flame through the obstacle array. Pressure losses prevent further flame acceleration to speeds near the detonation velocity. At the end of the obstacle region the velocity decreases again due to decreasing turbulence. The flame in the mixture with 24% hydrogen accelerates very fast to speeds close to the detonation speed and eventually

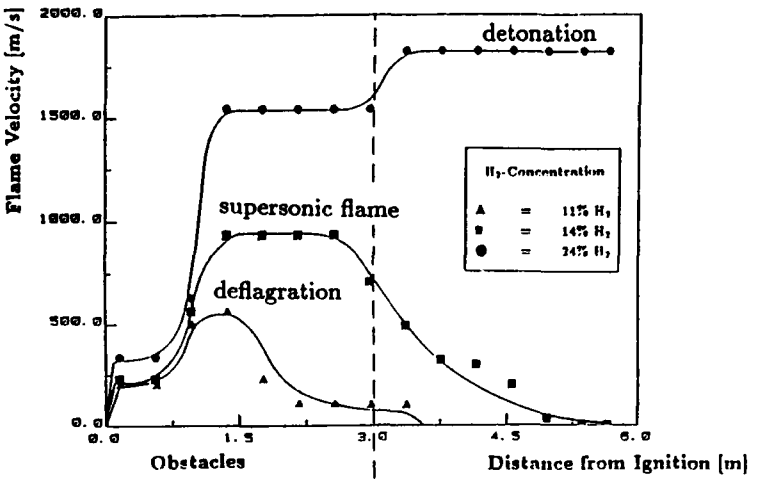

Fig.1 Flame velocity in detonation tube; obstacle distance 490 mm, blockage ratio 0.69

undergoes transition to detonation at the end of the obstacle array. A significant difference was observed in the combustion behaviour when the multichamber arrangement described above was replaced by an array of orifices with a blockage ratio of only 32%. Here the flame is accelerated by turbulence induced by the obstacles. *Fig. 2* shows the maximum flame front velocities reached within the obsatcle array for both blockage ratios used [5].

Due to the motion of the unburnt gas ahead of the flame the velocities obtained in the explosion tube are the added values of the velocity of the unburnt gases and the actual burning velocity. However, the burning velocity is the key parameter for stationary combustion. Therefore LDV measurements of the gas velocity are currently conducted in the explosion tube. The burning velocity can both be calculated from the difference of the gas velocity in front of and behind the reaction zone by applying the conservation laws of mass, momentum and energy as well as from the difference between the gas velocity ahead of the flame and the total flame front velocity as it is obtained from the opto-electronic sensors. Although these measurements are very difficult due to the extremely fast processes involved, first results indicate, that during the transition to detonation the burning velocity reaches values close to the critical burning velocity.

To investigate stationary hydrogen combustion phenomena, two combustion chambers had been installed. One is designed as a tube-type subsonic burner equipped with removable turbulence promoting obstacles for the investigation of the structure of turbulent flames as they appear behind such obstacles [6]. The other setup is a transsonic wind tunnel in which high speed hydrogen/air flames are examined [7].

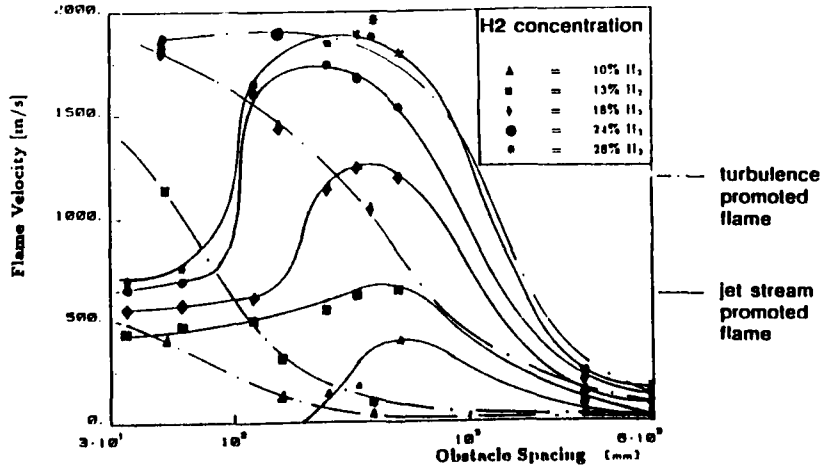

Fig.2 Maximum flame velocity as function of turbulence (represented by distance between obstacles)

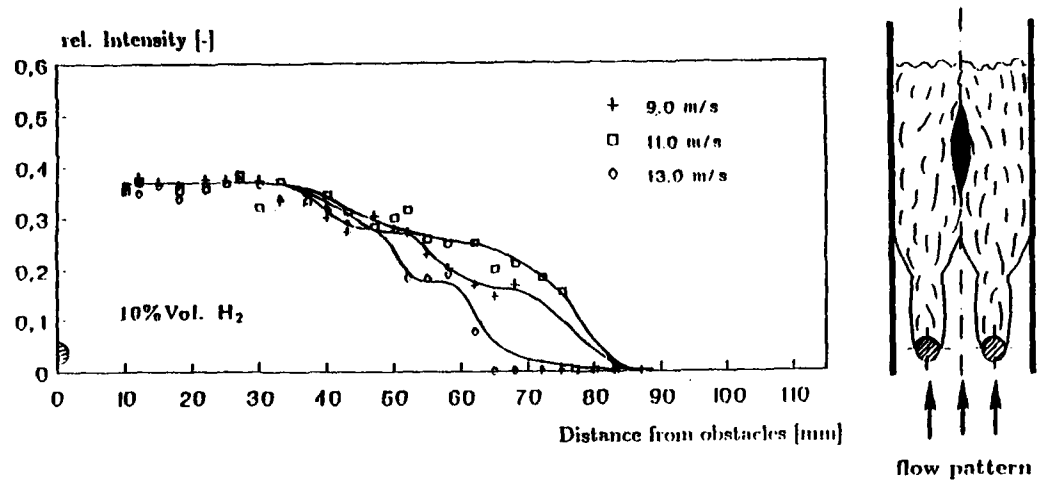

Fig.3 Hydrogen concentration profiles downstream of obstacles

The subsonic burner can be operated at various hydrogen concentrations and main stream velocities and the obstacle configuration can also be changed. Depending on the flow field induced by the obstacles the process of combustion varies. The method of raman scattering was used to simultaneously measure the concentration of H_2, N_2, O_2 and H_2O along the main stream axis of the burner. This simultaneous measurement of all species is achieved by the employment of a pulsed excimer laser as a high energy light source and an intensified diode-array detector as a highly sensitive detector. *Fig. 3* shows the profiles of the hydrogen concentration at main gas velocities of 9, 11 and 13 m/s when the burner is equipped with two parallel obstacles and the hydrogen content is set to 10% [6]. Each flame exhibits distinct non-reactive regions which are assumed to be caused by quenching effects within the flame. The number and position of these region is determined by the flow field which varies with the main gas velocity. This setup should also be suitable for future examinations to optimize combustion in a stabilized recirculation area at higher main gas velocities.

In the transsonic wind tunnel both the mixing of hydrogen and air as well as the stabilization of flames by induced recirculation zones are investigated over a wide range of main air flow velocities up to the transsonic region and different injection systems for hydrogen [7]. The distribution of hydrogen in air is detected by holographic interferometry. This measurement technique allows large regions to be examined with a single measurement. The stabilization of the flames is achieved by either one or two reward facing steps inducing recirculation zones. Like in the subsonic burner the method of raman scattering is employed to investigate the structure of the combustion zone. However, by using a pulsed dye laser and an intensified CCD-camera the obtained species distribution will be one dimensional instead of point measurements. First results of these investigations expected within the next few months.

References:

[1] Strehlow R.A.: *Combustion Fundamentals*; McGraw-Hill, New York ; 1984

[2] Bartlmä F.: *Gasdynamik der Verbrennung*; Springer Verlag, Berlin; 1975

[3] Brehm N.: *Ein Beitrag zum Phänomen des Übergangs Deflagration-Detonation*; Dissertation; TU München; 1987

[4] Brehm N., Mayinger F.: *Turbulent Flame Acceleration: The Transition from Deflagration to Detonation*; Proc. of Second Int. Symp. Heat Transfer; Peking; 1988

[5] Haibel M., Mayinger F., Strube G.: *High Speed Hydrogen Combustion: Former and Future Research Activities*; R & D-Support Group Aerothermodynamics of Combustion Chamber and Nozzles in the FRG Hypersonic Technology Programme; Internal Report; Aachen; 1990

[6] Mayinger F., Strube G.: *Struktur und Brenngeschwindigkeit hochturbulenter Wasserstoffflammen*; BMFT- Abschlußbericht RS 1 500 769; FIZ Karlsruhe; 1990

[7] Haibel M., Mayinger F.: *Hochgeschwindigkeits-Wasserstoff-Luft-Verbrennung*; Annual Meeting of the SFB-project 255 in Munich; TU Munich; 1990

IUTAM Symposium on
Aerothermodynamics in Combustors
June 3-5, 1991, Taipei

COMPOSITION EFFECT ON INTERFEROMETRIC TEMPERATURE MEASUREMENT

C.C. Chen, K.C. Chang, and S.M. Tieng

Institute of Aeronautics and Astronautics
National Cheng Kung University
Tainan, Taiwan/R.O.C.

INTRODUCTION

Recent progress in laser optical diagnostics provides the scientist and engineer with the capability for remote, nonintrusive, in-situ, spatially and temporally precise measurements of important parameters in flame study. Application of holographic interferometry to temperature measurements in flames has been demonstrated as a viable means in engineering practices [1-5]. Nevertheless, the deflection of light in a homogeneous medium arises from refractive index gradients, which in turn arise from a combination of density (primary factor) and composition changes across the flow field being observed. Often the effect of composition changes on the previous applications of holographic interferometry to the temperature measurements in flames was either neglected [4] or assumed by a simpler relationship [2] owing to lack of distribution information of species composition.

The relation between refractive index and temperature can be found from the ideal gas law and the Gladstone-Dale relation [6]. For a mixture of gases the ideal gas law is expressed by

$$\rho(r) = P \sum_i M_i x_i(r) / [RT(r)] \qquad (1)$$

where $\rho(r)$ and $T(r)$ are the density and absolute temperature at the position of r, respectively; P is the presure, R is the universal gas constant, and $x_i(r)$ and M_i are, respectively, the mole fraction and molecular weight of the ith species in the gas mixture. The Gladstone-Dale relation gives the dependence of refractive index on density as follows.

$$n(r) - 1 = \rho(r) \sum_i K_i x_i(r) \qquad (2)$$

where $n(r)$ is the refractive index at the position of r, and K_i is the Gladstone-Dale constant of the ith species. Combination of Eqs. (1) and (2) yields

$$n(r) - 1 = P \sum_i M_i x_i(r) \sum_i K_i x_i(r) / [RT(r)] \qquad (3)$$

Apparantly, the relationship of temperature and refractive index is a function of species composition as described in Eq. (3). Reuss [4] measured the temperature distribution of a premixed, lean propane-air flame (the equivalence ratio = 0.55) by using holographic interferometry. He argued that the values of $\sum K_i x_i$ of the reactants and products vary by less than 2% in the flame; he, then, assumed the constant value of $\sum K_i x_i$ throughout the flame.

The Gladstone-Dale constants of the species composed of the propane-air flame for the ruby laser wavelength 694.3 nm are listed in Table 1 [7]. Obviously, the variations of K values are significant for different species; the constant assumption for $\sum K_i x_i$ may bring in errors in temperature measurements using holographic interferometry. South and Hayward [2] assumed that $\sum K_i x_i$ varied linearly in terms of mixture fraction from the reactants to the products through the flame in the absence of experimental measurements of species composition. As we will find later, the species composition distributions are much complex than the linear form in some kinds of flame. The assumption of linear dependence may be too rough to obtain adequately accurate temperature results for all flames.

Table 1 Gladstone-Dale constants

Species	K (g/mℓ)	Species	K (g/mℓ)
Air	6.284	CH_4	9.831
CO	7.460	C_2H_2	13.071
CO_2	9.940	C_2H_4	15.890
H_2	3.096	C_3H_8	23.986
H_2O	5.602		

The objective of this study is to investigate the effect of composition changes on temperature measurements by holographic interferometry. To achieve this objective, the distribution information of species composition should be also measured in the study. The precision of the holographic interferometry is determined by comparing with the temperature measurements obtained with thermocouple.

EXPERIMENTAL METHODS

The test apparatus consists of a Bunsen burner of 20 mm i.d. injecting vertically upward within a screened enclosure (one-layer of 24-mesh screen 500 mm square and 800 mm in height) to reduce effects of room disturbances. The 99% purity of propane

is used as the gaseous fuel. The radially symmetric, laminar premixed propane-air flames, stationary in unconfined air, are investigated.

A double-exposure holographic interferometer is used to obtain the interferograms. A 3 J ruby pulse laser serves as a coherent light source. The interferograms are analyzed by a video digitizer and the sectional distributions of fringe number are, then, obtained. Temperature measurements are also made with a bare thermocouple using 25 μm diameter Pt versus Pt 10% Rh wire. Temperature corrections due to radiation loss in this high-temperature domain of interest need to be made and follow the estimation procedure specified in Ref. 8. The thermocouple is mounted on a two-dimensional traversing gear that allows it to be moved horizontally through the flames to obtain temperature profiles and vertically along the axial direction.

The gas analysis is performed by using a gas chromatograph with thermal conductivity detector. A tapered quartz microprobe with a small sonic inlet is used for gas sampling to allow rapid decompression and withdrawal of the sample to a cool region outside the flame for analysis. The microprobe is inserted into the flame along the flow streamline for sampling to avoid the disturbance of the flame. Twelve species including N_2, O_2, CO, CO_2, H_2, CH_4, C_2H_2, C_2H_4, C_2H_6, C_3H_4, C_3H_6 and C_3H_8 are analyzed in this work. Details of gas chromatographic measurements are referred to Ref. 9. One major combustion product, H_2O, cannot be detected with the thermal conductivity detector. The local water vapor content can be, however, estimated by the measured species composition through the relationship for the conservation of atoms.

RESULTS AND DISCUSSION

Two cases: fuel lean-flame and fuel-rich flame are studied and summarized in Table 2. Prelimary study [9] reveals that the flame structures of these two cases are quite different. Figure 1 shows schematically the flame structures of the lean and rich cases. Clearly, the rich flame has a much complicated structure than that of the lean flame. The Gladstone-Dale constant of the reactants for the rich flame is calculated from the propane-air mixture of the given equivalence ratio, while the Gladstone-Dale constant of the product for the rich flame is calculated from the assumption of complete combustion. For the case of lean flame, the constants of the reactants and the products are calculated with the given equivalence ratio. These K values are listed in Table 3. Clearly, the variations of K value are much significant in the rich flame than those in the lean flame. Comparison of composition distributions between the rich and lean flames

Table 2 Test conditions

Flame type	Rich	Lean
Equivalence ratio*	1.90	0.64
Reynolds number†	58	765
Inlet temperature (K)	350	350

* molar ratio of fuel to air/stoichiometric molar ratio of fuel to air.

† based on the inlet conditions.

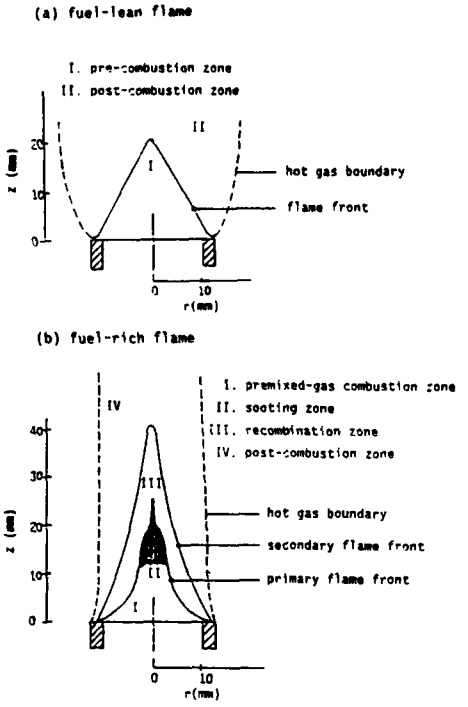

Fig. 1 Schematics of flame structure

Table 3 Gladstone-Dale constants of the mixture

Flame type	Rich	Lean
K for the reactants ($g/m\ell$)	5.320	4.660
K for the products ($g/m\ell$)	4.580	4.511

[9] provides an explanation to this substantial difference. The lean-flame structure is relatively simple [9] and can be described by an one-dimensional model [10] which assumes that the reaction course through the flame zone is a function of a single distance parameter. This implies that the linear assumption of $\sum K_i x_i$ between the reactants and products may be applicable to the interferometric temperature reconstruction of the lean flame. On the other hand, the composition variation in the rich flame is more complicated than that in the lean flame as shown in Ref. 9. It is reasonably speculated that the composition effect on interferometric temperature measurements may be much significantly in the rich flame than in the lean flame.

Three different K distributions are used to reconstruct the interferometric temperatures.

T_1: linear interpolation of K at the axis (K of the reactants) and at the hot gas boundary (K of the products)

T_2: uniform distribution using K of the products

T_3: uniform distribution using K of the reactants

The reconstructed interferometric temperatures obtained with these three K distributions are plotted in Fig. 2 and compared with the thermocouple measurements at the axial station of $z = 12$ mm for the lean and rich flames. Note that both thermocouple temperatures with and without corrections to radiation loss are presented in Fig. 2. Generally, the agreements between the interferometric and thermocouple

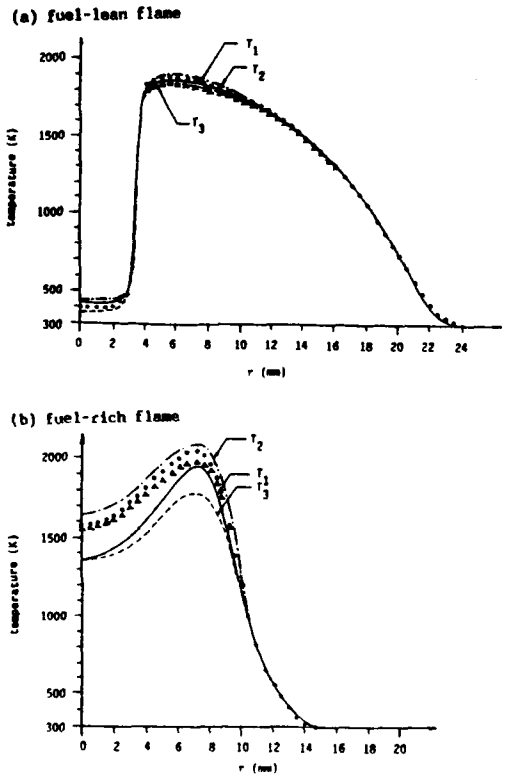

Fig. 2 Comparison of interferometric temperatures (without consideration of composition effect) with thermocouple temperature at z = 12 mm

(with correction to radiation loss) temperatures are satisfactory, in particular for T_2's. The interferometric temperatures using the linear K distribution is within 60 K (3.1%) of the thermocouple temperatures. On the other hand, no satisfactory agreements between the interferometric and thermocouple temperatures are obtained in the rich-flame case. One inference can be drawn that the effect of composition change on K has to be considered in reconstruction procedure of interferometric temperatures for the rich flame which exhibits a complicated flame structure.

To validate this inference, the effect of composition changes is taken into account in temperature reconstruction, that is, K values are determined with the measured concentration information provided in Ref. 9. Figure 3 compare the interferometric temperature reconstructed by real K distributions with the thermocouple temperatures at axial station of z = 12 mm for both lean and rich flames. It shows that these interferometric temperatures are in excellent agreements with the thermocoouple tempeatures with corrections to radiation loss. It is, then, concluded that composition effect on temperature measurements using holographic interferometry is necessarily considered as applying to the case of premixed rich flame.

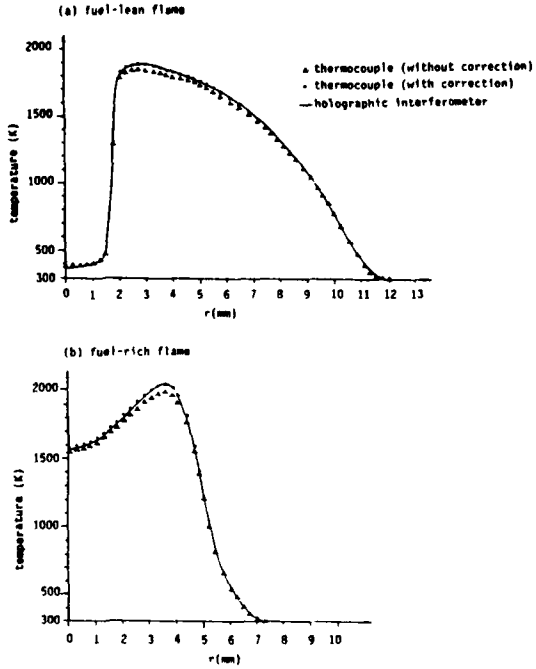

Fig. 3 Comparison of interferometric temperature (with consideration of composition effect) with thermocouple temperature at z = 12 mm

REFERENCES

1. Abdel-Khalik, S.I., Tamaru, T. and El-Wakil, "A chromatographic and interferometric study of the diffusion flame around a simulated fuel drop," 15th Symp. (Int.) on Combust., The Combust. Inst., Philadelphia, pp. 389-399 (1974).
2. South, R. and Hayward, B.M., "Temperature measurements in conical flames by laser holographic interferometry," Combust. Sci. Tech., Vol. 21, pp. 183-195 (1976).
3. Trolinger, J.D., "Holographic interferometry as a diagnostic tool for reacting flows," Combust. Sci. Tech., Vol. 13, pp. 229-244 (1976).
4. Reuss, D.L., "Temperature measurements in a radially symmetric flame using holographic interferometry," Combust. Flame, Vol. 49, pp. 207-219 (1983).
5. Reuss, D.L. and Schultz, P.H., "Interferometric tempeature measurements of a flame in a cylindrical tube using holography," Appl. Optics, Vol. 26, pp. 1661-1667 (1987).
6. Vest, C.M., Holographic Interferometry, Chap. 6, John Wiley (1979).
7. Gardiner, W.C., Hidaka, Y. and Tanzawa, T., "Refractivity of combustion gases," Combust. Flame, Vol. 40, pp. 213-219 (1981).
8. Kaskan, W.E., "The dependence of flame temperature on mass burning velocity," 6th Symp. (Int.) on Combust., The Combust. Inst., Philadelphia, pp. 134-143 (1957).
9. Chen, C.C., Chang, K.C. and Yuan, H.F., "Studies of premixed laminar flame structure: concentration measurement," to appear in J. Chinese Inst. Engineers.
10. Fristrom, R.M., "Flame studies II. applicability of 1-D models to 3-D laminar Bunsen flame fronts," J. Chem. Phys., Vol. 24, pp. 888-894 (1956).

IUTAM Symposium on
Aerothermodynamics in Combustors
June 3-5, 1991, Taipei

AN EXPERIMENTAL AND NUMERICAL STUDY OF COMPLEX FLOW IN THREE DIMENSIONAL SWIRLING COMBUSTORS

Liu Wei, Yan Chuanjun, Tang Ming, Wang Hongji

Dept. of Aeroengine, Northwestern Polytechnical University

Xi'an,710072, Shaanxi, P.R.C

INTRODUCTION

In this paper, an experimental and numerical study of velocity and temperature fields in model swirling combustors has been conducted. With the emphasis on the experiment, a large amount of experimental results has been gained. The purpose of this paper is to help the design of combustors and the development of numerical modeling.

THE EXPERIMENTAL APPARATUS

Two model combustors have been designed for measurement of both velocity and temperature fields. The first one, which is made of plexiglass, is for cooling conditions. The second, which is made of high temperature-resistant steel, is for reacting flow. For the latter, an air-cooling system has been designed to protect the combustor wall from the high temperature resulting from combustion. Some primary holes have been designed around both combustors, so that the secondary airflow can be introduced. In addition to the above mentioned, the exit area of the combustor for isothermal flow, thus the convergent-ratio of the exit area to the combustor's cross-section area, can be changed. These two simplified combustors, with some specific sizes and sections for measurement designated in the diagram, are shown in Fig.1 (1).(2).

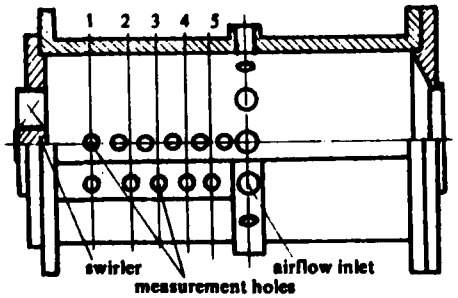

(1)

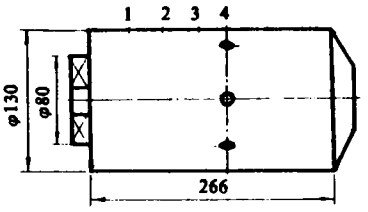

(2)

Fig.1 Schematic of model combustors

(1) For isothermal flow
(2) For reacting flow (The cooling system has been removed)

In the study, two vane swirlers, with the swirling number S being 0.6 and 3.2, have been used. A fuel nozzle, which has many small holes with a certain angle to give uniform fuel injection, has been specially designed for swirling diffusion combustion. In this case, the acetylene has been used as the gaseous fuel. Both airflow and acetylene can be respectively controlled in a convenient way.

A small size seven-hole probe has been used for measurement of velocity. Two kinds of high temperature thermocouples have been used to measure the temperature field in the combustor.

THE ISOTHERMAL EXPERIMENT

In this experiment, isothermal swirling flows without or with secondary airflow have been created. The effect of several factors on the flow, such as the convergent-ratio(R), the swirl number (S), and the flow-rate ratio of primary / secondary (G), has been studied.

The experiment shows that the size (both length and width) of the recirculation zone in the combustor is highly dependent on the swirl number S and convergent-ratio R. Fig.2 (1)(2) is the profile of the axial velocity. The S is 3.2 in both cases. It is clearly seen that the size of the recirculation zone changes significantly,when the convergent-ratio is increased. Noteworthy is the shape of the recirculation zone which is dif-

ferent in these two cases. An annular zone is formed in the first case, when a certain convergent-ratio is given.

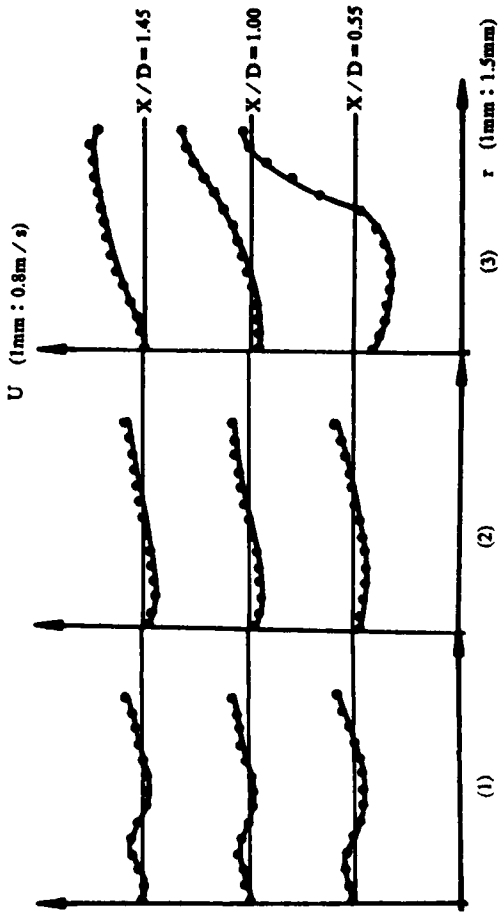

Fig.2 The profile of axial velocity

(1) R = 0.5, S = 3.2
(2) R = 1.0, S = 3.2
(3) R = 1.0, S = 0.6

The profile of axial velocity with different S is demonstrated in Fig.2(3). The size of the recirculation zone is obviously smaller when S decreases, though at the first section, the reverse velocity is larger in (3) than in (2). In case (2), more kinetic energy is used in tangential direction due to stronger swirling flow.

The effect of different flow rate ratios of primary to secondary airflows on the flow field has been studied under different conditions, such as different primary holes, different measurement sections, different secondary flow rates, etc. Fig.3 presents only two cases.

As can be seen in (1), when the flow-rate ratio G is 1.5 and the primary holes N are 12, the recirculation zone is of annular shape, which is similar to one without a secondary flow. Whereas in (2), when the primary holes are 6 and the flow rate of the second airflow is smaller, the recirculation zone is greatly increased and is of a central shape. The experiments in our study indicate that the formation of recirculation zone is combined result of both primary and secondary flows. Only with an appropriate secondary flow rate, as well as suitable numbers of primary holes, can the recirculation zone be strengthed.

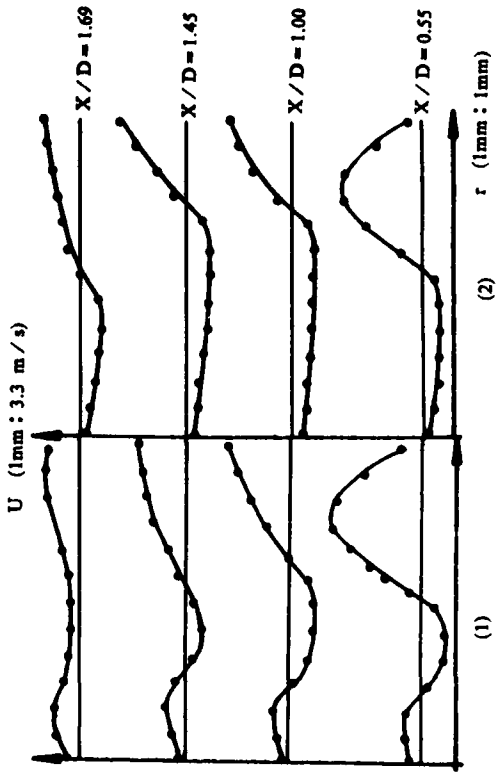

Fig.3 The profile of axial velocity

(1) N = 12, G = 1.5, S = 0.6
(2) N = 6, G = 2.3, S = 0.6

THE REACTING FLOW EXPERIMENT

In the experiment with the reacting flow, the temperature field in the combustor is measured for flow conditions with or without secondary airflow and different flow rate ratios of fuel to airflow (F).

When there is no secondary air flow through primary holes, the temperature profile is given in Fig.4(1), as an example. As can be seen, the temperature profile of each section shows a greater gradient and higher temperature zone is near the central line of the combustor. The experiment with swirling number 3.2 was also conducted.The results indicate that the shape of the temperature profile remains the same with different S,though the value and its gradient at the same section are somewhat different.

Fig.4(2) (3) is the experiment results when the flow rate ratios of primary to secondary airflows are different. It can be seen from the profile that when the secondary airflow is introduced through primary holes, an annular high temperature zone forms, and that makes the temperature profile more uniform.

The value of G (the flow rate ratio of primary to secondary flows) has a very important effect on the temperature profile of each section. For example, when G equals to 1.6, the temperature profile still has its peak value near the central line at section 3, whereas the temperature profile has its peak value at section 2 when G is 1.3. The annular recirculation zone is in agreement with what was measured, as mentioned above, by the seven-hole probe under cooling conditions.

The experiments also reveal the temperature gradient decreases at the same section under the same G and that the temperature profile are not as uniform when the ratio of fuel to airflow decreases.

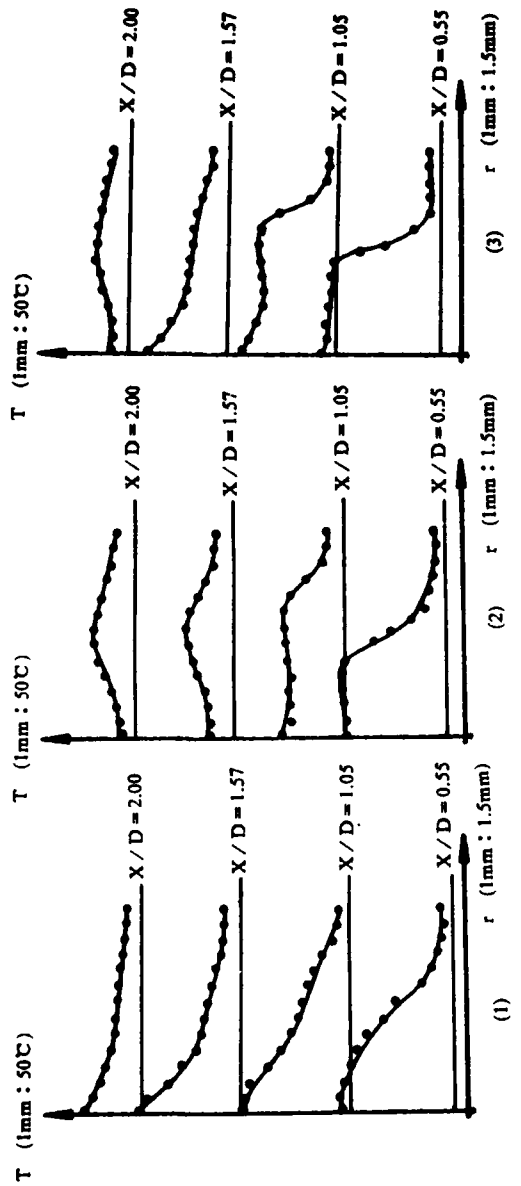

Fig.4 The profile of temperature

(1) No secondary airflow, F = 2.76(× 1000)
(2) G = 1.3, F = 3.25(× 1000)
(3) G = 1.6, F = 2.87(× 1000)

THE NUMERICAL CALCULATION

As a preliminary work in this present paper, part of the numerical calculation, mainly for the isothermal swirling flow and swirling reacting flow without secondary airflow, has been carried out. The "SIMPLE" method, which has been widely used,was employed. In the calculation, a k–ε two–equation turbulent model and a k–ε–g reaction model for diffusion combustion were used.

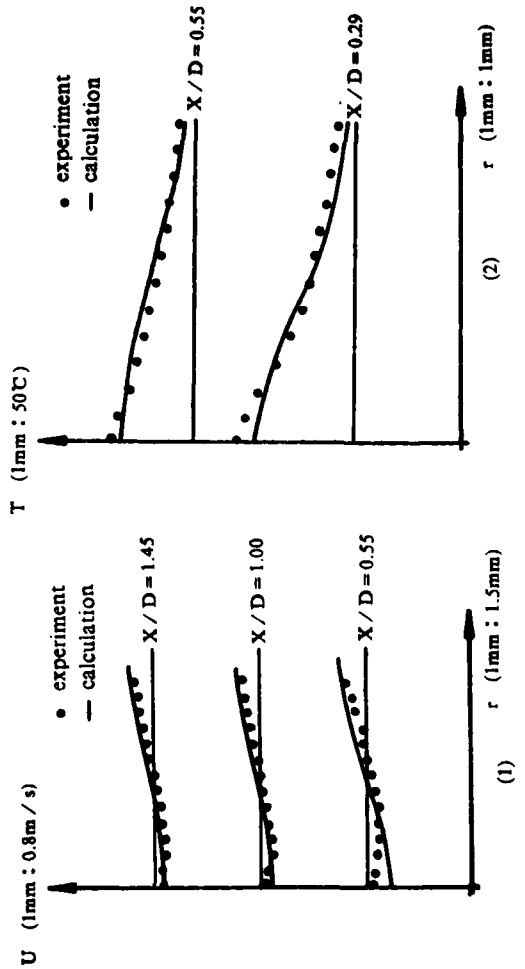

Fig.5 The comparision of calculated & experimental results
(1) The axial velocity profile, S = 3.2, R = 1.0
(2) The temperature profile, S = 0.6, F = 1.0(× 1000)

Fig.5 presents only some of the calculated results. (1) is the comparision of velocity profile gained by both experiments and calculations under cooling condition. (2) is the comparision of temperature profile with the reacting flow. A lot of results in our calculations are qualitatively in agreement with the experimental results. This suggests that the calculation, including various physical models, needs to be further improved.

IUTAM Symposium on
Aerothermodynamics in Combustors
June 3-5, 1991, Taipei

A PERFECTLY-STIRRED-REACTOR DESCRIPTION OF TURBULENT METHANE-AIR NONPREMIXED FLAMES

J.-Y. Chen

Combustion Research Facility
Sandia National Laboratories, Livermore, CA 94550, U.S.A.

Robert W. Dibble

Department of Mechanical Engineering
University of California, Berkeley, CA 94720, U.S.A.

INTRODUCTION

Recent measurements of turbulent methane-air nonpremixed flames by Masri *et al.* [1] showed high levels of CO concentrations (peak value $\approx$ 9% mass fraction) that cannot be explained by steady state laminar flamelet results (peak value $\approx$ 5%). This disagreement raises a fundamental question about the general validity of flamelet concept in modeling turbulent nonpremixed flames. Mauss *et al.* [2] suggested that the *unsteady* nature of the flamelets could be responsible for CO mass fractions as high as 7% during the reignition process for mixture that has been extinguished temporarily. In this paper, an alternative explanation of such high CO mass fractions is offered using a perfectly-stirred-reactor (PSR) description of turbulent jet nonpremixed flames.

PERFECTLY-STIRRED-REACTOR (PSR)

In order to understand the complex chemical reactions occurring in turbulent jet flames, a phenomenological model has been proposed by Broadwell and Breidenthal [3] to treat a turbulent nonpremixed jet flame as an ensemble of well mixed zones that are separated by diffusion layers. The well mixed zones are approximated by a PSR, which can include detailed chemical kinetics. Such a model offers the ability to predict complex chemical kinetic behavior but uses simplified fluid mechanical models, such as overall entrainment laws. A detailed model has been developed by Lutz *et al.* [4] to study NO_x formation in turbulent nonpremixed jet flames. According to their model, much of the jet has zones of the well-mixed fluids. Therefore, for simplicity, we may represent the jet in a Lagrangian sense by a single PSR that evolves downstream.

The governing equations for the PSR at constant pressure are given by

$$\frac{dY_k}{dt} = -\frac{1}{\tau}(Y_k - Y_k^*) + \frac{\dot{w}_k W_k}{\rho}, \qquad (1)$$

$$C_p\frac{dT}{dt} = \frac{1}{\tau}\sum_{k=1}^{k=K} Y_k(h_k^* - h_k) + \sum_{k=1}^{k=K}\frac{h_k\dot{w}_k W_k}{\rho} - \frac{Q}{\rho V}, \qquad (2)$$

where Y_k is the mass fraction of the kth species; W_k, the molecular weight; V the reactor volume; $\dot{w}_k$, the molar rate of production rate; h_k, the specific enthalpy; Q, the reactor heat loss; $\tau = \rho V/\dot{m}$, the residence time with $\dot{m}$ being the mass flow rate of reactor; C_p, the mass-weighted specific heat; superscript *, the inlet condition. These two equations are solved by CHEMKIN II and LSODE [5] subroutine programs developed at Sandia.

RESULTS FORM STEADY STATE PSR

To explore the possible high CO concentrations that can result from a PSR, we obtain the steady state PSR outlet concentrations at various residence times using a 42-step C1 methane kinetic mechanism from Smooke *et al.* [6] for mixture fractions 0-0.11 (the stoichiometric value for methane=0.055). The predicted profiles of temperature and CO versus residence time are shown in Figure 1. For stoichiometric mixture, as residence time decreases below 70 microseconds, the outlet temperature drops suddenly to inlet temperature indicating the reactor is unable to sustain combustion. As the reactor approaches this flame-out condition, CO concentration increases. In Figure 2, the maximum CO mass fractions are plotted versus mixture fraction and compared to the experimental data from Masri *et al.* [1]. Also shown in the figure are the steady state opposed jet laminar flame results at high and low strain rates. The steady state PSR results show that the maximum CO concentration increases from lean mixtures toward the stoichiometric mixture (at f=0.055) and continues to increase until CO reaches its 9% peak at $f = 0.085$ or equivalence ratio 1.6. Beyond $f = 0.085$, CO drops in richer mixtures, and eventually the reactor cannot sustain combustion for very rich mixtures.

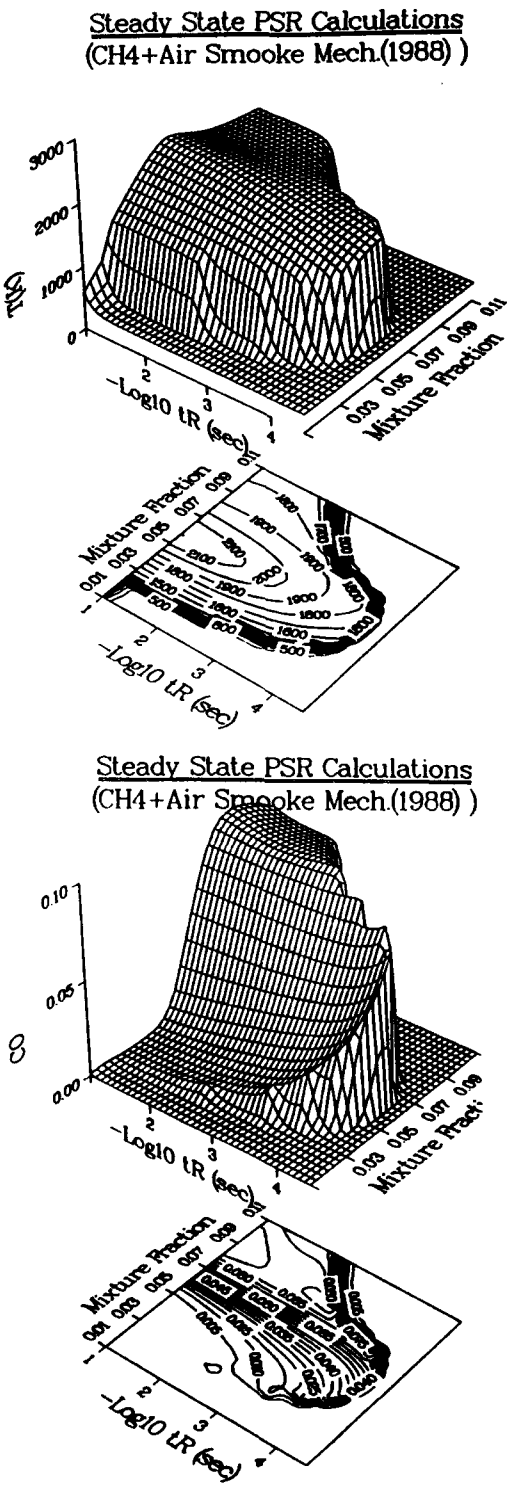

Fig. 1. Outlet temperature and CO concentration profiles versus residence time for a methane-air PSR with compositions near the stoichiometric mixture. Note the increase in CO as the residence time decreases.

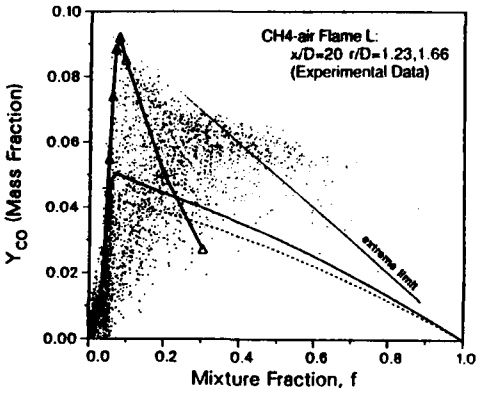

Fig. 2. CO mass fractions versus mixture fraction for a turbulent methane-air jet flame near extinction. Also plotted are maximum CO concentrations obtained for a steady state PSR with various mixtures, —△—, and opposed jet flame results at $a = 100/s$, - - -, $a = 300/s$ — - —, and $a = 450/s$ ——.

It is evident that the CO levels predicted by the PSR are much higher than those from the steady state flamelet results. More importantly, the maximum CO concentration is comparable to that from experiments and has its peak approximately at the same equivalence ratio. For methane combustion, the rich mixtures are almost inert because radicals are consumed rapidly by methane as pointed out by Bilger [7]. In turbulent jets, mixing of these rich mixtures and the lean mixtures is likely to occur and may result in mixtures that are too rich for combustion. Such extinct mixtures can contain high levels of CO and the limiting values can be represented by a straight line connected between the peak CO mass fraction from the PSR and the zero point at $f = 1$. We observe some experimental data outside this extreme limit. Although one cannot rule out possible experimental errors, the high CO levels could be attributed to the unsteady state behavior of a PSR, as shown next.

UNSTEADY PSR RESULTS

To simulate the unsteady behavior of a PSR in a turbulent environment, a transient PSR is calculated with varying residence times. For illustration, we start out a PSR calculation with the steady state compositions at a residence time not too far from its flame-out condition. We drop the residence time temporally for a short duration to a level at which the reactor cannot sustain combustion at steady state. This change of residence time corresponds to a condition of rapid turbulent mixing which causes flame extinction. The residence time is then increased to a high level simulating a slow mixing condition at which the temporally extinguished combustible mixture will be re-ignited. Figure 3 shows the results from such a transient PSR calculation. When the residence time drops for a duration 7×10^{-5}s, the CO concentration increases initially and decreases as the reactor is unable to sustain combustion due to the

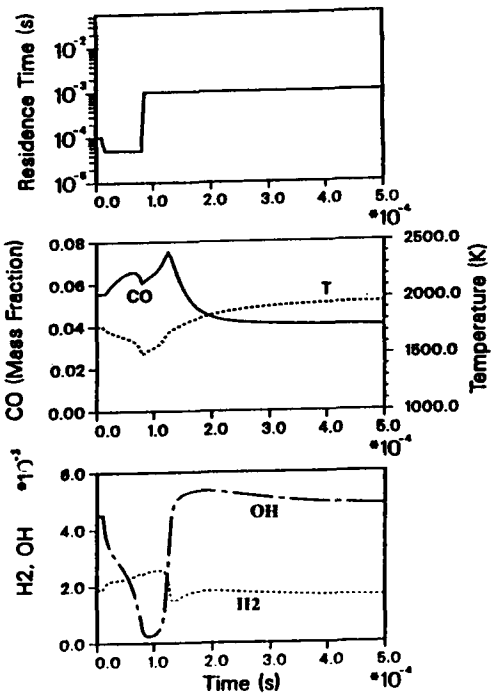

Fig. 3. Unsteady state response of a PSR to varying residence time with a mixture of equivalence ratio 1.1 or f = 0.066. Note the overshoot of CO concentration after increase of residence time at $t = 8.x10^{-5}$s.

low residence time as evident by the temperature decrease. As the residence time increases to 1000 microseconds at t=$8x10^{-5}$s, we observe an overshoot of CO which is very similar to that obtained from the unsteady state flamelet results by Mauss *et al.* [2]. The corresponding OH and H_2 histories are also similar to those from transient flamelet results during extinction and re-ignition.

CONCLUSION

A PSR description of turbulent jet flames is used to provide another plausible explanation for the observed high CO concentrations in turbulent methane nonpremixed jet flames near extinction. The maximal CO mass fractions obtained from a steady state PSR can be as high as 9% at equivalence ratio 1.6. Calculations of a transient PSR subject to sudden changes of residence times indicate an overshoot of CO during the re-ignition process similar to that obtained from a unsteady flamelet. It is concluded that the observed high CO concentrations could be also resulted from a PSR type flame and that the structure of turbulent methane nonpremixed jet flames cannot be inferred alone from the observed high CO concentrations.

ACKNOWLEDGEMENT

This research is supported by the United States Department of Energy, Office of Basic Energy Sciences, Division of Chemical Sciences.

REFERENCES

1. Masri, A.R., Bilger, R.W., and Dibble, R.W. (1988): *Combust. Flame*, **73**, 261.
2. Mauss, F., Keller, D., and Peters, N. (1990): A Lagrangian Simulation of Flamelet Extinction and Re-Ignition in Turbulent Jet Diffusion Flames. *23rd Symposium on Combustion*, The Combustion Institute, to appear.
3. Broadwell, J.E. and Breidenthal, R.E. (1982): *J. Fluid Mech.*, **125**, 397.
4. Lutz, A.E., Dibble, R.W., Kee, R.W., and Broadwell, J.E. (1990): A Model for Detailed Chemical Kinetics in Turbulent Nonpremixed Jet Flames, Presented at the AIAA 29*th* Aerospace Sciences Meeting, Reno, Jan. 1991, paper no. 91-0478.
5. Kee, R.J., Rupley, F.M., and Miller, J.A. (1989): *Chemkin-II: A Fortran Chemical Kinetics Package for the Analysis of Gas-Phase Chemical Kinetics*, Sandia Report, SAND89-8009.
6. Smooke, M.D., Mitchell, R.E., and Keyes, D.E. (1988): Numerical Solution of Confined Axisymmetric Laminar Diffusion Flames, in *Adaptive Methods for Partial Differential Equations*, Edited by Flaherty *et al.*, SIAM.
7. Bilger, R.W. (1988): *22nd Symposium on Combustion*, The Combustion Institute, p. 475.

IUTAM Symposium on
Aerothermodynamics in Combustors
June 3-5, 1991, Taipei

EXPERIMENTAL INVESTIGATION OF A COMBUSTION ZONE BEHIND A WEDGE

P. Blazart, S. Duplantier
M. Champion, B. Deshaies, P. Bruel

Laboratoire d'Energétique et de Détonique
URA-CNRS 193
E.N.S.M.A. rue Guillaume VII
86034 POITIERS - FRANCE

Introduction

In many combustors as these of RAMJET and Turbojet engines, a combustion zone is stabilized by a flow recirculation. In particular, this is the case when obstacles such as vee gutters or wedges are used. In this situation the combustion process is controlled by numerous parameters related to local transport properties, turbulent mixing, flow geometry and chemical kinetics. Due to the complexity of such a reacting flow and in view of numerical calculations, there is a need of simplification which is usually satisfied by defining limiting regimes controlled by a fewer numbers of parameters. The goal of this work is to characterize experimentally the different kinds of limiting combustion regimes that can be found in the flow downstream of a wedge. Clearly, it is expected that not only one limiting combustion regime is necessary to describe the entire flowfield where the combustion process take place. On an other way il should be noted that numerical model are usually mainly based on one limiting combustion regime and, accordingly, are more adapted to describe a part of the entire combustion process. Another goal of this work is to provide a better knowledge of the exact flow structure thus i) to indicate the exact region where a given model should be applied, ii) to provide test points for numerical computation, iii) to emphasize the need for setting new models in some specific regions.

Experimental conditions

A schematic representation of the flow configuration is given in fig. 1. A two dimensional flow is obtained in a rectangular section adiabatic channel, made of refractory ceramic, whose width is d = 16 cm and hight h = 3 cm. In this channel a stainless steel wedge whose blokage ratio is 33 % is positionned. This two dimensionnal configuration was chosen in order to facilitate further comparison with numerical studies. To perform 2D L.D.A. measurements and reaction zone visualisations, windows are positionned on both side of the channel and upstream and downstream of the stainless-steel wedge. The incoming flow is made of a turbulent propane air-mixture of controlled fuel-air ratio. The intensity of turbulence $I = \frac{\sqrt{u'^2}}{\bar{U}}$ measured on the plane of symetry of the channel in the usptream flow is 5%. Mean velocity and turbulence intensity profiles are given in figure 2. Mean temperature measurements can be obtained by using Chromel-Alumel thermocouples ($25\ \mu < \phi < 200\ \mu$).

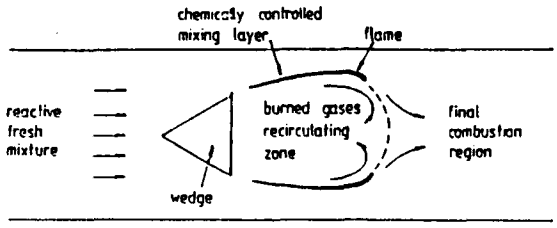

Figure 1

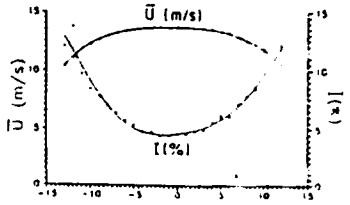

Figure 2

In this experimental device a stationnary combustion zone, anchored downstream of the wedge is obtained, for various values of the blockage ratio, the total mass flow rate and the fuel-air ratio φ of the incoming mixture.

Results and discussion

The results presented in this abstract have been obtained for a blockage ratio of 33%, an equivalence ratio $\varphi = 0.67$ which corresponds to the lowest practical value for a stable combustion to be obtained, a total massflow rate $m = 177\ m^3$ per hour. The mean experimental 2D flow fields obtained under these conditions are given in fig. 2 concerning the flow upstream of the wedge and fig. 3 concerning the downstream flow. The corresponding mean velocity field obtained with a downstream stationnary combustion is presented in fig. 4. As already observed in previous studies (cf. ref./1//2/) the extension of the recirculation zone is longer in this latter case. (Approximately 3 times longer than in the cold flow).

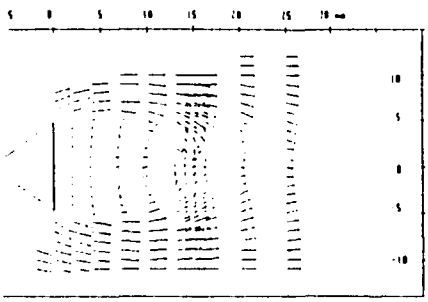

Figure 3

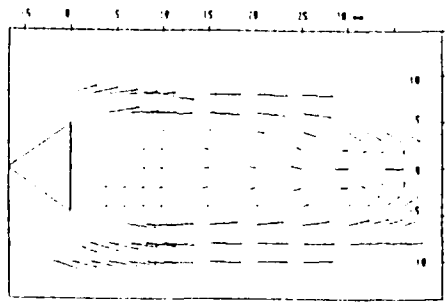

Figure 4

A combustion layer is located in the peripherical part of the recirculation zone. Going from the back side of the wedge to the exhaust of the reactor, as shown in figure 1, using temperature and velocity profiles together with combustion zone visualisations, three types of combustion regimes have been exhibited :

- A turbulent mixing layer where combustion is chemically controlled.
- A flame front whose relative normal velocity is of the order of magnitude of the flame burning velocity of the mixture.
- A turbulent combustion region

The mechanisms of flame spread involved in the two first regions seem similar to these already described by Marble and Anderson /3/ and Williams /4/. The third combustion region is currently under investigation and identification (well stirred reactor ? flamelets regime ?).

A detailed description and analysis of the combustion process are beyond the scope of this abstract and will be given in the full version of the paper.

REFERENCES

/1/ S. FUJII, M. GOMI, K. EGUCHI, Journal of Fluids Engineering, Vol. 100, p.323, (Sept.78)

/2/ S. FUJII, K. EGUCHI, Journal of Fluids Engineering Vol.103, p. 328, (June 81)

/3/ F.E. MARBLE, T.C. ANDERSON, Jr Jet propulsion Vol. 24, p. 85, (1954)

/4/ F.A. WILLIAMS, Combustion Theory The Benjamin/Cummings Publishing Company Inc., (1985).

IUTAM Symposium on
Aerothermodynamics in Combustors
June 3-5, 1991, Taipei

THE INFLUENCE OF SWIRL GENERATOR CHARACTERISTICS ON FLOW AND COMBUSTION IN TURBULENT DIFFUSION FLAMES

B. MUNDUS; H. KREMER

B. MUNDUS, GASWÄRME-INSTITUT, ESSEN, FEDERAL REPUBLIC OF GERMANY
H. KREMER, BOCHUM UNIVERSITY, BOCHUM, FEDERAL REPUBLIC OF GERMANY

OBJECTIVES AND METHODS OF MEASUREMENT

In industrial burner engineering, different swirl generators are used to produce turbulent diffusion flames. The design of the swirl generating system controls the velocity profiles of the different flow components at the burner exit. The velocity profile of the tangential component is critical as it controls the type of vortex in swirl flow. Tests were made to correlate the type of vortex, turbulent jet properties and turbulent flame properties by velocity, temperature and concentration measurements.

Swirl was produced by a tangential combustion air injector swirl generator (design TA), an axial blade grid swirl generator (design AS), a radial blade grid swirl generator (design RS) and a "movable block" swirl generator (design MB), as depicted in Fig. 1. To create identical conditions for testing the different swirl generators, they were designed for incorporation into the same burner body. The swirl intensity could be changed continuously by variation of the blade angle with the swirl generators RS and AS and by variation of the mixing ratio of tangential - to axial - flow air with the swirl generator TA. Fixed and movable blocks formed radial and tangential slots by pairs with the design MB. The ratio of the cross-sections of the tangential and radial slots and in this way the swirl intensity could be varied by turning the movable blocks against the fixed blocks.

Velocities were measured by a Laser doppler flowmeter and two thermocouples were employed for temperature measurement. Concentrations were measured by a physical gas analysis method. The degree of swirl was varied for the tests. The air ratio of the turbulent flames was 1.1.

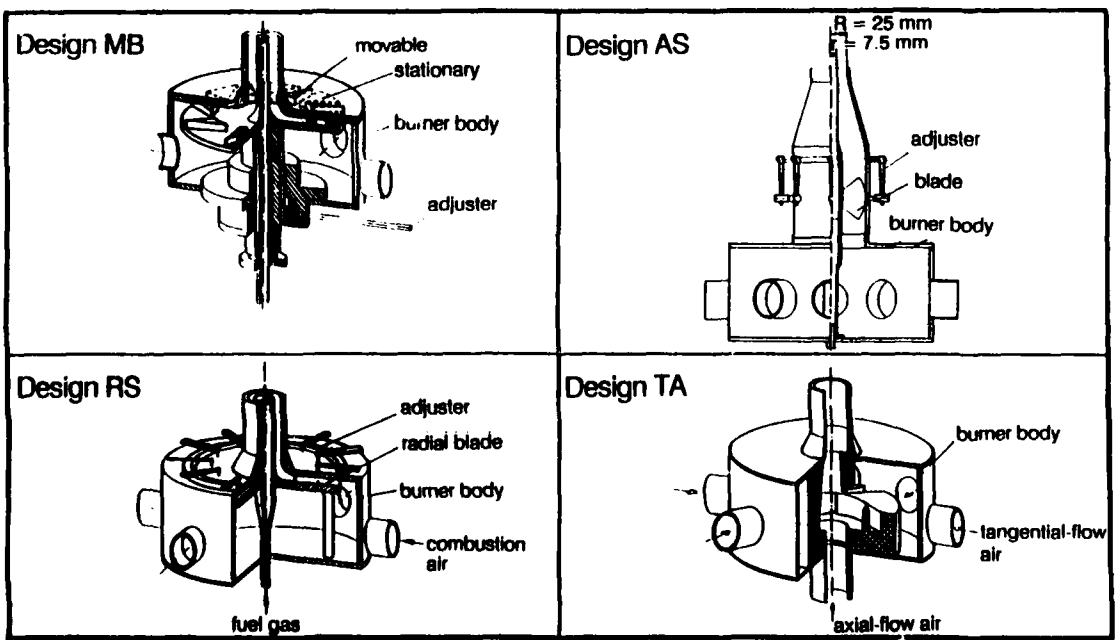

The swirl intensity is characterized by the swirl number So and the theoretical swirl number So,th. These nondimensional numbers represent axial flux of swirl momentum devided by axial flux of axial momentum, times the radius of the burner exit. The flux of swirl momentum is calculated from experimental data in case of swirl number So. Using the design data of the swirl generators like vane angles, nozzle and hubdiameters etc., the flux of swirl momentum may be determined theoretically neglecting the swirl momentum losses on the way between the swirl generator and the burner exit. With this theoretical flux of swirl momentum the theoretical swirl number is formed. The values of the described swirl numbers are in good agreement.

The velocity measurements were concentrated near the burner exit as there the clearest effects of the swirl generator construction on the flow field were expected. The minimum distance between the burner exit plane and the lowest measuring plane was 5 mm.

VORTEX CHARACTERIZATION

Fig. 2 shows the tangential velocity distributions for generator designs RS and TA at a distance of x/D = 0.1 from the burner as a function of the degree of swirl. As the degree of swirl increases, the velocity peak moves towards the outer flow edge in the case of the RS swirl generator, while the jet centerline vortices tend to lose their solid-body character. For high degrees of swirl, the curvature of the velocity distribution is positive.

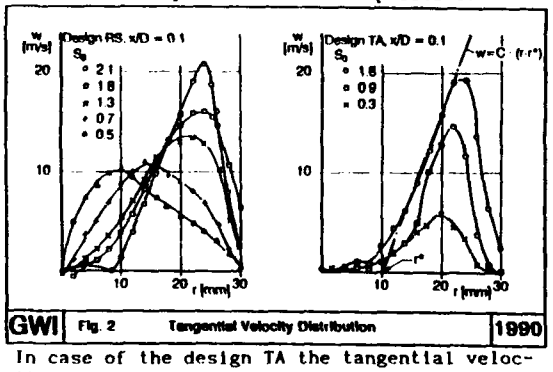

GWI Fig. 2 Tangential Velocity Distribution 1990

In case of the design TA the tangential velocity distribution develops different. The location of the peak velocity is nearly independent of the degree of swirl. A solid-body vortex does not develop at any degrees of swirl. The distribution always has a positive curvature. In the outer flow region, the tangential velocity profiles are very similar for the different swirl generator designs. Here the influence of the swirl intensity predominates compared with the influence of the swirl generator design. The swirl flow characteristics must therefore be correlated with the swirl generator design by the distribution of the tangential velocity near the jet centerline.

This distribution may be described by the function given in the right-hand side graph of Fig. 2 for all swirl generators and all degrees of swirl. The modified solid-body vortex function accounts for the positive curvature of the velocity profile near the centerline by the incorporation of radius r* which marks the fictitious zero point of the solid-body vortex. The linear rise of the tangential velocity distribution is described by the gradient C. The radius r* and the gradient C may be obtained by linear regression from the velocity profile at the jet exit.

The two coefficients are plotted in Fig. 3 as a function of the degree of swirl and of swirl generator design for isothermal turbulent jets. The left-hand side graph of Fig. 3 shows the distribution of gradient C, which is very similar for the radial flow designs RS and MB, with a nearly constant gradient at low swirl intensities and a strong increase at high degrees of swirl. The change in gradient is entirely different for design TA, with a strong increase at low swirl intensities and stagnation at high degrees of swirl. The increase is linear in the case of design AS.

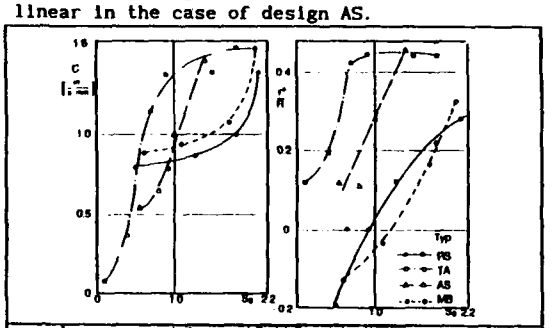

GWI Fig. 3 Influence of Swirl Generator Design on Type of Vortex 1990

The right-hand side graph of Fig. 3 shows the distribution of the normalized radius r*. R is the radius of the burner exit. Except the design TA radius r* increases continuously with the degree of swirl. The linear regression provides negative values in case of the designs RS and MB and weakly swirled jets. The values for the designs TA and AS are positive at any degree of swirl, that means the tangential velocity distributions always possess a positive curvature near the jet centerline. The differences between swirl flows generated by the four swirl generator designs remain similar if the chemical reactions are accounted for.

The reason for the similar vortex characters of the designs RS and MB is caused by the constructions of these swirl generators. In both cases the combustion air flow runs through the swirl generator in the radial way and is deflected subsequently in the vertical direction.

EXPERIMENTAL DATA

Figs. 4 to 8 plotting experimental data show the effect of the swirl generator design and the swirl flow produced on the properties of the turbulent jets and the turbulent flames. Fig. 4 depicts the radial size of the backflow region at a distance of x/D = 1.0 from the burner. In general the radial size increases with the degree of swirl. The backflow region is largest for swirl generator designs RS and MB. Different backflow regions are generated by designs TA and AS. If the curves are extrapolated for low degrees of swirl, the intersections of the curves and the abscissa represent the critical degrees of swirl at which the backflow sets in for the plane considered. These critical degrees of swirl are lower for designs RS and MB than for designs AS and TA.

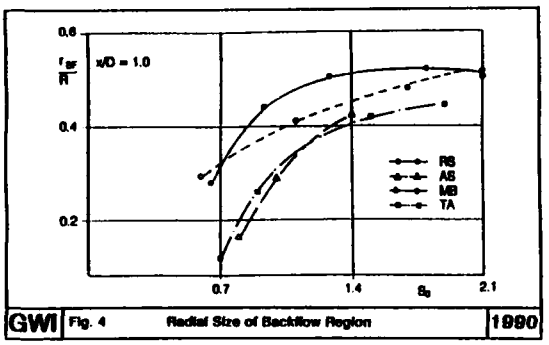

GWI Fig. 4 Radial Size of Backflow Region 1990

The length of the backflow region is obtained from the zeropoint of the axial velocity distribution on the jet centerline. Fig. 5 shows the values for the isothermal swirl jets and the swirl flames plotted as a function of the degree of swirl. The values are normalized by the diameter of the burner exit. The design RS produces the longest backflow regions. In the isothermal case the maximum length is about four times the exit diameter. The shortest backflow regions are produced by the designs TA and AS. The increase in the length of the backflow region, as the degree of swirl increases (Fig. 5), reflects the increase in gradient C for the different swirl generators. If the combustion reaction is accounted for, the length of the backflow region decreases, but the qualitative differences between the swirl generators remain the same.

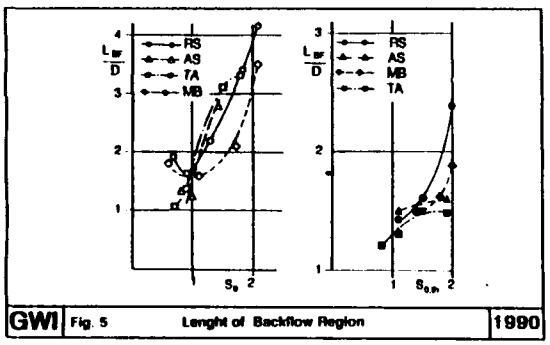

GWI Fig. 5 Lenght of Backflow Region 1990

The investigated swirled jets and flames were highly turbulent. The influence of the vortex type on the turbulence structure will be shown for the example of the turbulent normal stress of the tangential component. High intensities of turbulence occur in the regions of the gradients of the mean velocities. For each degree of swirl maximum intensities of turbulence may be determined. These maximum values are plotted in Fig. 6 as a function of the swirl intensity for each swirl generator. The change in the maximum intensity of turbulence of the tangential component corresponds to the variation of gradient C as a function of swirl in the immediate vicinity of the burner.

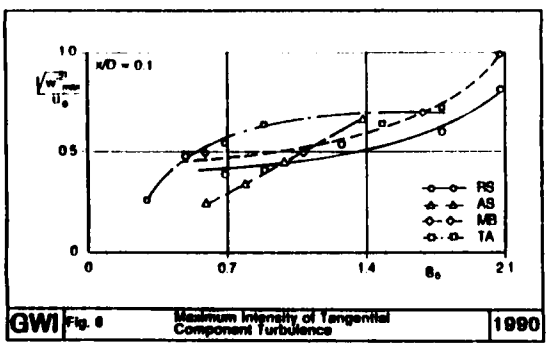

GWI Fig. 6 Maximum Intensity of Tangential Component Turbulence 1990

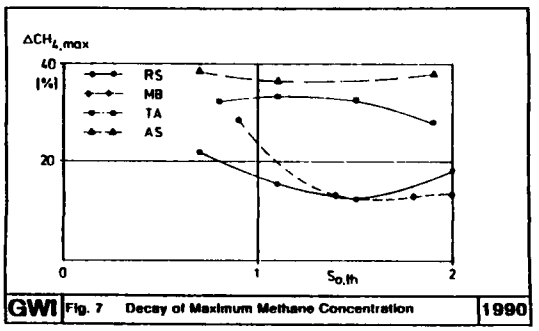

GWI Fig. 7 Decay of Maximum Methane Concentration 1990

The similarities between designs RS and MB were also confirmed by the concentration measurements. Fig. 7 shows the decrease in the maximum methane concentration in the turbulent flame for a distance of up to x/D = 2.0 from the burner. As the methane concentration drops more quickly in the cases of designs AS and TA, the flames produced by burners fitted with these swirl generators are shorter (Fig. 8).

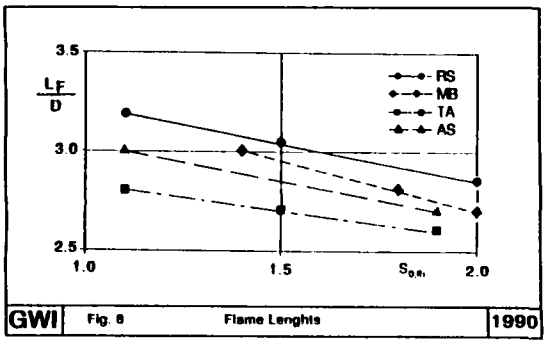

GWI Fig. 8 Flame Lenghts 1990

CONCLUSION

The type of vortex produced by a swirl generator may be described by a solid-body vortex approach. The type of vortex produced is reflected by velocity profile and concentration measurements. If the type of vortex produced by swirl generators are similar, the properties of the turbulent flames will be comparable.

IUTAM Symposium on
Aerothermodynamics in Combustors
June 3-5, 1991, Taipei

NATURAL GAS FREE JET FLAMES FROM A NEW HELICAL SWIRL BURNER

U.S.P.Shet[#], B.Hoffmann, P.Jansohn, B.Lenze and W.Leuckel

[#] Thermodynamics & Combustion Engg. Lab., Mechanical Engg. Department
Indian Institute of Technology, Madras 600 036, India

Combustion Research Laboratory, Engler-Bunte-Institut
University Karlsruhe, D-7500 Karlsruhe, Germany

ABSTRACT

This paper presents the performance characteristics of a new swirl burner which employs multi-start helical grooves for swirl generation. Hence the burner designation, Helical Swirl Burner, HSB. Burner design considerations and pressure drop across the swirler, swirl strength, flow field characteristics, mean temperture and species concentration in flames measured inside and near quarl exit zone are discussed.

BURNER FEATURES

The burner employed comprises a helical swirler unit of diameter D = 42 mm tightly fitted in a pipe of ID = 42 mm, a central stainless steel fuel pipe of ID = 10 mm protruding through the swirler, and a 15° quarl of height h = D mounted at a downstream distance of D/2 from the swirler face. The swirler unit is fabricated by cutting three-start helical grooves of helix angle 17.6° and depth 10 mm on an aluminium rod for a full pitch length, l = D i.e., for pitch number, PN = 1. Figure 1 shows the details of HSB studied in the present work.

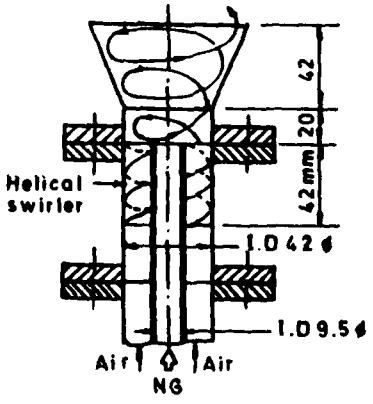

FIG.1. HELICAL SWIRL BURNER

The main feature of the helical swirler is that the swirl intensity can be varied by varying the helix angle as independent design parameter. The higher the helix angle, the lower is the level of swirl generation. The design consideration is such that for the given swirler helix angle, the pitch number is sufficient to ensure adequate overlap between the resulting curved vanes so as to facilitate effective flow deflection (swirl generation) and the pressure drop through the swirler is optimally low.

From the measurements made for cold flow it is found that the swirling flow at the quarl exit is of Rankine type [Ref.1]. The central recirculation zone (CRZ) is seen to extend up to a length of X/D = 2.7 from the quarl exit which is comparable with the measurements of movable block swirl generator [Ref.2]. The swirl strength measured was found to increase from S = 0.8 to 1.27 over the range of input flow rates, $\dot{V}_s$ = 28.7 to 57.6 m^3/h, which can be explained by Reynolds number dependency of the flow inside the swirler device.

The present experimental work is carried out to obtain information on pressure drop across the swirler and the species concentration levels inside the quarl and near burner exit zone.

EXPERIMENTAL

Free natural gas jet flames of throughput up to 15 m^3/h were studied. When axial fuel is injected directly into the spiralling air jets, HSB is seen to produce compact pre-mixed type flames. The burner operating range is assessed by determining the blow-off limits. The pressure drop across the swirler was measured by wall static pressure taken by 1 mm hole ID distance upstream of the swirler unit with a Betz manometer. The flame gases were analysed continuously for stable flue gas species namely CO, CO_2, H_2O, CH_4 (infrared absorption), H_2 (thermal conductivity), O_2 (paramagnetism) and NO_x (chemiluminescence using water cooled (70°C) stainless steel suction probe (ID = 1.5 mm). The gas temperatures were obtained by thermocouple measure-

ments. The temperature signals of the uncoated thermocouple (100μm, Pt-PtRh 10%) were corrected for radiative heat transfer.

The pressure drop (Δ P) variation across the swirler unit is found to be parabolic with respect to input flow rate. The wall static pressure (mmWC) at 1D upstream of the three-start, full pitch and 17.6° swirler was found to vary with air throughput, $\dot{V}_s$ (m^3/h) according to the relation:

$$\Delta p = 67.65 (\dot{V}_s)^{0.42} \quad \ldots (1)$$

In the presence of flames with input equivalence ratios ϕ = 0.75, 1.0 and 1.25, Δ p was found to be slightly higher by not more than 10 mm WC when operated over the range of swirling flows upto 80 m^3/h. The preliminary measurements conducted showed that the pressure drop is smaller considerably for a higher helix angles. Detailed measurements to study the influence of pitch number and helix angle on pressure drop and swirl generation are currently in progress.

Figure 2 presents the flame stability diagram of natural gas jet flames from HSB. Lean blow-off data for gas throughput $\dot{V}_F$ upto 6.8 m^3/h and also the stable flames observed at higher $\dot{V}_F$ are shown in the diagram. Here, $\dot{V}_F$ refers to fuel flow rate at 1013 mbar and 15° C and Φ is input equivalence ratio $[(\dot{V}_F/\dot{V}_a)/(\dot{V}_F/\dot{V}_a)_{stoich.}]$. Stability limits at higher fuel flow rates could not be obtained due to the limitation of the air flow capacity of the swirler employed. However, it is interesting to note that stable flames of 150 kW thermal load can be held in this compact burner.

From the species concentration measurements for the input stoichiometric condition (Fig.3) it can be concluded that the central quarl zone is filled with recirculated products and unburnt fuel but that there is practically no free oxygen. These fuel rich conditions and the lower level of temperature favour low level of NO_x. The combustion is seen to proceed faster above the quarl exit, as evidenced from the increased level of temperature.

The concentration profile of CO_2 also points out the closure of the recirculated zone. The fuel burnout is seen to be fairly complete at the plane corresponding to X/D = 3. The generation of NO_x is confined to the thin shear layer region between the fuel rich internal recirculation zone and the swirling air jets.

The NO_x produced in this narrow shear layer is a controlling factor for the total NO_x emission of the burner system. Under the operating conditions studied, the mean NO_x level did not exceed 30 ppm. The high CO level (1.5%) observed at X/D = 3 is caused through the cold air entrainment in the case of free jet flames and needs attention for reducing it to the ppm level by maintaining sufficient high temperature level with enclosed flames with low excess air factor for instance. Similar conclusions

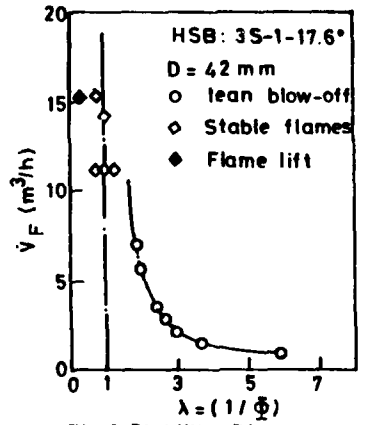

Fig.2. Stability Diagram.

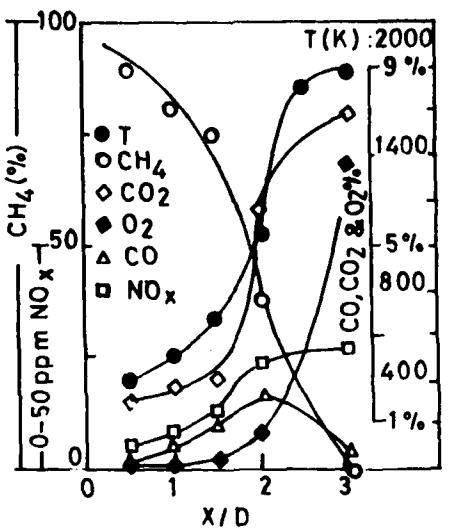

Fig.3. Axial variation of Temperature And Species Concentration
Φ=1.0, $\dot{V}_F$ =10.7m^3/h, Natural gas

can be drawn from the axial species concentration profile. For the same fuel input and ϕ = 1.2, the fuel burnout is seen to be delayed beyond quarl exit in contrast to the opposite trend noted for lean, ϕ = 0.8, operating condition.

It can be concluded that the swirl burner system under investigation is suitable for low NO_x emission combustion for the operating conditions reported in this work.

REFERENCES

[1] Vince Joseph, Ganesan, V. and Shet, U.S.P., Characteristics of open LPG Jet Flames in Helical and Tangential-Slot Swirl Burner: Journal of the Institute of Energy, London, December 1987, pp.193-198.

[2] Hillmanns, R.: Das Strömungs- und Reaktionsfeld sowie Stabilisierungseigenschaften von Dralliflammen unter dem Einfluss der inneren Rezirkulationzone, Diss. Univ. Karlsruhe, 1988.

IUTAM Symposium on
Aerothermodynamics in Combustors
June 3-5, 1991, Taipei

LASER VELOCITY AND DENSITY MEASUREMENTS OF A FLAT COUNTER FLOW DIFFUSION FLAME

J.C. Rolon*, D. Veynante*, J.P. Martin*, E. Dornberger**, F. Durst**, G. Jakob**

* Laboratoire E.M2.C., C.N.R.S. et Ecole Centrale des Arts et Manufactures, Grand Voie de Vignes, F-92290 Chatenay-Malabry, France
** Lehrstuhl für Strömungsmechanik, Universität Erlangen-Nürnberg, Cauerstr. 4, D-8520 Erlangen, West Germany

1. Introduction

The accuracy of laser techniques in gas flows with combustion yielding heterogeneous temperature and species concentration gradients can be limited by beam deviation when the light passes through a flowing fluid with non-homogeneous refractive index. The measuring volume is displaced and deformed, and may even not exist in the case of laser-Doppler anemometry, if the beams do not intersect due to asymmetric displacements. This work proposes a way to overcome this problem in the case of a flat axisymmetric counter flow diffusion flame, (Fig. 1).

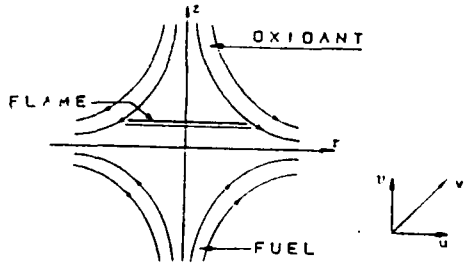

Fig. 1: Geometry of the flow. The flame is formed in the vicinity of a stagnation plane established by the counterflows of oxydant and fuel.

Plane, counter flow diffusion flames are of great interest to combustion research yielding a closer understanding of combustion mechanisms. They also constitute suitable test cases for the investigations of the interactions between fluid mechanics transport properties of combusting gases and the resulting chemical kinetics. Indeed, the overall shape of the resultant flame is simple, the flow is laminar and the resultant flame is fairly easy to stabilize in the stagnation region of the counter flowing jets.

Plane, counter flow diffusion flames have been extensively employed to study the effects of straining on combustion and have provided useful information for the so called "flamelet model" (see Peters (1984)), and particularly for the "Coherent Flame Model" (Marble and Broadwell (1977)), now used to predict turbulent combustion.

Experimental and theoretical aspects of flat counter flow diffusion flames have been studied by many authors. Theoretical studies are generally based on a potential flow theory description of the flow field, as proposed by Leclerc (1950), Spalding (1961), or Rosenhead (1966). The potential flow theory yields the following relationships for the velocity distribution.

$$u = a \cdot r \tag{1}$$

$$v = -2 \ a \cdot z \tag{2}$$

where u and v are the radial and axial velocity components, respectively, r is the radial and z the axial coordinate (with the origin at the stagnation point). The strain rate a is given as:

$$a = \partial u / \partial r \tag{3}$$

and turns out to be constant. Spalding (1961) proposed for a the value

$$a = V_0 / D \tag{4}$$

where V_0 is the jet velocity and D the jet diameter.

With the above idealized flow field, the combustion is treated separately, neglecting heat release effects, and hence is treated in contradiction to the physics of the true physical processes. As a matter of fact, no precise experimental velocity data are yet available in the flow when combustion takes place. A special diffculty is encoutered with laser-Doppler velocimetry: near flames with flame thickness of about 0.1 mm the resultant thermal gradients are very strong (about 1000 K per mm). They induce refractive index gradients that deviate laser beams from their straight-lined trajectories (Fig. 2).

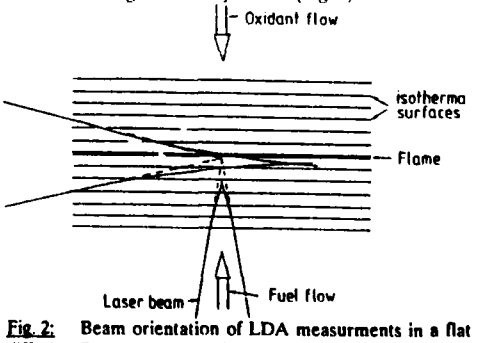

Fig. 2: Beam orientation of LDA measurments in a flat diffusion flame and measuring volume displacement under refractive index gradients: (a) in isothermal homogeneous flow, (b) in reactive flow with flame

2. Experimental Arrangement

2.1. Test Facility

The complex test facility employed in this study is shown in Fig. 3 in form of a block diagramme. The figure indicates the two separate flow control lines set up to supply the oxygen and the fuel to the oppositely located burner nozzles. The central nozzles are surrounded by N_2-annular flows protecting the actual flame form disturbances by chemical reactions due to the interference with the surrounding air. The protecting N_2-gas streams also help to reduce externally caused disturbances of the resultant flame sheet and are essential to establish flat diffusion flames. Oxygen and fuel were supplied from oxygen and fuel bottles. H_2, Ch_4 and C_3H_8 were employed as fuels. Each line also comprised mixing devices to yield well miced fuel-N_2 or air-N_2 mixtures prior to feeding the flow through the nozzles. To control the mass flow rates of the gases, pressure regulators and minute, chocked, sonic nozzles were employed.

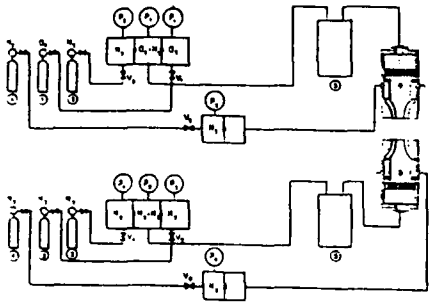

Fig. 3: Flow devices and control: 1 Oxygen supply, 2 Nitrogen supply, 3 Fuel supply, 4 Outer ring flow nitrogen supply, 5 Particle seeders for LDV measurements, P_1, P_8 Pressure captors for flow regulation and controls

In order to obtain laser-Doppler signals with combustion two fluidized beds with cyclone generators were employed to introduce titanium dioxide or magnesium oxide scattering particles to both flows.

To perform complete velocity profile measurements, the burner test rig was traversed. The displacement of the burner assembly relative to the spatially fixed optical system was provided by two stepping motors monitored by the computer through a serial line and a special motor driver.

2.2. Laser-Doppler System

The laser-Doppler anemometer (LDA) optical unit consisted of a double channel LDV-system. A periscope allowed the optical axis to be perpendicular to the flame surface (Fig 4). The incident beam separation was reduced to 20 mm in order of cross the lower burner through a glass wall after going through a 300 mm focal length lens.

The receiving optics are placed with an angle of 90° to the optical axis. In order to also assure sufficient scattered light for this 90°-scattering arrangement a 4 W Ar-Ion laser was employed. The length of the measuring volume was about 5 mm. Calculations showed that the displacement, due to the presence of refractive index gradients, of that part of the measuring volume (diameter about 300 μm) that was focused onto the photomultiplier was less than 70 μm in the vertical direction and could be neglected compared to the length of the control volume.

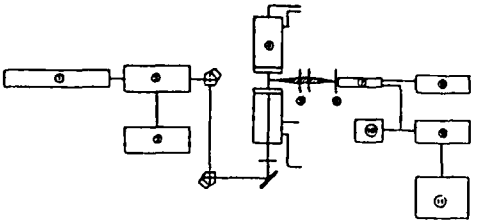

Fig. 4: Sketch of the optical arrangements used to measure the radial (u) velocity component in the case of flat diffusion flame, 1 He-Ne laser, 2 LDV transmission optic with double Bragg cell, 3 Bragg cell power supply, 4 Burners, 5 Light collecting lens with light stop for the incident laser beams, 6 Pinhole, 7 Photodetector, 8 Photodetector and preamplifier power supply, 9 LDA counter, 10 Oscilloscope, 11 Computer

In order to measure the axial component of the velocity in the flow with combustion the optical arrangement of conventional forward scattering were employed. Close to the flame front (+ 1.0 mm), no Doppler bursts were detected by the photomultiplier. Thermophoresis effects are the cause of the apparently particle free zone close to the flame.

3. Results and Discussions

The flow between the nozzles of Fig. 3 was studied extensively. In the present paper the experimental results are reported that correspond to different axial and radial locations in the flow with the flame. For the presentation of the results, the point $r=0$, $z=0$ is chosen to be located on the flow axis and at equal distances H/2 from the burners. The flow rate was controlled in order to reproduce the following outlet conditions:

- strain rate $a=24\ sec^{-1}$ as defined by formula (4)
- equivalence ratio $O=1$
- equal flow momentum for both jets

3.1. Flow Field with Combustion

The results now presented are obtained with a hydrogen-air diffusion flame.

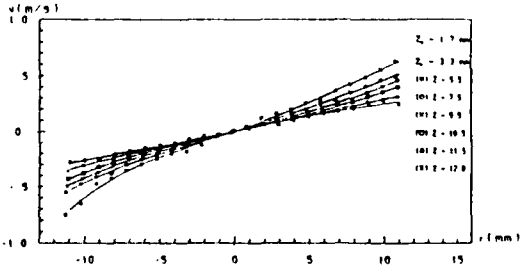

Fig. 5: Radial profiles of the u radial component of the velocity, z_0 and z_f are the stagnation point and the flame position respectively, in a coordinate system with the origin $z=0$ at H/2.

Fig. 5 shows radial velocity profiles as a function of radius r for several values of the axial coordinate z. Experimental data and fitted curves are displayed. The strain rate (i.e. the radial velocity gradient), is found to be a linear function of the radial position, for z equal constant, as predicted by the theory. The detailed measurements show that the local strain rate is also a function of z.

Fig. 6 provides the distribution of the v (axial) component of the velocity field in radial direction at different z locations. At the nozzle outlets they present the same behaviour as a previous cold flow measurement. In

approaching the reaction region they become more uniform due to the increasing strain rate.

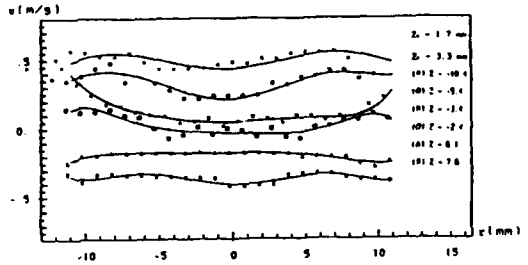

Fig. 6: Radial profiles of the v axial component of the velocity at different z locations

Fig. 7 displays the axial (v) component of the velocity in z direction at different r locations. The velocity increase due to thermal expansion is recognized at both sides of z_0 and z_f, which are the axial coordinates of the stagnation plane and the flame position, respectively. The interrupted range of these curves shows the area where Doppler bursts do not exist due to the thermophoretic effects.

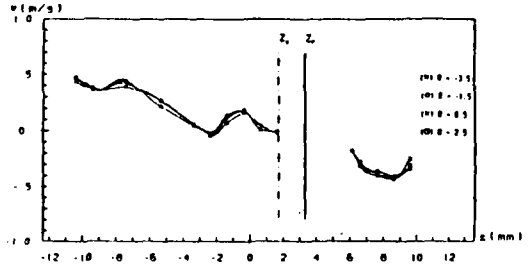

Fig. 7: Axial profiles of the v component of the velocity at different r locations

4. LDV-LBD Coupled System

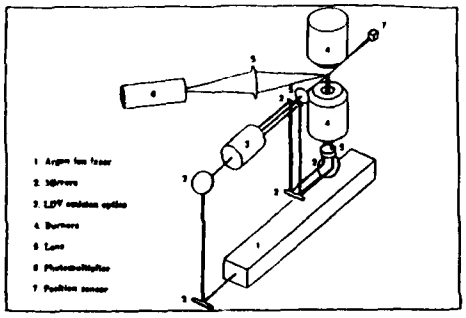

Fig. 8: LDV optical arrangement with laser beam position sensor for simultaneous velocity and density measurements.

With the current optical configuration, only the velocity components parallel to the flame front can be measured directly in the reaction region. To determine the axial (v) velocity component in this zone, the mass conservation equation can be applied in conjunction with direct measurements of the radial (u) component of the velocity and density measurements. For a simultaneous measurement of the velocity and density fields, a two colour laser is applied (Ar-Ion laser). The green beam of the laser is used for velocimetry as decribed above and the density is determined from the blue beam deviation, detected by a position sensor. The optical arrangement is shown in Fig. 8. Local density can be calculated from the laser beam deviation with an Abel integral transform in an axisymmetric flow field according to the formula

$$\rho(x,r) = \int_r^\infty -\frac{\partial\rho(z,r)}{\partial r}\,dr + \rho_1 \qquad (5)$$

4.1. Experimental results

the experimental conditions were chosen as follows: burner separation H = 16 mm, nozzle diameter D = 20 mm, theoretical flow strain rate a = 24 s^{-1}; the equivalence ratio of the hydrogen-air diffusion flame was equal to unity. With this setting the entire was investigated. As an example the result corresponding to a radial deviogram is reported, measured at the flame surface. Fig. 9 shows the density curve as a result of the Abel inversion of the fitted radial deviagram. The flat central part of this curve indicates the high temperature flame surface.

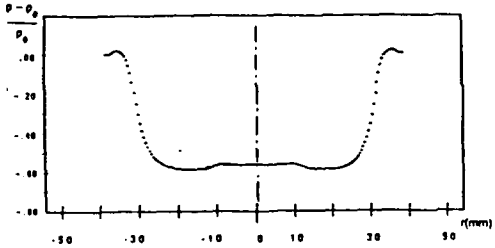

Fig. 9: + + + Density calculated by Abel inversion of fitted radial deviogramme

Bibliography

1. Spalding, D.B., J. Amer. Rocket Soc., Vol.3, pp. 763 - 771, 1961.

2. Leclerc, A. La Houille Blance, N° 6, pp. 3 - 8, 1950.

3. Marble, F.E. and Btoadwell, J.E., Technical Report TRW-9-PU Project Squid Headquarters, Chafee Hall, Purdue University, We Lafayette, Indiana 1977.

IUTAM Symposium on
Aerothermodynamics in Combustors
June 3-5, 1991, Taipei

TWO-DIMENSIONAL LASER TECHNIQUES FOR COMBUSTION RESEARCH

A. LEIPERTZ, K.-U. MÜNCH, G. KOWALEWSKI, AND S. KAMPMANN

LEHRSTUHL FÜR TECHNISCHE THERMODYNAMIK
FRIEDRICH-ALEXANDER-UNIVERSITÄT ERLANGEN-NÜRNBERG
AM WEICHSELGARTEN 9, D-8520 ERLANGEN
FEDERAL REPUBLIC OF GERMANY

Turbulent flow and combustion processes are three-dimensional in nature revealing large- and small-scale structures in the flow and combustion field. Those coherent structures play an important role in the development of turbulence and also for the interaction of flowfield and chemistry in combustion [1,2]. Their existence can easily be seen, e.g., from Schlieren pictures, providing, however, only qualitative information. For modelling purposes and thus for a better understanding of the phenomena, quantitative analysis is necessary. Using point-measurement techniques with quantitative potential, two- and three-dimensional structures cannot be resolved easily. Extending these techniques, however, by forming a light sheet and detecting the signal intensity within this sheet by a two-dimensional photo-electrical detector, the required informations can be obtained for a large number of fundamental applications, but also for a few more technical situations. Well-established quantitatively working laser techniques providing high spatial and temporal resolution are laser-induced fluorescence (LIF) and the laser scattering techniques (Mie, Rayleigh, Raman) [3]. Here, those techniques are discribed which in our Institute are applied to the investigation of combustion processes.

Fig. 1: Diesel distribution within the light sheet at 2.6 deg after injection begin

MIE SCATTERING

Combustion in Diesel engines is almost unknown. Its performance depends strongly on the quality of the mixing process of the injected Diesel fuel with the previously filled air charge. The efficiency of the combustion process within the engine chamber and thus also the reduction of emissions of hydrocarbons and of soot can be improved by the improvement of the mixing and evaporizing process during fuel injection and before ignition starts. For the development of suitable calculation codes, the injection and evaporizing process is going to be investigated experimentally in a mixing chamber and in a real engine as well [4].

Using a two-dimensional laser Mie scattering probe the distribution of Diesel fuel within the engine chamber can be detected. In a first step this has been done qualitatively in a test chamber. Finally it will be performed quantitatively within the combustion chamber of a real direct-injection (DI) Diesel engine. First test measurements indicate the suitability of the measurement system providing a temporal resolution of 4×10^{-5} mm³. The fundamentals of the technique are given in connection with the used setup configuration and the evaluation method based on particle Mie theory. As an example,

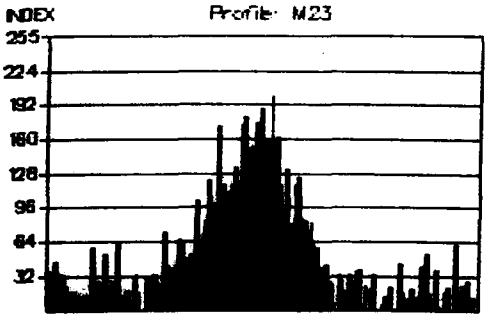

Fig. 2: Line profile across the Diesel distribution of Fig. 1 after linearization of the characteristics of the intensity values

Fig. 3: 2d-Rayleigh temperature measurement in the post-reaction zone of a methane/air flame

Fig. 1 shows the detected distribution of the spray droplets in form of a two-dimensional intensity distribution at a particular time position after injection begin and Fig. 2 the evaluated line profile across the droplet sample shown in Fig. 1.

Using the Mie laser probe, besides the local distribution of Diesel droplets or the liquid phase within the measurement area also information on the statistical droplet size distribution is required. Due to the problems of Mie sizing in engine situations a new approach is going to be tested taking into account the dependance of Mie intensities on refractive index, particle shape and multiple scattering by using reference jets with the same features as the Diesel spray. The ambiguity of Mie intensity on particle size in particular size regions is another problem to be solved. This may be overcome by using different wavelengths of an Argon laser simultaneously.

RAYLEIGH SCATTERING

Non-instrusive, instantaneous, quantitative gas density and temperature measurements can be performed by laser Rayleigh scattering [5,6]. In general, Rayleigh measurements are restricted to clean flows. Gas density determination is possible for known or constant gas composition over the flowfield and temperature determination for constant pressure. Gas concentration measurements can be done in binary gas mixtures with constant or known gas density. For many practical applications of interest those conditions are met.

By forming a laser beam to a 2-d light sheet and collecting the intensity distribution within the sheet by using a 2-d photoelectrical detector, instantaneous 2-d concentration, density or temperature measurements are possible providing as well qualitative visualization as quantitative results over an extended flow or combustion field of interest [5,7]. The application of this technique is shown in selected flow and combustion situations. As most of the published results are more qualitative in nature, emphasis of the first stage of our work is laid on the quantitative evaluation of 2d-Rayleigh images. This is done in laminar flames in comparison to point measurement techniques. Future steps will be related to engine [4] and to combustor measurements [8]. Figure 3 gives an example for flame temperature measurements taken in the post-reaction zone of a premixed methane/air flame (Re = 4.34 λ = 1.16).

RAMAN SCATTERING

Raman scattering is the technique with the most extended application range. Usable for all gas molecules of interest, in general it can be utilized for temperature and concentration measurements as well [9]. It suffers, however, from its weakness, which did not allow so far planar temperature measurements. Recently we performed a feasibility study indicating that under high pressure conditions (engine measurements) those measurements could be possible.

ACKNOWLEDGEMENTS

Parts of the research projects are financed by the Deutsche Forschungsgemeinschaft and by the Commission of the European Communities within the frame of the JOULE Programme, by the Swedish National Board for Technical Development, and by the Joint Research Committee of European automobile manufacturers (Fiat, Peugeot SA, Renault, Volkswagen and Volvo) within the IDEA-Programme.

REFERENCES

1. J. Jimenez: The Role of Coherent Structures in Modelling Turbulence and Mixing, Springer, Berlin - Heidelberg 1981

2. N. Peters, F.A. Williams: in Ref. (1), pp. 364-393

3. A. Leipertz: in Instrumentation for Combustion and Flow in Engines (Eds. D.F.G. Durao, J.M. Whitelaw, P.O. Witze), Kluwer Academic Publ., Dordrecht 1989, pp. 123-140

4. Joint research project of different European research institutes in cooperation with several car manufacturers in order to improve Diesel combustion financed by the CEC-JOULE Programme.

5. A. Leipertz, G. Kowalewski, J. Haumann, G. Wu: in Advances in Turbulence 2 (Eds. H.-H. Fernholz, H.E. Fiedler), Springer, Berlin - Heidelberg 1989, pp. 272-277

6. M.C. Escoda, M.B. Long: AIAA J. 21 (1983) 81-84

7. D.C. Fourguette, R.M. Zurn, M.B. Long: Combust. Sci. Technol. 44 (1986) 307-317

8. T. Sattelmayer, M.P. Felchlin, J. Haumann, J. Hellat, D. Styner: ASMA-Paper 90-GT-162 (1990)

9. see e.g. A. Leipertz: in Instrumentation for Combustion and Flow in Engines (Eds. D.F.G. Durao, J.M. Whitelaw, P.O. Witze), Kluwer Academic Publ., Dordrecht 1989, pp. 107-122

IUTAM Symposium on
Aerothermodynamics in Combustors
June 3-5, 1991, Taipei

FLAME DIAGNOSTICS BY PURE ROTATIONAL CARS

A. LEIPERTZ, E. MAGENS, T. SEEGER, B. HIRSCHMANN, AND H. SPIEGEL

LEHRSTUHL FÜR TECHNISCHE THERMODYNAMIK
FRIEDRICH-ALEXANDER-UNIVERSITÄT ERLANGEN-NÜRNBERG
AM WEICHSELGARTEN 9, D-8520 ERLANGEN
FEDERAL REPUBLIC OF GERMANY

Coherent anti-Stokes Raman-Scattering (CARS) has been used successfully since several years for the determination of temperature and concentration in combustion processes. For this, mostly the rotational-vibrational energy states of the molecules have been used for probing the population difference between these levels in order to determine the temperatures and number densities (vibrational CARS), see e.g. [1,2]. Alternatively, the pure rotational energy levels within the vibrational ground state of the molecules can be used for the same purposes (pure rotational CARS). In particular combustion situations, e.g. high pressure applications, rotational CARS may provide some advantages over vibrational CARS [3,4].

Using pure rotational CARS, in gas mixtures simultaneous multiple species measurements are possible as nearly all molecules of interest own rotational CARS contributions within a narrow spectral range. On the other hand this feature may complicate a temperature and concentration evaluation due to interferences between different molecules when using the conventional line integration technique (LTT) [5]. The difficulty in separating the different contributions can be overcome by using the Fourier analysis evaluation technique (FAT) [5,6]. Here, first results will be presented using this technique for the evaluation of experimentally obtained rotational CARS spectra in high temperature regions of premixed methane-air flames where only nitrogen is available for the evaluation process, and for concentration and temperature determination in the mixing region of partially premixed methane-air flames with surrounding air where besides nitrogen also oxygen can be used. The expected advantages of pure rotational CARS over vibrational CARS in high pressure situations will be considered theoretically and experimentally.

For the evaluation of pure rotational CARS spectra two different approaches may be used. Using conventional line integration technique (LIT) [7], the gas temperature can be found from a least square fit between the experimental data and the calculated spectral intensity distribution of the total integrated peak areas of the individual rotational lines. This approach does not exploit the specific periodic structure of rotational

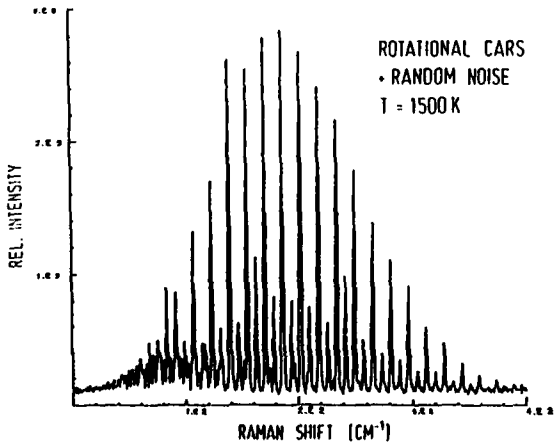

Fig. 1: Calculated pure rotational CARS spectrum for a gas mixture of 60% N_2, 6% O_2, 6% CO_2, 5% CO, 3% H_2 and 20% H_2O. Gas temperature: 1500 K. Additional contributions by random noise (Poisson statistics).

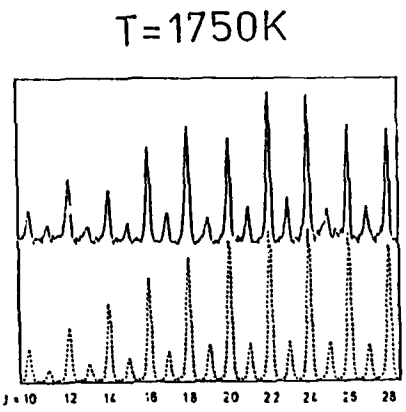

Fig. 2: Comparison of experimentally obtained pure rotational CARS spectrum taken in the high temperature region of a premixed methane-air flame with a calculated spectrum for pure nitrogen at 1750 K.

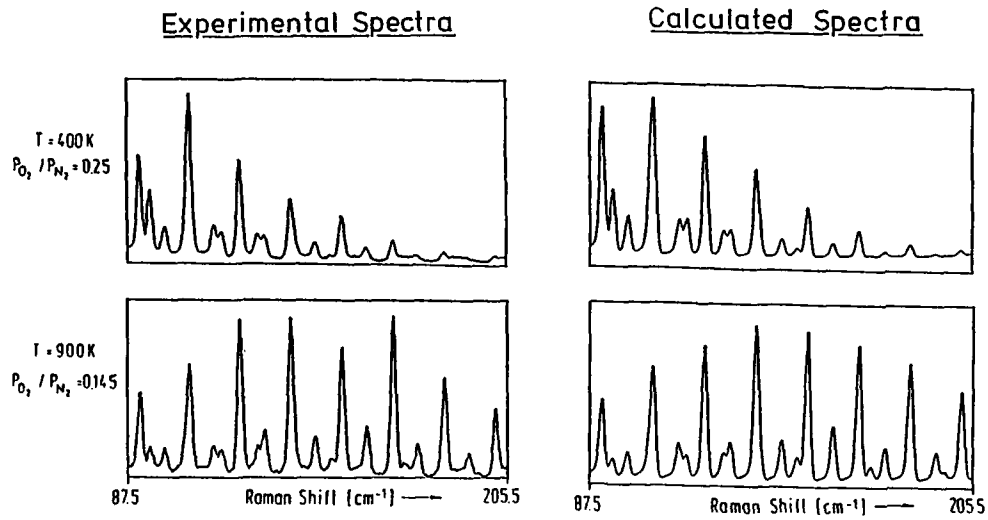

Fig. 3: Comparison of experimentally obtained pure rotational CARS spectra taken in the mixing zone of a partially premixed flame with surrounding air for two different flame conditions with calculated ones. In the calculation procedure, temperature and ratio of the partial pressure of O_2 and N_2 have to be adjusted simultaneously.

spectra. Using Fourier analysis for the evaluation of the experimentally obtained spectra, the periodicity of the rotational CARS spectra offers advantageous possibilities for gas temperature and concentration evaluation over LIT, which in particular is true in gas mixtures [5,6].

In order to proof the applicability of the FAT technique to rotational CARS spectra first tests have been performed with simulated spectra (Fig. 1). An independent evaluation was done for nitrogen, oxygen and carbon dioxide. The results for temperature and concentration for 50 such randomly calculated spectra indicate very good agreement between the input data and the calculated temperature and concentration values: $T \pm \Delta T$ [K] = 1508 $\pm$ 25 (N_2), 1507 $\pm$ 190 (O_2), and 1492 $\pm$ 110 (CO_2); $C \pm \Delta C$ [%] = 60.0 $\pm$ 0.6 (N_2), 6.11 $\pm$ 1.0 (O_2), and 5.95 $\pm$ 0.5 (CO_2).

The FAT technique has been used for the evaluation of conventionally obtained experimental rotational CARS spectra. Such spectra have been taken in the post flame region of a premixed methane-air flame generated by a flat flame burner of 50 millimeters diameter. The burner was driven in two different ways. In order to generate a well established high temperature zone downstream the flame front the burner gas was premixed to near-stoichiometric conditions. In a second different approach the air content to the fuel gas was decreased tremendeously. This pushed the flame to a more diffusion-like behaviour generating a fluctuating flame body.

Figure 2 shows an example of the results obtained in the high temperature region of the premixed methane-air flame. Here only nitrogen has been taken into account. Several of those measurements were used for the temperature evaluation for a particular combustion situation. The experimental CARS

Air ratio λ	Height over Burner	$T_{Equ.}$ [K]	Thermo-couple [K]	CARS FAT [K]	CARS LIT [K]
0.94	0.7d	2260	1780	1811 ± 75	1743 ±132
1.17	0.7d	2117	1865	1832 ± 85	1768 ±119
1.17	0.1d	2117	1970	1969 ±110	1951 ±181

Table 1: Rotational CARS gas temperature results obtained in the high temperature region of premixed methane-air flames in comparison with calculated equilibrium values and radiation corrected thermocouple readings. For both evaluation techniques (FAT, LIT) the results displayed are mean and rms values from sets of 10-30 single temperature measurements.

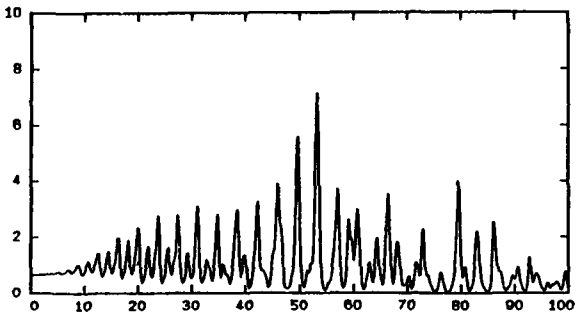

Fig. 4: Calculated pure rotational CARS spectrum of C_2H_4 at room temperature.

spectra were evaluated by both techniques (LIT, FAT). For three different burning conditions as varied by the flow rate of methane and air the results are given in Table 1.

The situation is much more complicated in the mixing region of a diffusion-like flame body with surrounding air. Very first results have been obtained in the mixing zone for three different situations which are related to preheated air and to fluctuation regions. Figure 3 shows the comparison between experimental and calculated spectrum for two different temperatures and different partial pressure ratios for O_2 and N_2.

We are now starting to investigate the influence of high pressure on the evaluation procedures in comparison to vibrational CARS and to calculate more complex nonlinear gas molecules which may appear ir real technical combustion. As an example, Fig. 4 shows the calculated pure rotational CARS spectrum of C_2H_4 at room temperature.

The authors gratefully acknowledge financial support for the work by Volkswagen-Stiftung.

REFERENCES

1. R.J. Hall, A.C. Eckbreth: in Laser Application 5 (Eds. J.F. Ready, R.K. Erf), Academic Press, New York 1984, p. 214-305

2. D.A. Greenhalgh: in Advances in Non--Linear-Spectroscopy (Eds. R.J.H. Clarke, R.E. Hester), Wiley, New York 1988, p. 193-251

3. A. Leipertz: in Instrumentation for Combustion and Flow in Engines (Eds. D.F.G. Durao, J.M. Whitelaw, P.O. Witze), Kluwer, Dordrecht 1989, p. 107-122

4. S. Kröll, P.E. Bengtson, M. Alden and D. Nilsson: Appl. Phys. B 51, 25 (1990)

5. A. Leipertz, E. Magens and T. Lasser: AIAA-Preprint No. 85-1569 (1985)

6. T. Lasser, E. Magens and A. Leipertz: Opt. Lett. 10, 535 (1985)

7. D. Murphy: Ph. D. dissertation Yale University 1981

IUTAM Symposium on
Aerothermodynamics in Combustors
June 3-5, 1991, Taipei

THERMOMETRY INSIDE A SWIRLING TURBULENT FLAME : CARS ADVANTAGES AND LIMITATIONS.

CLAUDE CAHEN, PASCALE BELLAICHE, DANIELE GARRETON*

Direction des Etudes et Recherches - Electricité de France
REME - 25 allée privée - 93206 Saint Denis, France.
*LNH - 6 quai Watier - 78400 Chatou, France.

INTRODUCTION

Our ultimate objective is the development of a general turbulence and combustion code. The first step describes the introduction of a combustion module inside a k-ε turbulent model. The theoretical assumptions, the major hypotheses and the numerical procedure to solve this problem are presented in a companion paper. Here, we address the experimental investigations to validate and document the modeling. A special attention is given to the measurements of the temperature.

CARS TEMPERATURE MEASUREMENTS

The experimental scenario is the study of a swirling turbulent diffusion methane flame. The swirl is used to reduce the flame dimension and is a realistic transposition of industrial processes. The 20 kW burner is set vertically to preserve the axial symmetry of the flow ; the methane is introduced axially and the air tangentially (Fig. 1). The swirling air creates a central depression which, in turn, produces a recirculation zone fueling the burning zone with fresh air and maintaining the flame hung at the burner nozzle. The air and methane flows are carefully controlled and, at the same time, the Laser Döppler Anemometry (LDA) is run to accurately restore the input velocities profile. This is a key point for the model predictions, since these profiles are considered to be the most sensitive input data. The LDA velocity measurements are also compared to the computed velocity field. This type of measurement is broadly used and is not discussed here as the comparison is presented in the companion paper. We focus this paper on the temperature field measurements and predictions.

To restore the temperature field, two techniques are used : thermocouple measurements for total monitoring and Coherent Anti-Stokes Raman Scattering (CARS) for local and instantaneous investigations.

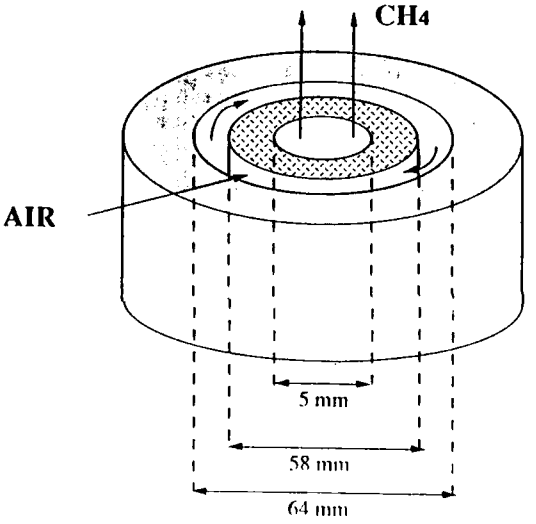

Fig. 1 : the burner schematic

Despite their intrusive features, the thermocouple measurements allow an easy comparison to the model predictions. In general, the average temperature values compare favourably with the predictions. However, since the thermocouple time response is flow dependent, both the turbulence and the recirculation zone preclude the reliability of the instantaneous measurements. In contrario, the non-intrusive, instantaneous CARS measurements can be used.

The CARS technique is now one of the most popular techniques to measure the temperature field and the basic principles are well known though the limitations are seldom emphasized. Since, in our experiment, the turbulence is high and the spatial inhomogeneity of the species concentration is large, the CARS data reduction is carefully processed and the CARS limitations encountered are examined.

The ideal measurement configuration for the best results [1] is the so-called BOX(USED)CARS and cross polarisation configuration (Fig. 2). This increases the spatial resolution and the characteristic features of the recorded spectra. Unfortunately, the experimental situation does not always enable this optimal choice and the subsequent trade-offs which are required, are hereby presented.

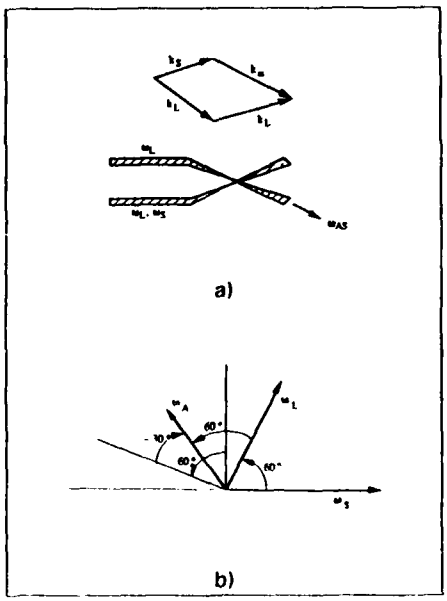

Fig. 2 : BOXCARS a) and cross polarizations b) configurations

BOXCARS ADVANTAGES AND LIMITATIONS

The BOXCARS configuration takes advantage of the two well- separated pump and Stokes laser beams to clearly localize the probe volume at the beams intersection. Simple geometrical considerations make it possible to size this probe volume (typically 5 mm * 100 μm for our experiment). We check the actual spatial resolution by recording temperature histograms for two equivalent positions with respect to the flow symmetry (Fig.3).

The largest dimension of the probe volume is either perpendicular or parallel to the steep temperature gradients. The difference between the two recorded histograms (double narrow peak distribution for parallel and broad single peak distribution for perpendicular) clearly indicates a spatial integration of the measurement over at least 10 mm which is greater than the expected 5 mm. It is probably due to the non-linear generation of the CARS signal combined with the effects of the turbulence.

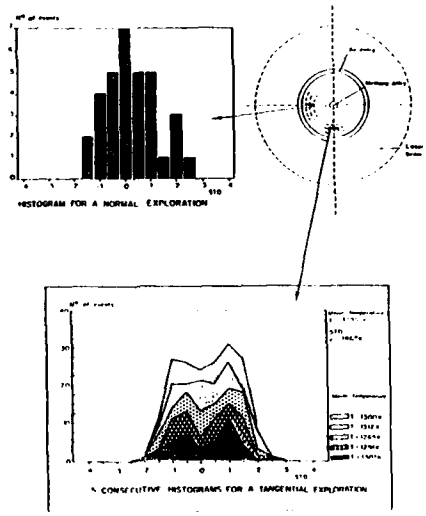

Fig. 3 : recorded histograms for two symmetric positions. The normal exploration smooths the double peak structure.

However, the BOXCARS configuration has to be selected to preserve a reasonable spatial resolution of the temperature measurements and, depending on the probe volume position inside the flame, either parallel or perpendicular measurements are retained. As an example, the double peak distribution of the temperatures at the boundary of the recirculation zone indicates the alternate crossing of hot and cold gas cells inside the probe volume. This crossing is confirmed by the position of the maximum of the recorded spectra on the CCD detector. A strong correlation (> 0.7) is found between the positions and the associated temperatures while the positions are independent of the CARS signal generation but related to the beams propagation through the flame. The sensitivity to these effects is clearly enhanced by the BOXCARS configuration. Definitely assuming the BOXCARS configuration to unbias the temperature histograms, their evolutions through the flame are compared with the probability density function (pdf) used to average the instantaneous passive scalar behaviour (in our case, f : the mixing rate related to the atomic species, see the companion paper [2]). The adopted β function for the modeling cannot depict such a double peak distribution. The spatial evolution of this distribution could yield some characteristic lengths for the diffusion mechanisms which are considered for the double correlation modeling, especially if these results are associated to the velocity measurements.

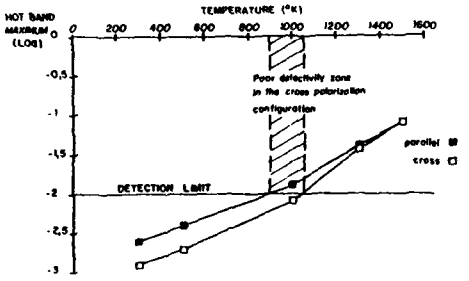

Fig. 4 : detectivity limits of the cross polarization *in the range 900 - 1200 K*

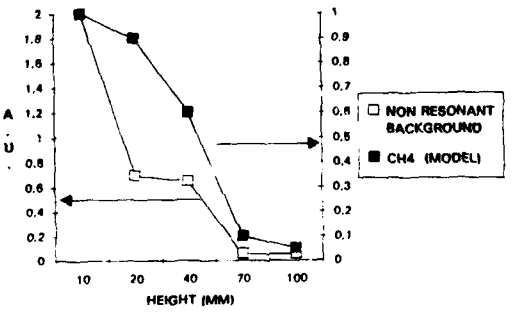

Fig. 6 : semi-quantitative CH_4 profiles at the center of the burner

CROSS POLARIZATION ADVANTAGES AND LIMITATIONS

The problem of the cross polarisation configuration is more complex. This configuration is adopted to cancel the non-resonant contribution of all the species present inside the probe volume (methane, by-products, oxygen or non-resonant nitrogen). If the corresponding spectra are better resolved, the signal intensity is decreased by at least two orders of magnitude compared to the generally adopted parallel polarisation configuration. First, we check that these configurations lead to comparable temperature measurements inside a steady medium[3]. Consequently, to ensure a good signal to noise ratio at any position, we can select either parallel (numerical account of the non-resonant background) or cross (physical account of the non-resonant background) polarisation configurations. This choice is particularly important in the intermediate temperature range (900 - 1200 K) where some detectivity considerations compel the parallel polarisation configuration (Fig. 4). Using a measurement set including either parallel or cross polarisation configurations, the measured and computed temperature fields inside the combustion zone compare favourably though a few small discrepancies (# 100-200 K) remain between the CARS and thermocouple measurements (Fig. 5).

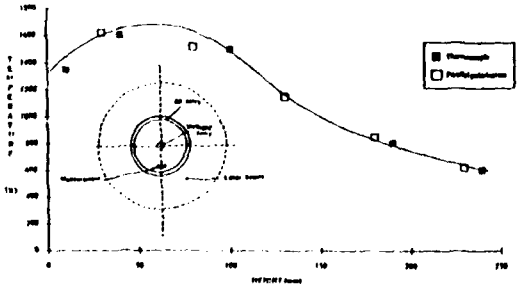

Fig. 5 : CARS and thermocouple comparison

Meanwhile, at the immediate vicinity of the burner exit, the high methane concentration precludes the temperature measurements even in the cross polarisation configuration. However, this important non-resonant background can be used to estimate the relative methane to air ratio. The observed semi-quantitative methane profile, recorded in the cross polarization configuration to cancel the pure air contribution, agrees correctly with the predicted profile, especially when a finite kinetic rate is taken into account (the PEUL approach) (Fig. 6).

CONCLUSION

Though the CARS technique cannot allow any systematic exploration of the flame, it brings an inestimable physical insight of the flame behaviour. Even if some limitations could appear, they can often be turned into advantages. Finally, the complementarity of different techniques is clearly required to assess the consistency of a measurement set.

[1] Eckbreth A. : " Laser diagnostics for combustion temperature and species", Gupta K. and Lilley D. Editors, Abacus press, Cambridge USA, 1988.

[2] Garréton D., Vervisch L. "Numerical study of a swirling turbulent diffusion flame" , abstract # T034, IUTAM Symposium on Aerothermodynamics Combustors, June 3-5, 1991, Taipei.

[3] Bachmann M., Bellaïche P., Cahen C., Garréton D., Vervisch L.,"Modeling and thermometric study of a swirl stabilized turbulent diffusion flame" 23rd Combustion Institute symposium, Orléans, 1990.

IUTAM Symposium on
Aerothermodynamics in Combustors
June 3-5, 1991, Taipei

BLENDING IN INDUSTRIAL PROCESSES TO REDUCE POLLUTANT EMISSIONS

B. KLOCKE, H. KREMER

B. KLOCKE, GASWÄRME-INSTITUT, ESSEN, FEDERAL REPUBLIC OF GERMANY
H. KREMER, RUHR-UNIVERSITY, BOCHUM, FEDERAL REPUBLIC OF GERMANY

INTRODUCTION AND OBJECTIVE

This paper reviews experimental work in the field of flow mechanics undertaken to optimize fluid blending for the control of pollutant emissions from fuel-burning installations. In fact, the optimized mixing of a reactant with the flue gas is crucial for the efficiency of pollution control.

Reburning, standing here as one example for others, a technique involving secondary fuel injection into a coal-fired boiler, is one of the advanced processes proposed to control pollutant formation. The secondary fuel enters a large boiler combustion chamber above the firststage burners, increasing the fuel/air ratio. While the first stage burns a fuel-lean mixture, the second stage combusts a reducing fuel-rich mixture, lowering NO_x concentration by about 50 to 80 %. Tertiary air is added for complete burnout. Both the secondary fuel and the overfire air must be mixed efficiently with the first-stage products of combustion to optimize the NO_x-reducing effect, because the time for the reaction is less than 30 msec.

Two entirely different techniques can be applied to inject the reducing agent into the flue gas stream. The reducing agent may either be distributed through nozzles mounted on the wall of the flue gas duct or through a system incorporated directly in the duct. The project discussed in this paper focussed on the optimization of nozzle configurations, because the improvements in mixing behavior promised by an optimized design are greater.

METHOD OF MEASUREMENT AND TEST SET-UP

The wind tunnel depicted in Fig. 1 was used for the tests. The wind tunnel is a square cross-section tunnel of the open-flow type with a length of 80 cm. It consists of an inlet nozzle, a hexagonal honeycomb flow straightener and a turbulence generator to produce a controlled flow profile along the two axes of the duct.

In the wind tunnel model tests, air was injected into the turbulent wind tunnel main flow rather than a reducing agent. This air was heated to 200° C by an electric heating system and was pumped to the nozzles across a flow control valve. Temperature distribution across the wind tunnel was measured by 20 thermocouples at 20 different heights. As the mechanisms of heat and mass transfer are similar, temperature distribution models concentration distributions. To accelerate the measurements, the thermocouples were mounted on a grid-type arrangement across the entire width of the wind tunnel.

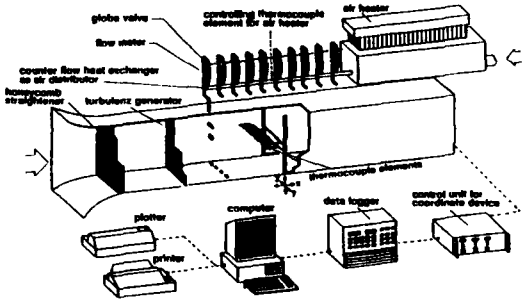

Fig. 1: Scheme of the wind tunnel testing stand

FLOW MODELLING

In laboratory-scale model tests of the type of the wind tunnel tests, it is, of course, important not to violate the principles of similarity. In model tests involving several flows, it is nearly impossible to maintain complete similitude, as the Reynolds number, the Froude number and other characteristics can hardly be kept constant for all flows.

In this project, it is important to realize that fluid blending is essentially controlled by impulse. Prior to modelling geometries to obtain a model scale, a model scaling down the ratio between the mainflow impulse and the injected air flow impulse, disregarding density differences, was developed to obtain equivalent nozzle diameters. The equivalent-diameter nozzle is a model nozzle with a diameter passing, with the same impulse, the same mass flow of the model fluid as the full-scale nozzle. Under these conditions, induced flow is also the same under model and full-scale conditions.

Differences in Reynolds numbers were neglected for the experiments, because frictional forces were negligible at the test Reynolds number levels.

Criteria to evaluate the quality of mixing are difficult to determine. To do this, the coefficient of variation V_k was therefore used. It is the ratio of the standard deviation which is the square root of the variance of a distribution and the arithmetic mean.

In the case of the two mixing operations the quality of mixing is high when the coefficient of variation is low. Under ideal conditions producing a fully homogeneous mixture, the coefficient of variation would be zero. The lowest coefficients of variation obtained in the experiments in cases in which the fluids were allowed to blend over long distances were about 20 %. If the quality of mixing is very low, the coefficient of variation may increase several 100 %. Nevertheless it is important to evaluate the quality of mixing by comparing coefficients of variation in different planes and by also analyzing three-dimensional concentration profiles.

OPTIMIZATION OF MIXING OPERATIONS

The angle of injection was the first parameter that was varied in the wind tunnel tests. Cross-flow injection is the most frequent configuration in the field. A right angle is enclosed between the secondary fluid axis and the main flow centerline. The angle of cross-flow injection is designated by $\beta = 0°$. If this angle is varied to obtain countercurrent-flow injection conditions, the angle is referred to as $\beta > 0$. $\beta < 0$ is used for cocurrent flow injection.

Fig. 2 depicts the coefficient of variation as a function of the angle of injection. As the countercurrent flow injection angle increases, the quality of mixing improves. The coefficient of variation is highest in the only cocurrent injection test, while the largest countercurrent flow injection angle of 45° only improves mixing in the planes above the plane of injection.

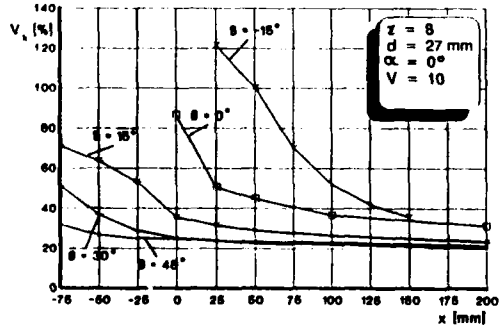

Fig. 2: Coefficient of variation depending on injection angle

Secondary fluid swirl was the second parameter that was varied in the experiments. Fig. 3 correlates swirl and the quality of mixing. As the graph shows, mixing improves as swirl is generated and the angle of the axial blades of swirl generator increases. However as the angle α is further increased beyond a limit, the coefficients of variation increase again.

The reason for this trend is very simple. Swirl-flow jets induce the surrounding fluid at a higher rate than swirl-free jets, improving mixing mainly at the interface between the secondary fluid and the main fluid. On the other hand, swirl reduces the impulse in the axial direction, shortening the length of the jet. In the test depicted, the length of the secondary fluid jet was no longer sufficient to penetrate main fluid flow.

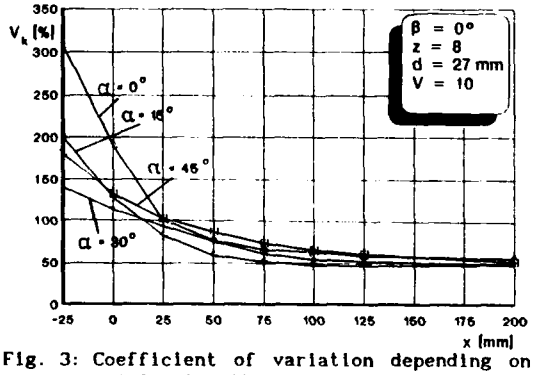

Fig. 3: Coefficient of variation depending on swirl intensity

Main fluid flow penetrations is also a critical consideration in the optimization of the ratio between the main fluid flow rate and the secondary fluid flow rate. This ratio depends, of course, on the stoichiometry of the reducing reaction. If the stoichiometric ratio were used, the main/secondary flow ratio V would be much too high for satisfactory mixing. For this reason, the reducing agent flow rate must be increased for example by adding recycle flue gas to obtain satisfactory mixing conditions.

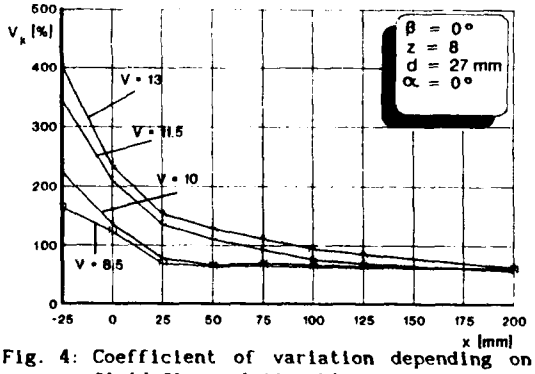

Fig. 4: Coefficient of variation depending on fluid flow relationship

Fig. 4 shows the coefficient of variation for several main flow/-secondary flow ratios. The inadequate main flow penetration is the reason for the decreasing mixing results with an increasing ratio. As the figure shows a ratio between 10:1 and 8.5:1 was approximately in optimum. Mixing could theoretically be improved further by further lowering this ratio but such a decrease would require more fan power for the injection of the secondary fluid.

Fig. 5 plots the coefficients of variation for different nozzle numbers z. The total secondary fluid flow is the same for all nozzle numbers. For this reason, the impulse of the jet from each nozzle is higher for a smaller number of nozzles.

The graph demonstrates the critical importance of the impulse of the jet, because the coefficients of variation are nearly the same for two nozzles as for four and six nozzles. Neverless, four or six nozzles represent an optimum as the coefficients of variation tend to rise. If the

number of nozzles used is very small, the fluid exchange area is too small for optimum mixing. On the other hand, if the number of nozzles is too high, main flow penetration poses a problem.

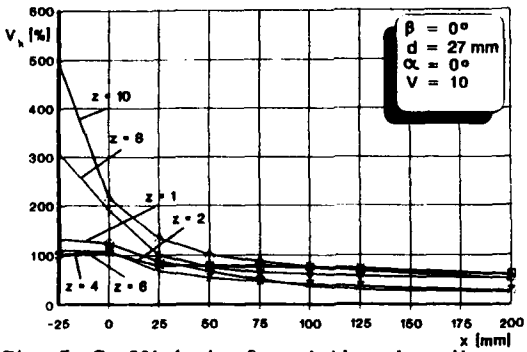

Fig. 5: Coefficient of variation depending on the number of peripheral arranged jets

Impulse may also be varied by varying the nozzle diameter d. Between the coefficients of variation for the smallest and the largest nozzle diameter was a multiplication factor of 2.5 for the secondary fluid injection plane, Fig. 6. Turbulent exchange at the interfaces between the jet and the main flow fully benefits from the increase in impulse achieved by reducing the nozzle diameter. For the same nozzle discharge flow rate and the same main flow/secondary flow density ratio, the smallest nozzle induced more than twice as much flow from the main stream than the largest nozzle.

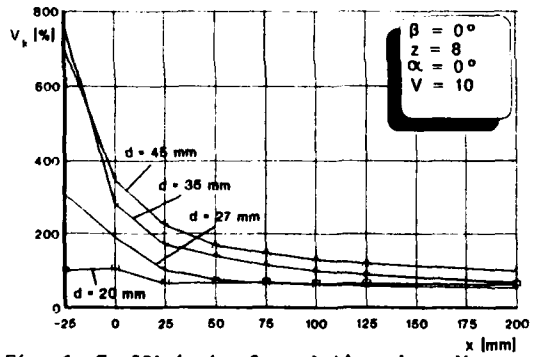

Fig. 6: Coefficient of variation depending on the nozzle diameter

Apart from the above parameters, a number of other factors influencing the quality of mixing were examined.

Nozzle arrangement on the wind tunnel wall was one such parameter. The tests showed that nozzles located exactly opposite each other represent the optimum configuration provided that the jets from the two nozzles penetrate to the center of the main flow, hit each other and are deflected sideways.

Mixing can also be improved by optimizing nozzle design provided that the nozzle discharge area is sufficiently small. The mixing achieved by reduced discharge-area nozzles of a complex design is very similar to that of simple design nozzles of corresponding discharge area.

MATHEMATICAL MODELLING TECHNIQUES

The mathematical modelling of such experiments is another significant aspect of this research work.

The approximation technique developed combines a model describing the propagation of an unconfined jet and a description of the axis of an unconfined jet under cross-flow conditions. The equations describing the propagation of an unconfined jet from a round nozzle in a motionless environment without buoyancy forces are projected into the bent jet axis, assuming for simplification that the jet contour remains unchanged. The secondary fluid concentration at any given point depends on the distance of the point from the jet axis along a line perpendicular to the jet centerline. The point at which the perpendicular and the jet center line intersect corresponds to the axial-direction coordinate of an unbent unconfined jet.

Fig. 7 shows the quality of the model that has been developed. For two jets which are not located opposite each other, predicted and measured concentrations are in good agreement. Differences between the predicted and the measured concentrations only increase for nozzles located opposite each other, ejecting jets which hit each other in the center of the main fluid flow. The quality of the prediction of the mixing process is nevertheless highly satisfactory, considering the short computing time of several seconds.

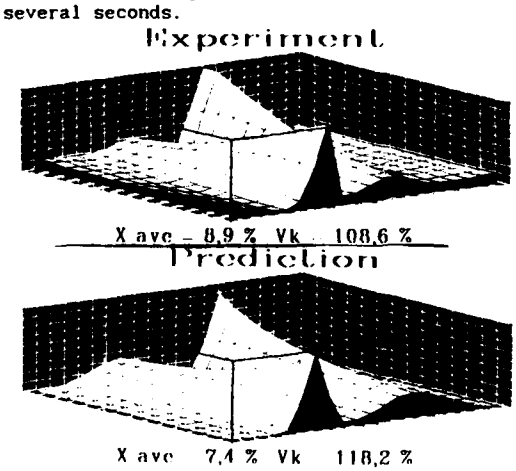

Fig. 7: Comparison of mixing patterns out of experiments and prediction

SUMMARY

Nozzles can produce a concentration profile where concentration differences are minimized if the following conditions are satisfied:

- Injection of the secondary fluid at a countercurrent flow angle of 15 to 30°
- Increase in the secondary fluid impulse through the selection of smaller nozzle diameters
- Decrease in the main flow/secondary flow ratio using recirculated flue gas or a similar fluid to increase the secondary fluid flow rate where necessary
- Injection of the secondary fluid through a limited number of nozzles, ensuring, though, that the fluid exchange surface area will not decrease below a minimum area
- Limited swirling of the secondary fluid, preferably combined with the use of nozzles producing swirl-free jets.

IUTAM Symposium on
Aerothermodynamics in Combustors
June 3-5, 1991, Taipei

The Turbulence and Mixing Characteristics of the Complex Flow Field in a Simulated Augmentor

by

Chao, Y.C*., Leu, J.H.,** and Yang, T.H.**
Institute of Aeronautics and Astronautics
National Cheng Kung University
Tainan, Taiwan 70101
R.O.C.

Extended Abstract

In modern aircraft, afterburners or augmentation devices are added to the gas turbine engines to increase their thrust during take-off or emergent maneuver. The oxygen content in the high speed gas stream leaving turbine blades is burnt with additional fuel in this secondary combustion device to increase the gas exit velocity and thrust. Steady burning in this high speed gas stream is very difficult unless sources of continuous ignition or proper flame stabilization devices are present in the combustion chamber. Flame stabilization is usually achieved in the wake of a bluff body, e.g. V-gutter, placed in the gas stream. In addition to the flame stabilization problem, ignition is usually harder to achieve than stabilization. The primary problems for afterburner ignition systems is the start-up ignition and the high altitude relight problems. A pilot burner is one of the solutions to these problems. However, in modern aircraft in order to reduce the weight, the pilot burner is usually of "V" shape, similar to the V-gutter with high angle swirl vans inside. The V-shaped pilot burner can be used to serve partly as a flame stabilization device. This special design of the V-shaped pilot burner produces a complex flow field with strong interaction of high swirl and axial velocities in the wake of the pilot burner. Furthermore, the flowfield will be further complicated by using both V-gutter and pilot burner. The turbulence and mixing characteristics are of vital importance to the ignition and the stabilization problems. Thus, the main purpose of this research are to measure the turbulent velocity and mixing characteristics of the complex flow field in a simulated augmentor.

Studies of the bluff-body stabilization and the afterburner characteristics can be found as early as in the 40's. Longwell [1] and Williams [2] studied the bluff-body turbulent flame stabilization and propagation. Recently, Sullerey et al. [3] characterized the turbulent near wake of bluff bodies of different kinds. Stwalley and Lefebvre [4] examined irregular shaped flame holders. Zukoski [5] offered an instructive review of the afterburner. Taylor and Whitelaw [6] studied the velocity characteristics in the near wake of the bluff body. Others [7~9] studied the interaction of the swirling component with the axial coaxial jet. However, the V-shaped pilot burner turbulence characteistics which are generated by the strong interaction of the high swirling and the axial components in the wake, are still open issues and deserve careful studies.

The experimental set-up consists of an air blower driven by a DC motor, a settling chamber and the simulated augmentor test section. Air in the settling chamber is first passed through a slowly divergent duct with an angle of 7°, and a honeycomb unit and 3 fine mesh screens are used to further reduce the fluctuations. Figure 1 shows schematically the arrangement of the test section of the simulated augmentor. The front portion of the center body is used to contract the flow reaving the mesh to further reduce the turbulent fluctuation and the rear portion is to simulated the diffuser of the augmentor. Both the laser Doppler velocimetry (TSI 9100-7) system and a concentration probe (TSI 1441-18) are used to measure the velocity component, turbulence and mixture fraction of the augmentor flow, as shown in Fig. 2. In order to eliminate the noise and difficulties encountered in the LDV measurements due to the curvature of the augmentor wall, sixteen circular windows of 30 mm diameter are attached to both sides of the wall. They are sealed with thin flat optical glasses to allow accurate intersection of the laser beams and to reduce the noise in the scattered light intensity. The binary mixing of air and helium is measured by an aspirating concentration probe made up of a hot-film sensor in a tube with a sonic throat. This type of probe has been used with success by Brown and Rebollow [10] and Ahmed and So [11]. Both mean and fluctuating binary mixture concentration can be measured with high resolution. The probe output is calibrated for the pressure dependence. The pressure calibration curve, accouding to Chao and Yang [12], can be written as

$$E^2/(T_w - T_e) = A + B(P - 1) + C(\rho^{\frac{1}{2}} P^{\frac{1}{2}})$$

where A, B, C are constants, P is the static pressure,

E^2 is probe output, T_w and T_e are the temperatures of the wire and the flow and ρ is the density of the binary mixture. Figure 3 shows the calibration curve for the probe used and the probe outputs for different pressure collapses into a single curve so that measurements in the situations where pressure is fluctuating due to flow can be achieved by using the aspirating probe together with a pressure sensing device using this general calibration curve.

The axial velocity distribution for the pilot burner flow in the augmentor is shown in Fig. 4. The dashed curves in the vicinity of the pilot burner indicate the zero axial velocity contour. The wakes due to the pilot burner and due to the central diffuser characterize the near field axial velocity distribution and the axial velocity profile becomes more uniform around X/D of 0.4. If one examine the velocity distribution in the vicinity of the pilot burner carefully, one can easily find that axial velocity distribution near the lower zero velocity region around Y/D of 0.6 is steeper than that near the upper zero velocity region around Y/D of 0.8. This phenomenon can further be seen in the turbulent fluctuation profiles in Fig. 5 where local peak fluctuations are found near the lower portion of the pilot burner corresponding to the zero-velocity contour in Fig. 4 while that in the upper portion is not so pronounced. This phenomenon is believed to be due to the effect of the interaction of the pilot burner swirl component and the shear in the pilot burner wake and this was also seen in a preliminary flow visualization study in the water tunnel by Chao and Chen [13]. In other words, stronger turbulent mixing can be expected in the lower portion of the pilot burner shear layer in the wake. In the presence of a V-gutter, the pilot burner recirculation becomes smaller and the wake due to the diffuser disappears. The axial velocity distribution recovers earlier in X/D of 3.5 in Fig. 6. On the other hand in Fig. 7, the peak turbulent fluctuations downstream of the pilot burner becomes less pronounced. The local peak fluctuations in the wake of the V-gutter is "symmetric". Globally, the turbulent fluctuation in Fig. 7 is stronger than that in Fig. 5. It reveals that stronger mixing in the lower portion in the pilot burner wake and the strong mixing in the wake of the V-gutter provides a convenient path for the pilot flame to propagate to the V-gutter and the strong swirl component helps to stabilize the pilot flame in the wake of the pilot burner. Due to an unexpected accident, the concentration probe was broken and it is now sent back to the manufacturer in the U.S. to repair so that the concentration results are not included here. The concentration data will be given later as soon as the probe is fixed.

References

1. Longwell, J.P., "Flame Stabilization by Bluff Bodies and Turbulent Flames in Ducts," 4th International Symposium on Combustion, pp. 90-97 (1952).
2. William, G.C., H.C. Hottel and A.C. Scurlock, "Flame Stabilization and Propagation in High Velocity Gas Stream," 3rd Symposium on Combustion and Flame and Explosion Phenomena, pp. 21-40 (1949).
3. Sullerey, R.K., A.K. Gupta and C.S. Moorthy, "Similarity in the Turbulent Near Wake of Bluff Bodies," AIAA Journal, Vol. 13, pp. 1425-1429 (1975).
4. Stwalley, R.M. and A.H. Lefebvre, "Flame Stabilization Using Large Flame-holders of Irregular Shape," AIAA-87-0469 (1987).
5. Zukoski, E.E., "After Burners," Chapter 21 in the Aerothermodynamics of Aircraft Gas Turbine Engines, (Ed. by G.C. Oates.), AFAPL TR 78-52 (1978).
6. Taylor, A.M.K. and Whitelaw, J.H., "Velocity Characteristics in the Turbulent Near Wakes of Confined Axisymmetric Bluff Bodies," J.F.M. Vol. 139, pp.391-416, 1984.
7. Ribeiro, M.M. and J.H. Whitelaw, "Coaxial Jets with and without Swirl," J.F.M., Vol. 96, pp. 769-795 (1980).
8. So, R.M.C., S.A. Ahmed and H.C. Mongia, "Jet Characteristics in Confined Swirling Flow," Exp. in Fluids 3, pp. 221-230 (1985).
9. Brondum, D.C. and J.C. Bennett, "Numerical and Experimental Investigation of Nonswirling and Swirling Confined Jets," AIAA-86-0040 (1986).
10. Brown, G.L., and Rebollo, M.R., "A Small Fast-Response Probe to Measure Composition of a Binary Gas Mixture," AIAA J. Vol. 10, pp. 649-652, 1972.
11. Ahmed, S.A. and So, R.M.C., "Concentration Distributions in a Model Combustor," Exp. Fluids, Vol. 4, pp. 107-113, 1986.
12. Chao, Y.C. and Yang, Y.S., "The Calibration and Measurement of the Concentration using an Aspirating Probe," The 14th National Conference on Theoretical and Applied Mechanics, Chungli, Taiwan, R.O.C., 1990.
13. Chao, Y.C. and Chen, T.C., "Studies of the Flow Field Characteristics of a pilot Burner in the After Burner," Proceedings of the 5th National Conference on Mechanical Engineering, CSME, Taipei, pp. 253-264, 1988.

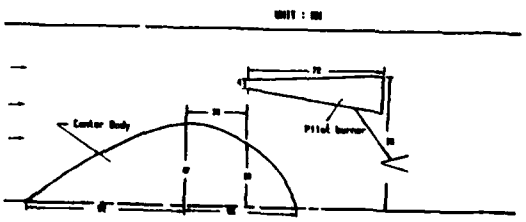

Fig.1 Schematic of the simulated augmentor test section

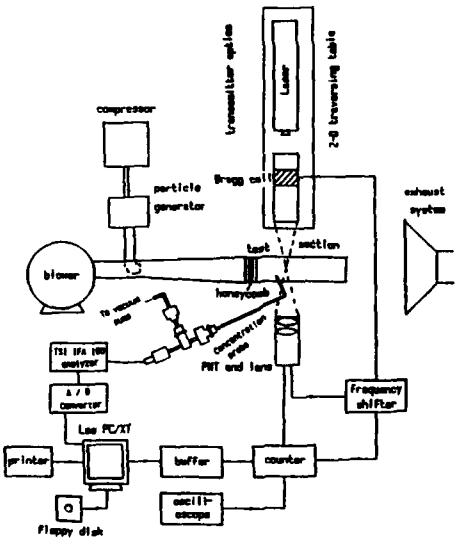

Fig.2 Experimental set-up and instrumentations

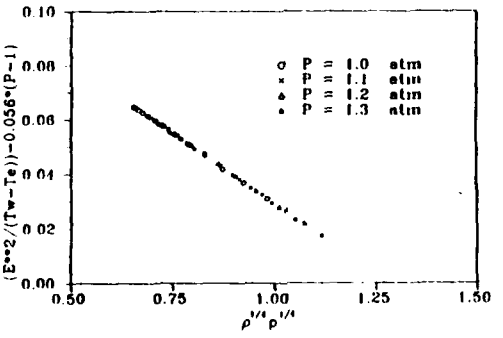

Fig.3 The universal calibration curve for the concentration probe including pressure dependence

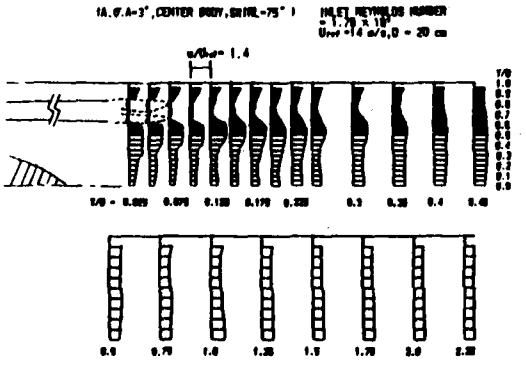

Fig.4 The axial velocity distribution for the pilot burner flow

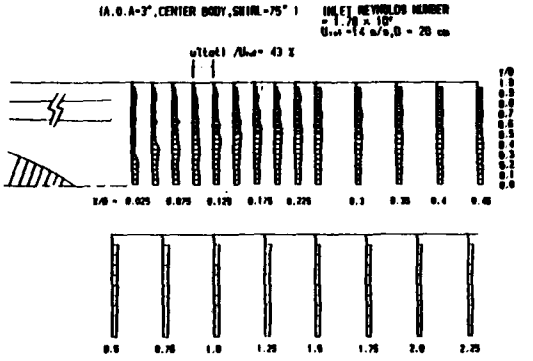

Fig.5 The turbulent fluctuation distribution for the pilot burner flow

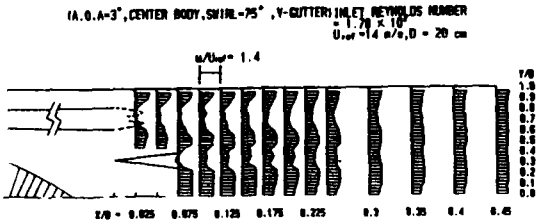

Fig.6 The axial velocity distribution for the simulated augmentor flow

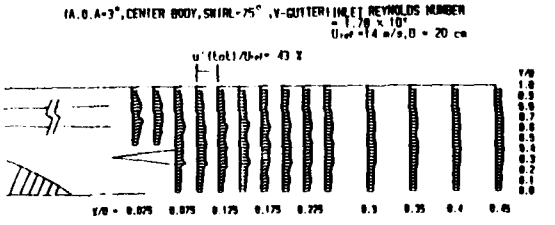

Fig.7 The turbulent fluctuation distribution for the simulated augmentor flow

IUTAM Symposium on
Aerothermodynamics in Combustors
June 3-5, 1991, Taipei

ENHANCEMENT OF TURBULENT MIXING IN A CONFINED SQUARE SIDE-DUMP COMBUSTOR MODEL

Sun, Dar-Jen and Miau, Jiun-Jih

Institute of Aeronautics and Astronautics
National Cheng Kung University, Tainan 70101, Taiwan, R.O.C.

INTRODUCTION

An experimental study was conducted to investigate the enhancement of turbulent mixing in a confined dual-inlet square side-dump combustor model which is characterized by the impingingement of two counter-directional jets. It was found earlier [1-3] that counter-rotating streamwise vortical structures generated in a confined impinging stagnation flow play a major role responsible for turbulent mixing. Further, a previous work by the first author [4] suggested that the Taylor–Görtler type centrifugal instability mechanism initiate these vortical structures in the curved shear layers which casts off from each of inlet ducts. Based on these physical understandings on the flow, the major emphasis of the present work is placed upon enhancing turbulent mixing by introducing several kinds of artificial disturbances upstream of the curved shear layers, from which one examines the responses of the curved shear layers due to these disturbances imposed.

EXPERIMENTAL METHODS

The water tunnel employed for the present study has two identical side-inlet ducts of 5 cm × 20 cm × 150 cm which connect to a square duct (test section) of 20 cm × 20 cm × 250 cm. Further detailed documentation of the tunnel facility can be found in the Miau and Sun [5]. In comparison with the previous work [5], a modification on the test section of removing the dome region was made in the present study. A schematic view of the side-inlet square duct and the coordinate system chosen for the present study is shown in Figure 1. In experiment the speeds of the two inlet flows were set to equal, varying in a range from 2.3 cm/sec to 9.1 cm/sec. The corresponding Reynolds numbers, Re, based on the width of inlet duct and the bulk velocity of inlet duct, are between 1150 and 4550.

In flow visualization experiments, the techniques of dye-injection and laser-induced fluorescence were adopted to reveal the instantaneous flow structures at the desirable cross-sectional planes of the flow. The light source employed in the dye injection method was photo studio bulbs each of which was 500 watts. An argon-ion laser was employed for the latter technique metioned as the light source.

RESULTS AND DISCUSSIONS

There are three kinds of uptsream artificial disturbance generators installed in the side-inlet ducts which included 2-D trip cylinder, 3-D square-wave trip plate, and the multiple cylinders.

For the sake of comparison, a cross-sectional photograph obtained under the reference condition, namely without installation of disturbance generators in the side-inlet ducts, is shown in Figure 2. This photograph was taken at x=2.5 cm at Re = 2000 which reveals the formation of streamwise vortical structures in the test section. It should be mentioned that these streamwise vortical structures observed vary in sizes and unsteady with time.

With 2-D trip cylinders The imposed 2-D trip cylinders are all of 20 cm in length, equivalent to the height of the test section. Three different sizes of diameter, 4, 6 and 8 mm, were chosen denoting as d1, d2 and d3, respectively. Each of the cylinders is located in the inlet duct on upstream side wall surface vertically. The photograph shown in Figure 3 was obtained with a symmetrical arrangement of two cylinders (type d2) located at $y = \pm 11.5$ cm for Re=2000. It shows a feature that the sizes of the two recirculating regions situated on the upstream end plate of the test section are not equal. It should be noted that this device influences these recirculating zones to oscillate in large amplitude. Evidently, this feature is due to the upstream boundary layers tripped by the cylinders that introduce the unsteadiness. A sequence of top view pictures depicting the time evolution of recirculating flow structures on the upstream end plate are shown in Figure 4. As illustrated by the blue and red dye streaks the oscillating behavior of separation regions is apparent. Thus, the streamwise vortical structures shedding downstream in the test section appear in a quasi-periodic manner. The time period estimated is about 3.6 sec. This oscillating characteristic can be illustrated from an end view at the cross-sectional plane of x = 2.5 cm shown in Figure 5. The time-series photographs in Figure 5 show an alternative appearance of counter-rotating streamwise vortical structures on either side of the presumed stagnation interface. This appearance implies that the streamwise vortices are shed downstream in a quasi-periodic manner as mentioned.

Cases with trip cylinders located at different positions on side wall surface were also made in this

study. In summary, the imposed 2-D trip circular cylinder which introduces a disturbance with vertical vorticity, ω_z, to the upstream inlet flow can effectively alter the characteristics of the curved shear layer as far as the development of the streamwise vortices is concerned. Meanwhile, these studies show that the streamwise vortical structures can be generated in a quasi-periodic manner.

With 3-D square wave trip plates In this case, experiments were performed with the 3-D trips located at y = 11.5 cm and −11.5 cm on the upstream side walls of the inlet ducts, respectively, at Re= 2000. According to our visualizations, the wake pattern resulted behind each of the square-wave trip consists of the so-called "ladder-like" loop structures [6] and with prescribed spacing between loops. A typical picture obtained from the end view at the cross-sectional plane of x =2.5 cm are shown in Figure 6. The entire flow field illustrates a random character of the three-dimensional vortices. Previous observation of spanwise periodicity of the steamwise vortices in the cases with 2-D trip cylinders is not found. It is seen that in the present case the streamwise vortices are evolved from the wake of the square-wave trip. Thus these observations infer that the imposed streamwise vorticity disturbances in the curved shear layer affect the development of the streamwise vortical structures in the test section.

With multiple cylinders In the experiments with the multiple cylinders placed in the inlet ducts, each of the cylinders employed is 5 cm in length spanning the width of the inlet duct. If the solidity is defined as the ratio of diameter of the cylinder to spacing between neighboring cylinders, two configurations with different solidities, 0.067 and 0.1, were studied. These wake generators, i.e. the multiple cylinders, were arranged in the inlet ducts at the vertical planes $y = \pm 24$ cm.

Figure 7 presents a picture obtained from the end view of the flow for staggering arrangement of multiple cylinders in the two inlet ducts at Re = 2000. A sketch describing the arrangement of models and a schematic drawing of flow pattern observed are also enclosed in this figure. Features observed are described below. First, the number of counter-rotating vortex pairs observed is equal to the number of cylinders in each wake generator and the positions are about the same vertical levels as those of the corresponding cylinders. Next, the dye streaks of Kármán vortex streets associated with the cylinders actually delineate the outer boundary of streamwise vortices as these streamwise vortical structures seen in the photograph. Further, it is also seen that the vortex pairs developing from the two sides of inlet flows strongly interact with each other. Thus, a highly turbulent mixing process takes place in the test section. This appearance implies that the effectiveness of mixing of two impinging fluids is enhanced . Experiments of other cases indicate that similar flow structures are seen irrespective of different solidity and arrangement of cylinders.

Based on the flow visualization results obtained a summary is made here. By introducing the forced disturbances into the present combustor model, the development of streamwise vortices in the test section can be manipulated to a somewhat extent. While the 3-D square wave trip destructs the orderly patterns of streamwise vortical structures seen in the case without the imposed disturbance, the multiple cylinders device can control the number of vortex pairs developed in the test section. Dimotakis and Brown [7] suggests a process of efficient mixing that fresh fluid can be entrained by the mean vorticity of large-scale structure which is followed by fine-scale mixing due to vorticity fluctuation. In the present case one can expect that a rapid process can be achieved with an installation of the multiple cylinders in the side-inlet ducts.

REFERENCES

1. F. D. Stull, R. R. Craig, G. D. Streby, and S. P. Vanka 1985 Investigation of a dual-inlet side-dump combustor using liquid fuel injection. *J. Propulsion and Power* 1, pp. 83–88.
2. N. S. Nosseir and S. Behar 1986 Characteristics of jet impingement in side-dump combustor. *AIAA J.* 24, pp. 1952-1957.
3. J. J. Miau, D. J. Sun, and L. S. Yao 1989 Streamwise vortices generated by impinging flows in a confined duct. *Experiments in Fluids* 7, pp. 497-500.
4. D. J. Sun 1990 On the mechanism for generating streamwise vortices in a confined impinging flow. Ph.D. Thesis, Institute of Aeronautics and Astronautics, National Cheng Kung University, Taiwan, R.O.C.
5. J. J. Miau and D. J. Sun 1988 Visualization of impinging flow in a side-inlet square duct. *AIAA paper* 88-0502.
6. A. E. Perry and T. T. Lim 1978 Coherent structures in coflowing jets and wakes. *J. Fluid Mech.* 88, pp. 451–463.
7. P. E. Dimotakis and G. L. Brown 1976 The mixing layer at high Reynolds number: large structure dynamics and entrainment. *J. Fluid Mech.* 78, pp. 535–560.

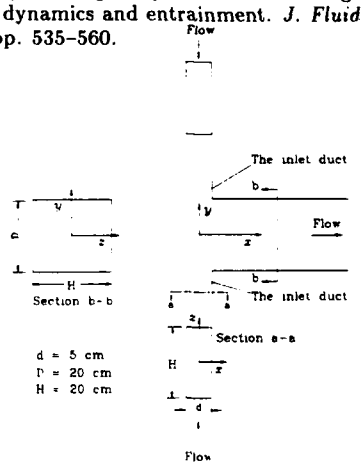

Figure 1 A cross-sectional sketch of the side-inlet square duct and the coordinate system.

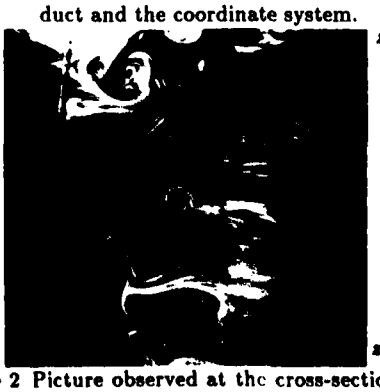

Figure 2 Picture observed at the cross-sectional plane of x = 2.5 cm in the reference case for Re = 2000.

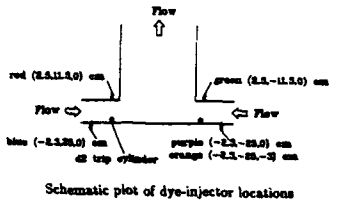

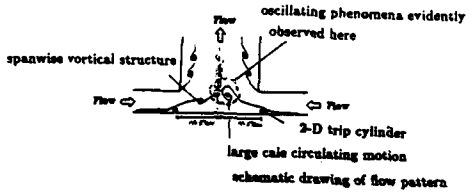

Figure 3 Picture and global flow pattern observed from top view in the case of 2-D trip cylinders (type d2) located at $(-2.5, \pm 11.5)$ cm for $Re = 2000$.

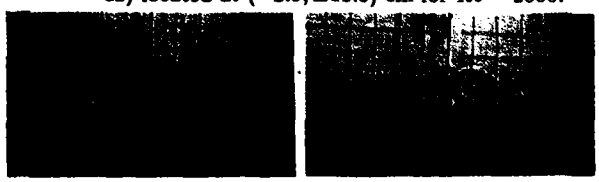

(a) $t = 0$ (b) $t = 1.16$ sec

(c) $t = 3.1$ sec (d) $t = 3.9$ sec

Figure 4 A sequence of pictures observed from top view in the case of 2-D trip cylinders (type d2) located at $(-2.5, \pm 11.5)$ cm for $Re = 2000$.

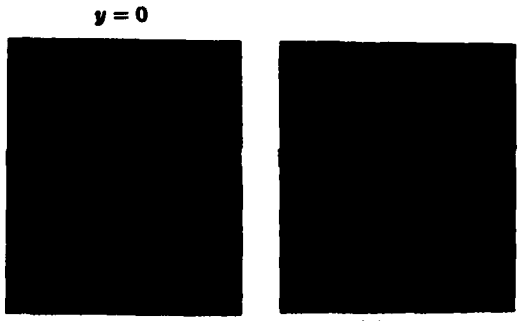

(a) $t = 0$ (b) $t = 1.2$ sec

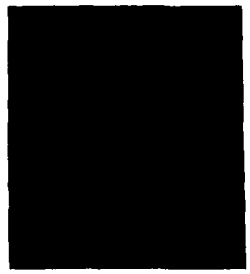

(c) $t = 2.4$ sec

Figure 5 A sequence of pictures observed at the cross-sectional plane of $x = 2.5$ cm in the case of 2-D trip cylinders (type d2) located at $(-2.5, \pm 11.5)$ cm for $Re = 2000$.

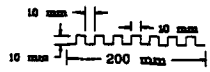

3-D square-wave trip plate geometrical configuration. (Thickness 0.5 mm)

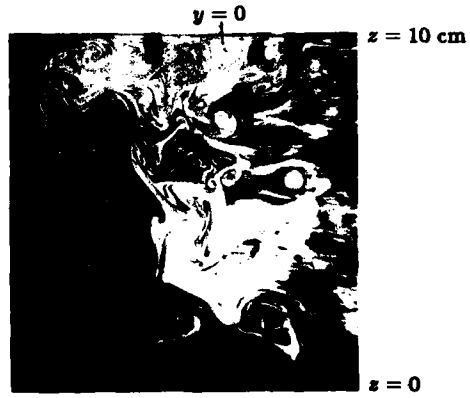

Figure 6 Picture observed at the cross-sectional plane of $x = 2.5$ cm in the case of 3-D square-wave trip located at $(-2.5, \pm 11.5)$ cm for $Re = 2000$.

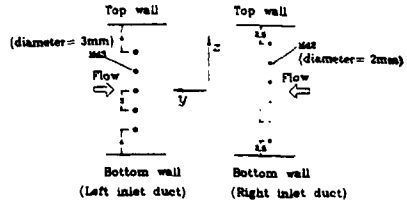

Schematic drawing of the multiple wake generators installed in the side-inlet ducts (cm).

Figure 7 Picture observed at the cross-sectional plane of $x = 2.5$ cm in the installation of multiple wakes for $Re = 2000$.

IUTAM Symposium on
Aerothermodynamics in Combustors
June 3-5, 1991, Taipei

FLOW STRUCTURE OF SWIRLING FLOW INTERFERING WITH CROSS FLOWS

Yuji Ikeda, Shigeo Hosokawa, and Tsuyoshi Nakajima

Department of Mechanical Engineering
Kobe University
Rokkodai, Nada, Kobe 657 Japan

1. INTRODUCTION

Swirling flow interfering with cross flows is a fundamental flow in swirl-stabilized combustors and used to control size of the recirculating vortex and dilution of the combustion air. In the combustor, the flame holding,flow mixing, and dilution are carried out by the swirl-stabilized flow with cross jets. The flow is, therefore, complicated and three dimensional. The understanding of this flow structure can contribute to satisfy action of the demands for high power, high efficiency, and low NOx in the combustor performance.

Although many researches for the swirling flow have been carried out in cold and combusting models, the detail data of swirling flow with cross flow and the mixing properties have not been made clear yet. Green and Whitlaw [1] measured three-dimensional isothermal flow in a model combustor, but the model did not include swirl flow. Ahmed and So [2] made detail measurement of penetration of signal cross jet in a swirl flow. Koutmos and McGrirk [3] measured three velocity components of cold flow in a model combustor but the measured data were not enough to provide a interfering flow structure. Richards and Samuelsen [4] made experiment in a combusting model to understand the role of the primary jet in the swirl flow. Further understandings of the swirl flow interfering with cross jets require the radial velocity component of the jet and its mixing characteristics with the swirl flow. Three velocity components were measured in a cold combustor model with four cross jets [5]. The flow structure was complex and there were four major flows, which interfered each other.

The purpose of the present investigation is to elucidate flow structure in the interfering area by the measurement of three dimensional three velocity components of swirl flow interfering with cross flows.

2. EXPERIMENTAL APPARATUS AND CONDITIONS

In this study, a can-type water model gas turbine combustor shown in Fig. 1 was used in order to simulate primary zone and interference flow in the combustor. The model combustor was made of acrylic resin. The swirl number calculated from the swirler dimensions was 0.817. Velocity measurements were carried out using two types of fiber LDVs (FLDV) [6]. The axial velocity components were measured by a He-Ne FLDV with a probe of 18 mm in diameter. The FLDV probe of 6 mm in diameter was immersed into water to measure the radial and the tangential velocity components. An FFT possessor called Burst Spectrum Analyzer (DANTEC) was used for signal processing, and 3000 bursts were sampled at each measurement point.

The flow rate of the swirl flow was fixed to be 30 l/min, and the flow rate of the primary jets was changed from 45 l/min to 90 l/min. The momentum ratio of the jet flows to the swirling flow was thus changed from 1.78 to 7.01.

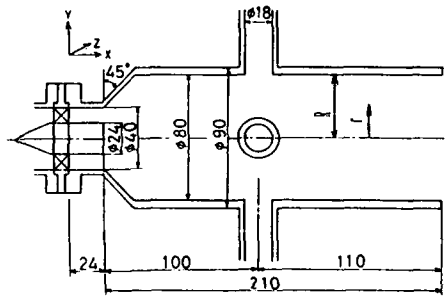

Fig. 1 Schematic layout of test section

3. RESULTS AND DISCUSSION

Figure 2 shows velocity vectors in an isothermal flow, which was obtained in the previous experiment [5]. Four major flows were observed in the model combustor: the recirculating vortex made by the swirling flow, the reverse flow near the wall upstream of the jet ports, recirculating flow behind the bluff body, and the swirling trochoidal flow near the center axis in the region of X = 75 - 125 mm (let us call it interacting region). With increasing of the momentum ratio, both the swirling trochoidal flow and the reverse flow in the near-wall region grew upward, while the recirculating vortex became smaller and moved upstream and to the combustor wall. In the interacting region, the flow from the swirler avoided the swirling trochoidal flow (let us call it blocking area), and passed through the near-wall area. In the present study, we placed emphasis on four subjects: the trochoidal vortex formation process, the negative flow in the near-wall region which affects the recirculating vortex formation, the characteristics of the blocking area where the swirling flow is blocked, and the turbulence characteristics generated by interference of the swirling flow with the four cross jets.

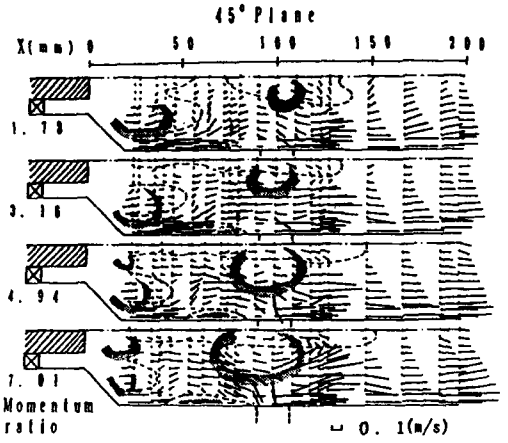

Fig. 2 Flow pattern in the swirling flow interfer'ng with cross flows

3.1 Jet behavior

In order to understand the generation process of the trochoidal vortex and the jet penetration, the radial and tangential velocity was measured in the interacting region as shown in Fig. 3.

In the plane of X = 80 mm, the flow field was almost axisymmetric, and little changed with increasing of the momentum ratio. At the jet port cross-section (X = 100 mm) the jets were bent near the jet ports and collided with the neighbor jet, which produced the strong swirling trochoidal vortex at the center. With increasing the momentum ratio, the velocity vector become large but the angle was constant. This means that the tangential velocity was accelerated, and the flow in the downstream region of strong swirling flow is inhaled into the center, then the trochoidal vortex become strong and large with increasing of the momentum ratio.

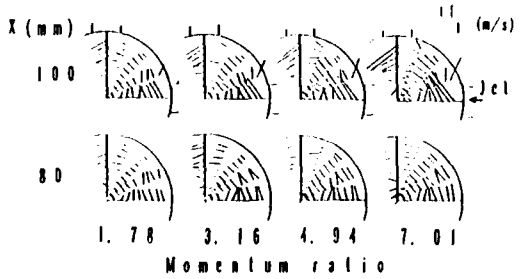

Fig. 3 Velocity vector profiles (v-w) in cross-section area

The reverse flow near the wall, which push the recirculating vortex with the trochoidal vortex, was understand by the axial velocity profiles in the upper stream of jet ports (X = 90 mm) as shown in Fig. 4. The negative axial velocity was observed near the wall and increased with increasing of the momentum ratio. Although this reverse flow existed in the vicinity of r/R = 0.8 on the 22.5° -plane, a small reverse flow was also observed near the wall on the 45° -plane and the 67.5° -plane, which means that the main part of the jet collides with the neighbor jet just, and a part of the jet separates upstream along the wall and with tangential velocity. When the momentum ratio was high, the collision of the jets became more violently, and the reverse flow in the near-wall region grew upstream and pushed the recirculation vortex upstream.

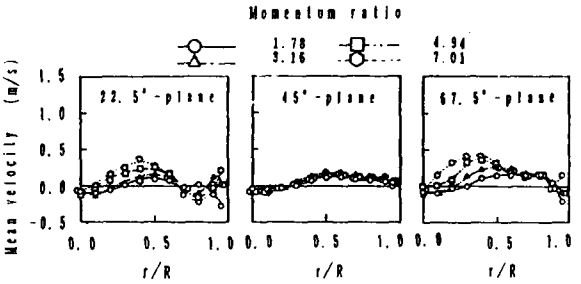

Fig. 4 Axial velocity profiles at X = 90 mm

3.2 Blocking area

The region of the strong swirling flow was generated by the jets and blocked the flow from the swirler, and this blocking area influence the flow in upstream region.

For understanding of the jet penetration and mixing characteristics in the blocking area, the tangential velocity contours were measured on 0° , 22.5° , 45° , and 67.5° -planes as shown in Fig. 5. The large tangential velocity region exists near wall at the 0° -plane. With flowing downstream and in the swirling direction, this large tangential velocity area shifted toward the center and the tangential velocity decreased. Conventionally, the jet penetrate to the combustor center and reverse upstream, which form the recirculation zone. These measured tangential contour indicates that the jet bent at the port exit to the swirl direction and push the neighbor jet, which demonstrate strong swirling trochoidal vortex.

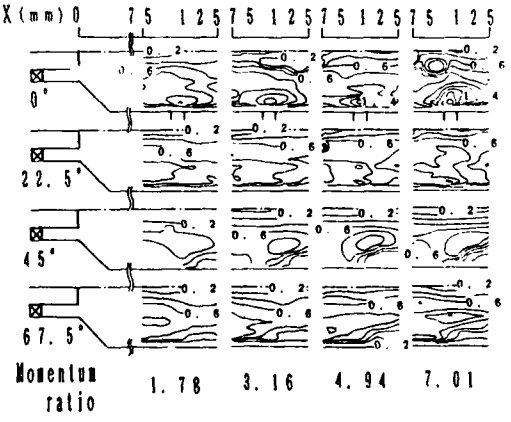

Fig. 5 Tangential velocity contures in the interfering area

The characteristics of the swirling flow in the blocking area were made clear and then the size of the blocking area and the flow from the swirler was investigated. The results are shown in Fig. 6. In the plane of the jet ports (X=100 mm),there are two peaks in the axial velocity profiles. The peak near the center, formed by the jet flows became high with increasing of the momentum ratio while the peaks near the wall was negligibly affected by the change of the momentum ratio. This means that the near-wall axial velocity peak shows the flow from the swirler avoiding the blocking area. The hollows between two peaks correspond to the outline of the blocking area. The position of the hollow did not move on each plane even when the momentum ratio changed, which means that the blocking area is almost fixed in spite of momentum ratio.

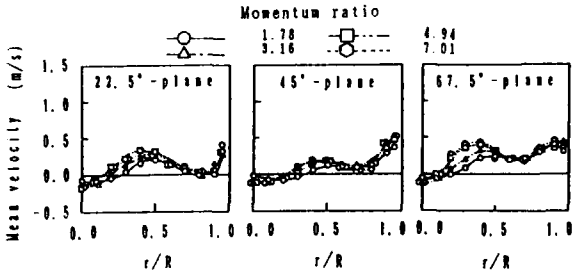

Fig. 6 Axial velocity profiles at X = 100 mm

With flowing downstream and in the swirling direction the hollow come near to center, which make clear the form of the blocking area as shown in Fig. 7. The blocking area formed by the jets have strong tangential velocity and is not axisymmetrical. The flow from the swirler passes through the restricted area, and the axial velocity is accelerated. There are turbulent shear layers in the axial and tangential directions along the outline of the blocking area.

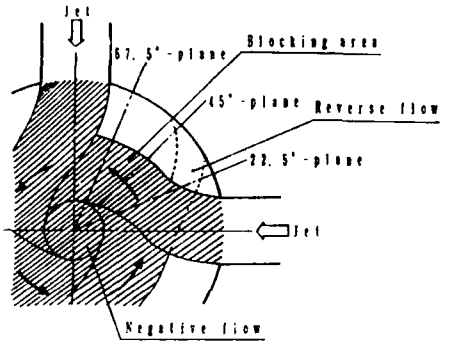

Fig. 7 Illustration of the blocking area

3.3 Turbulence energy

Strong turbulence was generated in the collision region of the jets and in the interaction region between the blocking area and the flow from the swirler. Detail information about this turbulence is important not only to make clear the mixing characteristics of the jet flows and the flow from the swirler, but also to know flow structure which dominates the flow field.

The maximum of the turbulence energy was located in the center of the radius of test section shown in Fig. 8. The region of the maximum intensity corresponds to the jets collision area and the turbulent shear layer in the outline of the blocking area. The high turbulence energy region was almost isotropic in the case of the momentum ratio of 1.78. In this condition, the turbulence was governed by the collision of the jets and the turbulence shear flow in the outside of the blocking area. When momentum ratio was high, the tangential turbulence governed the turbulence energy in this region and the high turbulence region shifted toward the center. It means that when momentum ratio is high, the collision and the interaction becomes significant and the turbulence energy become large, but the increasing of the turbulence generated by the collision is larger than that generated by the interference, so that the collision of the jets governed the turbulence in the interfering area.

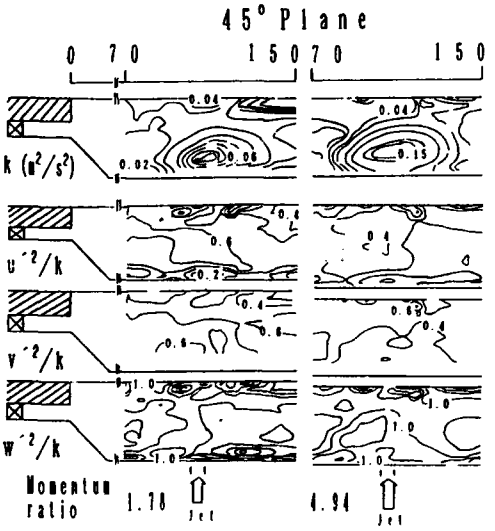

Fig. 8 Turbulence Energy and turbulence rate contours.

4. CONCLUSION

Three-dimensional three velocity components were measured by FLDVs in order to elucidate the interfering flow structure.

The obtained results are summarized as follows:

(1) The jets collided with the neighbor jets and separated into two flows. One of the separated jet flowed upstream along the wall with tangential velocity.

(2) The blocking area was formed by the jets and had strong tangential velocity, which was not axisymmetric. The change of the momentum ratio did not affected the blocking area.

(3) The flow from the swirler avoided the blocking area and passed downstream along the outline of the blocking area where strong turbulence was formed.

(4) An isotropic turbulence area existed in the case of the momentum ratio of 1.78. When the momentum ratio was high, the isotropic area disappeared and the tangential turbulence dominated the flow field due to the strong jet collisions.

REFERENCES

[1] Green, A.S., and Whitelaw, J.H., 1983, Isothermal models of gas-turbine combustors, Journal of Fluid Mechanics, Vol.126, 399.

[2] Ahmed, A.S., and So, R.M.C., 1987, Characteristics of air jets discharging normally into a swirling cross flow, AIAA Journal, Vol.25, No.3, 429-435.

[3] Koutomos, P., and McGuik, J.J., 1989, Investigation of swirler/dilution jet flow split on primary zone flow patterns in a water model can-type combustor.

[4] Richarads, C.D., and Samuelsen, G.S.,1990, The role of primary jet injection on mixing in gas turbine combustion, 23th Symposium on Combustion.

[5] Ikeda, Y., Hosokawa, S., and Nakajima, T., 1990, Flow characteristic measurement in a model gas turbine combustor, 5th International Symposium on Application of Laser Techniques to Fluid Mechanics, 4.5.

[6] Ikeda, Y., Nakajima, T., Hosokawa, S., and Matsumoto, R., 1990, A compact fiber LDV with a perforated beam expander, Measurement Science and Technology, Vol.1, No.3, 260.

IUTAM Symposium on
Aerothermodynamics in Combustors
June 3-5, 1991, Taipei

Numerical computation of the flowfield distribution of a gas turbine combustor

Yunfang Yu. Bin-Quan Zhang

Dept of propulsion Beijing University of Acronautics and Astronautics .P.R.China

Abstrct

Numerical computation method is widely used in the design of most fluid mechanical equipment.But. In comburtors.It is merely in the state of beginning since 1970-1980s. Now.It is just developing in most contries.

This paper is a numerical computational results of the flowfield distribution of a annular combustor.

as you know. The flow parameter of the viscosic fluid chang intensely near the wall of tube, So that. the treatiment of the boundary condition is a very important problem of the solution of the governing equations. Recently. a curvelinear body-fitted coordinate had been dedeveloped.It, needs a transformation of coordinates that transforms a perpendicular coordinate of the calculated region(ξ,η,ζ)as fowllowing.

The initial governing equations in polar-cylinder coordinate.

$$\frac{\partial}{\partial x}(\rho u\varphi)+\frac{1}{r}\frac{\partial}{\partial r}(r\rho v\varphi)=\frac{\partial}{\partial x}\frac{\mu_{ef}}{\sigma_\varphi}\frac{\partial\varphi}{\partial x}+\frac{1}{r}\frac{\partial}{\partial r}(\mu_{ef}/\sigma_\varphi\ \frac{\partial\varphi}{\partial r})+S_\varphi \qquad (1)$$

φ and corresponding τ_φ, $S_\varphi$in following table.

φ	S_φ
1	0
u	$-\frac{\partial P}{\partial x}+\frac{\partial}{\partial x}\mu_{ef}\frac{\partial u}{\partial x}+\frac{1}{r}\frac{\partial}{\partial r}(r\mu_{ef}\frac{\partial v}{\partial x})$
v	$-\frac{\partial P}{\partial x}+\frac{\partial}{\partial x}(\mu_{ef}\frac{\partial u}{\partial r})+\frac{1}{r}\frac{\partial}{\partial r}(r\mu_{ef}\frac{\partial v}{\partial r})-\frac{2\mu_{ef}v}{r^2}+\frac{\rho w^2}{r}$
w	$\frac{\mu_{ef}}{r}\frac{dw}{\partial r}-\frac{1}{r^2}\frac{\partial}{\partial r}(\mu_{ef}rw)-\frac{\rho vw}{r}$
K	$G_K-\rho\varepsilon$
ε	$(C_1\varepsilon/_K-C_2\rho\varepsilon^2)/K$

$$\mu_{ef}=\mu+\mu_t \quad and \quad G_K=\mu_t[2(\frac{\partial u}{\partial x})^2+2(\frac{\partial v}{\partial r})^2+2(\frac{v}{r})^2+(\frac{\partial u}{\partial r}+\partial v/\partial x\ )^2+(\frac{\partial w}{\partial x})^2+(r\frac{\partial w}{\partial r\cdot r})^2] \qquad (2)$$

The transformation equation is

$$q_1(x_{\xi\xi}+FX_\xi)-2q_2X_{\xi\eta}+q_{23}(X_{\eta\eta}+GX_\eta)=0 \qquad (3)$$

$$q_1(r_{\xi\xi}+Fr_\xi)-2q_2r_{\xi\eta}+q_3(r_{\eta\eta}+Gr_\eta)=0 \qquad (4)$$

where

$$F=-(X_\xi X_{\xi\xi}+r_\xi r_{\xi\xi})/(X_\xi^2+r_\xi^2) \qquad (5)$$

$$G=-(X_\eta X_{\eta\eta}+r_\eta r_{\eta\eta})/(X_\eta^2+r_\eta^2) \qquad (6)$$

$$q_1=X_\eta^2+r_\eta^2 \qquad (7)$$

$$q_2=X_\xi X_\eta+r_\xi r_\eta \qquad (8)$$

$$q_3=X_\xi^2+r_\xi^2 \qquad (9)$$

Then the final equation becomes.

$$\frac{\partial}{\partial\xi}(r\rho U\varphi)+\frac{\partial}{\partial\eta}(r\rho V\varphi)=\frac{\partial}{\partial\xi}[\frac{r\Gamma}{J}(q_1\varphi_\xi-q_2\varphi_\eta)]+\frac{\partial}{\partial\eta}[r\Gamma/J\ \ (-q_2\varphi_\xi+q_3\varphi_\eta)]+S(x,r)\cdot r\cdot J \qquad (10)$$

Where $U=ur_\eta-vX_\eta$ (11)

$$V=vX_\xi-ur_\xi \qquad (12)$$

$$J=X_\xi r_\eta-X_\eta r_\xi \qquad (13)$$

$$\Gamma=\frac{\mu_{ef}}{\sigma_\varphi} \qquad (14)$$

Fig1 is the typical example of curvelinear body-fitted grid.

Besides, Some calculated results of the gas phase flowfield distribution in an annular combustor had been done, one with swirl (By vane swirler angle $\theta=50°$), and another without swirl ($\theta=0°$).

Fig2 shows the calculated velocitg vectors distribution, you can see that a recirculation zone located near the wall of combustor in noswirl condition. and its length is quite long. But in the swirl flow condition. This boundary recirclation zone dissappearcs and a strong center recirculation zone

appcares instead.

Fig3 is the axial veloity contour. you can see, There is a large velocity gradiant over the place where the contour liness crowd together, It induces to produce a strong turbulent mixing between air and fuel drops or vapour. because it is inside of primary zone–initiation of combustion. So it is a very useful factor for the combustion and flame spreading.

Fig4 is the pressure contour. Obviously The pressure chang is almost along the axis direction only.

Fig5 is the stream line distributron. It Shows the axisting of the center recirclation zone more obviosly near the axis. Some experiment datas had been plotted in it, you can see, The experiment size of the center recirculation zone is lager than the calculated result. Perhaps it is due to the selection of the turbulence model.

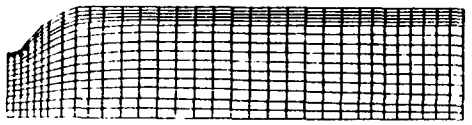

Fig 1

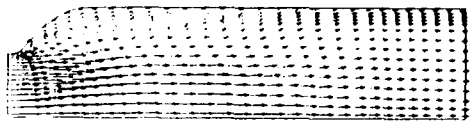

a) $\theta=0$

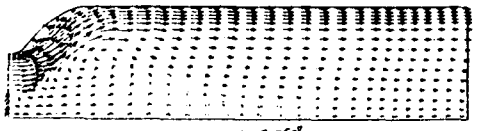

Fig 2 b) $\theta=50^{\circ}$

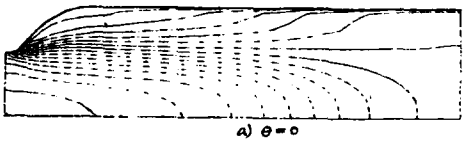

a) $\theta=0$

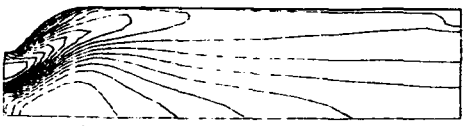

Fig 3 b) $\theta=50$

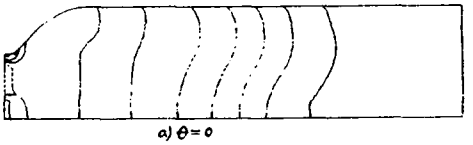

a) $\theta=0$

Fig 4 b) $\theta=50$

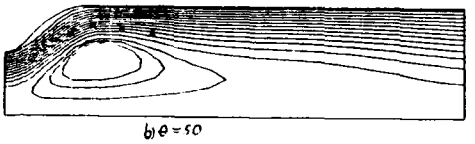

b) $\theta=50$

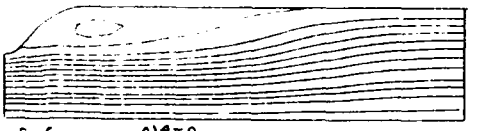

Fig 5 a) $\theta=0$

IUTAM Symposium on
Aerothermodynamics in Combustors
June 3-5, 1991, Taipei

Investigation of the atomization of a fuel / air injector.

Bin-Quan Zhang

Dept of propulsion, Beijing University of Aeronautics and Astronautics.P.R.China

Abstract

In usual fuel injectors. The liquid fuel is atomized by the supply pressure of the fuel system. Its major drawback is that the control of the atomization and the flow rate of the fuel supply both are accomplished by the same parameter-supply pressure only. In the low flow rate condition, especially in the high altitude of flight. the fineness of the atomization will become worse. The. It induces the Combustion performances decrease.

A development of the injector is airblast injector. it can provide good atomization than the usual injector over the entire range of fuel flowrate. But the basic drawback of this injector is its limited size of the injector. In the other words the limited path of the air restricts the avaliable range of the parameters of the atomization air-flow rate and pressure drop of the air.

This paper is a investigation of the atomization of the liguid fuel in a fuel / air injertor like fig,1. It includs a usual injector in front of the flametube. The liguid fuel jets from the injertor into a cylindrical tube which is in line with the center line of the primary zone of flametube. and mix with the air *which flow in the tube surrounding* the injector. Thus, a two phase mixtare of fuel and air is formed in the tube. and it flows downstream. At the end of the tube, it turns 90 degree and emergs from the annular canal near the bottom of the tube. then flows into two recirculation zones in the primary zone of flametube.

Test facilities are shown in fig2. The test seetion is a plexi-glass model of the primary zone of a flametube. Thus the test can modell the full atomization process, at the same time. we can obtain the flow and atomization pattern visualization results. A laser device was used to measure the degree of fineness of atomization and Sauter mean diameters of the fuel drops.

A series of experiment results show that this fuel / air injoctor device retains the main advantage of the airblast injector - good fineness of atomization over the entire work conditions of the injector, even in very small supply pressure (0.5 ata). its typical diameter is about 40-60 μm. as you know, a usual injector cannot gives so good finenes under very low supply pressure like this. Besides, the air canal of this device can spread the avaliable range of the regulation of fuel atomization, without the requirement of high supply pressure or high velocity of the air.

Fig3 is the typical experiment result. you can obtain very small fuel drop even under very low supply pressure of the fuel. as you know, a usual mean drop size of a general injector is about 100μm under standard work condition. Besides, Increasing the velocity of the inlet air v_a in front of the flametube can decreasre the drop size.

Fig4 is shown the effect of chang of width of the annular canal on the fuel drop size, Obviously, small width can produce the narrow and small path of the air passing through the annular canal. then. the outlet velocity of the air is higher than the large width, so the entrainment of the fuel by the air is more strong and it produces small fuel drops.

We changed the form of flange of the disk, it forms a turn-angle θ. we obtained a experiment result for the fuel drop size in different value of θ. See Fig5. Inereasing the value θ. That means the inereasing of the resistance of the air which flow out from the annular canal. and the velocity of it. So the drop size inereases.

At last. From the visualisation of the model. the full pattern and machanism of the atomization of this injector device can be derived following.

In the first stage, the fuel jets out from the injector, and form a initial atomization distribution in the cylindrical tube. then it flows down with the airstream which flowout the annular canal.

Near the outlet and of the cylindrical tube beeause a lot of the fuel drops impact on the inner surface of the tube. then they form a fuel film. In the flange part of the disk there is another fuel film formed. when the air flow out the annular canal. It entrains the fuel films slipping away from the flanges of the anular canal. then they form a secendary atomization process in the primary zone. From the total process of the

fuel atomization. it is a more important and decisive process of the full atomization proces. See Fig6.

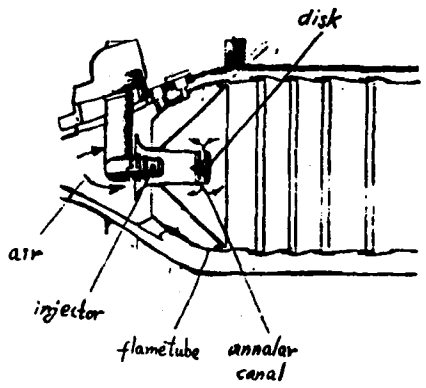

Fig 1

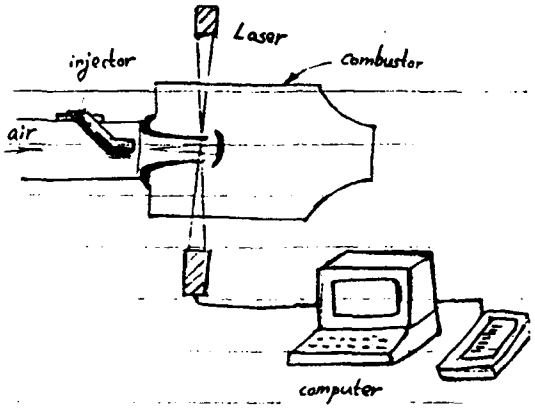

Fig 2

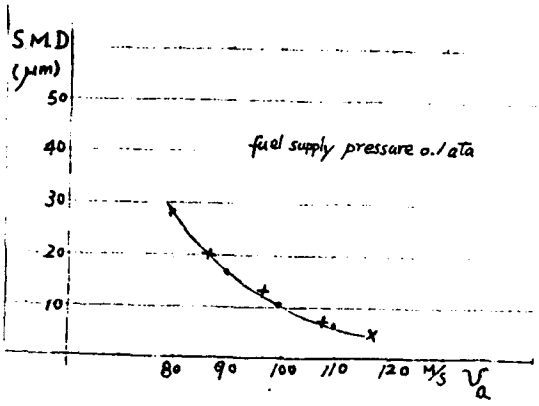

Fig 3

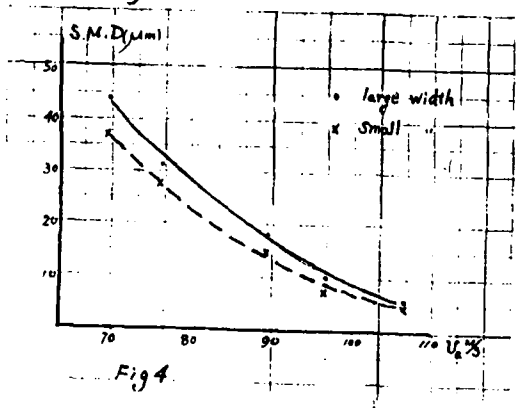

Fig 4

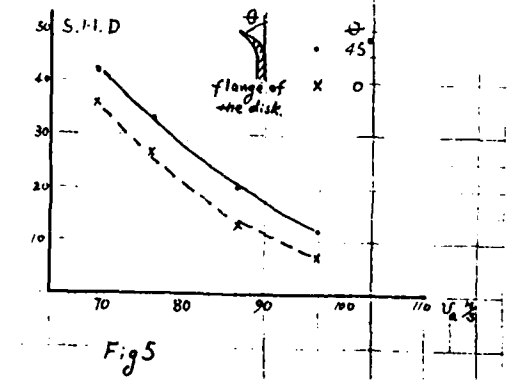

Fig 5

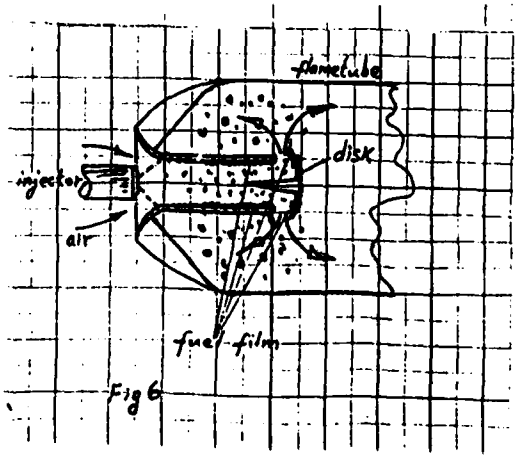

Fig 6

IUTAM Symposium on
Aerothermodynamics in Combustors
June 3-5, 1991, Taipei

SCALAR CHARACTERISTICS OF A LIQUID-FUELLED COMBUSTOR WITH CURVED EXIT NOZZLE

S.K. CHOW AND J.H. WHITELAW

IMPERIAL COLLEGE OF SCIENCE, TECHNOLOGY AND MEDICINE
DEPARTMENT OF MECHANICAL ENGINEERING, FLUIDS SECTION
EXHIBITION ROAD, LONDON SW7 2BX, ENGLAND

1. INTRODUCTION

This investigation was carried out to improve understanding of the processes which determine the performance of a model of a reverse-flow annular combustor of the type used in small gas turbines. The model combustor incoporated a T-vaporiser for fuel supply, Sotheran (1984), and air supplied through dilution holes and film-cooling slots.

Chow, Senda and Whitelaw (1989) measured the scalar characteristics of a similar model combustor, but without the curved exit nozzle, representing the primary and dilution zone only with preheated air, at 515K, and kerosene as fuel and the same experimental conditions were employed in this study. The extent to which the nozzle influenced the combustion characteristics within the combustor were examined by comparing results measured in configurations with and without the exit nozzle.

The following section provides a brief description of the geometry of the combustor and instrumentation with consideration of experimental uncertainties. Results are presented and discussed in Section 3 and summary conclusions are stated in the final section.

2. FLOW CONFIGURATION AND INSTRUMENTATION

Air at near atmospheric pressure and 515K was supplied to the combustor with fuel delivered through an airblast atomiser comprising two coaxial metal tubes with inner diameters of 0.5mm and 4mm. The air flow through the vaporiser was the minimum required to vaporise the spray and led to an air-fuel-ratio of 2 for the mixture emerged from the vaporiser. Overall air-fuel ratios were 36 and 60 corresponding to the take-off and ground-idle conditions respectively for the Gem-60 engine with the mass flow rates scaled according to the parameter $mT^{1/2}/AP$, where m is the mass flow rate, T is the temperature, P is the pressure at the inlet to the combustor and A is the cross-sectional area of the combustor.

The geometry of the model combustor is shown in Figure 1. It consists of nine film-cooling slots, a set of five primary holes located on the lower wall with two in line with the vaporiser exits and two sets of dilution holes staggered by a half pitch with respect to the primary holes. The first set of four dilution holes is located on the upper wall and the second set of two on the lower wall.

Temperature measurements were obtained with thermocouples made from 80 μm platinum / 13% rhodium and platinum wires. The temperature signal was amplified, digitised and processed in a microcomputer. The uncertainties in the temperature measurements due to conduction and radiation were found to be less than 0.1% and around 5% respectively. The results are close to unweighted mean values as suggested by Toral and Whitelaw (1982) and the comparatively low gas velocities imply that the thermocouple outputs are related to the local static temperature.

Gas samples were extracted through a stainless-steel water-cooled probe with outside and inside diameters of 8.0 and 1.0mm respectively. The sample was sucked through the probe by a pump and passed through to the infrared gas analysers (for CO and CO_2), paramagnetic analyser (for O_2) and flame ionisation detector (for UHC). Uncertainties in the measurement of the various gas concentrations were less than ± 0.5% of the full scale of each analyser and the uncertainty of each gas concentration, associated with sample handling, should be less than 10% of the maximum concentration as suggested by Heitor and Whitelaw (1986) and the measured concentrations of major species are expected to be close to density-weighted averages.

3. RESULTS AND DISCUSSION

The distributions of measured temperature, and the corresponding enthalpy balance temperature, are shown in Figure 2 and 3 for air-fuel ratios of 60 and 36 respectively. In both cases, high temperature regions were found close to the inner wall of the curved exit nozzle with maxima of 1350K and 1650K for the two air-fuel ratios. The enthalpy balance temperatures were generally about 50 to 100K

lower than the measured ones which is in accordance with the finding of Chow, Senda and Whitelaw (1989). The calculated pattern factors, based on 78% of the area of the exit plane, are 0.22 and 0.18 for air-fuel ratios of 60 and 36 respectively.

Figure 4 shows the distributions of major species concentrations, on a wet basis, and calculated equivalence ratio for the air-fuel ratio of 60. The maximum equivalence ratios, above 0.3, were found close to the inner wall of the curved bend and the equivalence ratios at the outer bend were generally about 0.2. No distinct hot zone was observed across the width of the exit plane and maximum levels of UHC and CO were 0.006 (mole fraction of $C_{12}H_{26}$) and 0.15% respectively. This corresponded to emission indices of CO and UHC of 50 and 5 respectively which led to a combustion efficiency of 98.3%.

The species-concentration distributions for the air-fuel ratio of 36 are shown in Figure 5. The fuel rich regions, with maximum equivalence ratios of 0.43, remained close to the inner wall as in the case for the higher air-fuel ratio. Maximum levels of UHC and CO increased to 0.009 and 0.18% respectively. Compared to the higher air-fuel ratio condition, the emission indices of CO and UHC increased to 68 and 6 respectively and a slight decrease in combustion efficiency to 97.8% resulted. The performance of the combustor with the curved exit nozzle in terms of combustion efficiency, emission indices of CO and UHC and pattern factor is also shown in Table 1.

The distributions of species concentrations at the exit of the curved nozzle of Figure 4 and 5 for the two air-fuel ratios are compared with those at the exit of the combustor without the nozzle to quantify the effect of the nozzle to the combustion processes. For ground-idle condition, the maximum value of equivalence ratio decreased from 0.42, at the entry to the nozzle, to 0.3, at the exit, due to the additional air from the cooling slots inside the curved nozzle. The two distinct hot zones at the entry disappeared at the exit due to the intense mixing within the nozzle caused by the severe contraction in cross-sectional area (the area ratio between the entry and the exit is 4.25). The high concentrations of fuel at the outer half of the combustor were pushed to regions near the inner wall due, in part, to the secondary flow inside the bend. Moreover, the fluid near the outer wall was diluted by the air coming out from the three film-cooling slots at the outer wall of the nozzle.

The average concentrations of UHC and CO dropped from 0.009 to 0.006% and from 0.18 to 0.12% respectively within the bend in the ground-idle condition. Taking into account the dilution by the extra air, which was about 40% of that coming into the combustor in further upstream regions, from the cooling slots within the bend, the absolute amount of CO and UHC actually decreased by very little inside the bend. Therefore, it can be concluded that the fuel and CO burn-up process almost ceased at the entry of the bend. This is because the temperature in regions of high concentrations of CO and UHC was below 1400K which is the kinetic limit on fuel and CO burn-up rate as suggested by Levebvre (1983).

For take-off condition, the average concentrations of UHC and CO dropped from 0.04 to 0.007% and 0.8 to 0.15% respectively. Contrary to the higher air-fuel ratio condition, the combustion processes continued beyond the entry of the curved bend and the fuel breakup and CO to CO2 conversion took place as a result of the higher temperature, about 1800K, at that plane since the kinetic limitation of the fuel and CO burn-up were overcome.

4. CONCLUSION

The main conclusions can be summarised by the following paragraphs:

1. For take-off condition, air-fuel ratio of 36, combustion processes continued beyond the entry to the curved nozzle led to lower emission indices of CO and UHC of 68 and 6 and a better combustion efficiency of 97.8% , as compared to the entry of the nozzle, at the exit of the nozzle.

2. An increase in air-fuel ratio from 36 to 60 resulted in an increase in pattern factor from 0.18 to 0.22 and in combustion efficiency from 97.8% to 98.3% at the exit of the nozzle.

ACKNOWLEDGEMENT

The authors would like to acknowledge the financial support from the Procurement Executive of the Ministry of Defence. They, and the paper, have benefitted from many useful discussions with colleagues at Rolls Royce, the Royal Aircraft Establishment at Pyestock and Imperial College.

REFERENCE

1. Chow, S.K., Senda, M. and Whitelaw, J.H. (1989), "Combustion Characteristics of a Liquid-Fuelled Model Annular Combustor", presented at the Ninth International Symposium on Air Breathing Engine, Athens.

2. Heitor, M.V. and Whitelaw, J.H. (1986), "Velocity, Temperature and Species Characteristics of the Flow in a Gas Turbine Combustor", *Comb. and Flame*, 64, 1-32.

3. Lefebvre, A.H. (1983), Gas Turbine Combustion, McGraw Hill text book.

4. Sotheran, A. (1984), "The Rolls Royce Annular Vaporiser Combustor", *J. Engng for Gas Turbines and Power*, 106, 88.

5. Toral, H. and Whitelaw, J.H. (1982), "Velocity and Scalar Characteristics of the Isothermal and Combusting Flows in a Combustor Sector Rig", *Comb. and Flame*, 45, 251.

Table 1

Air-fuel ratio	Pattern factor	EI_{CO} (g/kg fuel)	EI_{UHC} (g/kg fuel)	Combustion efficiency (%)
36	0.18	68	6	97.8
60	0.22	50	5	98.3

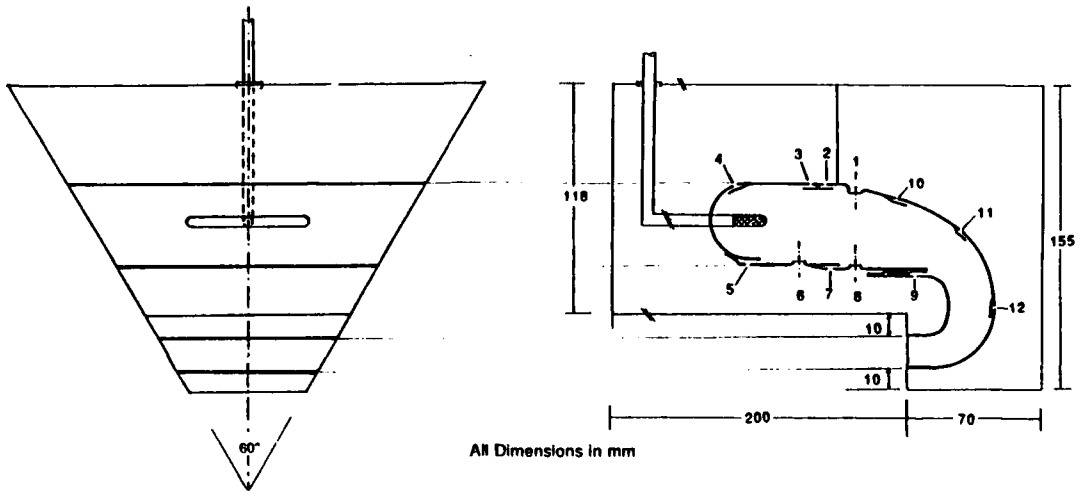

Figure 1 Combustor Geometry

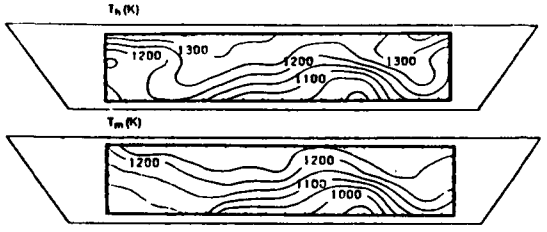

Figure 2 Measured and Enthalpy Balance Temperature in the Exit Plane for Air-Fuel Ratio of 60

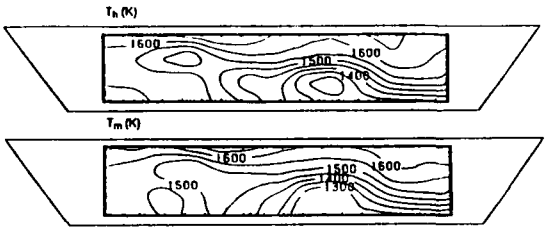

Figure 3 Measured and Enthalpy Balance Temperature in the Exit Plane for Air-Fuel Ratio of 36

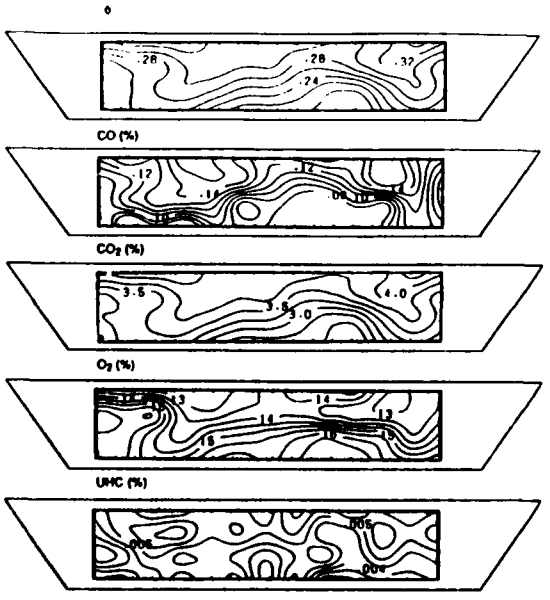

Figure 4 Distributions of Major Species Concentrations in the Exit Plane for Air-Fuel Ratio of 60

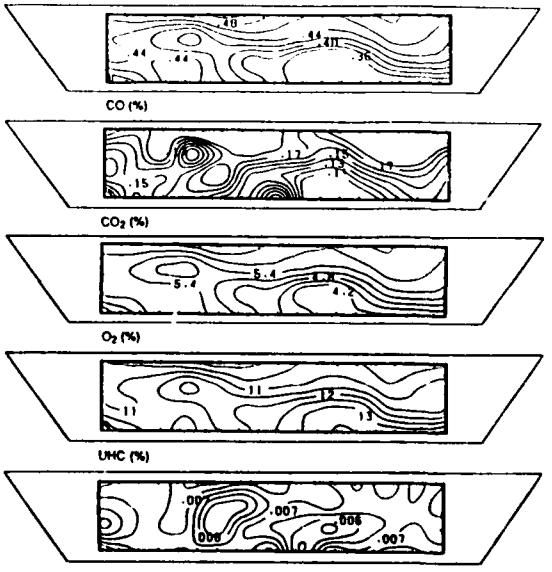

Figure 5 Distributions of Major Species Concentrations in the Exit Plane for Air-Fuel Ratio of 36

IUTAM Symposium on
Aerothermodynamics in Combustors
June 3-5, 1991, Taipei

STRUCTURE OF THE PRIMARY REGION OF A MODEL GAS TURBINE COMBUSTOR

Sunao NAKAMURA
Engineering Research Center, NKK Corporation

Katsuya HYODO
Nippon Telegraph and Telephone Corporation

Osamu KAWAGUCHI
Faculty of Science and Technology, Keio University

INTRODUCTION

Detailed data in the combution region of a gas turbine combustor have been obtained by using a model combustor to interpret the structure of combustion region. In the previous work the effects of secondary air on the exhaust emissions have been verified[1][2]. The authors report here the profile of gas flow, temperature and gas composition in the combustor for various operating conditions and discuss on the structure of the combustion region.

MODEL COMBUSTOR

The model combustor used for the experiments is shown in the Fig. 1. It is a can-type straight flow combustor with a liner of 125 mm in diameter and 350 mm in length. A peeping window with a quartz glass is provided at the liner wall to pass laser beams for velocity measurements. The downstream side is open to the atmosphere.

The combustion air is supplied through the annular path after passing through the swirl generator to give a settled swirl strength. Pure propane for industrial use (97% purity) is injected at the injection angle of 90 degrees from the multi-hole injector with 24 holes.

MEASUREMENTS

The laser doppler anemometry using a two-beam back scattering type optical system has been used to measure the flow in the combustion region. The beams from a 25 mW He-Ne laser pass through the quartz window of the liner. MgO particles less than 2 um in diameter were introduced directly to the combustion region as the scattering particles with a stainless tube of 2 mm in outer diameter.

The gas temperature was measured by a silica coated Pt/Pt-Rh13% thermocouple of 50 um in original diameter, which was inserted from the downstream of the combustor. Correction of the error of measured values was not made.

The combustion gas was sampled with a water-cooled stainless steel probe and analyzed by a gas chromatograph.

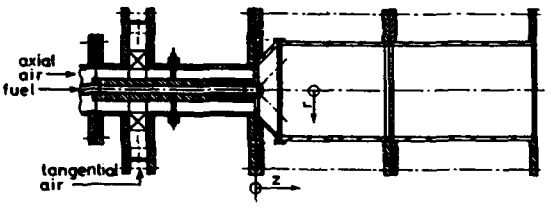

Fig. 1 Model combustor

Experimental parameters adopted were the amount of mass flow of combustion air, Ma (kg/s), the swirl number of combustion air, S, and the air/fuel ratio, Ma/Mf. The standard condition was fixed to Ma = 27×10^{-3} kg/s (reference velocity at inlet condition U = 3.15 m/s), S = 1.0 and Ma/Mf = 15.7.

EXPERIMENTAL RESULTS

3.1 Effects of Swirl Strength

Figure 2 shows the stream lines for three different swirl numbers. The stream lines are expressed by using the normalized stream function.

At the standard condition a recirculation zone (R. Z.) is developed in the combustion region and a stabilized flame is formed. The amount of recirculating gas is 7 to 9 % of the total mass flow. The radial position of the outer boundary of the R. Z. is 0.85 in r/R, and the downstream position of R. Z. is 0.9 in z/D.

On taking notice of the effects of swirl strength, the R. Z. is formed in the downstream region near the fuel injector at the swirl number larger than 0.6. With increase in the swirl number the vortex center shifts to the outer side and downstream side due to the increase of angular momentum of combustion gas. The size of R. Z. grows as the swirl number increases and at S = 1.5 it becomes 1.5 times compared with that at S = 0.7.

Figure 3 indicates the isothermal lines in the combustion region for three different swirl conditions. It can be inferred from the figures that the flame expands outside and shifts to the upstream. At this range of swirl strength, however, since a recirculation zone develops sufficiently near the fuel injector, the temperature profiles do not

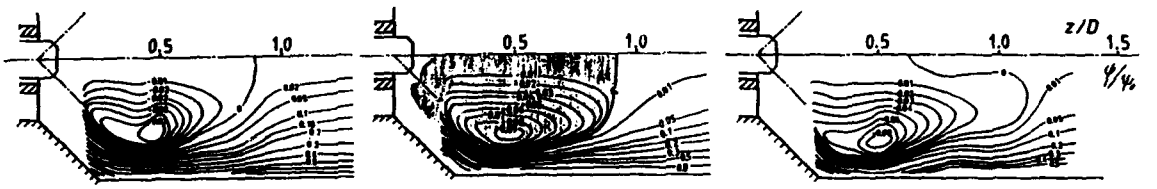

(a) S = 0.7 (b) S = 1.0 (c) S = 1.5

Fig. 2 Stream lines for various swirl numbers

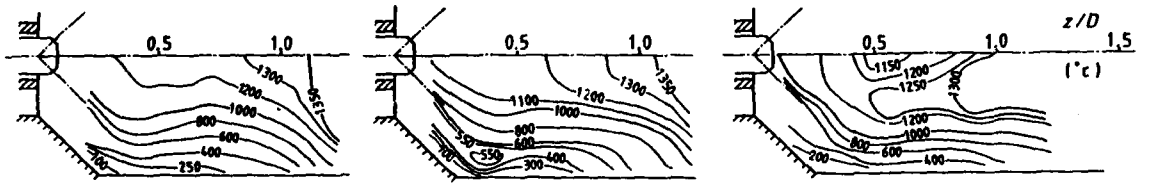

(a) S = 0.7 (b) S = 1.0 (c) S = 1.5

Fig. 3 Isothermal lines for various swirl numbers

differ so much each other and a high temperature zone exists near the injector.

The profiles of the axial component of flow velocity and its fluctuation at the cross section of z/D=0.4, where is the center of R. Z., are indicated in Fig. 4. There exist no large differences of velocity according to the swirl conditions but, on increasing the swirl strength, the reverse flow zone expands outside and the velocity gradient in the main stream region increases. The velocity fluctuation becomes less at the reverse flow zone with the swirl increase but in the forward flow zone it tends to increase. The tangential velocity component becomes high at every radial position with a swirl increase, as a matter of course.

From these experimental results, the volume of R. Z. grows with a swirl increase and the axial velocity in the main stream flowing downstream around the R. Z. increases. As the results, the fuel injected to a high swirl air flow cannot penetrate the main stream and most of the fuel flows downstream with the main stream and consequently, an excessive swirl lowers the combustion efficiency. The temperature in the R. Z., however, rises with swirl increase because the residence time in the R. Z. increases due to the increase of tangential velocity component (which was verified by measurement[2]) and

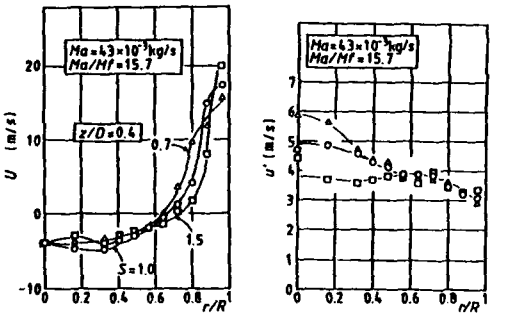

(a) Axial velocity (b) Velocity fluctuation

Fig. 4 Axial velocity distributions for various swirl numbers

chemical reactions in the zone progress sufficiently.

3.2 Effects of Air/Fuel Ratio

Figure 5 indicates the stream lines of the combustion region for three different air/fuel ratio conditions.

On increasing the air/fuel ratio from 15.7 to 26.2, the length of the R. Z. becomes short, but at a very lean condition of Ma/Mf=52.3 the flame expands as a cup-like shape and the length of R. Z. increases and nears that of the cold flow.

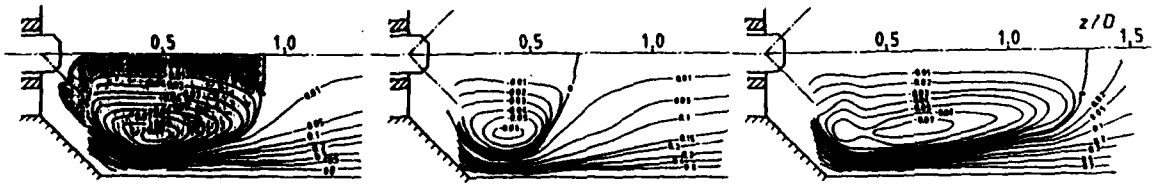

(a) Ma/Mf = 15.7 (b) Ma/Mf = 26.2 (c) Ma/Mf = 52.3

Fig. 5 Stream lines for various air/fuel ratios

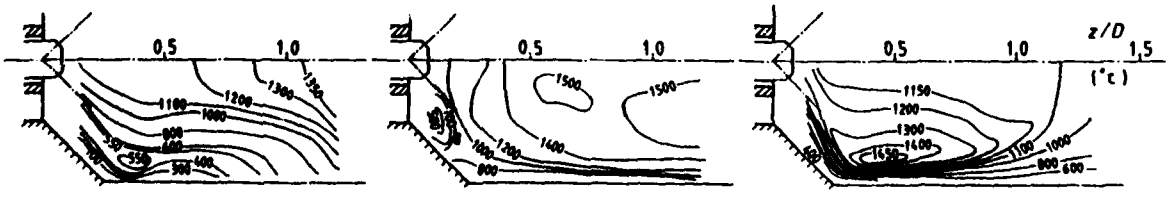

(a) Ma/Mf = 15.7 (b) Ma/Mf = 26.2 (c) Ma/Mf = 52.3

Fig. 6 Isothermal lines for various air/fuel ratios

The isothermal lines are indicated in Fig. 6 for three different air/fuel conditions. At the leaner condition, Ma/Mf = 26.2, compared with the standard, since the fuel injected diffuses immediately into the air flow and reacts rapidly, the temperature rises in the upstream region. The temperature inside the R. Z. reaches 1500 °C. At the leaner condition, Ma/Mf = 52.3, the temperature becomes high along the flame expanding like a cup-shape but it lowers in the R. Z, whose length becomes longer as the results.

The axial velocity component and its fluctuation at the cross section of z/D = 0.4 are shown in Fig. 7 for three different air/fuel ratio conditions.

The axial velocity presents about the same value for all air/fuel ratios but the fluctuation increases more at the leaner condition. The tangential velocity component does not change so much due to the change of air/fuel ratio but at an extremely lean condition the velocity and its fluctuation decrease because of less heat release.

3.3 Flow Lines of Each Gas Component

Mass flow of each gas component can be obtained from the velocity, temperature and gas composition data by using the same calculating process as the stream function. Mass flow lines of C_3H_8 and O_2 are indicated in Fig. 8 for the standard condition. The shaded area indicates the R. Z. obtained from the stream lines.

Mass exchange by eddy diffusion comes into existence at the shear flow region between the R. Z. and the main stream region. The boundary of R. Z. of oxygen flow exists inside the R. Z. boundary of the overall gas flow, which is due to the oxygen supply from the main flow to R. Z. Propane expands to some extent by the existence of R. Z. and, after reaching near the liner wall, seems to diffuse into the combustion gas flow. There exists propane of fairly high concentration in the upstream of the main stream, and chemical reactions producing CO and CO_2 seem to occur to a certain extent in the upstream. At the stoichiometric air/fuel ratio condition, fair amount of CO is sampled in the gas flowing at the downstream of the main combustion region, which means that the chemical reactions are not completed only around the R. Z.

3.4 Flame Stabilizing Mechanism

The enthalpy flow rate across the cross section of the R. Z. which passes the vortex center was estimated from the measured values of flow velocity and gas temperature. The enthalpy flows in the backward and forward direction following to the gas flow in the R. Z.

Due to calculations based on the experimental results the backward enthalpy flow exceeds the forward one. The difference between the two is equivalent to the heat supplied to the main combustible gas stream to ignite and react it.

Both the forward and backward enthalpy flows increase with the increase of swirl number from 0.7 to 1.5 and also

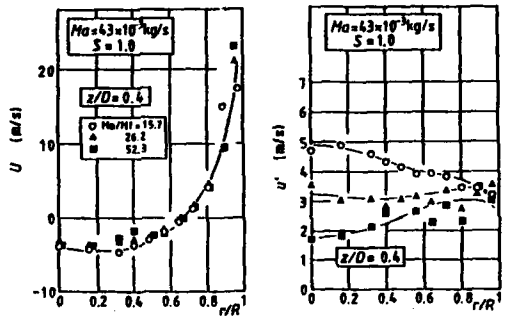

(a) Axial velocity (b) Velocity fluctuation

Fig. 7 Axial velocity distributions for various air/fuel ratios

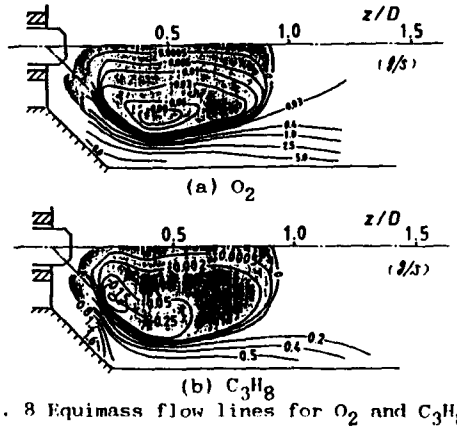

(a) O_2

(b) C_3H_8

Fig. 8 Equimass flow lines for O_2 and C_3H_8

the difference of the two increases from 2.6 to 4.3 % of the heating value of supplied fuel. It means that the air swirl contributes to flame stabilization at the combustion region.

When the air/fuel ratio is decreased to 52.3, the backward enthalpy flow in the recirculation zone decreases but the forward one changes little. As the results, the difference of the two decreases with air/fuel ratio decrease but the relative quantity normalized by the supplied heating value is kept almost constant to stabilize the flame.

CONCLUSION

Detailed measurements of temperature, velocity and gas composition in the combustion region of a model combustor were conducted and following results has been obtained.

(1) The size, shape and velocity distribution of a recirculation zone depend on the air swirl and air/fuel ratio.

(2) At a stable combustion condition, a fuel jet with suitable penetration reaches near the liner wall and diffuse in the air flow and reacts to form a high temperature region in the upstream.

(3) The enthalpy supplied to the main flow from the recirculation zone contributes to the flame stabilization.

REFERENCES

(1) Nakamura, S. et al., Proc. 1983 Tokyo Gas Turbine Congress, Vol.1.

(2) Nakamura, S. et al., Journal of GTSJ, Vol. 10-37 (1982) (in Japanese)

IUTAM Symposium on
Aerothermodynamics in Combustors
June 3-5, 1991, Taipei

Development of Gas Turbine Combustors for Low BTU Gas

I. Fukue, S. Mandai and M. Inada

1. INTRODUCTION

Large-capacity combined cycles with high-temperature gas turbines burning petroleum fuel or LNG have already been operated in large numbers in both domestic and foreign countries and have achieved good results. On the other hand, as the power generation technology utilizing coal burning the coal gasification combined plants are also under research. Since coal-gasified gas is lower in BTU and harder to burn than conventional fuel, development of this combustor is one of the important problems to be solved. To develop the combustor burning low BTU gas in our company, we have proceeded the study for blast furnace gas, i.e. by-product gas in the ironworks and have succeeded in practical use of the multi-can type combustor burning low BTU gas in the combined plant supplied to Chiba Works, Kawasaki Steel Corporation.

The following technical problems for this combustor have been overcome, and through the demonstration tests with actual gas the combustor has been made fit for practical use:

(1) Development of multi-can type combustor for large-capacity gas turbine
(2) Wide-range stable combustion technology by means of air by-pass mechanism
(3) Combustor cooling construction of high efficiency

This paper introduces the combustion technology obtained through development of the above combustor burning low BTU gas.

2. DEVELOPMENT OF COMBUSTOR

2.1 Development of Multi-Cannular Type Gas Turbine Combustor Burning Low BTU Gas

Recently in the ironworks most of the externally-dependent energy sources are covered by coal. This coal energy is converted to such various kinds of by-product gas as blast furnace gas, coke oven gas, converter gas, etc. in the processes where coal is used in iron-manufacturing processes. Table 1 shows the typical composition of by-product gas, combustion velocity as an index of the combustion quality (laminar flow maximum combustion velocity) and the combustible range. In the table also the values of LNG, i.e. typical high BTU fuel, are shown for the purpose of comparison.

Among the above product gas, since blast furnace gas contains plenty of inert gas in spite of its abundant product volume, its calorific value is as low as 600-800kcal/Nm³, and moreover it is remarkably poor in combustion quality. Therefore, its application was limited to such combustion equipment of relatively-low combustion load rates as boilers and so on.

Table 1 Typical composition and combustion quality of by-product gas

		Blast furnace gas	Converter gas	Coke oven gas	Methane (for ref.)
Component (Vol %)	H_2	1.9	1.9	52.8	-
	CO	19.2	61.4	5.8	-
	CH_4	-	-	27.8	100
	C_2H_4	-	-	3.8	-
	CO_2	22.1	15.4	1.9	-
	N_2	52.8	17.3	3.9	-
	H_2O	4.0	4.0	4.0	-
Calorific value	(kcal/Nm³)	630	1910	4450	8530
Laminar flow combustion velocity	(cm/sec)	~ 0	56	72	37
Combustible range (Air ratio)	Rich	0.84	0.28	0.46	0.54
	Lean	1.32	2.78	3.70	1.79
	Lean/Rich	1.6	9.9	8.0	3.3

On the other hand, in West Europe, U.S.A. and Japan, after World War II it was tried to apply blast furnace gas to gas turbine fuel. Several gas turbines burning blast furnace gas were constructed and put in practical use. However, in many of them, because of the low combustion quality of blast furnace gas large combustors of the single cylinder type with low combustion load rates were arranged.

Fig.1 shows the cross section of the 20,000kW class gas turbine burning blast furnace gas. In addition the cross section of the same class multi-cannular type gas turbine is shown for the purpose of comparison. The conventional gas turbine burning blast furnace gas was so designed that the combustor diameter was increased to lower the combustion load rate and its length was increased to lengthen the staying time of combustion gas. Thus, the size of the combustor became large and nearly equal to that of the turbine main body as shown in Fig.1.

For temperature increasing for the purpose of increasing the efficiency of the gas turbine proper or the combined efficiency for combination with the steam turbine, the gas turbine inlet temperature was limited to about 1000°C from the viewpoint of the combustion technology due to the low BTU of blast furnace gas and of the cooling technology of the scroll that guides combustion gas to the turbine.

Further, for capacity increasing of the gas turbine, two or more sets of the large combustors nearly-equal in size to the gas turbine proper are required as mentioned above, when they are designed with the combustion load rates equivalent to the conventional experience values. It is difficult realistically to materialize this from the viewpoint of their arrangement and so on.

In the above background it was indispensable in applying blast furnace gas to large-capacity high-temperature gas turbines to develop such compact multi-cannular type combustors as conventional ones used for high BTU fuel. For this purpose it was required to improve the combustion characteristics by increasing the BTU of blast

furnace gas and by increasing the turbine inlet temperature. Then, application of high BTU by-product gas in the ironworks was considered to this BTU increasing purpose. Coke oven gas or converter gas could be used for this purpose, but it was important to limit its use rate as low as possible because of the energy balance in the ironworks.

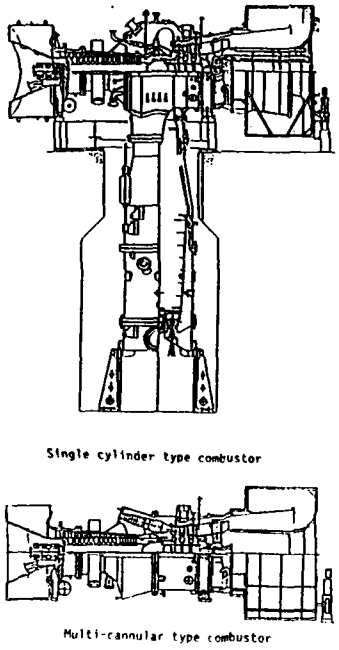

Fig.1 Cross section of gas turbine burning blast furnace gas

Fig.2 shows the expanding tendency of the combustible range for increased BTU gas when blast furnace gas is mixed with coke oven gas to increase the BTU.

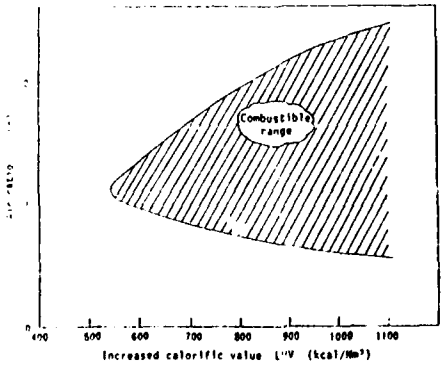

Fig.2 Combustion quality improving effect by increasing BTU of blast furnace gas

As seen in this figure, the BTU should be increased to about 900kcal/Nm³ at least in order to obtain the combustible range equal to that of conventional high BTU gas. (Refer to methane in Table 1.)

The combustible range more than that of natural gas could be obtained by increasing the BTU, because of the high combustion quality effect of coke oven gas. However, since the BTU increasing rate had to be kept as low as possible from the viewpoint of energy balance in the ironworks as mentioned above, it was necessary to overcome the technical problems in designing the combustor as shown below.

2.2 Development of Combustor that can Keep BTU Increase to Required Minimum and Maintain Stable and High Combustion Efficiency in Wide Gas Turbine Operation Range

Fig.3 shows the change of the combustion efficiency versus turbine inlet temperature when blast furnace gas mixed with coke oven gas to increase the BTU is burnt in the multi-cannular type combustor of the normal size.

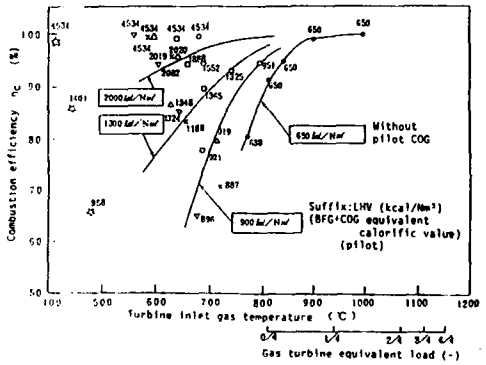

Fig.3 Effect of increased BTU on combustion efficiency

In order to carry out combustion with the stable and high combustion efficiency maintained in all load range of the gas turbine, the BTU had to be increased to about 2,000kcal/Nm³ for the conventional combustor.

Further, we have noticed in Fig.3 that even in combustion of low BTU gas the high combustion efficiency can be attained by maintaining the turbine inlet gas temperature at about 900°C or higher. Thus, we have tried to solve the above technical problems by supplying part of combustor air to the downstream side of the combustion region and also by adopting the air flow regulating variable mechanism that can control the above air flow in accordannce with the gas turbine load (see Fig.4).

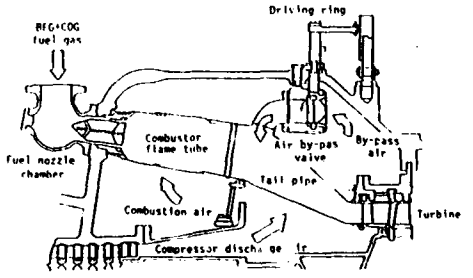

Fig.4 Construction of combustor

Fig.5 shows the combustion efficiency improvement effect of this air flow regulating variable mechanism at the gas turbine no-load condition when the blast furnace gas BTU is increased to 1000kcal/Nm³.

The multi-cannular type combustor having this air flow regulating mechanism can keep the BTU increasing rate of blast furnace gas as low as possible and moreover enables the operation that can maintain the stable and high combustion efficiency in the wide operation range from the no-load of the gas turbine to its rated load.

By overcoming the above-mentioned technical problems in developing the multi-cannular type combustor burning low BTU gas, we obtained the prospect to make the large-capacity high-temperature gas turbine burning

low BTU gas fit for practical use.

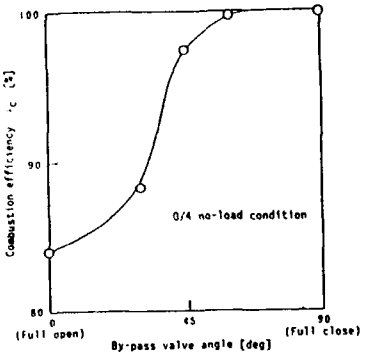

Fig.5 Combustion efficiency improvement effect by means of air flow regulating variable mechanism

However, in making this combustor fit for practical use, the final verification/confirmation of the following items in the actual device design had to be carried out:

- Shape of fuel nozzle
- Selection of air velocity in cross section of combustor
- Optimization of air distribution by means of air hole arrangement
- Confirmation of direct firing with ignition plug
- Combustion characteristics during firing and speed increasing

For this purpose, before carrying out fundamental designing of the plant, we have carried out the atmospheric pressure combustion test with the full-scale combustor and actual blast furnace gas in the site of Chiba Ironworks, Kawasaki Steel Corporation.

(1) Firing performance ---------- Fig.7-1

When blast furnace gas is mixed with coke oven gas to increase the BTU to about 1,000kcal/Nm³ or higher, direct firing is possible with an ignition plug.

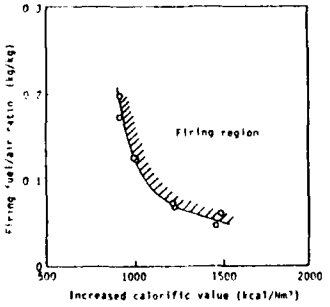

Fig.7-1 Firing performance

(2) Blowing-out performance ---------- Fig.7-2

It is confirmed that the flame stability at assumed gas turbine load cutoff has no hindrance specially in operating the actual combustor with fuel of 1,000kcal/Nm³ or higher in increased calorific value.

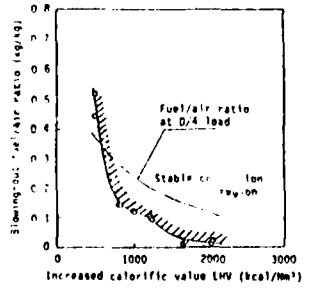

Fig.7-2 Blowing-out performance

(3) Combustion characteristic during speed increase ----------Fig.7-3

The multi-cannular type combustor with the air flow regulating variable mechanism can increase the speed during the firing and speed increasing operations with fuel of 1,000kcal/Nm³ in calorific value, maintaining the combustion efficiency at 99% or higher.

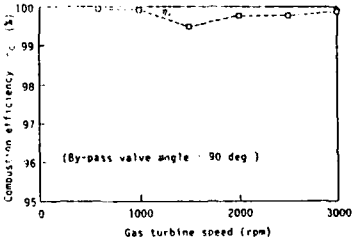

Fig.7-3 Combustion characteristic during gas turbine speed increase

(4) Load characteristic---------- Fig.7-4

The combustor can keep stable combustion with the air flow regulating variable mechanism within the range from gas turbine no-load to its rated load, maintaining the combustion efficiency at 99.5% or higher. In addition, low BTU gas having an intrinsically-low flame temperature has the advantage of a low NOx generation rate. Therefore, the combustor can have low NOx combustion of 20ppm in exhaust density (O_2 5% conversion) or lower without such low-NOx countermeasure as water or steam injection into the combustion as shown in the figure.

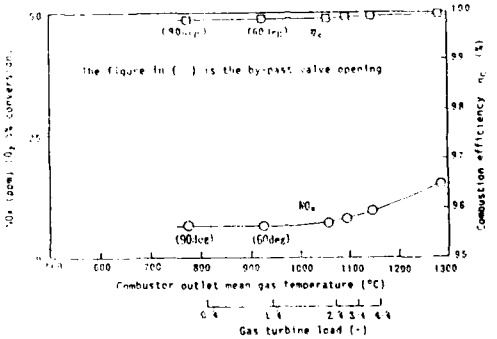

Fig.7-4 Load characteristic: Combustion efficiency and NOx exhaust density

As mentioned above, practical use of the multi-cannular type combustor burning low BTU gas has become possible through overcoming of its technical problems and verification with the full-scale atmospheric pressure combustion tests with actual gas.

POSTSCRIPT

The combustion technology for the combustor burning low BTU gas, which has been developed and made fit to practical use with ironworks by-product gas, can be applied to the coal gasification combined plant. However, in future this should be made fit to practical use further by trying to adopt higher temperature and give lower public nuisances.

(1) Higher temperature → 1300°C class of turbine inlet gas temperature

(2) Lower public nuisances → Decrease of fuel NOx

IUTAM Symposium on
Aerothermodynamics in Combustors
June 3-5, 1991, Taipei

MEASUREMENTS OF GAS COMPOSITION AND TEMPERATURE INSIDE A CAN TYPE MODEL COMBUSTOR

BY W.P. JONES AND A. TOBER

DEPARTMENT OF CHEMICAL ENGINEERING & CHEMICAL TECHNOLOGY
IMPERIAL COLLEGE OF SCIENCE, TECHNOLOGY & MEDICINE
LONDON, SW7 2BY, ENGLAND

INTRODUCTION

The combustor involved in the present experimental study is a model of a can type combustion chamber typically found in aircraft gas turbines. The combustor is fuelled via a liquid kerosene spray and the flame is stabilised by a recirculation zone driven by a swirler air flow through the head of the combustor and by primary dilution jet flows; the inlet air flow is preheated with an electrical heater. Detailed flow studies in a perspex water flow model of the same combustor have previously been reported in [1], and for the combusting case detailed measurements are available [2], over a range of operating conditions burning gaseous fuel (propane). Further combusting flow measurements in closely similar geometries are described in [3], [4] and [5]. The aim of the present investigation is to obtain measurements of gas composition and temperature so as to allow the effects of a change from a gaseous fuel to a liquid kerosene fuel spray to be quantified. Mixture species concentrations were obtained by probe sampling and temperatures were measured by thermocouple. All experiments were conducted at atmospheric pressure.

EXPERIMENTAL SET UP

The combustor together with its dimensions is shown in figure 1. Air is supplied through a plenum chamber surrounding the combustor which itself exhausts freely into the laboratory. The combustor is fabricated from a laminated porous sheet material called Transply which provides cooling of the combustor walls. Air also enters through a vaned "aerodynamic" swirler located concentrically in the hemispherical head of the combustor and through two rows of six dilution holes equally spaced around the circumference of the combustion chamber. These rows of holes are staggered with respect to each other such that the angle between the axial planes in which the holes lie is 30°. The dimensions of the swirler and dilution holes determine the relative air inflow rates and were designed to give a flow split and flow pattern representative of that arising in practical gas turbine combustors. Measurements made with pitot and hot wire probes in the cold flow confirmed the design. Thus 9.9% of the total air flow enters through the swirler, 3.0% through the perforations in the domed head, 13.7% through the first set of holes, here termed primary holes, 15.4% through the barrel cooling and 58% through the second set of holes here called dilution holes. The airflow was preheated with an electrical heater and enters the combustor at a temperature of 400K.

The pressure jet atomizer which produces a hollow cone spray with an included angle of about 70° is located in the centre of and is concentric with the swirler. The fuel used was aviation grade kerosene (JET A-1) and the fuel pressures were 60 bar and 27 bar for the two cases measured. These pressures resulted in a fuel flow rate of 1.33 ml/m and 0.84 ml/min and with a constant air flow rates of 100 g/s resulted in AFRs of 57 and 91 respectively.

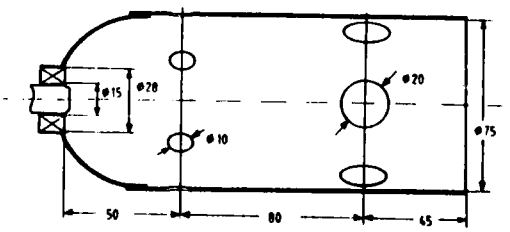

Fig. 1 Combustor geometry

MEASUREMENT METHODS

Temperatures were measured by uncoated fine wire (80 micron) thermocouples (pt/pt13%rh) and the mean values shown were obtained after averaging over a 4 sec period. The measurements were uncompensated for radiation losses or thermal inertia effects. For the higher air to fuel ratio case temperature measurements were limited to the dilution zone where probe temperatures were sufficiently below the melting point of platinum to avoid destruction of the probe. Gas composition was measured by analysing samples taken by a watercooled stainless steel probe. For a detailed description see [3]. To avoid condensation of water and fuel vapours in the probe the probe cooling water was kept at a temperature above 150°C in accordance with SAE ARP 1256A. The species measured were CO_2, CO, H_2, O_2 and total unburnt hydrocarbon (UHC). These were sufficient to allow the calculation of the concentrations of the remaining major species, N_2 and H_2O by mass balance. The assumptions made in this calculation were that the gas is composed of the above seven species plus an intermediate hydrocarbon (C_2H_2) only and that the carbon to hydrogen ratio and the oxygen to nitrogen ratio are those of the raw fuel and air respectively at any point in the combustor. The measured and calculated concentrations allowed the profiles of mean mixture fraction, f(= 1/(AFR + 1) to be determined and the gas temperatures to be obtained by enthalpy balance.

RESULTS

A general overview of conditions inside the combustor can be seen from figure 2 shows contours of mean mixture fraction in the axial plane which passes through the centre of the dilution hole and lies mid way between two primary holes. At the measurement station closest to the fuel injector (20mm) the mixture fraction reaches 0.47 but declines rapidly to values below 0.15 before the station where the primary jet enters the combustor (outside the plane shown). The effect of the primary jets on mixture fraction in the plane shown can be seen near the centre line of the combustor where mixture fraction values are greatly reduced with a minimum arising between 10mm and 20mm downstream of the jet. A fuel-air mixture with a low fuel content (the average composition of swirler air, head air and fuel should have a mixture fraction of 0.11) is found upstream of the primary air jets on the centreline which suggests that these jets contribute to a central recirculation zone. With much of the primary jet air going downstream in the vicinity of the centreline the mixture strength remains fuel rich towards the combustor wall and mixture fraction is still above 0.1 at half the combustor length, falling below to values of 0.05 only downstream of the dilution air jets. For comparison, the average mixture fraction based on the swirler, head and primary jet air flows is 0.06; a value which reduces to 0.039 on addition of the barrel cooling air. The dilution jet is clearly visible in this plane and as can be observed is deflected and does not reach the centreline. Mixture with high fuel content is forced toward the centreline and is deflected around the dilution jet and is further diluted with air originating from wall cooling and the jet itself. The maximum mixture fraction in the exit plane is twice the average value of 0.017 based on the AFR. The differences between the two AFRs measured are shown in the radial profiles of figure 3a to c. Together with the profiles of mixture fraction, the concentrations of CO_2, CO and UHC are shown and these indicate to what extent the fuel has been consumed at those stations. The profile at x = 30 (in the primary zone) shows an area of high CO_2, moderate CO and low UHC concentrations around the centreline. At the lower AFR the increase in mixture fraction brings an increase in CO levels and a corresponding reduction in CO_2 concentrations. The

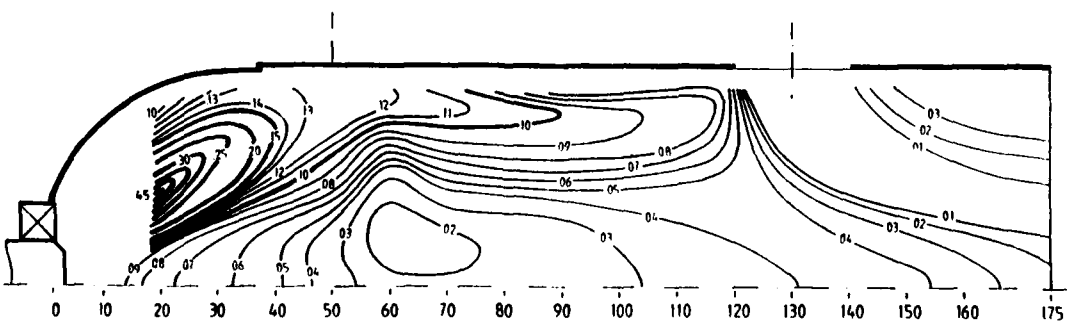

Fig.2
Contours of constant mixture fraction of fuel in axial plane 270°, AFR 57

concentration of unburnt fuel rises towards the combustor wall but reaches a maximum at about two thirds of the combustor's radius. The reduction from here to the combustor wall together with a fall in both CO and CO_2 shows the coexistence in this turbulent flow of unconsumed oxygen with fuel and some combustion products. The most obvious difference between the higher and lower AFR cases, where the general pattern is the same, is that for the higher AFR, the fuel concentration is more strongly reduced on the inner shoulder of the maximum. In line with the overall lower levels of fuel content a larger part of the fuel is burnt. At stations further downstream the similarity between the concentration profiles for the two AFRs is increased. As the area with mixture fraction above stoichiometric values becomes larger in the lower AFR case high concentrations of UHC are found and values for CO exceed those of CO_2. The highest fuel concentrations are now found to occur close to the combustor wall but at the station mid way between the primary and dilution hole (x = 90mm) the effect of the wall cooling air causes a sharp drop as the wall is approached - the closest measurement was 4mm from the wall. A more detailed picture of the situation in the vicinity of the dilution jets is shown by the temperature measurements plotted in figure 4a, b and figure 5. The temperature contours plotted in axial planes in line with the dilution hole centre and half way between dilution holes explain why the highest temperatures are found behind the dilution jets in the cross section in the exit plane. The in line plane shows the hot gases to be displaced towards the centreline, and that their temperature is reduced by mixing with colder gas which flows down the centreline region. The plane between jets (which of course has the centreline in common with the other plane) shows the same displacement but in addition a displacement towards the wall caused by the spreading of the cold jet air into this plane. It is this gas which fills the lee of the jet indicated in figure 4a and can be seen enveloped by the horseshoe shaped wake of the dilution jet in the exit plane cross section. (fig 5).

Fig. 3 Radial profiles of measured composition in 270° plane

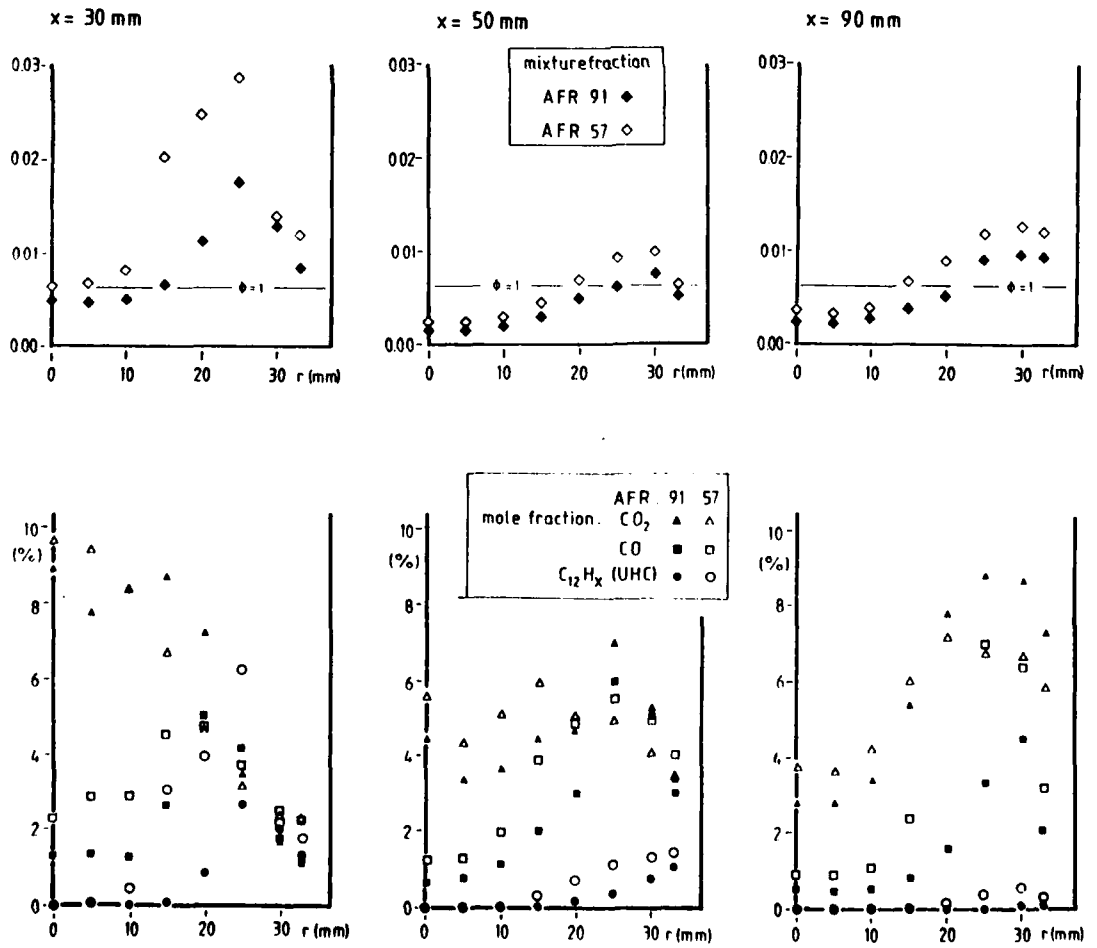

CONCLUSIONS

Though for reasons of space not shown here, the presently measured distribution of fuel in the combustor are closely similar to those measured with gaseous propane as fuel [2]. At radial positions outside the primary combustion zone and upstream of the first row of jets there is close agreement in the measured values for mixture fraction for both propane and kerosene fuels. This would indicate, perhaps somewhat surprisingly, that the liquid fuel with its ability to penetrate the air stream does not in fact spread in a significantly different way from the gaseous fuel. If this is the case then some conclusions can be drawn about the flow pattern occurring inside the combustor. This suggests that a central recirculation exists which is partly fed by the impingement of the primary jets and there are no indications of a 'corner' recirculation zone in the head of the combustor outside the air stream from the swirler. In the downstream region the flow pattern is indicated more clearly by the dilution jets where reaction plays only a minor role. Here too the jet trajectory follows the pattern intended in the design of the combustor and is successful in reducing the temperatures and fuel content of the exhaust gases so that by the exit plane reasonably uniform profiles result.

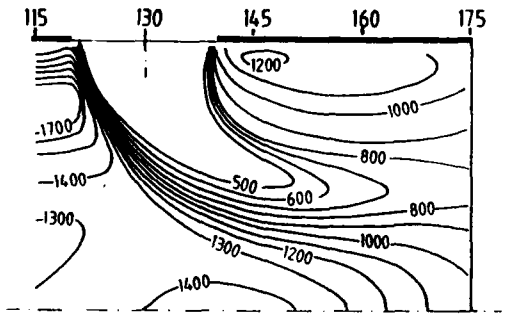

Fig. 4a Isothermal contours (K) around dilution jet axial plane 270°, AFR 91

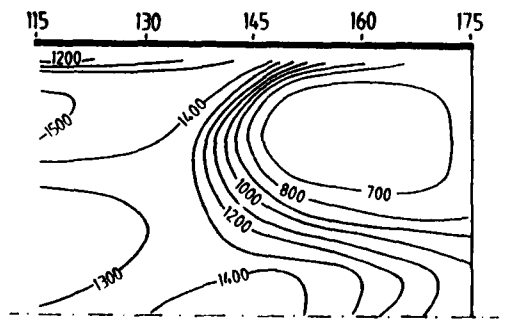

Fig. 4b Isothermal contours (K) around dilution jet axial plane 240°, AFR 91

ACKNOWLEDGEMENTS

The authors would like to acknowledge the financial support provided by Rolls-Royce plc and useful discussions with colleagues at Imperial College and staff at Rolls-Royce and RAE/Pyestock.

REFERENCES

[1] Palma, J.M.L.M. (1988), "Mixing in non reacting gas-turbine combustor flows", Ph.D. Thesis, University of London.

[2] Tse, D.G.N. (1988), "Flow and Combustion Characteristics of model annular and Can Type Combustors", Ph.D. Thesis, University of London.

[3] Jones, W.P. and Toral, H. (1983), "Temperature and Composition Measurements in a Research Gas-Turbine Combustion Chamber", Comb. Sci. and Tech., 31, 249.

[4] Bicen, A.F., Heitor, M.V. and Whitelaw, J.H. (1986) "Velocity and Temperature Measurements in a Can-Type Gas-Turbine Combustor", AGARD-CP-399, paper no. 14.

[5] Jones, W.P. and Tober, A. (1988), "Velocity, Composition and Temperature Fields in an Axisymmetric Model Combustor", Proceedings of the Fourth International Symposium on Applications of Laser Anemometry to Fluid Mechanics, Lisbon, Portugal July 1988.

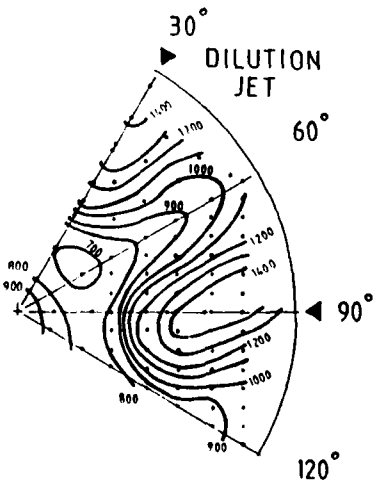

Fig. 5 Isothermal contours (K) in a sector of exit plane, AFR 91

IUTAM Symposium on
Aerothermodynamics in Combustors
June 3-5, 1991, Taipei

NUMERICAL MODEL FOR PREDICTIONS OF REVERSE FLOW COMBUSTOR AEROTHERMAL CHARACTERISTICS

P. Di Martino, E. Narciso, G. Cinque

Alfa Romeo Avio S.p.A.
Research and Development Department
Pomigliano d'Arco (NA) - ITALY

1. Introduction

The advent of more powerful digital computers has provided the means whereby mathematical modeling can be applied to gas turbine combustor problems to facilitate greatly the arduous initial stages of combustor design and to reduce the time and cost associated with experimental work.
In this study a comprehensive mathematical model of three-dimensional fluid mechanics and two-phase turbulent combustion processes is approached in order to give combustor engineers efficient tools of analysis.

2. Gas phase model

Steady fully elliptic time-averaged equations describing gas phase, under low Mach number approximation, coupled to the energy and momentum balance equations for the liquid phase, are considered in cylindrical coordinates [1]. The k-ε model provides for turbulence closure. Conservation equations solved for the gas phase are those for u,v,w momentum, mass, stagnation enthalpy (h), turbulent kinetic energy (k) and its rate of dissipation (ε), mixture fraction (f). The general form of these conservation equations is:

$$\frac{1}{r}\left[\frac{\partial}{\partial x}(r\rho u\phi) + \frac{\partial}{\partial r}(r\rho v\phi) + \frac{\partial}{\partial \theta}(\rho w\phi)\right] = \frac{1}{r}\left[\frac{\partial}{\partial x}\left(r\Gamma_\phi \frac{\partial \phi}{\partial x}\right) + \frac{\partial}{\partial r}\left(r\Gamma_\phi \frac{\partial \phi}{\partial r}\right) + \frac{\partial}{\partial \theta}\left(\frac{1}{r}\Gamma_\phi \frac{\partial \phi}{\partial \theta}\right)\right] + S_\phi + S_d \qquad (1)$$

where ϕ is any one of the general flow variables, Γ_ϕ is the effective diffusion coefficient for ϕ and S_d and S_ϕ are the sources for ϕ from liquid droplets and gas phase, respectively.
The definition of stagnation enthalpy is:

$$h = C_p \cdot T + m_{fu} \cdot H + \tfrac{1}{2}(u^2 + v^2 + w^2) \qquad (2)$$

which is used to calculate temperature T. In this equation m_{fu} is the unburned fuel mass fraction, H is its heat of combustion and C_p is the specific heat of the mixture at constant pressure.
The chemical reaction is described by the "fast chemistry" model. This implies the reaction will go to completion instantaneously once the mixing of fuel and oxidant has been achieved on a molecular level. In this idealized case the conservation equations for chemical species, assuming a single exotermic chemical reaction, are:

$$0<f\leq f_{st} \quad m_{fu}=0; \quad m_{ox}=\left(1-\frac{f}{f_{st}}\right)m_{ox,air} \qquad (3)$$

$$1>f>f_{st} \quad m_{fu}=\left(\frac{f-f_{st}}{1-f_{st}}\right); \quad m_{ox}=0 \qquad (4)$$

$$f_{st} = \frac{1}{[1 + s(m_{fu}/m_{ox}),air]} \qquad (5)$$

where s stands for oxygen/fuel mass stoichiometric ratio, m_{fu} and m_{ox} are the fuel and oxygen mass fraction respectively and st stands for stoichiometric value. The mixture fraction fluctuations are neglected. It is, however, economic of computer storage and time and, in view of the additional uncertainties imposed by the droplet model, probably of acceptable precision. The density is calculated from the equation of state:

$$\rho = P/RT\Sigma_j(m_j/M_j) \qquad (6)$$

where M_j is the molecular weight of species j and R is the universal gas constant.
The effects of radiative heat transfer are described by reference to the six-flux model, based on the solution of a set of six ordinary differential equations, which provides the energy source term for the gas phase [1].

3. Droplet model

The liquid-phase equations are based on the Lagrangian formulation of the droplet trajectory, transient

heating and vaporization. The entire fuel spray is constructed using a finite number of size ranges obeying a two parameter droplet size distribution, which is assumed to be of Rosin-Rammler type. The equations of motion for each of the droplets, representing the size groups which constitute the spray, are written neglecting all external effects except the drag force [2]. The description of droplet heating and evaporation is added to the computational model using two equations which are solved separately, assuming that during the first phase the droplet is heated to an equilibrium temperature, followed by the second phase in which the evaporation process causes a decrease in diameter. These equations may be expressed as

$$\frac{dD}{dt} = -\left(\frac{C_b}{2D}\right)(1+0.23Re^{\frac{1}{2}}) \qquad (7)$$

and

$$\frac{dT}{dt} = 6\lambda(2+Re^{\frac{1}{2}}\cdot Pr^{1/3})\frac{(T - T_d)}{\rho_d D^2 C_p L} \qquad (8)$$

where C_b is the vaporization rate constant whose value depends on the physical properties of the surrounding medium as well as of the fuel itself; Re is the relative Reynolds number, D is the droplet diameter, ρ_d is the liquid density, λ and C_p are the thermal conductivity and the specific heat at constant pressure of the surrounding gas, L is the latent heat of vaporization and T and T_d are the gas and droplet temperatures respectively. With this liquid phase model is possible to simulate also gas fuels by choosing a very low boiling point in order to obtain a flash evaporation.

4. Numerical features

The partial differential equations described earlier have been transformed into difference equations by integrating over each control volume and solved numerically employing a semi-implicit iterative scheme (SIMPLE [3]). All dependent variables are calculated at mesh grid points centered at an elementary volume except velocity components, which are evaluated at the control volume faces. Wall functions have been used to avoid detailed calculations in the near-wall regions. Simulation of contoured flowpath boundaries was accomplished by the so called "stairstep" boundary treatment into the model. The grid used in calculations possessed 47x27x27 nodes in the x,r and θ directions respectively.

The gas-spray interaction terms are supplied from the set of simultaneous ordinary differential equations integrated numerically by the fourth order Runge-Kutta method at suitable intervals within the iterative solution procedure.

5. Model validation and results

The previous model was applied to perform a calculation of the internal reactive flowfield of the GEM-60 reverse flow combustion chamber for which experimental results are available [4,5]. The geometry of combustor and the operative conditions are given in [4]. The mesh used in the calculation is shown in Fig. 1. The convergence history of the residuals is given in Fig. 2. After 1000 iterations the maximum residual is of the order 1.E-05 and pressure difference in the chamber is stabilized, thus showing that the solution is reasonably converged at this point. In Fig. 3 gas temperatures patterns are presented as to Z=14 mm, Z=28 mm and Z=42 mm sections respectively. The velocity field for the same sections is shown in Fig. 4. A strong recirculation vortex can be observed in the primary zone. Gas temperatures patterns at the combustor discharge plane are presented in Fig. 5 in a plane near the lower wall (a), in a medium plane (b) and in a plane near the upper wall (c) respectively. The calculated temperature profile is in good agreement with experiment as to planes (a) and (b). In plane (c) temperature is underestimated even if the trend is correct.

6. Conclusions

A two-phase turbulent reactive flow model for a gas turbine combustor has been numerically solved. The computed results reproduce the main features of the reactive flow and show a good agreement with experimental data, in view of the many interdepent processes involved.

REFERENCES

[1] Gupta A.K., Lilley D.G.: "Flowfield Modeling and Diagnostics", Abacus Press, 1985.

[2] Kuo K.K.:"Principles of Combustion", John Wiley and Sons, 1986

[3] Patankar, S.V. and Spalding, D.B.: "A Calculation Procedure for Heat, Mass and Momentum Transfer in Three-Dimensional Parabolic Flows", International Journal of Heat and Mass Transfer, Vol. 15, 1972, pp.1787, 1806.

[4] Bicen A.F., Senda M., Whitelaw J.H.: "Scalar Characteristics of Combusting Flow in a Model Annular Combustor", Journal of Engineering for Gas Turbines and Power, Transaction of the ASME, Vol.111, Jan. 1989.

[5] Bicen A.F., Tse D., Whitelaw J.H.: "Flow Characteristics of a Model Annular Combustor", Propulsion and Energetic Panel 70h Symposium, Crete 1987, AGARD CP-422.

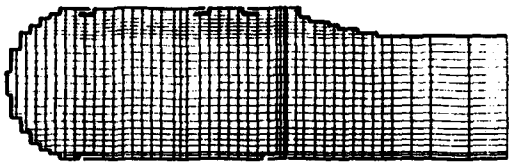

Fig. 1 MESH = 47x27x27

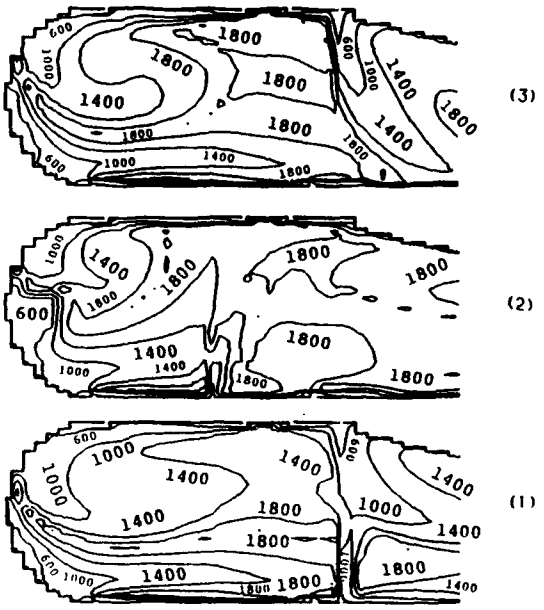

Fig. 3 GAS TEMPERATURES (K)

(1) Z = 14 mm
(2) Z = 28 mm
(3) Z = 42 mm

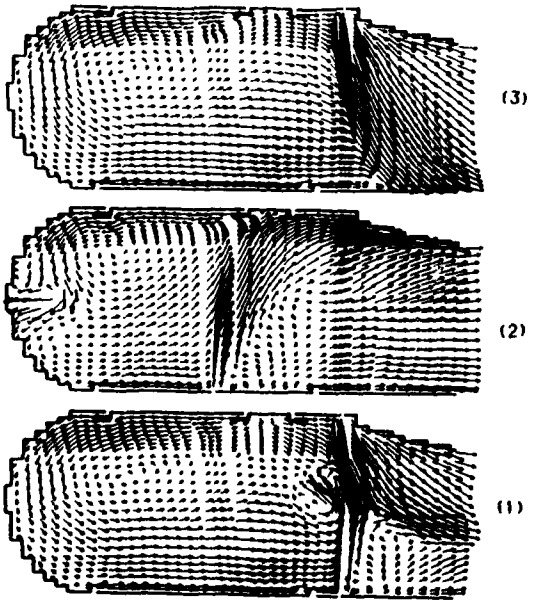

Fig. 4 FLOW FIELD

(1) Z = 14 mm
(2) Z = 28 mm
(3) Z = 42 mm

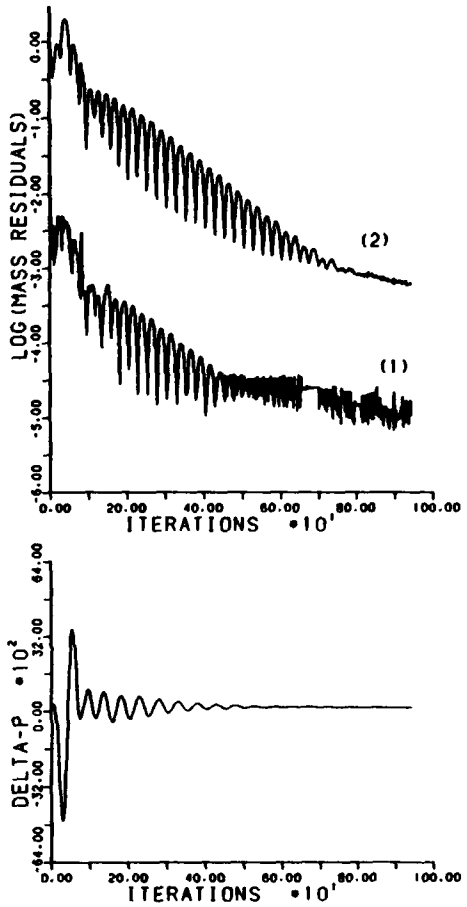

Fig. 2 NUMERICAL FEATURES

(1) MAXIMUM OF MASS RESIDUALS
(2) SUMMATION OF MASS RESIDUALS

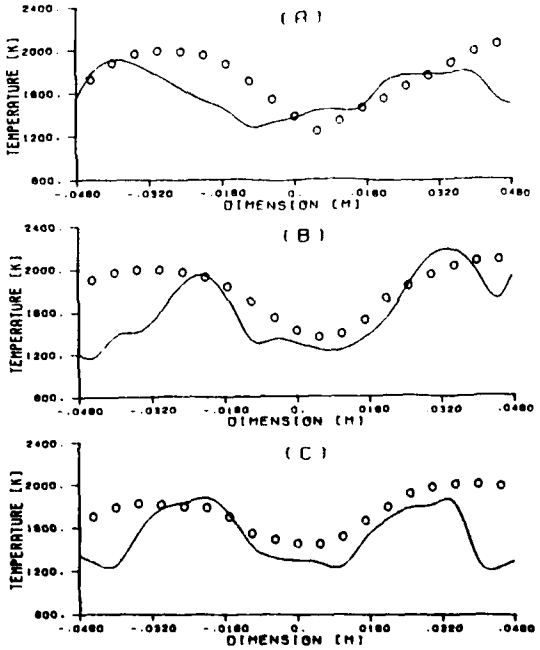

Fig. 5 GAS TEMPERATURES AT DISCHARGE PLANE

MODEL ——
EXPERIMENTS o

IUTAM Symposium on
Aerothermodynamics in Combustors
June 3-5, 1991, Taipei

Computational Analysis of the Three-Dimensional Steady and Transient SSME Fuel Preburner Combustor

Ten-See Wang*

Computational Fluid Dynamics Branch
NASA Marshall Space Flight Center
Huntsville, Alabama

A computational fluid dynamics (CFD) model with finite rate and equilibrium chemistry reactions, has been developed to study the steady-state and start transient of the Space Shuttle Main Engine (SSME) Fuel Preburner (FPB) combustor operations. The numerical model is a time accurate, pressure based CFD code. An upwind scheme is employed for spatial discretization. The upwind scheme is based on second and fourth order central differencing with adaptive artificial dissipation. A two-equation turbulence model is employed for the turbulence calculation. A Pade' Rational Solution (PARASOL) was developed for finite rate chemistry calculation, and a CHMQGM algorithm was used for equilibrium chemistry calculation.

The Fuel preburner combustor of the SSME, as shown schematically on the upper left corner in Fig. 1, consists of three major parts: the augmented spark igniter (ASI), injectors, and the combustion chamber. The fuel preburner itself is structurally supported by the hot gas manifold to which it is welded and is a fuel cooled, double-walled chamber, in which hot gas (hydrogen-rich steam) is generated to power the high pressure turbopump. The ASI initiates the combustion of gaseous hydrogen fuel and liquid oxygen near the injector elements on the faceplate. The preburned fuel then flows over a circular dome of the high-pressure turbopump and into a turbine inlet flow passage where it drives the turbines of the turbopump. The combustor wall is film cooled.

Numerous flow anomalies have been found in both the SSME fuel and oxidizer preburners and turbine hot end parts. Cracks have been found on housings, Kaiser-hat nuts (located at the top of the turbopump dome), struts, sheetmetal, nozzles, and shrouds. After many studies and modifications to the preburner components, several problems remain with the SSME preburner operation, such as cracking of the first and second stage blade shanks, of the blade root fillets and under the blade platform. The damage is more severe on the fuel side since it operates at a higher temperature. It is postulated that the extreme thermal environment during the start up transient produces the initial blade cracks; the severity of the cracks will depend on the specific transient operations the engine experiences. The cracks can continue to grow due to both high cycle fatigue and low cycle fatigue as the number of turbine load cycles accumulate. Other flow anomaly theories such as inefficient atomization and possible unmixedness of the gaseous oxygen during steady state operation are considered to be of secondary importance in creating locally excessive heating problems.

Computational analyses of steady-state axisymmetric and three-dimensional fuel preburner combustor flowfields were performed. The effect of baffle and wall film coolant flows was considered. Fig. 2 shows a cutaway view of the three-dimensional computational grid. The baffles can be seen at the inlet injector faceplate and at the upper portion of the two straight-cuts of the combustor. The hemispherical turbopump dome is exposed at the lower portion of the combustor. Radial and circumferential temperature distributions near the combustor exit were compared with those of the experimental data. These analyses indicated that under steady operating conditions, striated flows go through the preburner chamber between the parallel shear layers. Results from such analyses show that striations severe enough to cause local streamlines to be at near stoichiometric mixture ratios should not be present at the inlet to the turbopump under steady-state operations. Temperature measurements at the turbine inlet show that two temperature spikes exist under start-up. Estimates of thermocouple

* Technical Lead, Member AIAA

response suggest that the actual temperatures are sufficiently high to create blade cracking. A transient fuel preburner thermal flowfield computational analysis was performed so as to understand the combustor ignition transient and to make recommendations for improving the component life of the SSME engine.

A pressure based solution method was selected so that a wide range of flow speeds could be analyzed. For time accuracy, a time-centered, time-marching scheme with a multiple pressure corrector algorithm was employed. Finite rate chemistry calculations were performed to capture the time dependent flame propagation phenomena inside the combustor during transient start-up process. The finite rate source terms were evaluated with a point implicit procedure before the species equations were solved. At the start command, the fuel preburner is filled with atmospheric nitrogen purge gas. After the start command, the fuel and oxidizer flow out the ASI and the injector elements on the faceplate, to prime the chamber and the turbine. The transient upstream boundary conditions included the ASI and injector fuel and oxidizer flow rates, temperatures and pressures. They were obtained from an engine system model.

The results of the CFD calculation have shown temperature spikes near the top of the turbopump dome and the combustor exit. In addition, an appreciable amount of oxidizer was left unburned to enter the turbine stages, which could cause chemical attack on the metal surface. A comparison of the calculated combustor temperature history for the first one second operation at the combustor exit and the measured turbine inlet temperature is shown in Fig. 3. The timing and magnitude of the calculated temperature spikes agreed well in general with those of the measurements. The swirling motion of the igniter torch created a center recirculation zone to serve as a flame holder. The bulk of the propellants was ignited after the igniter torch has reached the turbopump dome. The temperature spikes were caused by the mismatch of the fuel and oxidizer flow rates. The propellants flow rates were controlled by the engine valve sequencing.

The significance of this study is that a time accurate CFD design tool has been developed to accurately predict the severe thermal gradients which are impressed upon the SSME fuel preburner and turbine stages during the start transient. Previously, various scenarios were proposed to explain the causes of the SSME fuel preburner flow anomalies, without proper verifications. These scenarios included the local accumulation of unreacted propellants, the mismatch of the fuel and oxidizer supply rates, and a combustible mixture maldistribution prior to and during ignition. These factors can now be studied with the numerical analysis. Furthermore, the reduction of thermal loads can also be studied by numerically varying the ignition and shut-down characteristics.

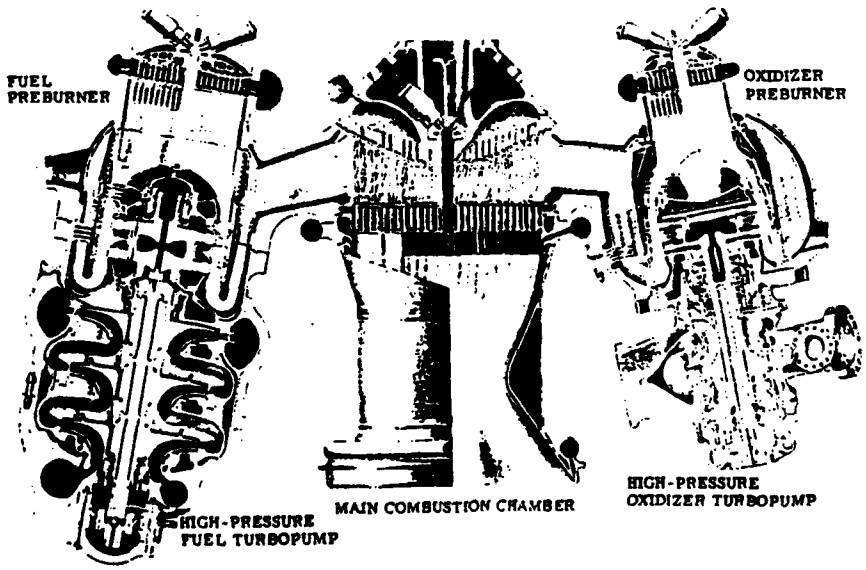

Fig. 1 Space Shuttle Main Engine power head component arrangement.

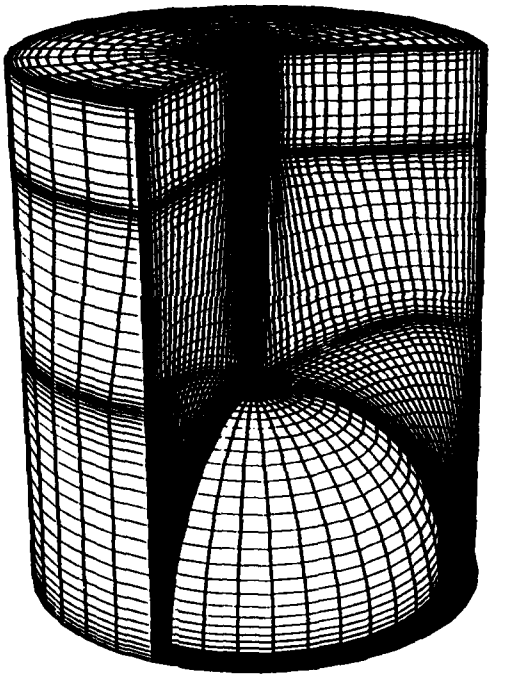

Fig. 2 A cutaway view of the three-dimensional computational grid for the SSME fuel preburner combustor.

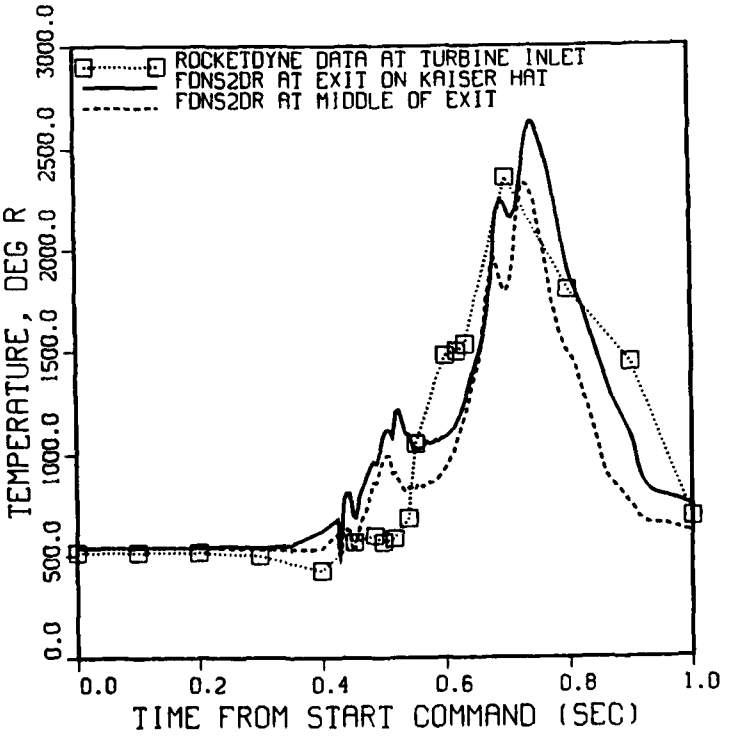

Fig. 3 Comparison of temperature histories at computed fuel preburner exit and measured turbine inlet.

IUTAM Symposium on
Aerothermodynamics in Combustors
June 3-5, 1991, Taipei

VELOCITY MEASUREMENTS OF NON-REACTING AND REACTING FLOWS IN A RESEARCH COMBUSTOR

T. H. Chen, M. E. Post, L. P. Goss, D. D. Trump, B. Sarka, and L. Brainard
Systems Research Laboratories, Inc., A Division of Arvin/Calspan
2800 Indian Ripple Road, Dayton, OH 45440-3696 USA

W. M. Roquemore
Wright Laboratory, Aero Propulsion and Power Directorate
Wright-Patterson Air Force Base, OH 45433-6563 USA

The flowfields of a research combustor were characterized using two-component Laser Doppler Velocimetry (LDV). This combustor was adapted by the Wright Laboratory/Aero Propulsion and Power Directorate and research contractors for the establishment of a data base to be acquired using on-site-developed techniques such as LDV, Coherent Anti-Stokes Raman Spectroscopy (CARS), Thin-Filament Pyrometry (TFP), and Planar Laser-Induced Fluorescence (PLIF). The flow properties to be measured include velocity, temperature, and species concentration. This data base will be utilized for evaluation of combustor modeling and to provide fundamental understanding of the combustion process which occurs inside a combustor. The point velocity information presented here can be combined with measured scalar quantities for joint examination of aerothermodynamics in combustors.

The research combustor was designed [1] to simulate the main features of an engine combustor, such as the recirculating-flow patterns and lean-blowout (LBO) processes, and also to provide good optical access. A schematic diagram of the combustor is shown in Fig. 1. The flowfield inside this combustor consists of coaxial jets with sudden expansion (rear-facing step); this flowfield has been studied to some extent [2-4]. Minor modifications in geometry were made to convert the axisymmetric, cylindrical configuration to a semi-square combustor section. The resulting flat window facilitates the complicated optical-beam pass needed for joint velocity and scalar measurements. For the combustion experiments, gaseous fuel was issued from the inner tube and the coflowing air through the annulus. Fuel and air were not premixed before entering the combustor. The mixture resulting from the shear-layer mixing was recirculated back along the combustor wall into the recirculation zone established by the rear-facing step, which serves to stabilize combustion. Under the fuel-rich condition, the flame base became attached to the jet exit. With reduction of the fuel flowrate, the flame was lifted and stabilized by the recirculation zone. Eventually, after a sufficient decrease in the fuel flowrate, LBO occurred. For this combustor, LBO occurs at a fuel-equivalence ratio, ϕ, of 0.5 which is very near the lean-flammability limit (ϕ = 0.51) of the propane fuel and air [5]. This value of ϕ at LBO was essentially

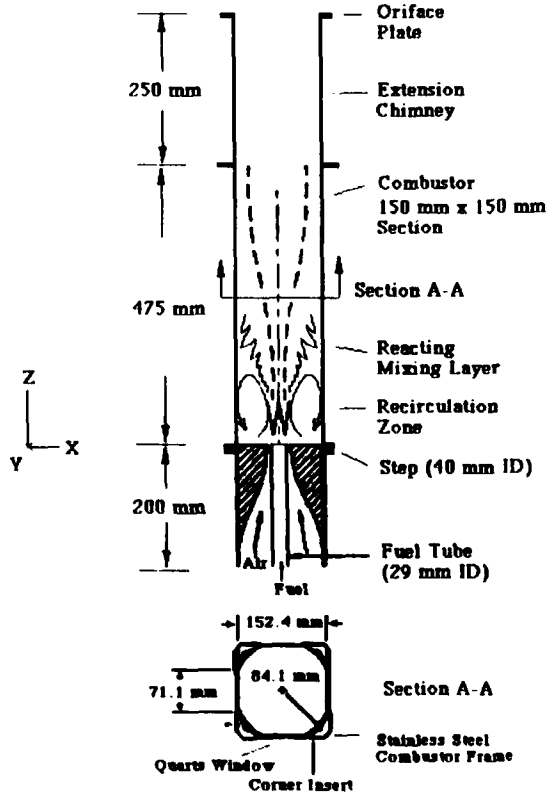

Fig. 1. Schematic diagram of confined coaxial jet combustor with sudden expansion.

unchanged over a wide range of air flowrates.

Under liftoff conditions the motion of the flame base was highly intermittent with changing liftoff height and radial flame position--behavior which is similar to that found in previous studies of lifted jet flames [6]. Under attached conditions the flame base was affected by the recirculating flowfield and displayed intermittent hole formation on the flame surface. As a result of the acoustic coupling of the combustor geometry and the variation of the heat release due to intermittent flame fluctuation, modeling of the combustion process inside the combustor remains a difficult task. A fundamental understanding of the dynamic flame/flow interaction inside the combustor will significantly aid the modeling process. Such fundamental knowledge is related to statistical flame characteristics such as the velocity and length scales associated with the flame surface fluctuation which can be measured by the TFP technique [6]. For better utilization of scalar information, velocity data are needed for comparison in the interpretation, as was demonstrated in a recent study [7].

In this initial phase, velocity measurements were performed under one nonreacting and three reacting flow conditions. For the reacting flow conditions, the air flowrate was fixed at 1000 lpm, with the propane fuel flowrates being 23, 41, and 63 lpm, corresponding to ϕ values of 0.55, 1.05, and 1.56, respectively. These conditions correspond to near LBO, lifted flame, and attached flame, respectively. For the nonreacting flow case, the air flowrate was 1000 lpm, with the CO_2 in the fuel tube being 23 lpm. These flow conditions were selected to 1) characterize the detailed recirculating flow patterns, 2) highlight the interaction between the flame and the recirculating flow patterns, and 3) provide a data base which would allow evaluation of computational modeling. The Reynolds number based upon the annulus-air-flow condition is ~ 2.3×10^5. In this flow regime, the established flame zone near the jet exit has been found, by examining planar OH-imaging, to be shaped by the coherent structures [5]. These dynamic features of the flame propagation inside the combustor can be studied in detail by diagnostics such as TFP which has been utilized for the study of lifted-flame fluctuations [6].

The velocity measurements were performed using an LDV system--a two-component real-fringe system based upon polarization separation of the velocity components. The 514.5-nm line from a Spectra-Physics argon-ion laser was used as the light source, with 0.5-mm-diam. alumina (Al_2O_3) particles serving as the scattering medium. Two seeders were used for the fuel flow and the air flow to provide uniform, equal seeding density for prevention of sampling errors. The Doppler burst was collected in the forward direction slightly off-axis (~ 20 deg.). Dual Bragg cells having a 5-MHz frequency difference were employed to remove directional ambiguities and maintain the Doppler-burst frequencies in an optimum range for the velocity under study. The data sampling rate was in the range 50 - 1000 Hz for the two-component measurement.

The sending and receiving optics of the LDV were mounted on separate optical tables. The burner was mounted on a three-axis traversing mechanism located between these tables. For the axial- and tangential-component measurement, the burner was scanned along the LDV beam axis. For the axial- and radial-component measurement, the burner was scanned perpendicular to the LDV beam axis. Both types of scans intercepted the centerline of the combustor. For each scan, ~ 50 locations were chosen, and 2,000 to 3,000 velocity data points were measured at each location.

Statistical analysis of the measured velocity data yields the mean, root-mean-square (rms) fluctuation, Reynolds stresses, and higher order moments. In this paper, the results of velocity statistics are presented in the form of vector and contour maps to facilitate two-dimensional visualization of the flow patterns. Examples of such maps are shown in Figs. 2 - 3. Figure 2 displays the measured mean velocity vector for one of the combustion cases tested and clearly shows the recirculation pattern near the exit of the fuel jet. The contour lines of the mean axial velocity are shown in Fig. 3. The large area with negative axial velocity was formed at the combustor wall near the sudden-expansion step. The area near the contour line of zero axial velocity could be the preferred location for stabilization of the flame base. This will be confirmed later through TFP temperature measurements.

The mean velocity can also be applied in computing the stream function which determines the recirculation volume--an important parameter in flame-stabilization mechanisms. Considering that the flow is reasonably axisymmetric, the stream function representing the volume flowrate can be defined as

$$\psi = \int_0^r \bar{u} \cdot r \, dr \Big/ \int_0^{R_0} \bar{u} \cdot r \, dr \qquad (1)$$

where $\bar{u}$ is the axial velocity and R_0 the radius of the combustor. The stream-line

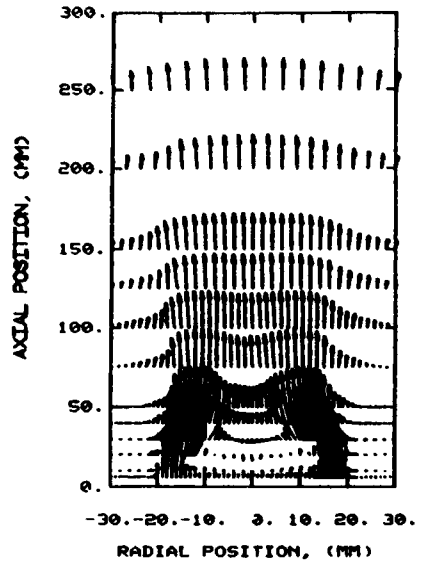

Fig. 2. Measured mean velocity vector for reacting flow with air at 1000 lpm and C_3H_8 at 41 lpm.

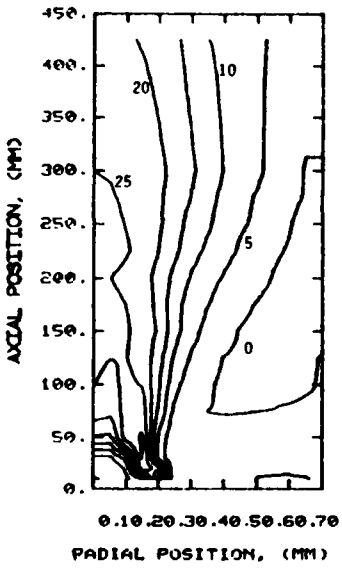

Fig. 3. Contour lines of mean axial velocity for reacting flow with air at 1000 lpm and C_3H_8 at 41 lpm.

values computed from the measured velocity can then be shown, for example, as in Fig. 4. The area enclosed by the line of $\psi = 1$ is the recirculation zone. Inside this zone more than 22% of the total volume flow was "trapped;" this value can be used to assess the performance of the rear-facing step in inducing recirculation. A similar property, which is defined as the recirculation efficiency, for the center-body-stabilized premixed flame near LBO was measured to be 33% by Chen, *et al.* [8]; its importance was later emphasized by Chen, *et al.* [9], in

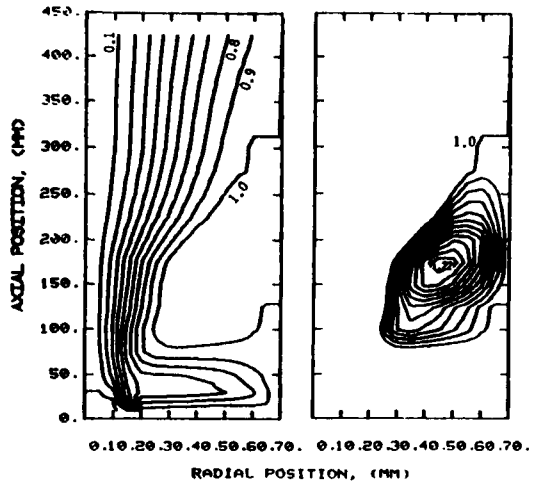

Fig. 4. Stream lines for reacting flow with air at 1000 lpm and C_3H_8 at 41 lpm.

correlating the flame-blowout behavior and the recirculation strength. The values corresponding to LBO and other flow conditions have been measured and will be compared.

This work was supported by and performed at the Wright Laboratory/Aero Propulsion and Power Directorate under Contract No. F33615-90-C-2033. The editorial assistance of M. Whitaker is appreciated.

REFERENCES

1. G. J. Sturgess, D. G. Sloan, A. L. Lesmerises, S. P. Henneghan, and D. R. Ballal, "Design and Development of a Research Combustor for Lean Blowout Studies," 35th Int. Gas Turbine and Aero-Engine Congress and Exposition, Brussels, June 1990.
2. M. A. Habib and J. H. Whitelaw, *ASME J. Fluids Engrg. 101*, 521 (1979).
3. B. V. Johnson and J. C. Bennett, in *Fluid Mechanics of Combustion Systems* (ASME, New York, 1981), pp. 145-160.
4. S. P. Vanka, AFWAL-TR-88-2140 (AF Wright Aeronautical Laboratories, Wright-Patterson Air Force Base, OH, 1988).
5. W. M. Roquemore, V. K. Reddy, P. O. Hedman, M. E. Post, T. H. Chen, L. P. Goss, D. D. Trump, V. Vilimpoc, and G. J. Sturgess, AIAA Paper 91-0639.
6. T. H. Chen and L. P. Goss, AIAA Paper 89-0156.
7. J. P. Seaba, *Burner Statistics of Jet Diffusion Flames*, Ph.D. Dissertation (University of Iowa, Iowa City, IA, December 1990).
8. T. H. Chen, L. P. Goss, D. D. Trump, and W. J. Schmoll, *J. Propul. Power 6*, 106 (1990).
9. R. H. Chen, J. F. Driscoll, J. Kelly, M. Namazian, and R. W. Schefer, "A Comparison of Bluff-Body and Swirl-Stabilized Flames," To be published in *Comb. Sci. Technol.*, 1991.

IUTAM Symposium on
Aerothermodynamics in Combustors
June 3-5, 1991, Taipei

ON THE GENERATION OF NOISE IN AXISYMMETRIC COMBUSTORS

E.C. Fernandes and M.V. Heitor

Instituto Superior Técnico
Technical University of Lisbon
Av. Rovisco Pais
1096 Lisboa Codex
PORTUGAL

The amplitude and frequency characteristics of the sound emitted by highly turbulent flames stabilized in a confined swirl combustor are analysed and discussed together with the time-resolved variation of the heat release rate. The work involves the analysis of the on-set of combustion induced oscillations through the identification of the phase relationship between the unsteady emission of C_2 radicals in the primary zone of the combustor and the distribution of pressure fluctuations along the combustor, and is relevant to the analysis of noise generation in pratical combustors.

The existence of combustion-driven oscillations at discrete frequencies has been observed in turbulent combusting flows with emphasis on ducted premixed systems, e.g. [1-5]. The motivations for the investigations include the improvement of ramjet and augmentor combustors and all have been concerned with simplified arrangements. The results have shown that for most of the cases the oscillations are acoustically-driven and occur for a wide range of equivalence ratios located within the flammability limits, e.g., [6]. The nature of the acoustic frequency has been readily identified and, with an unconstricted duct exit, usually corresponds to a quarter-wave with a pressure node close to the flame stabilizer in disc-stabilized flames and an anti-node in dump combustors. Comparatively small attention has been paid to the understanding of oscillations in non-premixed systems and most of the works published in the literature have been devoted to the analysis of the influence of the acoustics of the air supply system on the excitation of combustion-induced vibrations in industrial boilers, e.g. [7, 8]. This paper is concerned with the low-frequency oscillations which are known to occur in non-premixed flames confined in swirling combustors, such as those typical of many engineering systems, including gas turbines and furnaces.

The experiments were performed in the model combustor shown in figure 1 a), which allows the representation of the important features of the primary zone of practical combustors. It consists of an 186 mm I.D. cylindrical stainless steel tube, which was assembled in most of the experiments reported here with a length of 0.50 mm. The combustion air is provided through an annular pipe, 55 mm in diameter, which can be fed separatly through an axial entry to provide a non-swirling air flow (i.e., M_{ax}), or through a swirl chamber which generates a circunferential flow by the injection of air through tangential slots (i.e., M_{rot}). The swirling level is, therefore, variable and set by adequate control of the two air inlets. A diverging section is assembled at the end of the air duct, downstream of the confined tube, to allow the formation of a primary zone typical of practical combustors. It is surrounded by sixteen peripheral air jets, 10 mm in diameter, inclined at 4° towards the combustor axis. Propane gas is injected through the central injection

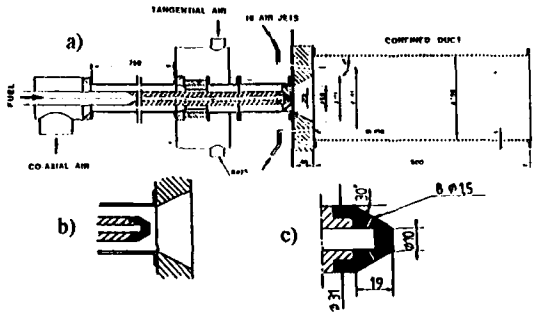

Figure 1. Schematic diagram of flow configuration

a) burner arrangement
b) geometry of primary zone
c) fuel injector

device shown in figure 1 c), which was assembled upstream the divergent quarl, as shown in figure 1 b). Optical access to the flow within the confined duct was provided by quartz windows, 30 mm large, located on the confined duct along the horizontal plane of symmetry.

The experiments presented here were obtained at atmospheric pressure for an equivalence ratio (based on the total primary air) in the range $\phi = 0.33$ to 4.0, representing a total energy dissipation up to 200 KW.

The sound intensity was measured by freefield condenser microphones with frequency responses which were flat up to at least 20 kHz. The sound radiated by the flow was measured with the microphone located approximately 1.5 m from the confining pipe, at 90° to its axis, although the results were found to be insensitive to the location. The local pressure fluctuations at the pipe wall were measured by connecting purpose-built probe tubes to the condenser microphones: the frequency response of the combination remained appropriate to the range of frequencies under consideration. The spectral content of the sound was determined by both an analog (constant percentage bandwidth) frequency analyzer and also by a fast Fourier transform algorithm operating on digitally sampled records of the sound.

Detailed mean temperature measurements were obtained with thermoucouples fabricated from 0.080 mm diameter platinum, 13% rhodium-platinum wire. The wires were supported on 0.500 mm diameter wires of the same material cemented with alumina (2.5 mm O.D. tube), which in turn was placed in a stainless steel tube of 4 mm O.D.. A long "L"-shaped probe was fabricated and introduced into the flame far downstream of the burner head in a way that minimized disturbing effects.

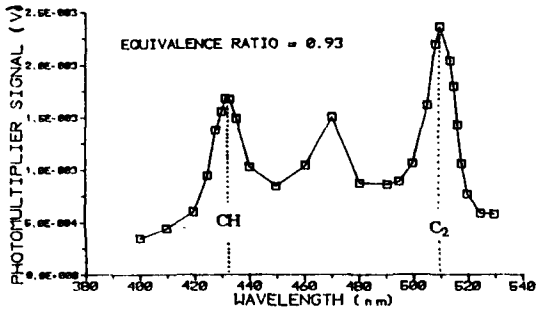

Figure 2. Wavelength scanning of light emitted by a typical flame (non-luminous) for $\phi = 0.93$ and $M_{ax}/M_{rot} \approx 0.526$.

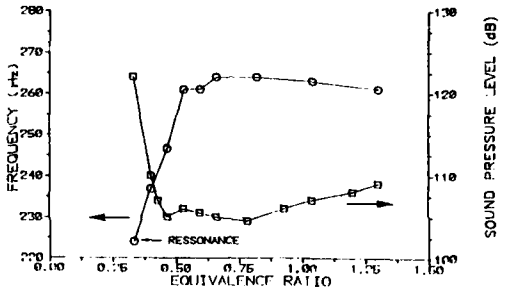

Figure 4. Predominant frequency of the sound emitted by the flames and associated energy of oscillations as a function of the equivalence ratio.

The rate of change of the heat release rate was monitored through the detection of the time-resolved emission of free radicals existing in the reaction zone, such as CH or C_2, [4]. Spectral radiation intensities were measured through the flame using a 1200 lines/mm grating monochromator (WDG 30) equipped with a photomultiplier (EMI-9658A) operating at room temperature. The optical system was set-up in order to allow a field of view of 4mm in diameter and, therefore, smaller than the smallest integral length scales of the turbulence (estimated to be roughly 15mm) in the region where most of the measurements were made. For the experiments discussed here a grating covering the wavelength range 380nm-760nm was used, which have allowed the detection of CH (λ = 431.5 nm) and C_2 (λ = 516.5 nm) radicals, figure 2, with a resolution of about 7nm at half-peak transmission. The spatial resolution of the system and wavelength readout were evaluated and calibrated using an Argon-Ion laser and uncertainties in the measurements are estimated to be less than 10%.

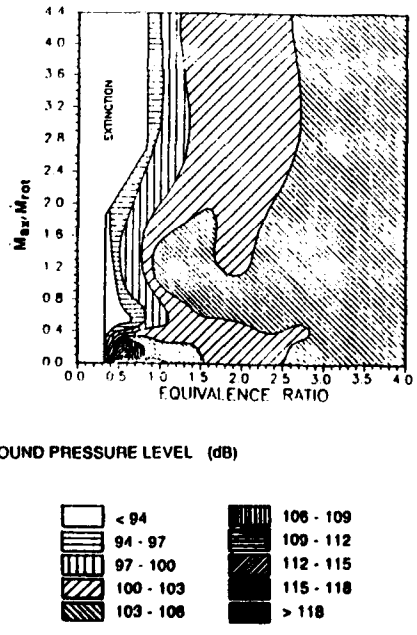

Figure 3. Sound pressure level as a function of equivalence ratio and swirl level.

Figure 3 shows the variation of the extinction limits and of the sound pressure level as a function of the equivalence ratio and swirl level and define the conditions for which high intensity combustion-induced oscillations occur (i.e., black zones in figure 3). These conditions are associated with sound levels higher than 110 db and are characterized by a single peak at 225 Hz in the frequency spectrum as defined in figure 4. This corresponds to the

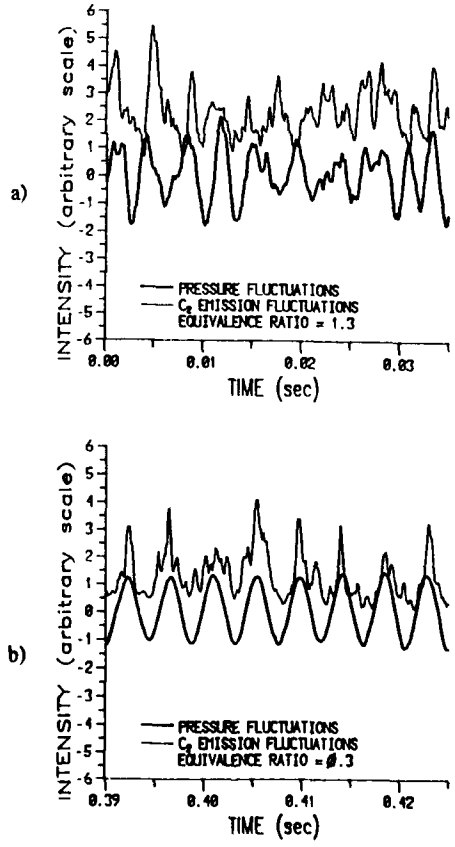

Figure 5. Sample time-resolved series of emission of C_2 radicals from the near-burner zone and sound level radiated from the combustor for a) steady combustion, 106 dB (ϕ = 1.3) and b) unsteady combustion, 122 dB (ϕ = 0.3).

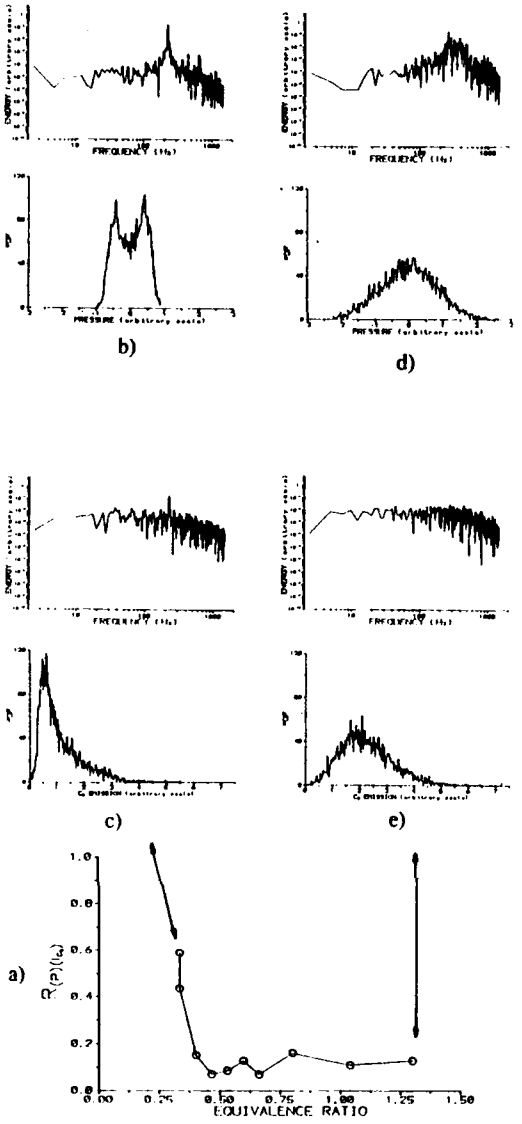

Figure 6. Statistical analysis of the light emitted from the near burner zone together with the sound pressure level

a) Correlation coefficient between C_2 emission and sound level as a function of equivalence ratio.

b) Frequency spectrum and probability density function of sound level for unsteady combustion ($\phi = 0.3$)

c) Frequency spectrum and probability density function of light emitted for unsteady combustion ($\phi = 0.3$)

d) Frequency spectrum and probability density function of sound level for steady combustion ($\phi = 1.3$)

e) Frequency spectrum and probability density function of light emitted for steady combustion ($\phi = 1.3$)

natural frequency of the combustor calculated for an average gas mean-temperature of 900 K and based on the excitation of a quarter-wave mode of a standing pressure-wave within the combustor. The effect of the geometry of the primary zone and of the fuel injector on the on-set of the oscillations is discussed elsewhere, [9]. Here we are concerned with the necessary coupling which should exist between the rate of change of the heat release rate with the pressure distribution in the combustor, so that the heat driven oscillation can be sustained. The chemiluminescent emissions of C_2 are interpreted as signatures of chemical reaction and, therefore, used to achieve this aim.

Figure 5 shows samples of time series of the emission of C_2 free radicals from the near-burner zone together with those of the sound emitted from the combustor for two different operating conditions, namely steady (a) and unsteady combustion (b). The randon nature of the two signals of the unsteady operation of the combustor is considerably altered with the on-set of the high intensity oscillations, which are characterized by typical periodic sound waves with the maxima coupled short rises in the emission of light. The statistical analysis of these time series is shown in figure 6, which identifies an increase of the correlation coefficient between the two signals from 0.1 to 0.6 with the on-set of the oscillations. This value is kept along the fuel length of the combustion, as expected for a standing wave and shown in figure 7.

The results are a clear evidence of the phase relationship between the varying rate of the heat release and the fluctuating component of pressure, which drives the oscillation. Perturbations in the turbulent heat release rate induce pressure fluctuations [e.g., 10] which, in turn, couple with the acoustic behaviour of the combustor when the extent of the zone where heat is released is limited to the pressure antinode located in the near burner zone. This occurs close to the extinction ($\phi \simeq 0.3$; see for example [9]) and is characterized by an abrupt change in the amplitude of the sound radiated from the combustor.

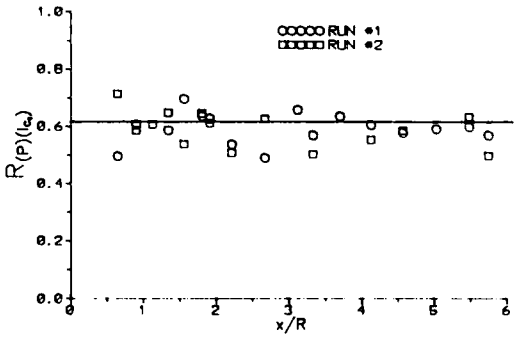

Figure 7. Correlation coefficient between C_2 emission from near burner zone and local pressure fluctuations along the combustor for unsteady combustion ($\phi = 0.3$).

REFERENCES

1. Heitor, M.V., Taylor, A.M.K.P. and Whitelaw, J.H. (1984). Influence of Confinement on Combustion Instabilities of Premixed Flames Stabilized on Axisymmetric Baffles. Comb. and Flame, 57, pp. 109-121.
2. Crump, J.E., Schadow, K.C., Yang, V. and Culick, F.E.C. (1986). Longitudinal Combustion Instabilities in Ramjet Engines: Identification of Acoustic Nodes. J. Propulsion and Power, 2, pp. 105.
3. Sivasegaram, S. and Whitelaw, J.H. (1988). Combustion Oscillations in Dump Combustors with a Constricted Exit. Proc. Instr. Mech. Engrs., 202 C3, pp. 205-210.
4. Langhorne, P.J. (1988). Reheat Buzz - An Acoustically Coupled Combustion Instability: Part 1 - Experiment. Cambridge Univ., Engng. Dept. Rept., Cambridge.
5. Hedge, V.G., Renter, D., Zinn, B.T. and Daniel, B.R. (1987). Fluid Mechanically Coupled Combustion Instabilities in Ramjet Combustors. AIAA 87-0216.
6. Sivasegaram S. and Whitelaw, J.H. (1989). Combustion Oscillations in Ducts. In: "Instrumentation for Combustion and Flow in Engines", ed. D.F.G. Durão et al, Kluwer Academic Publ., pp. 45-54.
7. Gupta, A.K., Syred, N. and Béer,J.M. (1976). Noise Sources in Swirl Burners. Applied Acoustics, 9, pp. 151-163.
8. Lawn, C.J. (1982). Criteria for Acoustic Pressure Oscillations to be Driven by a Diffusion Flame. 19th Symp. (Intl.) on Combustion, The Combustion Institute, pp. 277-285.
9. Fernandes, E.C., Heitor, M.V. (1990). On the Noise Characteristics of Confined Swirl Combustors. ASME Paper, 90-WA/HT-6.
10. Katsuki, M., Nizutani, Y., Chikani, M. and Kittaka, T. (1986). Sound Emission from a Turbulent Flame. 21st Symp. (Intl.) on Combustion. The Combustion Institute, pp. 1543-1550.

IUTAM Symposium on
Aerothermodynamics in Combustors
June 3-5, 1991, Taipei

KNOWLEDGE-BASED CONTROL OF OSCILLATIONS IN DUCTED PREMIXED FLAMES

E. Hendricks
Naval Ocean Systems Center, San Diego, Ca 92152-5000, USA
and
S. Sivasegaram and J. H. Whitelaw
Imperial College of Science Technology and Medicine, London SW7 2BX, UK

Rough combustion in ducted premixed flames is associated with oscillations of high amplitude dominated by an acoustic or a bulk-mode frequency of the duct. Passive methods of attenuation of oscillations [1-3] imply modifications to the geometry which may be inadmissible in many instances, and active control, which entails the imposition of oscillations on the mean flow, the pressure field or the heat release in the combustor to counteract the source of oscillations, could be an alternative. Although active control by the oscillation of the pressure field using a loudspeaker [4,5] has been demonstrated in combustors with heat release rates of up to 25 kW and by the oscillation of mean flow [6] for heat release rates of up to 250 kW, the high levels of input which may be needed at the large heat release rates of practical combustors are more readily provided by the oscillation of fuel [7,8,9]. Attenuation of oscillations can be further enhanced by improving the response of the input to the feedback. Adaptive control involves the modulation of the input in anticipation of the feedback and, in the absence of a universal transfer function relating the feedback to the oscillatory input, knowledge-based control with the input regulated on the basis of a periodically monitored feedback signal could be an option.

The present work concerns knowledge-based control of oscillations in premixed flames stabilised behind disks of area blockage ratio 0.25 and sudden expansions of area ratios 2.5 and 4.0 in ducts of diameter between 40 and 80 mm without and with exit nozzles for air and fuel flow rates of up to 3.0 and 0.15 kg/min, respectively, with heat release rates of up to 120 kW in the flow arrangements of Fig. 1. Air and fuel, mixed in a swirl register, flowed past a honeycomb flow-straightener, except in the arrangement of Fig. 1b where mixing was by impingement of radial jets of air and fuel, before combustion downstream of the flame holder. Control was mainly by the oscillation of secondary fuel injected upstream of the flame holder by a needle valve attached to a vibrator (Ling 403) driven by a power amplifier (Derritron TA120). The oscillation of the fuel was not quantified in absolute terms and some measurements were carried out, for purposes of comparison, with control by the oscillation of the pressure field using a diaphragm attached to the duct wall (Fig. 1a) and driven by the vibrator and using a 100 W wide range loudspeaker (Fig. 1b).

The control circuit was as shown in Figure 2 and the band-pass filtered (Krohn-Hite 3202) feedback signal from a pressure transducer (Kistler 6121 with charge amplifier 5007) was phase shifted and preamplified by a custom-built phase shifter which also monitored the feedback frequency. The software-controlled preamplified signal was incremented in the ratio $2^{\pm n/4}$ where n was any integer between 0 and 63, and the preamplified signal amplitude was maintained constant by setting n=0. Control was based on sampling the digitised (Data Translation A/D board DT2824-PGL) feedback for 5 ms in a microcomputer (Tandon TM-7104) and comparing the largest amplitude in that period with that of the previous sample and incrementing the preamplified input to the power amplifier through an interface board (Amplicon PC-14A). The amplitude and dominant frequency of the feedback were measured using an FFT spectrum analyser (Spectral Dynamics 340), the phase shift monitored by a dual beam oscilloscope (Tektronix 2225), and the feedback and preamplifier output recorded using a data recorder (Hewlett-Packard 3968A). Measurements also included the free-field sound level (Bruel & Kjaer meter 2215 with microphone 4134) in the exit plane of the combustor and 20 duct diameters from the axis.

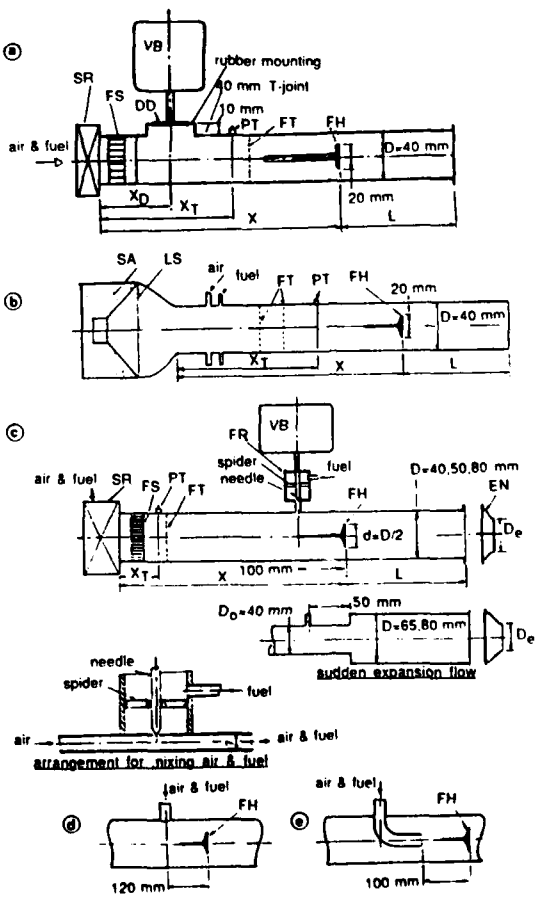

Figure 1: Burner Geometries

a) arrangement with oscillating diaphragm;
b) with loudspeaker; c) with direct injection of fuel;
d) modification of 1c for radial injection of secondary air and fuel; e) modification of 1c for axial injection.
DD - disk diaphragm, EN - exit nozzle, FH - flame holder, FT - flame trap, FR - fuel receiver, LS - loudspeaker, PT - pressure transducer, SA - sound absorbent packing, SR - swirl register, VB - vibrator

Figures 3 and 4 show that the attenuation of the 120 Hz quarter-wave oscillations in the arrangement of Fig. 1a was insensitive to phase within 30° of the optimum and to power input greater than the necessary minimum. The diaphragm was oscillated at constant amplitude and rms pressures of up to 2 kPa close to the antinode were attenuated by 10 dB, with the diaphragm located close to the antinode. The attenuation of sound level was, as in all other measurements in the present work, nearly the same as that in rms pressure. Attenuation of oscillations was less than 10 dB for rms pressures greater than 2 kPa because the maximum acoustic input was only 2 mW for a power input of 120 W to the vibrator.

The acoustic input was increased to 1 W in the arrangement of Fig. 1b, but the input was at a node of a 120 Hz half-wave frequency owing to the dimensions of the loudspeaker. Attenuation of 10 dB in rms pressures of up to 3 kPa close to the antinode was possible (Fig. 5a), but the feedback amplitude varied periodically (Fig. 5b) and when the peak amplitude of the feedback was less than 500 Pa the input lost lock with the feedback. Lock was regained when the amplitude recovered. This behaviour prevented further enhancement of attenuation with a constant amplitude of input. The use of knowledge-based control increased attenuation by 5 dB to 15 dB.

Of the three arrangements for control by oscillaton of fuel, axial injection of air and fuel (Fig. 1e) was the most effective *and rms pressures up to 3 kPa close to the antinode were* attenuated by 10 dB with a constant amplitude of oscillation of secondary fuel constituting 12% of the total (Fig. 6). Attenuation of rms pressures up to 4 kPa was possible with 18% of the fuel injected as secondary fuel and the use of knowledge-based control increased attenuation by 5 dB to 15 dB. Figure 6 also shows that insensitivity to phase was limited to 10° about the optimum compared with around 20° with the loudspeaker. This was possibly due to uncertainties in the mixing between primary and secondary flows and in the chemical reaction. The sensitivity of attenuation to phase and the dependence of optimum phase on flow conditions made it more difficult to impose control before the onset of oscillations of high amplitude than was possible with a loudspeaker.

Figure 7 shows the feedback traces for three values of the gain parameter n and Fig. 8 the influence of the gain parameter on attenuation for the flow conditions of Fig. 6. The variation in signal amplitude is a minimum and the attenuation a maximum for n=2. The dependence of attenuation on the gain parameter is, however, small so that the precise determination of transfer functions does not seem critical to active control of a single dominant frequency.

Bulk mode oscillations in ducts with an acoustically closed end and an exit nozzle were attenuated by about 8 dB for rms pressures of around 2 kPa by the oscillation of secondary fuel (Fig 9). Attenuation was poor at higher amplitudes, mainly because the instability was associated with poor flame stabilisation.

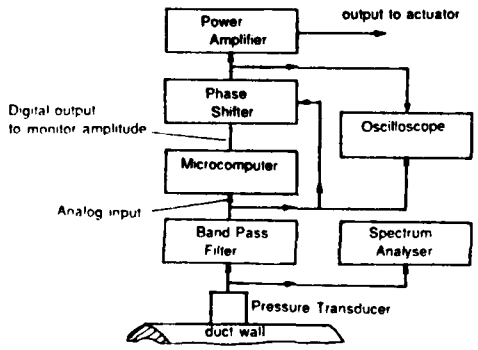

Figure 2: Knowledge-based control circuit

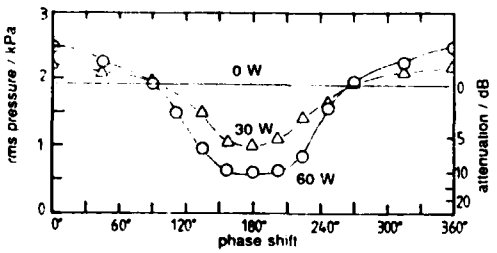

Figure 3: Influence of phase on oscillations

Geometry 1a, D=40 mm, X/D=17.5, L/D=7, X_T/D=5, X_D/D=2, U=mean upstream velocity=16 m/s, Re=UD/v=42 000, ϕ=equivalence ratio=0.85, heat release rate=45 kW

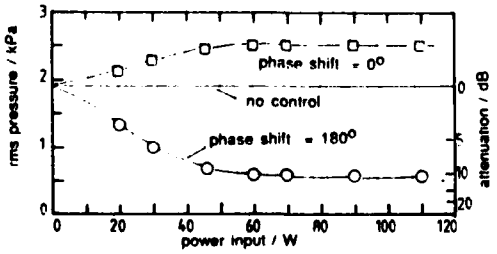

Figure 4: Influence of power input

Flow conditions as for Fig. 3; optimum phase.

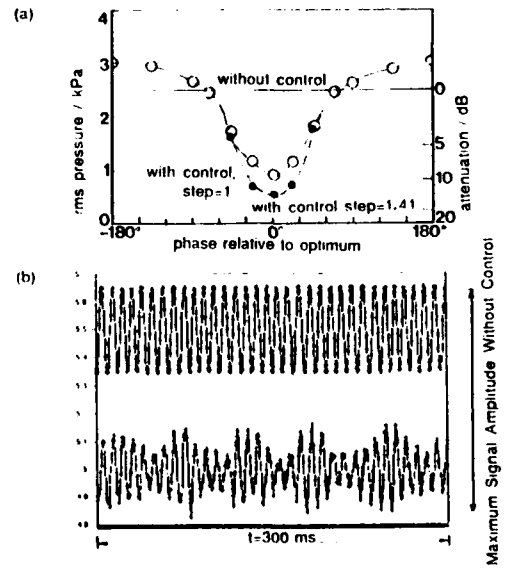

Figure 5: Control using loudspeaker

Geometry 1b, D=40 mm, X/D=35, X_T/D=17, L/D=8, U=16 m/s, Re=42 000, ϕ=0.83, heat release=45 kW. a) influence of phase on rms pressure, b) input (upper) and feedback (lower) signal traces for control with constant amplitude input.

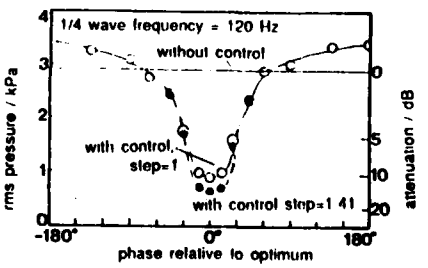

Figure 6: Control by oscillation of fuel

Geometry 1e without exit nozzle, D=40 mm, X/D=16.5, L/D=8, X_T/D=2, U=16 m/s, Re=42 000, ϕ=0.9 (12% of fuel injected as secondary fuel at ϕ=1.3), heat release=50 kW.

Control of quarter-wave oscillations at 200 Hz and a heat release rate of 80 kW in disk stabilised flames in a 40 mm duct resulted in attenuation by about 10 dB at rms pressures of up to 2.5 kPa. The smaller attenuation was possibly due to reduced oscillation of the fuel at the higher frequency and the distribution of heat release over a longer distance downstream of the flame holder at the higher flow rate. Quarter-wave oscillations at 200 Hz with rms pressures of up to 4 kPa near an antinode in sudden expansion flows with an area ratio of 2.5 and heat release rates of around 100 kW were attenuated by between 10 and 15 dB. Control was less effective for an area ratio of 4.0 due to high amplitudes of oscillation.

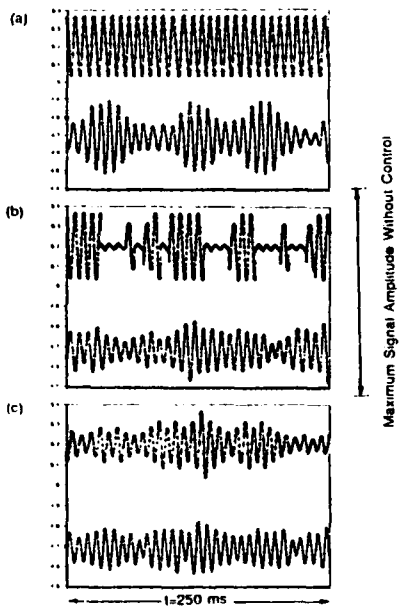

Figure 7: Influence of gain parameter on feedback signal

Flow conditions of Fig. 6. The upper trace is input and the lower feedback.
a) constant input amplitude, n=0; b) on/off control, n>>0; c) input voltage step ratio 1.41, n=2.

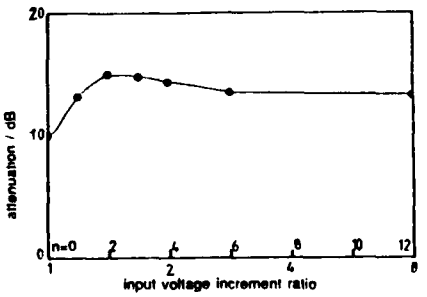

Figure 8: Influence of step size on attenuation

Flow conditions of Fig. 6; optimum phase.

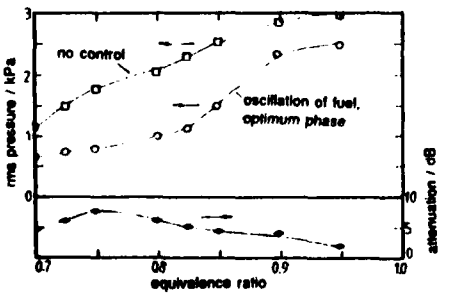

Figure 9: Control of bulk mode oscillations

Geometry 1e with exit nozzle, D=40 mm, X/D=10, L/D=6, D_e/D=0.7, X_T/D=2, U=16 m/s, Re=42 000, phase optimum. Approximately 10% of fuel injected as secondary fuel at ϕ=1

Table 1 compares the maximum attenuation in rms pressure close to a pressure antinode in the arrangements of Fig. 1 with values reported in earlier work. It is evident that attenuation greater than 20 dB is possible with rms pressures less than 2 kPa and heat release rates less than 25 kW. Higher amplitudes of oscillation associated with larger heat release rates are attenuated by up to 15 dB, which is comparable with the attenuation reported for passive control [2]. The 8 dB attenuation of [7] is possibly due to difficulties in modulating the oscillation of fuel in response to the feedback, and the attenuation of the low amplitude of oscillation in the 1 MW burner of [8] with a short duct is small possibly because of a small amplitude of oscillation of fuel.

TABLE 1: Attenuation of Oscillations in Ducted Flames

Geometry	Technique	Heat Release, kW	RMS Pressure, kPa	Attenuation, dB
Poinsot et al. [4]	Loudspeaker	25	1.7	22
Gulati & Mani [5]	Loudspeaker	1	0.2	33
Bloxsidge et al [6]	Oscillation of flow	250	4.0	15
Langhorne & Hooper [7]	Oscillation of fuel	250	4.0	8
Wilson et al. [8]	Oscillation of fuel	1000	small	6
Figure 1a	Oscillation of diaphragm	45	2	10
Figure 1b	Loudspeaker	50	3	15
Figure 1e (disk)	Oscillation of fuel	50	4	15
(sudden expansion)		100	4	15

References

1. Putnam, A.A., Murphy, M.J. and Locklin, D.W. (1985) Burner Technology Bulletin: Control of Combustion Noise for Small Gas Burners, Gas Research Institute, Chicago, Topical Report, GR1-85/210

2. Sivasegaram, S. and Whitelaw, J.H. (1987) J. Prop. Power 3, 291.

3. Schadow, K.C., Gutmark, E., Parr, T.P., Parr, D.M. and Wilson, K.J. (1986) Passive Shear Flow Control to Minimise Ramjet Instabilities, 23rd JANNAF Combustion Meeting.

4. Poinsot, T., Bourienne, F., Candel, S., Esposito, E. and Lang, W. (1989) J. Prop. Power 5, 14.

5. Gulati, A. and Mani, R. (1990) AIAA Paper 90-0270.

6. Bloxsidge, G.J., Dowling, A.P., Hooper, N. and Langhorne, P.J. (1988) AIAA J. 26, 783.

7. Langhorne, P.J. and Hooper, N. (1988) AGARD-CP-450, Paper 11.

8. Wilson, K.J., Gutmark, E., Schadow, K.C. and Smith, R.A. (1991) AIAA Paper 91-0368.

9. Hockey, R. and Sivasegaram, S. (1990) Knowledge-Based Active Control of Oscillations in a Premixed Disk-Stabilised Flame, Mech. Eng. Dept, Imperial College, London, Report FS/90/17.

IUTAM Symposium on
Aerothermodynamics in Combustors
June 3-5, 1991, Taipei

Dispersion and self-ignition characteristics of boronorganic compounds behind the shock waves.

B.E.Gelfand,S.A.Tsyganov,V.G.Slutskii,E.S.Severin

Institute of Chemical Physics,USSR Academy of Sciences,Moscow

Nearly complete absence of factual information on the behavior of the perspective boronorganic compound in high-speed and high temperature gas flows makes it difficult to draw competent conclusions about the prospects and limits of expedient using of this class of high energy compounds. The problem of full burning of powdered boron of various modifications of dispersions(including the combustible suspensions) urgently demands that the alternative ways of organizing the combustion process of boron containing fuels in gas(mainly air) flows be searched for. The most promising one is to use the compounds in which boron is contained at the molecular or atomic level,i.e. boronhydrids,carboranes and boronalkyles.

To clear up the comparative role of physico-mechanical and chemical factors at dispersion and combustion of carboranes in air (oxygen),peculiarities of dispersion of liguid carboranes behind the shock waves were investigated with carborane-10 derivatives. Despite their comparatively high viscosity carborane-10 derivatives were found to be dispersed thinner than the hydrocarbons under the same Weber and Reinolds numbers.

In the experiments with gaseous carborane-4 and liguid derivatives of carborane-10 the dependences of self-ignition delays upon temperature and pressure of the shock compressed air were determinated.Exceptionally high chemical activity of carboranes was observed.

Possibilities of using carborane-10 derivatives as promoters of self-ignition were noted for various kinds of hydrocarbon fuels.

IUTAM Symposium on
Aerothermodynamics in Combustors
June 3-5, 1991, Taipei

CATALYTIC IGNITION MODEL IN A MONOLITHIC REACTOR WITH IN-DEPTH REACTION

TA-CHING TIEN* AND JAMES S. T'IEN

DEPARTMENT OF MECHANICAL AND AEROSPACE ENGINEERING
CASE WESTERN RESERVE UNIVERSITY
CLEVELAND, OHIO 44106
U.S.A.

Catalytic igniter is a passive ignition device which requires no external energy source. After a combustible mixture is injected into the catalytic reactor, heterogeneous catalytic reactions are initiated spontaneously which triggers the homogeneous reactions. The granular bed catalytic igniter has been in use for many years in small rocket thrusters for the altitude control of satellites [1]. The use of monolithic bed catalytic combustors has been considered in gas turbines [2,3]. Recently, there has been interest in adopting monolithic reactor for the ignition of hydrogen/oxygen mixture in rockets [4].

A monolithic catalytic reactor consists of a solid substrate block with parallel flow channels (e.g., honeycomb). On the surface of the channel, a layer of porous material (i.e., alumina) is coated. Within the pores, catalysts are deposited (see Fig. 1). When the gaseous reactants flow through the channel, they diffuse toward the porous layer and into the pore. There they get absorbed and reacted, with a rate depends on the local temperature, concentration and the type of catalyst. The heat released in the reaction is transferred through this catalytic layer to both the substrate and the gas in the channel. When the temperature of the gas in the channel becomes sufficiently high, gas-phase reaction is triggered.

There are many rate processes involved in this ignition event: gas phase diffusion across the channel, reactant diffusion and heat conduction in the porous catalytic layer, heat conduction and heat-up of the substrate, gas transient through the channel and catalytic and gas-phase reactions. Estimation of the rates associated with these transient processes have been made which indicates the possibility of a large range of time scales [5,6]. Typically substrate heat-up is the slowest and mass diffusion across the catalytic layer is the fastest (chemical reaction rates are not included in this comparison because they vary greatly during the ignition transient). Although the formulation of a model including all the transient processes are straightforward, the actual numerical computation from fuel injection, ignition to steady state is too time consuming and impractical.

One way to accelerate the computational process is to assume quasi-steadiness for all the faster processes and only treating the substrate heat-up as unsteady. This was adopted in a number of transient models (e.g. [5]) but it bypassed the details in the initial unsteady period. Also, all the previous monolithic catalytic combustion models have assumed that the catalytic reaction occurs only on the surface of the substrate, i.e., there is no structure of the reaction zone within the porous catalytic layer. This is in contrast to earlier works on catalytic reaction in pellets where in-depth mass diffusion, heat conduction and reaction are treated (catalytic reaction only, no gas phase reaction). These works show that when the pellet temperature is low (before ignition), the reaction is kinetically-controlled and when the pellet temperature becomes high enough (after ignition), the reaction becomes diffusionally controlled.

In the present work, the transport and reaction processes inside the porous catalytic layer are included. In the mass diffusion and heat conduction equations, effective diffusion coefficient and heat conductivity are utilized. In the computation performed, the reactants are assumed to be a rich hydrogen-oxygen mixture and the catalyst is platinum.

A one-step catalytic reaction is assumed with rate constants taken from available experimental data. The model consists of two submodels: a full-transient submodel with all the unsteady processes (including the shortest mass diffusion in catalytic layer) and an energy-integral submodel which includes only the solid heat-up as the transient process and quasi-steady state for the rest. Both submodels are self-contained and can be run by itself. The energy-integral model is

*Present address: Aeronautical Research Laboratory, Chung-Shan Institute of Science and Technology, Taichung, Taiwan, ROC.

computationally efficient and is capable of catching only the longer time combustor responses. The full transient model, although capable of describing all the unsteady events, is computationally uneconomical. A logical approach is to combine the two if both the initial fast transient events and the computational economy are demanded. Such an approach is followed in this work which is described in detail in Ref. 6. The full-transient submodel is used initially because the early period of ignition process is fast. In a typical catalytic ignition process, all the processes become quasi steady except the solid heating-up after the initial transient. At that time we switch to the energy-integral model (with considerably larger integration time step) until the steady state is reached.

The following figures give an example of some of the computed results. Because of page limit, only the long-time behavior is shown here. Fig. 2 gives the in-depth profile in the solid (catalytic layer $1 \geq r \geq 0$, substrate, $3 \geq r > 1$) when the nondimensional time is equal to 3 (nondimensionalized by the solid heat-up time). Fig. 2(a) shows that the temperature gradient in the radial direction is uniform inside the substrate. There is only a small radial temperature gradient in the catalytic layer. Fig. 2(b), however, shows large oxygen gradient in both radial and axial directions. These produce very non-uniform reactivity contours shown in Fig. 2(c). Fig. 3 presents the axial profiles of temperatures, oxygen concentrations and reactivities at several different instances. When nondimensional time is equal to one, the catalytic surface temperature is higher than the gas temperature. Although catalytic reaction is significant, the gaseous reaction rate is negligible. When nondimensional time is two, small amount of gas phase reaction occurs at the end of the combustor. When nondimensional time reaches three, gas ignition is achieved at $x = 0.6$ and sudden temperature rise and abrupt drop of oxygen can be seen. At this time, steady state is practically achieved. Fig. 4 gives an ignition map. When the combustor length and catalyst loading are too small, no ignition occurs. When they become large enough both catalytic and gas-phase ignitions can be obtained. In between, catalytic ignition occurs but gas-phase ignition does not.

Detailed formulation of the models and computed results of various cases can be found in Ref. 6.

ACKNOWLEDGMENT

This work is supported by NASA Grant 3-809.

REFERENCES

1. Sackheim, R. L.: Survey of Space Applications of Monopropellant Hydrazine Propulsion Systems, Tenth International Symposium on Space Technology and Science, Tokyo (1973).

2. Pfefferle, W. C. and Pfefferle, L. D., Cat. Rev. Sci. Eng., 1987.

3. Kesselring, J. P.: Catalytic Combustion, Advanced Combustion Methods, Academic Press, ed., F. J. Weinberg, 1986.

4. Zurawski, R. L. and Green, J.: Catalytic Ignition of Hydrogen and Oxygen Propellants, AIAA Paper 88-3300 (1988), NASA TM 100957. Also Green, J. M.: A Premixed Hydrogen/Oxygen Catalytic Igniter, AIAA Paper 89-2302 (1989).

5. T'ien, J. S.: Transient Catalytic Combustor Model, Combustion Science and Technology, Vol. 26, pp. 65-75 (1981).

6. Tlen, T. C.: Catalytic Ignition Model in a Monolithic Reactor with In-Depth Reaction, Ph.D. Thesis, Department of Mechanical and Aerospace Engineering, Case Western Reserve University. Also Technical Report EMAE/TR-90-200 (1990).

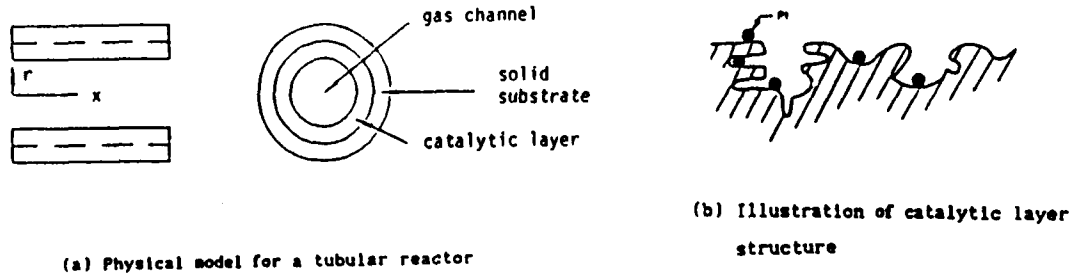

(a) Physical model for a tubular reactor

(b) Illustration of catalytic layer structure

Figure 1. Monolithic reactor model description

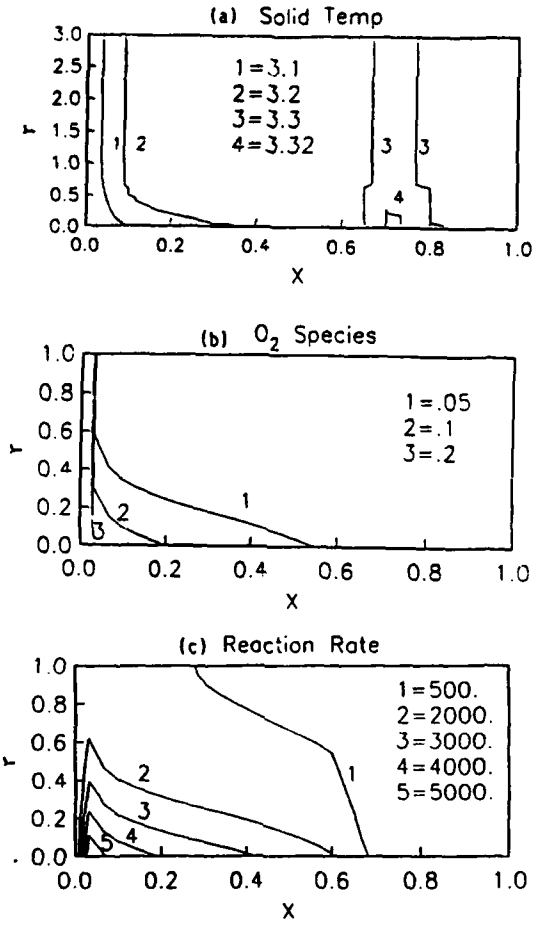

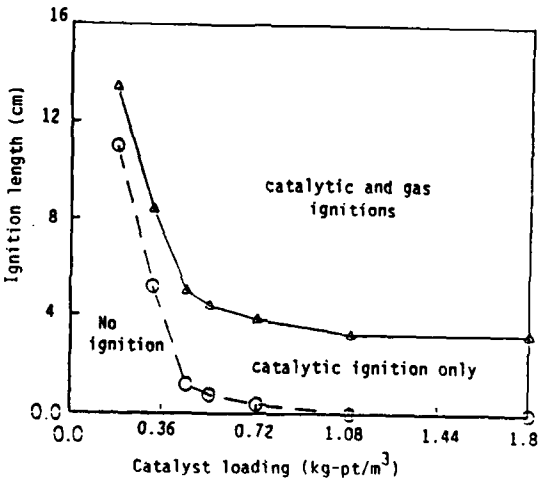

Figure 4 Ignition boundary map (u_∞ = 10 m/sec)

Figure 2. Example of solid contours at $t^* = 3\ \tau^*_{HT}$

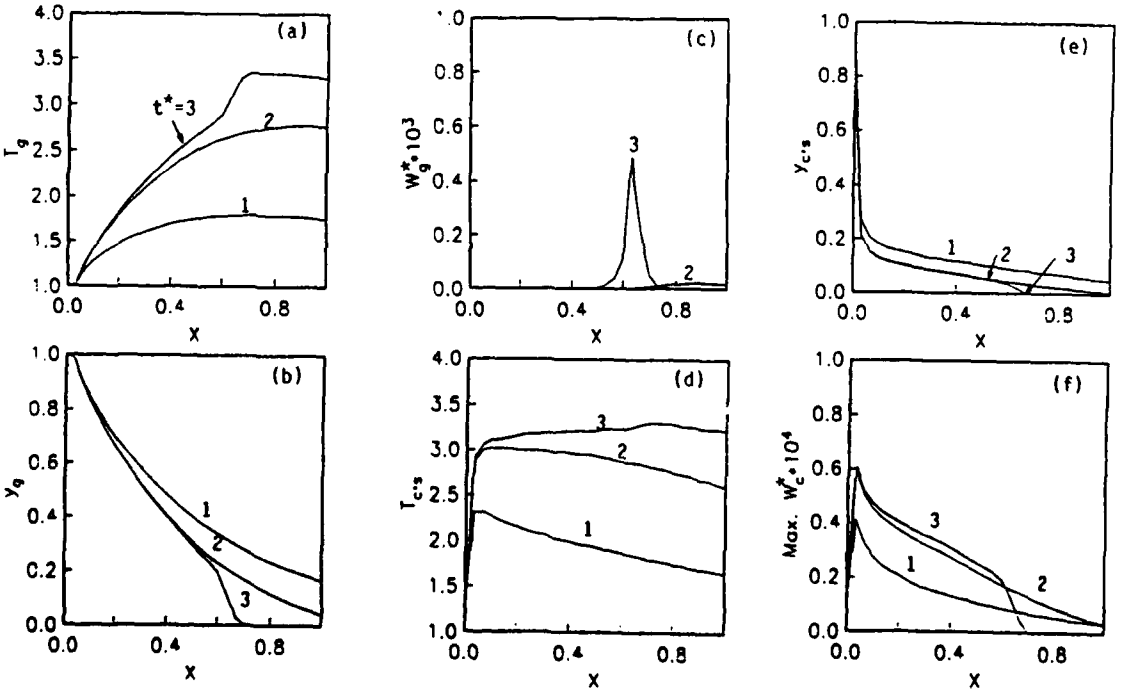

Figure 3. Example of transient profiles at $t^* = 1, 2, 3\ \tau^*_{HT}$ (β^* = 1.8 kg-pt/m^3, L^* = 5 cm, ϕ = 8)

IUTAM Symposium on
Aerothermodynamics in Combustors
June 3-5, 1991, Taipei

COMBUSTION OF HEAVY FUEL OILS IN A RIJKE TYPE PULSE COMBUSTOR WITH A TANGENTIAL INJECTION SYSTEM*

T. Bai, S. Shani, B. R. Daniel and B. T. Zinn

School of Aerospace Engineering
Georgia Institute of Technology
Atlanta, Georgia 30332

ABSTRACT

This paper describes the results of an investigation of the combustion of heavy liquid fuels in an insulated, Rijke type, pulse combustor which utilizes a recently developed tangential fuel and air injection system. This study was stimulated by the need to develop combustors which can burn low quality fuels, such as heavy fuel oils, with high combustion efficiencies and low pollutant emissions. It had been previously demonstrated that pulse combustors can burn various fuels with high combustion efficiencies and intensities while utilizing low excess air values. These attributes of pulse combustors are directly related to the presence of flow pulsations which increase the rates of mass, momentum and heat transfer within the combustor. Consequently, it had been expected that burning heavy liquid fuels in a pulsating flow environment will accelerate their rates of combustion and minimize pollutant emissions.

A Rijke type pulse combustor consists of a tube of length L which is open at both ends. Air is generally supplied at one end and arrangements are made to assure that the majority of the combustion process energy is released in a combustion zone that is concentrated at a distance of L/4 from the combustor entrance. This can be attained with solid fuels, such as coal and wood, by burning the fuel on a metal grid that is located at the L/4 position. This can be also accomplished with gaseous fuels by simply injecting them into the air stream in the vicinity of the L/4 position because gaseous fuels react rapidly once they are mixed. It is considerably more difficult to accomplish this goal with liquid fuels. To burn a liquid fuel in a Rijke type pulse combustor it is necessary to atomize, evaporate, mix and react the fuel within a short distance in the vicinity of the L/4 location. A liquid fuel burning Rijke pulse combustor which can attain this goal was developed earlier under this program while using kerosine and light fuel oils. In order to determine whether heavy fuel oils can be also burned efficiently in the developed combustor, the combustion of fuel oils Nos. 5 and 6 in this pulse combustor was investigated and the results are reported in this paper. Of special interest was the need to determine whether operational problems related to poor atomization, long flames, incomplete combustion, soot formation, heavy wall deposits and clogging of fuel lines and injectors, which are often encountered with these fuels in conventional combustors, will be also encountered in the developed Rijke pulse combustor.

The search for a method which permits combustion of liquid fuels within a relatively short region in a tube led to the development of a unique fuel/air injection system. A schematic of the developed Rijke pulse combustor which utilizes this injection system is shown in Fig. 1. It consists of a long, vertical, refractory lined, combustor tube that is attached to decoupling chambers at both ends to assure that the acoustic pressure nodes exist at the combustor exit and entrance planes. The combustion air is divided

* This research was supported by DOE Contract No. DE-AS04-85AL31881; Mr. Marvin Gunn, Contract Monitor.

into two streams. The axial stream enters the combustor through the upper decoupler while the remaining air is further divided into swirling and atomizing streams which enter the combustor with the fuel through the air/fuel injection system. The atomizing air stream is used to entrain the liquid fuel and the swirling air stream is used to provide the swirling flow rate necessary for stabilizing the combustion process. The resulting air/fuel mixture is injected tangentially into the combustor.

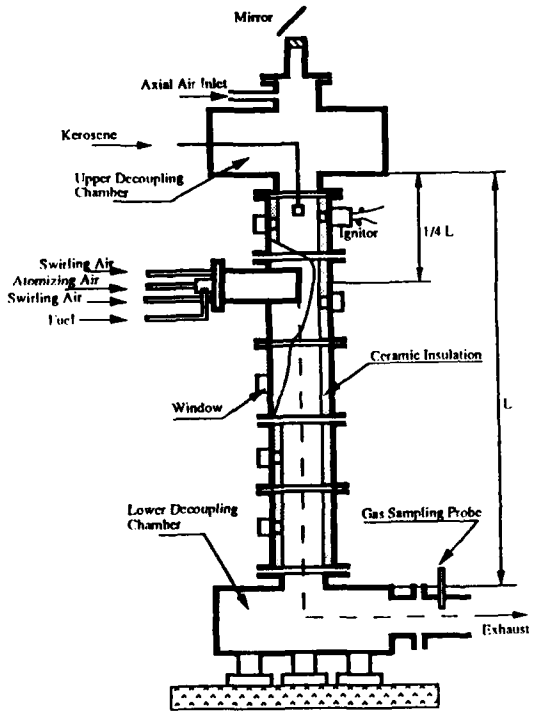

Figure 1. A Schematic of the Developed Insulated Liquid Fuel Burning Rijke Type Pulse Combustor with Tangential Air and Fuel Injection System.

To optimize the combustor performance, its dependence upon the relative flow rates of the axial, atomizing and swirling air flow rates were investigated initially. These tests were conducted by keeping two of the three air flow rates fixed and varying the third one and, thus, the overall air/fuel ratio. The performance of the combustor was determined from measurements of the amplitudes of the pressure and C-C radiation oscillations and the phase between the two. These tests revealed that the amplitude of pulsations decreased monotonically as the axial air flow rate increased, and that there exist ranges of atomizing and swirling air flow rates which maximize the amplitude of pulsations. Significantly, pulse combustion operation with amplitudes higher than 165 dB was attained at those flow rates for which the pulse combustion operation was optimized. The paper also presents the measured radiation amplitude and phase data and relates them to the Rayleigh's criterion and the measured pressure amplitudes. Furthermore, high combustion efficiencies were attained with less than 10% excess air. Finally, examination of the combustor walls after the tests revealed no carbon or tar accumulations and no smoke was visible in the exhaust flow during the tests, further indicating that the developed pulse combustor produced complete combustion of the heavy fuel oils.

The combustor shown in Fig. 1 is a duplicate of an identical, uninsulated, pulse combustor which had been developed earlier under this program. The insulated version of the combustor was developed in order to assess the effect of temperature upon the developed combustor performance. Comparisons of the performances of both pulse combustors under identical operating conditions revealed that the addition of insulation increased the maximum temperature inside the pulse combustor by approximately 100^0C and it decreased the amplitude of pulsations by several dB. The latter must be the result of sound attenuation by the refractory lining. More importantly, the addition of the refractory lining did not affect the range of operating conditions of the pulse combustor. These results indicate that unless there is a need to minimize heat losses from the combustor, there is no advantage in insulating the combustor, and operating at higher temperature.

IUTAM Symposium on
Aerothermodynamics in Combustors
June 3-5, 1991, Taipei

IGNITION TRANSIENT STUDY OF SEGMENTED SOLID ROCKET MOTORS

JIR-MING CHAR

DEPARTMENT OF AERONAUTICAL ENGINEERING
THE CHINESE AIR FORCE ACADEMY

This study describes the application of analytical techniques which are being developed to predict the ignition transients of segmented solid propellant rocket motors particular attention is given to the large, solid rocket motor (SRM) which is being developed for the Space Shuttle, Ariane 5, etc. The booster is refered to as a segmented motor (as opposed to a monolithic motor) since it consists of several large motor segments which are joined together. The development of large SRM's is accompanied by a number of questions pertaining to optimizing performance, improving reliability, and reducing the costs of qualification tests. During the formative phases of development, it is natural to employ analytical techniques that yield a more comprehensive understanding of complex interactions between the igniter gas flow, heat transfer to the propellant, flame spreading, developing flow field, erosive burning, and burn-back of propellant grains. Indeed, because of the costs of manufacturing and testing each solid rocket booster, predictions and design recommendations based on comprehensive analytical models can play an important role in defining the SRM configurations. While the emphasis of this research is on large SRM's, the methodologh is not dependent on motor diameter and thus can be applied to a wide variety of high length-to-diameter ratio motors. The igition transient comprises a complex series of interrelated events processed, such as 1)the initiation of igniter discharge signal; 2)heat generation caused by chemical reaction between igniter species; 3)conductive, convective, and radiative heat transfer from igniter products to the propellant surface; 4)flame spreading over the entire propellant surface; 5)development of the flow field in the chamber; and 6)increase of chamber pressure to the sometimes accompanied by many abnormalities, such as over-pressures, hang-fire (delayed ignition), damaging shock waves (detonation), combustion oscillation, chuffing, and extinguishment. For simulating the actual conditions in segmented solid rocket motors, however, several essential elements, which should be incorporated into the char's model [1] include: real gas effect, canted impingement-type pyrogen igniter, submerged exit nozzle, grain burn back, optional burning-rate law, dynamic thrust, and so on.

The primary objectives of the research described in this work are: 1) To advance the stated-of-the-art in the study of internal ballistics of modern segmented SRM, by upgrading the theoretical model, through the incorporation of a number of real factors encountered in actual rocket motors; 2) To develop a new version of the computer program and obtain analytical solutions which can help explain the physical mechanisms; and 3) to introduce the parametric study by changing the key parameters of the model, and observe the effects of these parameters on the internal ballistics.

Figure 1 is a sketch of the segmented solid rocket motor with a submerged nozzle and a pyrogen type head-end igniter. Three slots exist in the rocket motor. In fig. 2 a longitudinal section through slot is shown and nomenclature used in the analysis of slots are also given. The mathematical formulation of the approach to the above-described problem consists of the following:

(a) Mass, momentum, and energy conservation equations in unsteady, quasi-two-dimensional form for the gas phase;
(b) Equation of state for the gas flowing in the motor;
(c) Proper initial conditions at the start of the transient (onset of igniter-flow);
(d) Two boundary conditions at the fore-end of the propellant section, obtained from a pair of ordinary differential equiations, which describe the rate of change of pressure and temperature in the entrance section;

(e) Two boundary conditions at the aft-end of the propellant section, obtained from a pair of ordinary differential equations, which described the rate of change of pressure and temperature in the aft-end nozzle section;

(f) A third boundary condition, which described the gas velocity at the entrance to the motor nozzle, for either choked or unchoked flow;

(g) Semi-empirical correlations for the convective heat-transfer and friction coefficients for the highly turbulent flow in the port;

(h) Burning rate law for the solid propellant, including the effects of initial temperature, pressure, and velocity(erosive burning);

(i) A solid-phase heat-up equation for the determination of the propellant surface temperature during the induction interval, coupled to an ignition criterion for the solid propellant;

(j) A grain burn-back equation for the determination of the burning parameter and port area in the main chamber; and

(k) Thrust calculations based on nozzle-end stagnation pressure and the output of pyrogen igniter.

Goupling of the fluid flow processes between the several circumferential slots and the main chamber is accounted for by simultaneously sloving the continuity, energy and momentum equations for flow into (or out of) each slot and coupling the result with the complete PDE solution for the main chamber flow.

Figure 3 shows the pressure versus time relation at different locations in the main chamber. Small disturbance is observed in the initial stage of the flame spreading period. In fig. 4, temperature history in the motor at different locations are shown. In Fig. 5, the calculated velocity-time traces at three different locations are plotted. In the beginning, the velocity at the upstream location is faster than that at other locations. After t=0.1 *sec.*, the gas velocities become steady at all locations, and the velocity downstram is faster than the velocity upstream due to the higher mass flow rate. Fig. 6 shows the temperature history at various slots. One can see the temperature-rise-time in the slots is slower than that in the main chamber. This indicates the time required to flush the warm gases from the slots is appreciable. As shown in fig. 7, the net flow rate variation in the slots is quite complex. The flows entering and exiting the slots are closely coupled to the pressure wave that occur in the main chamber. The flow oscillations in the slots are complicated, since each slot has its own characteristic filling and venting time. During the flame spreading interval, the net flow is entering the slots. After ignition of the burning suface area in the slots, the small amount of mass is generated from the slots and approaches a constant level. It is also found that the mass flow entering and exiting the slots serve to damp the longitudinal instability waves. More detailed results and parametric study of this research will be given in the full paper.

REFERENCES

1. Char, J.M., "Simulation of Internal Ballistics of Large Solid Rocket Motors," Transaction of AASRC, Vol. 22, Taipei, Dec., 1989, p. 39-54.

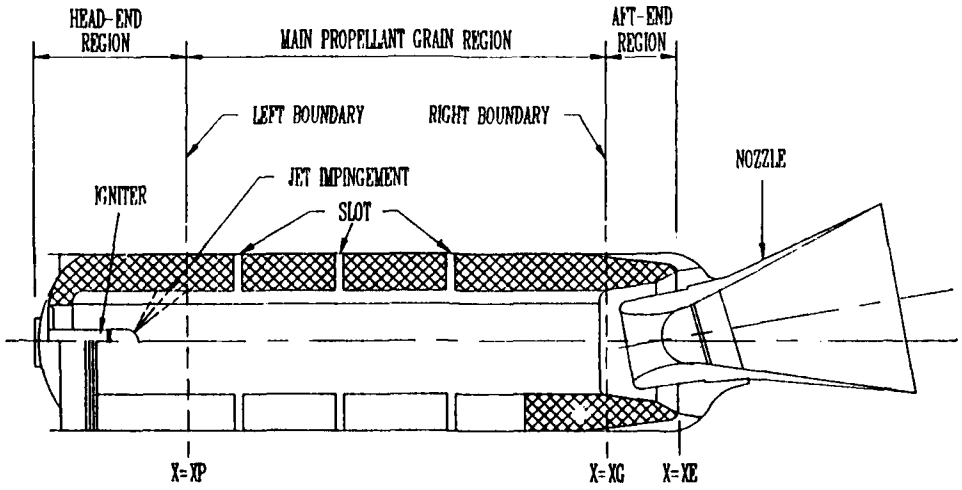

Fig. 1. Schematic Diagram of Analytical Model

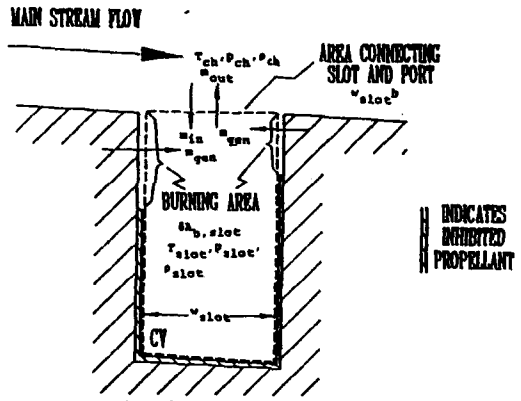

Fig 2. Longitudinal Section Through Slot Showing Nomenclature Use In Analysis of Slot

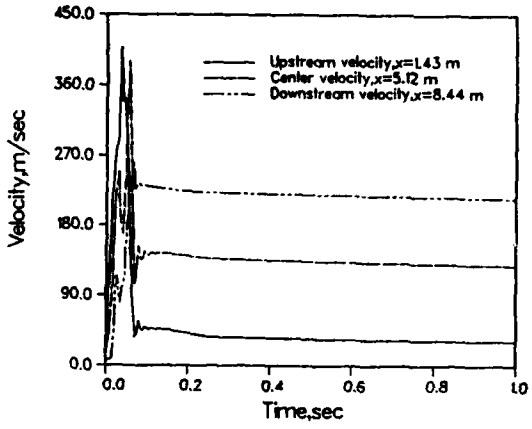

Fig 5. Calculated Velocity History at Various Locations

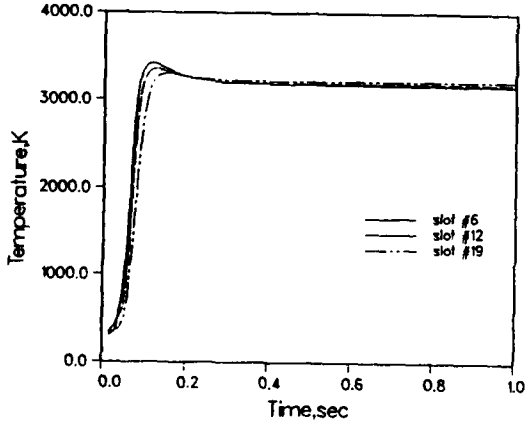

Fig 3. Calculated Temperature History of Various Slots

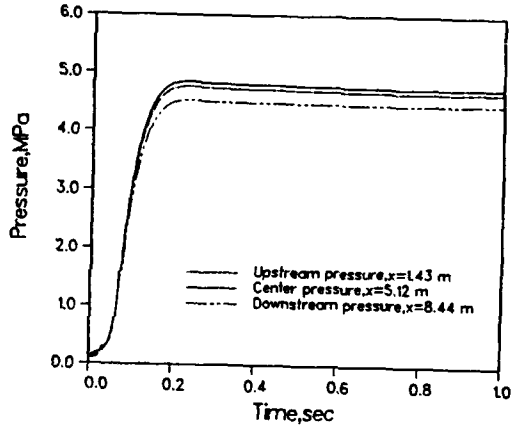

Fig 6. Calculated Pressure History at Various Locations

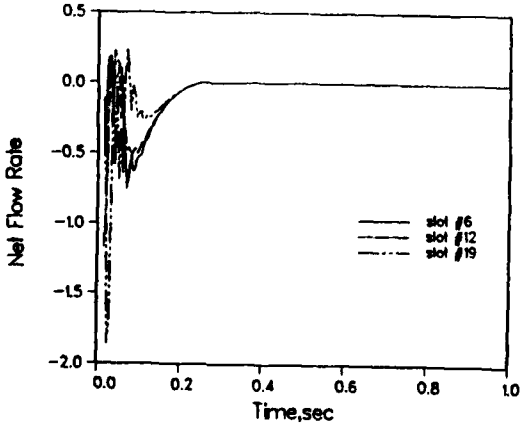

Fig 4. Net Flow Rate History of Various Slots
Distribution at Various Times

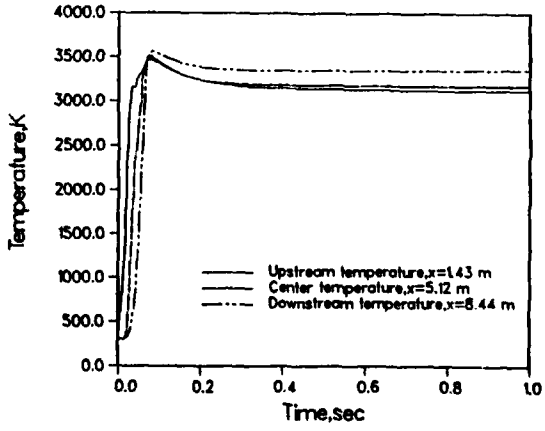

Fig 7. Calculated Temperature History at Various Locations

IUTAM Symposium on
Aerothermodynamics in Combustors
June 3-5, 1991, Taipei

Effects of Particle Loading on the Transition of A Plane Mixing Layer

M. R. Wang† and Y. C. Liu‡

Institute of Aeronautics and Astronatics
National Cheng-Kung University
Tainan, Taiwan, 70101, R. O. C.

Abstract

The plane mixing layer is loaded with polydispersed drops at the upstream of the high speed side. A two component phase Doppler particle analyzer (PDPA) is used to measure the size and velocity of the two phase flow. Results show that the initial momentum thickness and turbulence fluctuations of the gas phase in the boundary layer of central splitter plate increase due to the disturbances of the dispersed phase. Results also show that the momentum transport process is enhanced through the dispersed particle motion in the transition region of the mixing layer. This implies the higher developing rate than the single phase flow. Therefore, the transition region becomes shorter in the two phase mixing layer. Moreover, the turbulence intensities and Reynolds stresses of the two phase flow show its maximum in the near field of the mixing layer then decrease monotonously in the downstream, and those are lower than that of the single phase flow at fully developed region. It is interested to note that the vortex formation and merging processes which are prevailed in the single phase flow are not observed in the two phase flow condition.

Introduction

This paper investigates the transition process of a plane mixing layer under particles loading. The initial condition of the mixing layer determines the flow properties in the downstream and, in turn, is very important in determining the efficiency of a liquid or solid fueled combustion system. The single phase mixing layer problem has been widely studied in the literature. For example, Bradshaw[3] and Browand and Latigo[4] had studied the effects of initial conditions on the mixing layer flow by using trip controlling device. Both laminar and turbulent boundary layer conditions were conducted in their tests. Bradshaw[3] found that the increase of turbulent kinetic energy to a higher level in the mixing layer absorbs a large proportion of the available energy production for a considerable distance downstream when the initial boundary layer is turbulent. The self-preservation phenomenon is hence attained slowly. Browand and Latigo[4] also found that the lateral length scale, i.e. the momentum thickness, which characterizing the thickness of the mixing region, grows more slowly in a initial condition of turbulent boundary layer. Ho[8] further suggested that the length scale in the initial region of the mixing layer should be the thickness of the boundary layer on the high speed side and that is important in determining the flow structure downstream.

Koochesfahani[11] investigated the linear spatial instability characteristics of both uniform and nonuniform density plane mixing layers. He found that the shear layer mode dominates the wake mode when the density is uniform across the mixing layer. The wake mode, however, becomes comparable or even stronger than the shear layer mode if the density of the low speed stream is higher than that of the high speed stream. Moreover, Brown and Roshko[5] found that the spreading angle decreases as the density of the high speed gas stream is higher than that of the low speed stream. It is postulated that the density ratio of the two layers is also concerned with the development of the mixing layer.

The effect of particles loading on the fluid motion is due to the different inertia between phases and is depended on their size, relative velocity and the difference in densities. For example, in an attempt to investigate the velocity difference between phases, Ruck and Makiola[15] showed that the particles of 15 μm diameter deviate from the motion of the smaller particles in a backward-facing step flow. This phenomenon becomes more pronounced as the particle size increases and is further demonstrated by Wang and Liu[18] in their two phase mixing layer experiment. The effects of the particles loading on the flow turbulence were also studied in the literature. Rogers and Eaton[14] studied the response of solid particles to a vertical turbulent boundary layer in air. They found that, in the boundary layer, the velocity fluctuations of particles with 50 μm and 90 μm diameters are almost the same as flow turbulence of the continuous phase in the streamwise direction, but those in the normal direction are strongly attenuated. Tsuji et al[16,17] further studied the interaction between particle phase and the gas phase in the horizontal and vertical pipes. They found that the smaller particles result in suppression of the mainstream turbulence and the bigger particles, on the other hand, result in an increase of the flow turbulence

† Associate Professor
‡ Graduate Assistant

in the mainstream. Hetsronic[6] concluded the studies in the literature and suggested that particles with low Reynolds number, i.e. $Re_p < 100$, cause suppression of the turbulence, while particles with higher Reynolds number, i.e. $Re_p > 400$, cause enhancement of turbulence. The latter result is due to the wake phenomenon with the presence of the larger particles[1].

It can be seen from the above investigations that the dynamics of the two phase flow is quite different from the single phase flow due to the existence of the particles. This phenomenon becomes more complicated when the particles are loaded in the free shear layer flow. Hetsronic and Sokolov[7] and Modarress et al.[12] investigated the fully turbulent, two phase round jet and found the expansion rate and turbulence intensities of the jet flow decrease under particles loading. Interaction between phases in a plane mixing layer was further studied by Wang and Liu[18] in their experiment with polydispersed spray. They measured the dispersion rates and velocity fluctuations of the polydispersed spray in the mixing layer and identified the dispersion rates depend on each individual size. However, the above mentioned investigations do not cover the dynamic behavior of the particles in the transition region of the mixing layer which is very important in the understanding of the evolution processes of the particle motion from the separation point to the fully developed region. This paper first describes the characteristics of the initial conditions of the two phase flow at the splitter plate and then describes the evolution of the mixing layer under particles loading in the transition region. Comparison of the developing processes between the single phase flow and two phase flow are also carried out in this paper.

Experimental facility

Experimental works were conducted in a vertical tunnel as shown in Fig.1(a). This tunnel is divided into two independent flow paths by a center splitter plate. A perforated plate was placed in the upstream of the honeycomb to generate the required pressure drop for one of the flow paths. This will, in turn, result in the desired velocity difference of the two flow paths. The contraction ratio of the tunnel is 16:1 with a cross-section area of 15 cm × 15 cm at the test section. The free stream turbulence levels are less than 0.5% in both the low speed and high speed streams. The coordinate as shown in Fig.1(a) is selected such that the transverse coordinate Y is positive toward the high speed stream and the streamwise coordinate X is positive from the separation point toward the downstream. The polydispersed drops is supplied by a Sono-Tek ultrasonic nozzle located at 95 cm upstream of the test section in the high speed stream. The arrangement of the ultrasonic atomizing nozzle system in the settling chamber is shown in Fig.1(b). The turbulence generatd from the drops supply system is relatively low because the flow velocity in the settling chamber is as low as 0.625 m/s. The central splitter is less than three degrees to ensure a parallel flow at initial condition. The trailing edge of the splitter plate extends 15 cm into the test section. Consequently, the drops become equilibrium with continuous phase before leaving the splitter plate. The atomizing nozzle was operated at a flow rate of 25.0 ml/min with water. Experiments were performed under the condition that the high speed stream velocity, U_1, equals to 10.0 m/s and the low speed stream velocity, U_2, is changed to achieve the required velocity ratios. The velocity ratio, $R = \Delta U/2\overline{U}$, is defined as the ratio of the shear velocity, $\Delta U = U_1 - U_2$, to the convection velocity, $\overline{U} = (U_1+U_2)/2$. The sauter mean diameter and number density of the polydispersed drops under this condition are 50 μm and 1200 #/c.c, respectively.

The two-component phase Doppler particle analyzer (Aerometric model PDP-3200) was used to measure the velocity distribution, particle size, number density and volume flux of the polydispersed drops in the plane mixing layer. The local averaged quantities are calculated by colleting 30,000 samples for every measurement point. The detailed description of the system has been described by Bachalo and Houser[2]. To distinguish the velocity of continuous phase from the dispersed phase the system is seeded with smoke particles of size less than one micrometer. The velocities of both phases are then determined by the statistical calculations.

Results and Discussion

Results under a velocity ratio of 0.64 is described in this paper. Figure 2 shows the initial distributions of the number density and sauter mean diameter of the polydispersed drops measured at X = 0 mm. Those at 20 mm are also illustrated in this figure as a comparison. It can be seen from this figure, the sauter mean diameter is quite uniform initially at X = 0 mm. Moreover, at X = 0 mm, the local number density is almost uniform in the high speed stream and the local number density near the wall of the splitter plate is declined because of the boundary layer effect. Comparing the variations of number density and sauter mean diameter at X = 0 mm and 20 mm locations (see Fig.2), it seems that the changes of the number density and sauter mean diameter are not significant except in the shear layer. The variation of the number density distribution in the shear layer indicates the particle dispersion. As shown in Fig.2, the particle number density in the shear layer at X = 20 mm is higher than that at X = 0 mm. The existence of particles at X = 20 mm in the low speed stream (i.e., Y < 0) indicates the particle dispersion from the higher speed stream. However, the size of the drops found in the low speed side is much smaller than that in the high speed side, implying that the dispersion rate of the smaller particles is higher than the larger ones at X = 20 mm.

In an effort to investigate the dynamics of the two phase flow, measurements of the aerodynamic properties of the gas phase and the dispersed phase are carried out in this paper. The aerodynamic properties presented in this paper are normalized by a characteristic flow velocity, U_1, which is measured in the high speed stream without particle loading, i.e., under the single phase flow condition. Figure 3(a) depicts the evolutions of the mean streamwise velocities of each phase from X = 0 mm to 20 mm. As shown in this figure, the velocity profiles of the continuous phase without particle loading at X = 0 mm fit the Blasius profile quite well on both sides of the splitter plate. However, the velocity profile of the gas phase at high speed side under particles loading is different from the above result. The boundary layer thickness of the gas phase

under particles loading is thicker than that of the single phase flow due to the momentum transport from the dispersed phase. Analysis shows that the momentum thickness of the continuous phase in the high speed side increases 1.7 times of the single phase flow from 0.50 mm without particle loading to 0.85 mm under particles loading. Figure 3(a) also shows that the initial velocity of the single phase is lower than that of the two phase flow near the wall. The lower velocity of the single phase flow is attributed to the viscous effect near the wall. The higher velocity of the two phase flow near the wall may include the momentum transport of the particle (which is with higher inertia) into the boundary layer.

The velocity deficits of both the single phase and two phase flow conditions are observed at X = 5 mm station (see Fig.3(a)). However, at X = 20 mm, the velocity deficit occurs only under single phase flow condition. Results show that the streamwise velocities near the centerline region under the two phase flow condition are higher than that of the single phase case in the transition region. As has been shown in Fig.2, there are significant dispersion of particles with higher momentum from the high speed stream into the low speed gas stream. Therefore, the velocity of the continuous phase near the centerline region is accelerated by these dispersing drops. This explains the higher velocity of the two phase flow in the centerline from X = 5 mm to 20 mm. It also explains the earlier completion of the wake mode under two phase flow condition.

The evolutions of streamwise velocity fluctuations of each phase in the near field of the mixing layer are illustrated in Fig.3(b). As can be seen from this figure, the turbulence intensities of the two phase flow are almost the same as that of the single phase flow in the free stream. This implies that the flow conditions in the free stream remain the same under the particles loading. However, the turbulence levels of both the gas phase and dispersed phase in the two phase flow are higher than that of the single phase flow in the boundary layer at X = 0 mm. The higher velocity fluctuations near the wall under two phase flow condition are due to the momentum transport between the two phases. It also can be seen from this figure, the initial turbulence fluctuations of the single phase flow are not significant at X = 0 mm and 5 mm, comparing that under two phase flow condition. It has been known that the mixing layer of the single phase flow grow based on the Kelvin-Helmholtz instability mechanism and the vortex formation and merging processes occur in the downstream. However, these phenomena are quite different in the two phase flow condition. The profiles of the velocity fluctuations of both phases in the two phase flow are similar from X = 5 mm to 20 mm in the high speed side (see Fig.3(b)). It seems that the turbulence intensities of the two phase flow does not grow at the high speed side. On the other hand, as can be seen from this figure, the intensities of the gas phase in the shear layer of the low speed stream increase when the particles entrain into the low speed side. It is revealed obviously at the position X = 20 mm in Fig.3(b), the dispersing drops from the high speed side enhance the gas phase at the low speed stream. This also indicates that the dispersing drops from the high speed side transport the momentum to the gas phase in the low speed side. It also shown that the distributions of the peak intensities under the two phase flow condition at X = 20 mm are deviated toward the low speed side.

References

1. Achenbach, E, "Vortex Shedding from Spheres," *J. Fluid Mech.* Vol. 62, 1974, pp. 209-221.
2. Bachalo, W. D. and Houser, M. J., "Phase/Doppler Spray Analyzer for Simultaneous Measurements of Drop Size and Velocity Distributions," *Optical Engineering*, Vol. 23, No. 5, 1984, pp. 583-590.
3. Bradshaw, P., "The Effect of Initial Conditions on the Development of a Free Shear Layer," *J. Fluid Mech.*, Vol.26, 1966, pp. 225-236.
4. Browand, F. K. and Latigo, B. O., "Growth of the Two-Dimensional Mixing Layer from a Turbulent and Nonturbulent Boundary Layer," *Phys. Fluids*, Vol. 22, June, 1979, pp. 1011-1019.
5. Brown, G. L. and Roshko, A., "On Density Effects and Large Structure in Turbulent Mixing Layers," *J. Fluid Mech.*, Vol. 64, 1974, pp. 775-816.
6. Hetsroni, G., "Particles-Turbulence Interaction," *Int. J. Multiphase Flow*, Vol. 15, No. 5, 1989, pp. 735-746.
7. Hetsroni, G. and Sokolov, M., "Distribution of Mass, Velocity, and Intensity of Turbulent in a Two-Phase Turbulent Jet," *J. Applied Mech.*, June, 1971, pp. 315-327.
8. Ho, C. M. and Huang, L. S., "Subharmonics and Vortex Merging in Mixing Layers," *J. Fluid Mech.*, Vol. 119, 1982, pp. 443-473.
9. Hsiao, F. B., "Small Scale Transition and Preferred Mode in an Initially Laminar Plane Jet," Ph. D. thesis, University of Southern California, Los Angeles, 1985.
10. Huang, J M., "On the Evolution of Instabilities and Vortex Interaction Processes in the Developing Region of a Plane Jet," Ph. D. thesis, Institute of Aeronautics and Astronautics National Cheng-Kung University, 1989.
11. Koochesfahani, M. M. and Frieler, C. E., "Instability of Nonuniform Density Free Shear Layers with a Wake Profile," *AIAA Journal*, Vol. 27, No. 12, 1989, pp. 1735-1740.
12. Modarress, D., Tan, H. and Elghobashi, S., "Two-Component LDA Measurement in a Two-Phase Turbulent Jet," *AIAA Journal*, Vol. 22, No. 5, 1984, pp. 624-630.
13. Rashidi, M., Hetsroni, G. and Banerjee, S., "Particle-Turbulence Interaction in a Boundary Layer," *Int. J. Multiphase Flow*, Vol. 16, No. 6, 1990, pp. 935-949.
14. Rogers, C. B. and Eaton, J. K., "The Interaction between Dispersed Particles and Fluid Turbulence in a Flat Plate Turbulent Boundary Layer in Air," Report MD-52, Stanford Univ., Calif.
15. Ruck, B. and Makiola, B., "Particle Dispersion in a Single-Sided Backward-Facing Step Flow," *Int. J. Multiphase Flow*, Vol. 14, No. 6, 1988, pp. 787-800.
16. Tsuji, Y. and Morikawa, Y., "LDV Measurements of an Air-Solid Two-Phase Flow in a Horizontal Pipe," *J. Fluid Mech.*, Vol. 120, 1982, pp. 385-409.
17. Tsuji, Y., Morikawa, Y. and Shiomi, H., "LDV Measurements of an Air-Solid Two-Phase Flow in

a Vertical Pipe," *J. Fluid Mech.*, Vol. 130, 1984, pp. 417-434.

18. Wang, M. R. and Liu, Y. C., "Behavior of Polydispersed Sprays in a Plane Mixing Layer," *ASME-JSME Forum on Turbulent Flows*, Portland, June, 1991.

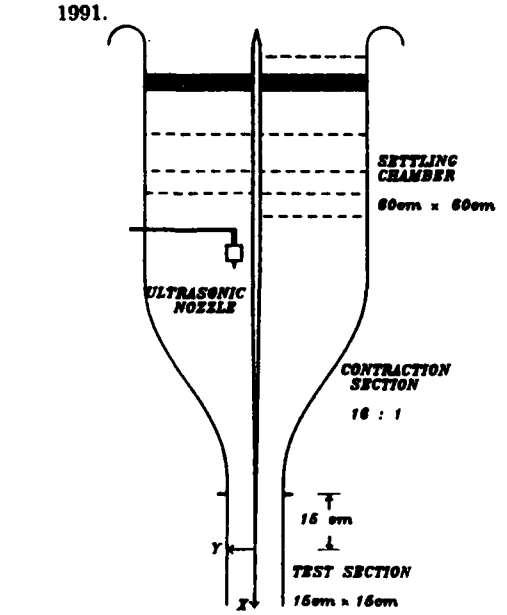

Fig.1 Experimental facility

(a) schematic of the two phase mixing layer tunnel

(b) arrangement of ultrasonic atomizing nozzle system

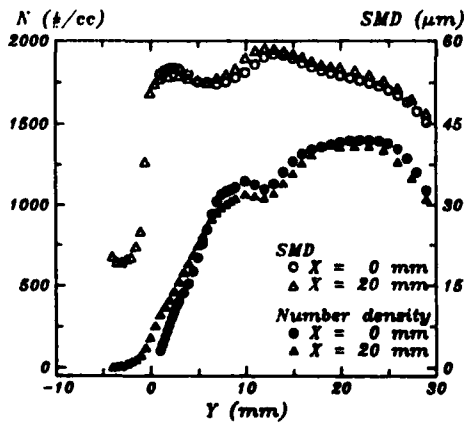

Fig.2 Distributions of number density and sauter mean diameter of the polydispersed drops at X = 0 and 20 mm

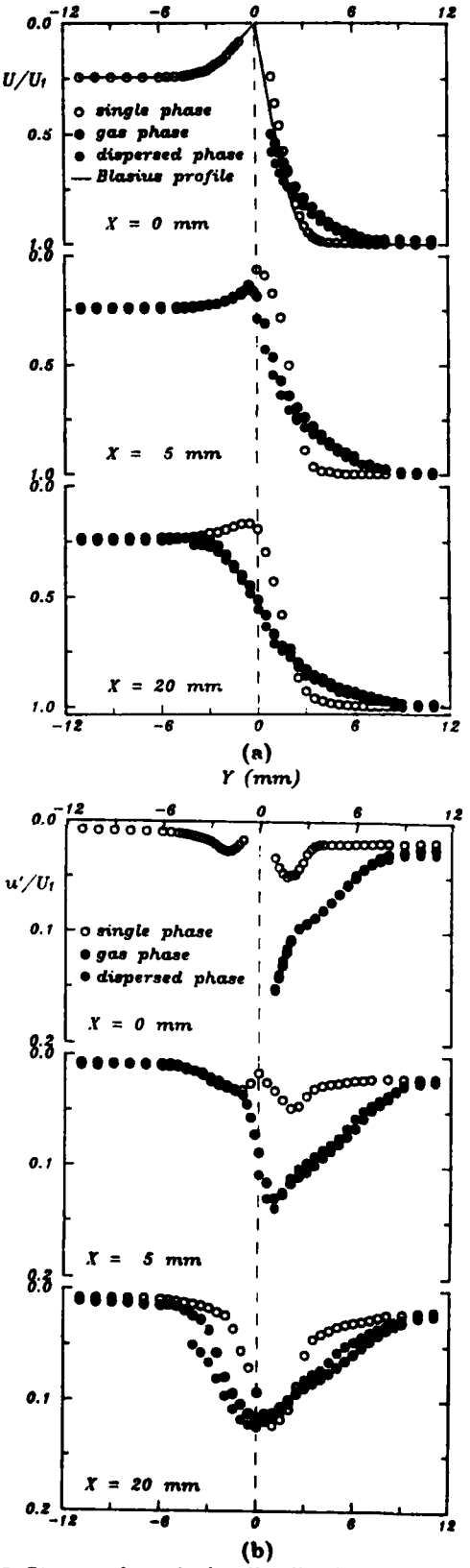

Fig.3 Streamwise velocity distributions of each phase in the transition region of the mixing layer

(a) mean velocity

(b) velocity fluctuation

IUTAM Symposium on
Aerothermodynamics in Combustors
June 3-5, 1991, Taipei

A COMBINED ELLIPTIC-PARABOLIC SOLUTION PROCEDURE FOR ANALYSIS OF PARTICLE-LADEN JETS

W.J. Wu and K.C. Chang

Institute of Aeronautics and Astronautics
National Cheng-Kung University
Tainan, Taiwan / R.O.C.

INTRODUCTION

Two-phase turbulent phenomena are fundamental importance in many flow systems of engineering practices. Applications in which two-phase turbulent jets occur include liquid-fuel combustors, pulverized-coal combustors, solid rocket nozzle, exhaust plumes, aerosols, etc. Strong couplings between the continuous and dispersed phases are the primary characteristics of these flows. It has been shown [1] that the inclusion of particles (or droplets) in turbulent flows might significatly change the turbulence structure. However, due to current progress in laser optical diagnostics, considerable experimental efforts have provided available data base of two-phase flows for evaluating the modeling analysis and have consequently led to the development of new theoretical methods in analyzing two-phase turbulent flows.

There are two fundamentally different methods generally used to predict the dispersed properties in two-phase flows [2]. One which is termed as the Lagrangian or tracking approach treats the particles as discrete entities in a flow field and the dispersed phase properties are calculated by using the Monte Caro procedure. The effect of particles on fluid is accounted for by estimating the particle source terms for each computational cell visited by the particles and by a recalculation of the flow field incorporating these source terms. The other method is termed as the Eulerian approach or two-fluid model. In this method, the cloud of particles is regarded as a continuum and the resulting, governing equations in partial differential form are simultaneously solved for both continuous and dispesed phases. The interactions between phases are incorporated with extra source terms appeared in the governing equations for both phases.

Durst [3] examined these two different methods and showed that the Lagrangian approach has advantage in predicting the two-phase turbulent flows which are consisted of polydispersed particle size distribution, while the Eulerian approach is numerically less expensive and has advantage for the two-phase flows associated with relatively high particle number density. Adeniji-Fashola and Chen [4] also came to similar conclusion.

It seems that all predictions for particle-laden jets, regardless of Lagrangian approaches [5-8] or Eulerian approaches [9-11], adopt the boundary layer approximation to simplify mathematical formulism; the governing equations, thus, become parabolic type. Nevertheless, some experimental observations [5, 12, 13] revealed that the axial pressure gradients and local recirculation zones were very likely to be present in the flow fields. In addition, Soloman [14] showed that at the downstream distance of 50 diameters of spray injector in a spray, the ratio of radial velocity component to axial velocity component for the dispersed phase along the spray boundary is about 0.7. In contrast, the employment of boundary layer approximation requires the condition that this velocity ratio should be in the same order of $1/Re$ which is much smaller (by a factor of 10^{-3}) than the ratio of droplet velocity components. These experimental observations imply that the boundary layer approximation may be inappropriate and the governing equations are elliptic type in near-inlet regions.

In this work, a combined elliptic-parabolic solution procedure is used for analysis of particle-laden jets. In the upstream region where the presumption of boundary layer approximation is invalid, the problem is solved by using the elliptic-type governing equations; the remaining regions are, next, solved by the mathematically simplified parabolic-type ones.

EXAMINED PROBLEM

The experiment of particle-laden jet conducted by Shuen et al. [5], which has been often selected as a comparison basis of model predictions [5,6,15,16], is considered as the first test case. The injector is an axisymmetrical tube with the diameter (D) of 10.9 mm from which the particle-laden jet directed vertically downward. Sand particles of 79 μm nearly uniform size and material density of 2,650 kg/m^3 were introduced into the jet tube. The centerline velocities for gas (u^o_{gc}) and particles (u^o_{pc}) measured at $x/D = 1$ are 26.1 and 24.1 m/s , respectively. Since this particle-laden jet is of dilute cases (the mass loading ratio is 0.2 or the particle volume fraction is 9×10^{-5}), the Lagrangian approach is employed to treat the dispersed phase in this work.

Turbulent jet flow field is determined by the $k-\varepsilon$ model with the modification of Jones and Launder [17] in which th C_μ and C_2 are expressed by

$$C_\mu = 0.09 - 0.04\, f \tag{1}$$

$$C_2 = 1.92 - 0.0667\, f \tag{2}$$

where

$$f = \left|\frac{R}{2u_{gc}}\left(\left|\frac{du_{gc}}{dx}\right| - \frac{du_{gc}}{dx}\right)\right|^{0.2} \tag{3}$$

u_{gc} denotes the centerline velocity for the continuous phase and R is the local jet width. The Lagrangian approach adopts the stochastic seperated flow (SSF) formulation and follows after those outlined by Refs. 5 and 18. The effect of turbulence modulation is modelled by that developed by Chen and Wood [10]. The numerical scheme adopted for the Lagrangian approach follows the PSI-Cell method [19]. To obtain a statistically stationary solution, 3000 representative particle groups are employed in this work in contrast to 2000 particle groups of Shuen et al. [5] and 1500 particle groups of Adeniji-Fashola and Chen [4].

RESULTS AND DISUCSSION

The predictions using the combined elliptic-parabolic solution procedure are compared with those using the conventional parabolic solution procedure for jet flows. Determination of jet length in the near-inlet region required for the elliptic solution procedure has been made by running with different lengths of the computational domain. Comparison results reveal that the flow becomes parabolic, i.e. $du/dx = 0$, when the length reaches 15 D. Thus, for the combined elliptic-parabolic solution procedure, the flow in the upstream domain (length of 15 D) is solved with the elliptic-type equations. The predicted profiles of two-phase flow properties at the outlet of the front domain are used as the inlet boundary conditions required for the parabolic-type computation in the rear domain of the particle-laden jet. Note that, due to lack of the measured radial velocity components at the inlet ($x/D = 1$) for both phases in the experiment of Shuen et al. [5], the uniform profiles of zero radial velocity components are assumed to be the required inlet boundary conditions at the axial station of $x/D = 1$ for computation.

Figure 1 compares both predicted centerline axial velocities using the combined elliptic-parabolic and conventional parabolic solution procedures with the measurements for both phases. The use of the combined elliptic-parabolic solution procedure improves the prediction accuracy in the upstream regions for the continuous phase (see Fig. 1a) where the boundary layer approximation does not work successfully as we anticipated, whereas results in much overpredictions in the downstream regions. Figure 2 compares both predicted sectional profiles of axial velocity for the continuous phase using the combined elliptic-parabolic and conventional parabolic solution procedures with the measurements at two axial stations. Since both axial stations of $x/D = 20$ and 40 are outside of the region of the elliptic-type flow field ($x/D = 15$), those two different solution procedures

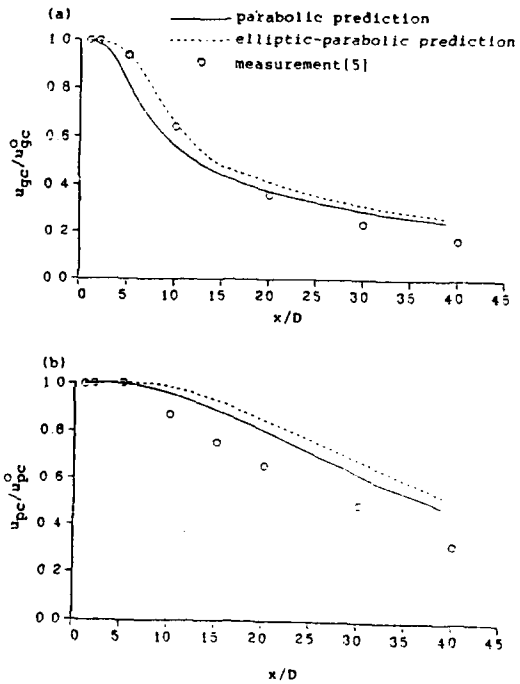

Fig. 1 Comparison of axial variations of centerline axial velocity for (a) continuous phase and (b) dispersed phase.

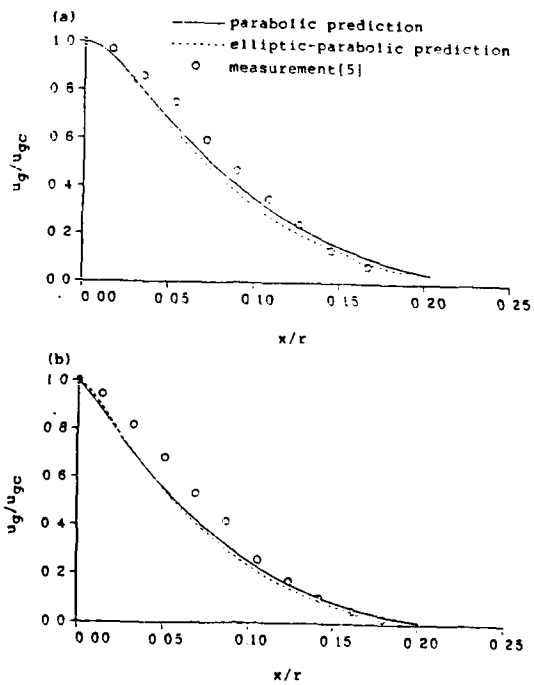

Fig. 2 Comparison of radial profiles of axial velocity for continous phase at two axial stations of x/D = (a) 20 and (b) 40.

yield minor differences of predictions. As a summary, the use of combined elliptic-parabolic solution procedure does improve predictions of the continuous phase in the very upstream region, but does not cause much prediction differences from those obtained with the conventional parabolic solution procedure in the other flow regions.

Figure 3 compares both predicted sectional profiles of axial velocoity for the dispersed phase using the combined elliptic-parabolic and conventional parabolic solution procedures at two axial stations. Note that the zig-zag profiles are stemmed from insufficient number of computational particles (3000 particle groups in this work) to obtain smooth profiles by using the SSF model. Adeniji-Fashola and Chen [4] made a similar inference too. Both predictions are in good agreement with the measurement in comparison with the results of Berlemont et al. [8] as well as Milojevic and Durst [16]. However, the combined elliptic-parabolic solution procedure lead to a smaller particle spreading rate than the conventional parabolic one. In other words, the particles are all confined in the centrol core of the particle-laden jet. This is because these two different solution procedures yield different predictions of entrainment rates. Figure 4 compares two predicted sectional profiles of radial velocity for the continuous phase by using the combined elliptic-parabolic and conventional parabolic solution procedures at two axial stations. Clearly, the entrainment rates predicted with the combined elliptic-parabolic solution procedure are greater than those predicted with the conventional parabolic one. Moreover, the differences of the predicted entrainment rates between these two solution procedures become greater in the more upstream regions (cf. Figs. 4a and 4b). Although the predicted values of radial velocity are two orders of magnitude smaller than those of axial velocity for the continuous phase, their influences on the particle spreading rate are significant as shown in Fig. 3. This implies that the boundary layer approximation, which has been conventionally adopted for the computations of particle-laden jets, may produce some errors in predictions of dispersed phase. Furthermore, the initial profiles of radial velocity for both continuous and dispersed phases are needed to be specified for computation no matter how small their values are in comparison with those of axial velocity.

Another cases associated with polydispersed size effect and measured with more reliable diagnostics will be tested further in this work.

REFERENCE

1. Popper, J., Abuaf, N. and Hetsroni, G., "Velocitry Measurements in a Two-Phase Turbulent Jet," Int. J. Multiphase Flow, Vol. 1, pp. 715-726 (1974).
2. Crowe, C.T., "Two-Fluid versus Trajectory Model: Range of Applicability," *Gas-Solid Flows*, ASME FED-Vol. 35, pp. 91-96 (1986).
3. Durst, F., "Eulerian and Lagrangian Predictions of Particulate Two-Phase Flows: a Numerical Study," Appl. Math. Modeling, Vol. 8, pp. 101-114 (1984).
4. Adeniji-Fashola, A. and Chen, C.P., "Modeling of Confined Turbulent Fluid-Particle Flows Using Eulerian and Lagrangian Schemes," Int. J. Heat Mass Transfer, Vol. 33, pp. 691-701 (1990).
5. Shuen, J-S., Soloman, A.S.P., Zhang, Q-F and Faeth, G.M., "Structure of Particle-Laden Jets: Measurements and Predictions," AIAA J., Vol. 23, pp. 396-404 (1985).

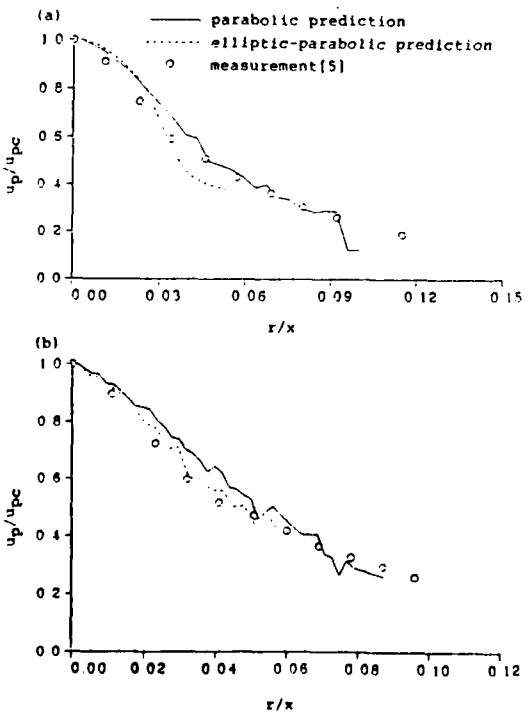

Fig. 3 Comparison of radial profiles of axial velocity for dispersed phase at two axial stations of x/D = (a) 20 and (b) 40.

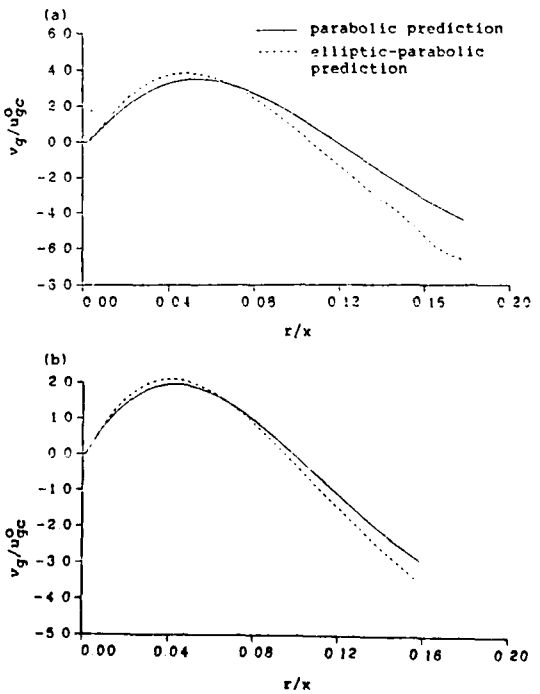

Fig. 4 Comparison of radial profiles of radial velocity for continuous phase at two axial stations of x/D = (a) 20 and (b) 40.

6. Tsuji, Y., Morikawa, Y., Tanaka, T. and Karimine, K., "Measurement of an Axisymmetric Jet Laden with Coarse Particles," Int. J. Multiphase Flow, Vol. 14, pp. 565-574 (1988).

7. Mostafa, A.A., Mongia, H.C., McDonell, V.G. and Samuelsen, G.S., "Evolution of Particle-Laden Jet Flows: a Theoretical and Experimental Study," AIAA J., Vol. 27, pp. 167-183 (1989).

8. Berlemont, A., Desjonqueres, P. and Gouesbet, G., "Particle Lagrangian Simulation in Turbulent Flows," Int. J. Multiphase Flow, Vol. 16, pp. 19-34 (1990).

9. Elghobashi, S., Abou-Arab, T., Rizk and Mostafa, A., "Prediction of the Particle Laden Jets with a Two-Equation Turbulence Model," Int. J. Multiphase Flow, Vol. 10, pp. 697-710 (1984).

10. Chen, C.P. and Wood, P.E., "Turbulence Closure Modeling of the Dilute Gas-Particle Axisymmetric Jet," AIChE J., Vol. 23, pp. 163-166 (1986).

11. Picart, A. Berlemont, A. and Gouesbet, G., "Modeling and Predicting Turbulence Fields and the Dispersion of Discrete Particles Transported by Turbulent Flows," Int. J. Multiphase Flow, Vol. 12, pp. 237-261 (1986).

12. Modarress, D. and Wuerer, J., "An Experimental Study of a Turbulent Round Two-Phase Jet," AIAA paper 82-0946 (1982).

13. Modarress, D. and Tan, H., "Two-Component LDA Measurement in a Two-Phase Turbulent Jet," AIAA paper 83-0052 (1983).

14. Solomon, A.S.P., "A Theoretical and Experimental Investigation of Turbulent Sprays," Ph. D Thesis, The Pennsylvania State University, 1984.

15. Mostafa, A.A. and Mongia, H.C., "On the Turbulence-Particles Interaction in Turbulent Two-Phase Flows," AIAA paper 86-0215 (1986).

16. Milojevic, D. and Durst, F., "Lagrangian Modeling of Gas-Particle Jet Flows and Comparison with Existing Experimental Data," Proceedings of Int. Conf. on Mechanics of Two-Phase Flows, pp. 145-151, Taipei, Taiwan, 1989.

17. Jones, W.P. and Launder, B.E., "The Prediction of Laminarization with Two-Equation Turbulence Model," Int. J. Heat Mass Transfer, Vol. 15, pp. 301-314 (1972).

18. Gosman, A.D. and Ioannides, E., "Aspects of Computer Simulation of Liquid Fueled Combustors," AIAA paper 81-0323 (1981).

19. Crowe, C.T., Sharma, M.P. and Stock, D.E., "The Particle-Source-In Cell Model for Gas-Droplet Flows," J. Fluid Engng., Vol. 99, pp. 325-332 (1977).

IUTAM Symposium on
Aerothermodynamics in Combustors
June 3-5, 1991, Taipei

Study on Dynamic Characteristics of a Hollow Cone Spray Jet

M. R. Wang† and C. H. Hong‡

Institute of Aeronautics and Astronautics
National Cheng-Kung University
Tainan, Taiwan, 70101, R. O. C.

Abstract

Detailed measurements of the initial condition of a hollow cone fuel spray jet and the physics involved in the phase interaction are decribed. A two-component phase Doppler particle analyzer is employed to measure the required data at Z/D = 20 Results show that the both phases are almost in equilibrium in the central region of the spray, but are quite different in the outer region. The ambient air is entrained into the spray by the momentum transported from the fast moving droplets. The negative radial velocity of the entrained air is turned to positive in the spray sheet indicating a complicated flow structure in the spray jet. In the central region there is a weak swirl that withdraws the gas phase to the centerline and results in the maximum axial velocity of the both phases. The distribution of sauter mean diameter ,number density and volume flux of the spray jet can be related to the disintegration phenomenon of liquid sheet.

Introduction

The numerical simulation on spray combustion requires a complete data set of the continuous phase(i.e., the gas phase) and the dispersed phase (i.e., the spray phase) for evaluating the computational models. The data set includes both the droplet size and aerodynamic quantities of the dispersed and continuous phases. Moreover, the number density and volume flux of the spray flow are also very important in the validation of numerical modelling. Although many experimental investigations have been conducted, only few have provided sufficient data for testing and guiding the numerical modelling[1,2]. Recently, the development of phase Doppler velocimetry technique[3], an extension of the laser Doppler velocimetry, provides a powerful tool to measure the above quantities simultaneously. For example, Samuelsen et al.[4] and Edwards[5] utilized the phase Doppler particle analyzer(**PDPA**) to measure the data base of a particle–laden coaxial jet and a research simplex atomizer(RSA), respectively. Their data sets were employed to develop the numerical code. However, the complete data set including the distribution of turbulent kinetic energy, the Reynolds stress and the velocity gradient are less explored in the literature. Hence, a detailed measurement on the spray jet issued from a hollow cone fuel nozzle is carried out in this program in order to describe its dynamic characteristics and provide the bench mark data for numerical modelling.

Study on the interactions between the continuous and dispersed phases is an important issue to describe the dynamic behavior of the droplets in the spray jet. This involes the difficulties to distinguish the velocity components of both the continuous and dispersed phases. This problem becomes more complicated in a free spray jet since the interactions between the two phases, normally resulted from the mass entrainment of the ambient air into the spray jet. Observations of the air entrainment have been undertaken by Binark et al.[6] and Benatt et al.[7]. They found that the surrounding air is set into motion due to the momentum transfered from the spray jet by seeding smoke particles from outside of the spray sheet. The air enters the spray envelope nearly perpendicular to the droplet trajectories. This, in turn, results in the droplet trajectories to deviate from the spray cone and bend toward the flow axis. In an effort to describe the velocity distribution of the continuous phase, Gluckert[8] theoretically studied the variation of the centerline velocity of the gas phase in a spray jet. He found the gas velocity distribution in the spray is similar to that of a turbulent jet. Dombrowski et al.[9] further studied the gas phase velocity in a spray jet by using photography technique. They found that the aerodynamic properties of the gaseous phase can be described by the Prandtl's mixing length theory.

Since the velocity of the gas phase depends on the phase interaction, its velocity distribution is normally more complicated than that of the single phase jet. Recently, Bachalo et al.[10] used the **PDPA** to measure the spray behavior produced by a pressure atomizer. They found a recirculation region in the central portion of the spray cone near the nozzle exit. For the hollow cone spray atomizer, the spray is usually produced by a small swirler existed in the nozzle. The swirling effect of the spray will become complicated in the phase interaction. Mao et al.[11], McDonell et al.[12] and McVey et al.[13] measured the air assist atomizers by laser anemometer or **PDPA** and found the swirling jet air field with solid body rotation in the core and free

† Associated professor
‡ Graduate assistant

vortex flow in the outer region of the spray.

The liquid medium injected from the nozzle will form a conical liquid sheets. Hence, the breakup phenomenon of the spray sheet will be similar to the disintegration of the liquid sheet. Mansour et al[14] investigated the liquid sheet disintegration mechanism and found that there are large, ordered, and small, chaotic "cell" strutures in the end of liquid sheet. The large, ordered cells will become large ligaments which are the origin of the large in the spray. The small, chaotic cells will become small membranes which contribute to the formation of the smaller droplets. In the study of the liquid sheet instability by Crapper et al.[15], the small droplets are shattered away from the liquid sheet, but the large droplets will keep the original trajectory of the liquid sheet. McDonell[16] measured a RSA nozzle and found that the small droplets are shed off both sides of the spray sheet as it breaks up, and the largest droplets remain near the original location of the spray sheet.

Experimental Setup and Diagnostics

Figure 1 shows the schematic of the experimental setup used in this program. It was designed to characterize a wide variaty of two-phase flow under isothermal conditions. The facility consists of a test stand, the air and fuel supply system. The test stand is composed of an optical table, a fuel collection tank, an exhausted system and a 3-axis traversing mechanism. The optical table is designed with an 80×80 cm square cutout for the installation of a two-component phase Doppler particle analyzer. The spray nozzle is mounted on the 3-axis traversing system and the positoin is controlled by a PC/XT. The exhausted system provides a uniform curtain flow of the surrounding air in the test section, i.e. $U\infty = 0.18\ m/s$, to avoid the flow reversal.

The spray nozzle used in this test program is a Monarch model F80 #1.35 hollow cone pressure atomizer. The orifice diameter of the nozzle is 0.64 mm and the spray angle is 80°. The working liquid fluid used is water with a flow rate of 1.19 g/s at the injection pressure of 120 psi. A two-component phase Doppler system is used to measure the flow field for both phases. The instrument can measure size and two orthogonal components of velocity for individual particle simultaneously. Measurement of the gas phase by the laser Doppler velocimetry needs to seed aerosol particles in the flow. The seeding particles employed to trace the gas phase are provided by a smoke generator with the particle size smaller than 2 μm. The effective samples of statical calculation for the dispersed phase velocities are over 30,000 and those for the gas phase are over 2,000. The error of velocity measurement is less than 3 % and that of particle size is 5 %. The measurements are carried out at the axial position of Z/D = 20. The coordinate is chosen that the negative radial velocity indicates the inward motion of the flow. Three velocity components of the both phases have been measured by turning the spray nozzle 90°.

Results and Discussion

The three velocity components of the both phases are shown in Fig.2. The axial and radial velocity distributions(see Figs.2 (a) and (b)) of the spray phase representing the typical characteristics of the hollow cone spray atomizer. The azimuthal velocity of the spray is much smaller than the other two components. The velocities of the both phases are almost equal in the central region, implying the equilibrium of the both phases in this region. However, the velocities of the both phases in the outer region are quit different. The momentum transfered from the dispersed phase results in an entrainment of the ambient air flow. The entraining air is accelerated in negative radial direction, i.e. the inward motion. However, the radial velocity of the gas phase in the spray sheet increases significantly because of the high radial momentum transfered from the dispersed phase. In the central region of the spray jet, there is a weak swirl in the spray that is inherited from the swirling effect in the spray nozzle. In the vortex the air is withdrawn from surrounding, so the radial velocity of the gas phase is negative and the axial velocity becomes maximum in the center. The axial velocity of the gas phase presented a hyperbolic profile, similar to that of the single phase jet flow. However, the aerodynamics involved in the two-phase jet is much complicated as shown in the radial and azimuthal velocity distributions(see Figs.2 (b) and (c)).

Figure 3. shows the Sauter mean diameter(SMD), the number density and volume flux of the hollow cone spray. As illustrated in Figs.3 (a) and (c), the peak values of SMD and volume flux are located at the spray cone. However, the peak value of the number density is located in the central region. These are the typical characteristics of the hollow cone spray. Most of the small droplets are produced in the both sides of the spray sheet, but most of the large droplets produced by the spray sheet will keep the same trajectory as the spray sheet. The small droplets in the inner side of the spray sheet will move into the central region of the spray. However, the small droplets in the outer side of the spray sheet are convected by the inward motion of the entrained air to the spray sheet. Hence the smallest SMD is located in the central region and the largest SMD is located at the spray cone. Moreover, the SMD in the outer region of the spray is a little smaller than that in the spray cone. Since the physical volume is small in the central region, the number density will become large in the central region. And the number density decreases monotonically toward the outer region because of increase of the physical volume. However, the volume flux is attributed to the large droplets, hence the peak value of the volume flux is in the spray cone.

Figure 4. illustrates the turbulent kinetic energy distribution of the gas phase. It is interesting to note that the peak kinetic energy is in the centerline of the spray jet. It is different from that of a turbulent free jet, in which the peak kinetic energy is in the shear layer region. Moreover, there is another peak value in the spray sheet indicating the shear layer region of the spray jet. This region is also located at the position of the maximum axial momentum of the dispersed phase, implying the maximum momentum tranfered from the dispersed phase.

References

1. A. S. P. Solomon, J-S Shuen, Q-F Zhang, and G. M. Faeth, "Structure of Particle-Laden Jet: Measurements and Predictions," *AIAA Journal*, Vol.23, No.3, pp.396-404, 1985.

2. A. S. P. Solomon, J-S Shuen, Q-F Zhang, and G. M. Faeth, "Structure of Noevaporatig Spray, Part I and Part II:," *AIAA Journal*, Vol.23, No.10, pp.1548-1555 and pp.1724-1730, 1985.
3. W. D. Bachalo and M. J. Houser, "Phase Doppler Spray Analyzer for Simultaneous Measurement of Drop Size and Velocity Distributions," *Optical Engeneering*, Vol.26, pp.2137, 1987.
4. A. A. Mostafa, H. C. Mongia, V. G. McDonell and G. S. Samuelsen, "On the Evolution of Particle-Laden Coaxial Jet Flows: A Theoretical and Experimental Study," *AIAA Journal*, Vol.27, No.2, pp.167-183, 1989.
5. C. F. Edwards, R. C. Rudoff and W. D. Bachalo," Measurement of Correlated Droplet Size and Velocity Statistics, Size Distribution, and Volume Flux in a Steady Spray Flame," *Fifth International Symposium on Application of Laser Techniques to Fluid Mechanics*, Lisbon, Portugal, 1990.
6. H. Binark and W. E. Ranz, "Induced Air Flows in Fuel Sprays," *ASME* paper No.58-A-284, 1958.
7. F. G. S. Benatt and P. Eisenklam, "Gaseous Entrainment into Axisymmetric Liquid Sprays," *J. Inst. Fuel*. Aug. 1969.
8. F. A. Gluckert, "A Theoretical Correlation of Spray Dryer Performance," *A.I.Ch.E. Journal*, Vol.8, 1962, p.460.
9. E. F. J. Briffa and N. Dombrowski, "Entrainment of Air into a Liquid Spray," *A.I.Ch.E. Journal*, Vol.12, 1966, p.708.
10. W. D. Bachalo, M. J. Houser and J. N. Smith, "Evolutionary Behavior of Sprays Produced by Pressure Atomizers," AIAA-86-0296.
11. C. -P. Mao, V. Oechsle and N. Chigier," Drop Size Distribution and Air Velocity Measurements in Air Assist Swirl Atomizer Sprays", *Trans. ASME*, Vol.109, pp.64-69, 1987.
12. V. G McDonell and G. S. Samuelsen," Symmetry Assessment of a Gas Turbine Air-Blast Atimizer Influence of the Continuous and Dispersed Phases," ICLASS-88, Tokyo, Japan, 1988.
13. J. B. McVey, J. B. Kennedy and S. Russel," Application of Advanced Diagnostics to Airblast Injector Flows," *Journal of Engineering for Gas Turbines and Power*, Vol.111, pp.53-61, 1989.
14. A. Mansour and N. Chigier," Disintegration of Liquid Sheets," *Phys. Fluids*, pp.706-719, 1990.
15. G. D. Capper, N. Dombrowski, W. P. Jepson and G. A. D. Pyott," A note on the growth of Kelvin-Helmholtz waves on thin sheets," *J. Fluid Mech.*, Vol.57, pp.671-672. 1973.
16. V. G. McDonell," Characterization of Liquid Fuel Sprays" UCICL-ARTR-90-8

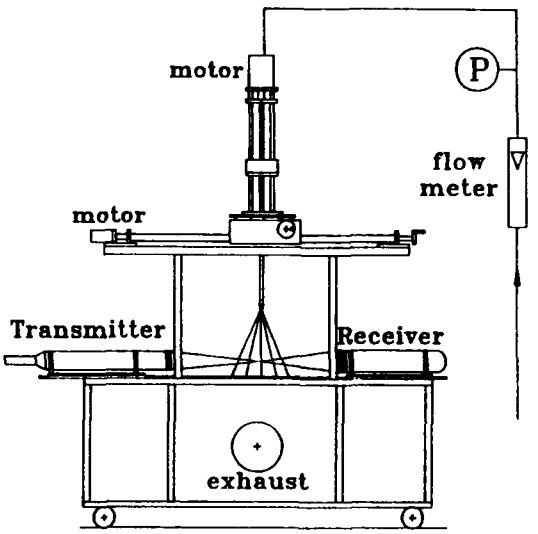

Figure 1. Schematic of the experimental setup

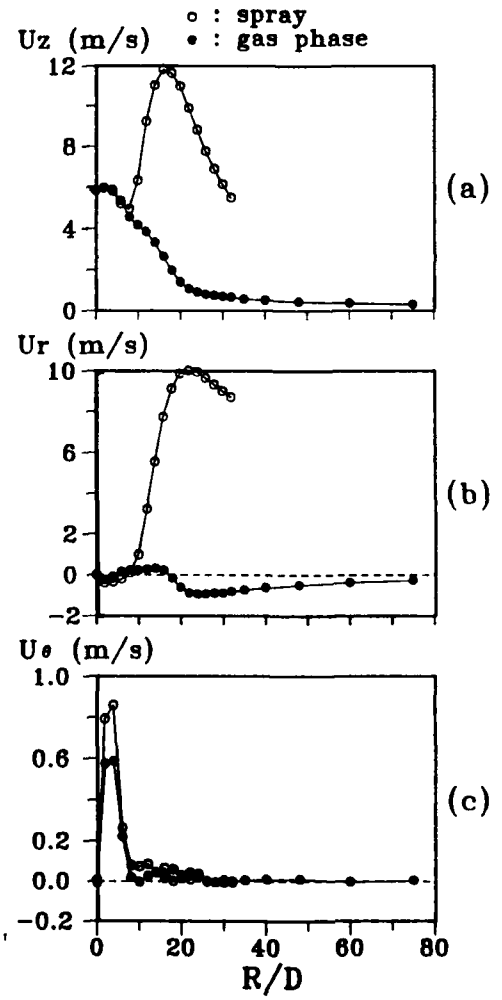

Figure 2. The velocity characteristics of the both phases at Z/D=20.
(a) the axial velocity
(b) the radial velocity
(c) the azimuthal velocity

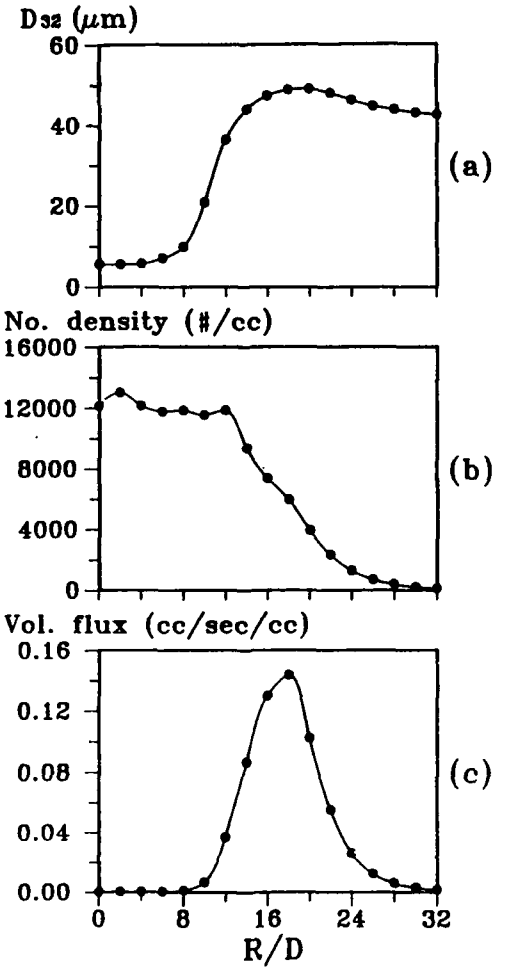

Figure 3. Characteristics of the spray jet at Z/D=20
(a) sauter mean diameter
(b) number density
(c) volume flux

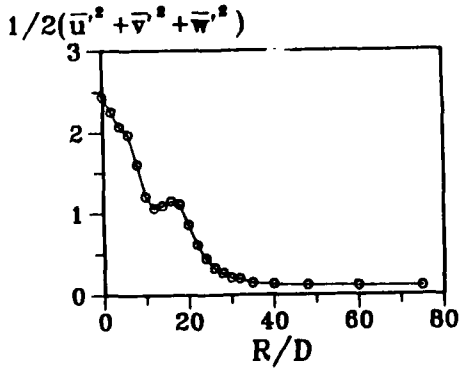

Figure 4. The turbulent kinetic energy distribution of the gas phase at Z/D=20

IUTAM Symposium on
Aerothermodynamics in Combustors
June 3-5, 1991, Taipei

DROPLET VAPORIZAION LAW IN NON-DILUTE SPRAYS

H.H. CHIU

INSTITUTE OF AERONAUTICS AND ASTRONAUTICS
NATIONAL CHENG-KUNG UNIVERSITY
TAINAN, TAIWAN, R.O.C.

ABSTRACT

Increasing theoretical findings[1-13] and experimental evidence[14-18] attest to the widely held belief that the short-range collective interaction[2-6,11-13] among the neighboring droplets and the long-range interaction [1,7,9,10] with the droplets at a distance, on a hydrodynamic scale, have profound impact on the state of a droplet. These collective interactions serve to control the percolative passage for dispersing mass, momentum energy fluxes and the effective interfacial area for the property exchange processes. These interactions result in the collective thermal quenching, the accumulation of vaporizing species and the tendency for stagnating the microscale local Stefan flow and mean flow through dynamic equilibration between the two phases. The objectives of this paper are to present the basic concepts, theoretical approaches and the results of Renormalized Droplet (RND) theory to establish vaporization laws for droplets in a stationary collisionless non-dilute cloud environment.

The present analysis follows the theoretical procedure and assumptions adopted in many modern theories of droplet and a could of droplets. All the droplets are spherically shaped and remain stationary relative to the gas. The Lewis number of the gas mixture is unity. The droplet vaporization process is quasi- steady and the surface regression rate is small. The transport properties are assumed to be constant. Note that the product of the gas phase density and diffusivity is assumed to be constant. Furthermore the droplet collision and distentegration are ignored. Finally, the droplet cloud is assumed to be stationary relative to the gas.

Non-dimensional equations governing RND are formulated separately for the inner DIB region and an external droplet cloud, respectively, as follows.

$$\frac{1}{\eta^2}\frac{d}{d\eta}\left(\eta^2\psi_i\right) = 0 \qquad 1 \le \eta \le \eta_{co} \tag{1}$$

and

$$\frac{1}{\eta^2}\frac{d}{d\eta}\left(\eta^2\hat{\psi}_i\right) = G_s g \mu \hat{B}_i \qquad \eta_{co} \le \eta \le \eta_{ts} \tag{2}$$

with

$$\psi_m = \rho v \tag{3}$$

$$\begin{pmatrix}\psi_F \\ \psi_T\end{pmatrix} = \psi_m \begin{pmatrix}\alpha_F \\ \alpha_T\end{pmatrix} - \sigma \frac{d}{d\eta}\begin{pmatrix}\alpha_F \\ \alpha_T\end{pmatrix} \tag{4}$$

where $\eta = r/r_l(0)$, ρ and v are non-dimensionalized by the gas density, and velocity on the droplet surface, respectively, $Gs = 4\pi n r_{lo}^3$, g is a normalized distribution function, μ is the vaporization shape factor defined by (12), ψ_i are the fluxes of various properties; mass for i=m, fuel vapor for i=F and thermal energy for i=T, and $\wedge$ refers to the properties pertaining to an outer region. The definitions of properties α_i and constants B_i are summarized in Table 1.

Table 1
Schvab-Zeldovichs Variables and Constants

i	α_i	$\hat{\alpha}_i$	$\hat{B}_i$
F	$-(y_F/W_f\nu_F)$	$(-\hat{y}_F/W_F v_F)$	$\varepsilon_F = -(W_F\nu_F)^{-1}$
T	$\int_{T_b}^{T} C_p dT/q$	$\int_{T_b}^{T} \hat{C}_p \hat{T} dT/q$	$\gamma_F = L/q$

where y is a mass fraction, W is a molecular weight, v is a stoichiometric coefficient, C_p is a specific heat, L is the latent heat of vaporization (per unit mass) of the fuel at the boiling temperature, q is the heat of combustion. The solutions of Eqns (1) to (4) are obtained and the characteristic vaporization rate "renormalized vaporization law" is derived as follows.

$$\dot{m}(o) = 4\pi\rho D r_\ell(o) C_v ln\left(1 + \frac{\hat{\alpha}_{T_{ts}}}{\gamma_F}\right) \tag{5}$$

$$\dot{m}(o) = 4\pi\rho D r_\ell(o) C_v ln\left(1 + \frac{\hat{\alpha}_{F_{ts}} - \hat{\alpha}_{F\ell}}{\hat{\alpha}_{F\ell} - \varepsilon_F}\right) \tag{6}$$

where C_v is the vaporization correction factor calculated as follows

$$C_v = \left\{1 - \zeta_{ts} + G_s \int_{\eta_{co}}^{\eta_{ts}} \int_{\eta_{co}}^{\eta} K(\eta|\xi)\theta(\xi)\Big[W_1(\xi) + BW_2(\xi)\Big] \left(\frac{\eta_{co}-1}{\eta-1}\right)\left(\frac{\eta}{\eta_{co}}\right) d\xi d\eta\right\}^{-1} \tag{7}$$

where

$$B = \left[\frac{1}{\Lambda} - W_1(\eta_{ts})\right] / W_2(\eta_{ts}) \tag{8}$$

and

$$\Lambda = (1 - \zeta_{ts} - G_s \int_{\eta_{co}}^{\eta_{ts}} \int_{\eta_{co}}^{\eta} K(\eta|\xi)\theta(\xi) \frac{1-\zeta_{co}}{1-\zeta(\xi)}$$

$$\frac{W_2(\xi)}{W_2(\eta_{ts})}d\xi d\eta)/$$

$$(1-\zeta_{ts}+G_s\int_{\eta_{co}}^{\eta_{ts}}\int_{\eta_{co}}^{\eta}K(\eta|\xi)\theta(\xi)$$

$$\frac{1-\zeta_{co}}{1-\zeta(\xi)}\left[W_1(\xi)-\frac{W_1(\eta_{ts})}{W_2(\eta_{ts})}W_2(\xi)\right]d\xi d\eta) \qquad (9)$$

Two functions, W_1 and W_2, which are the homogeneous solutions of the energy equation (2), satisfy the following canonical boundary conditions: $W_1(\eta_{co})=1$, $\frac{dW_1}{d\eta}(\eta_{co})=0$, $W_2(\eta_{co})=0$, $\frac{dW_2}{d\eta}(\eta_{co})=1$.where,

$$K(\eta|\xi)=\eta^{-2}\xi^2 g(\xi) \qquad (10)$$

The structure and scaling laws of RND and their dependence on the principal collective interaction parameters of a stationary cloud of n-octane droplets are determined for the droplets with the following fuel properties; $\rho_l=707\ kg/m^3$, $T_b=398.7\ K$, $L=71.7\ kcal/kg$, and $W_F=114.14\ kg/kg-mole$.

(1) Pair-Distribution Function and Canonical Bubble

A pair-distribution function is adopted for the numerical calculation.

$$g(\eta)=1+a\exp(-b\eta)\cos(2\pi\eta_{co}), \qquad 2\eta_{co}<\eta\le\eta_{ts} \qquad (11)$$

where a and b are constants to be determined from the experimental data. In the present analysis a=1.8, b=0.65 are chosen. The resulting distribution patterns are shown in Fig.2. The corresponding signatures of the inverse of the radius of canonical bubbles with η_{co}=5, 10, and 15 are shown in Fig. 3.

(2) Vaporization Shape Factor

A pronounced increase of μ in the radial direction is observed for a smaller value of droplet spacing, i.e. η_{co}=7.5 in Fig.4. The ratio of the vaporization rate of the droplet located at the first coordination shell, for the case of η_{co}=7.5, is only 5% of the corresponding value of RND with η_{co}=15. This trend of a higher increasing rate of μ at smaller canonical bubble radii; μ-stratification, is a common feature for a small droplet spacing in non-dilute sprays, as confirmed for a case study of various RND clouds featured with different values of a and b that appear in the pair distribution function.

(3) Temperature Distribution

High μ-stratification at a smaller droplet spacing, as illustrated in Fig. 4 is associsted with steep radial temperature gradients in the transition sphere, shown in Fig.5. Indeed, the comparison of "μ-T stratifications" suggests that (1) the rapid vaporization of droplets in the outer layer of the cloud collectively quench as the environment and thereby reduces the vaporization of the test droplet and (2) the increase in η_{ts}, at a fixed droplet spacing, tends to reduce the inward heat transfer rate and thus suppresses the vaporization of the test droplet.

(4) Vaporization Rate-Correction Factor

The correction factors of RNDs for three selected values of η_{co}, Fig. 6, are found to decrease monotonically as the group combustion number of RND increases. Saturation is projected to occur when $G_{RN}=30\sim40$ with η_{co}=7.5. While the group combustion number is a primary factor controlling the magnitude of C_v, Fig. 6 shows a small variation in the correction factor for two RND's which have the same group combustion number but a different value of renormalization number, $\beta=\eta_{ts}/\eta_{co}$.

(5) Scaling Laws with Linear Stratification Model

In order to facilitate the practical application of the scaling law, the correction factor is integrated by adopting the following functional form of $g\mu$

$$g\mu=\overline{g\mu}K_1\eta$$

where K_1 is a stratification coefficient, and $\overline{g\mu}$ is the mean value of the weighted vaporization shape factor. The correction factor predicted by the linear stratification model described above, is given by

$$C_v=\left\{1-\zeta_{ts}+G_{RN}\left[(1-\frac{1}{\beta})(1+\frac{1}{\beta}-\frac{2}{\beta^2})+\frac{1}{2}K_1\eta_{ts}(1-\frac{1}{\beta})(1+\frac{1}{\beta}+\frac{1}{\beta^2}-\frac{1}{\beta^3})\right]\right\} \qquad (12)$$

where

$$G_{RN}=\frac{1}{6}G_s\eta_{ts}^2\overline{g\mu}$$

(6) Spray Classification

Numerical assessment of the scaling law suggests the following structural classification of non-dilute sprays.

1. Diffusively Dense Cloud

In a moderately dense cloud, say, η_{co} equals to 10 or 15, shown in Fig.4, RND exhibits little or no μ-stratification. The reduction in the vaporization is attributed to a moderate thermal quenching. However, the thermal diffusion is large such that the temperature remains nearly constant throughout the transition sphere, see Fig.5, η_{co} =10 and 15. The corresponding correction factor is a function of the group combustion and a minor correction term of the order of $\frac{1}{\beta^2}$.

$$C_v\cong(1+G_{RN})^{-1}+O(\frac{1}{\beta^2}) \qquad (12-b)$$

2. Densely Stratified Cloud

This dense cloud, with a smaller droplet spacing, as shown in Fig.4 with η_{co} = 7.5, is featured with strong μ and T stratifications in a transition sphere casued by an intense collective quenching that exceeds the rate of thermal transfer in a transition sphere. The renormalization number η_{ts}/η_{co} is larger than unity so that the correction factor is given by

$$C_v\cong[1+G_{RN}(1+\frac{1}{2}k_1\eta_{ts})]^{-1}+O(\frac{1}{\beta^2}) \qquad (12-c)$$

3. Sharply Dense Cloud - Fine Structure

When the coordination shells contain a large number of droplets and the renormalization number is not excessively large compared with unity, the correction factor depends on all the collective parameters : G_{RN} , η_{ts} / η_{co} and η_{ts}. Two sharply dense clouds with the same group combustion number will exhibit structural variation when the renormalization number is different, for example, at G_{RN} = 4.2 the RND with β = 12 has a larger value of C_v than that of β = 9, see Fig.6.

REFERENCES

1. Chiu, H.H. and Liu, T.M.: COMB. SCI. AND TECH., 17, 127, 1(1977).

2. Labowsky, M. and Rosner, D.E., Advances in Chemistry Series No 166 Amer. Chem. Soc., (1978).
3. Twardus, E.M., and Brzustowski, T.A.: Comb. Sci. Tech 17, 215, (1978).
4. Tishkoff, J.M.: Int. J. Heat and Mass Transfer 22, 1407, (1979).
5. Labowsky, M.: Combust. Sci. Tech. 22, 127, (1980).
6. Umemura, A.: Eighteenth Symposium (International) on Combustion, 1335, The Combustion Institute, 1981.
7. Chiu, H.H., Kim, H.Y., and Croke, E.J.: Nineteenth Symposium (International) on Combustion, 971, The Combustion Institute, 1982.
8. Bellan, J. and Cuffel, R.: Combust. Flame 51, 55, (1983).
9. Sirignano, W.A.: Prog. Energy Combust. Sci. 9, 291, (1983).
10. Sichel, M. and Panlaniswamy, S.: Twentieth Symposium (Intenational) on Combustion, 1789, The Combustion Institute, 1984.
11. Chiu, H.H.: "Theory of Bipropellant Combustion, Part I-Conjugate, Normal and Composite Combustion Phenomena:" AIAA-86-0220 Presented at the AIAA 24th Aerospace Sciences Meeting, Reno, Nevada, 1986.
12. Chiu, H.H.: "Theory of Renormalized Droplets I Law of Droplet Vaporization Rate Under Short-Range Droplet Interaction" Presented at First Annual Conference on Liquid Atomization and Spray Systems ILASS Americas, Madison, Wisconsin, 1987.
13. Jang, S.D. and Chiu, H.H.:"Theory of Renormalized Droplets, II, Nonsteady Vaporization Droplet in Non-Dilute Sprays" AIAA-88-0639, presented at the AIAA 26th Aerospace Sciences Meeting, Reno Nevada, 1988.
14. McCreath, C.G. and Chigier, N.A.: Fourteenth Symposium (International) on Combustion, 1355, The Combustion Institute, 1973.
15. Miyasaka, K. and Law, C.K.: Eighteenth Symposium (International) on Combsution, 283, The Combustion Institute, 1981.
16. Yule, A.J. and Bolado: Combust Flame 55, 1, (1984).
17. Xiong, T.Y., Law, C.K. and Miyasaka, K.: Twentieth Symposium (International) on Combustion, 1781, The Combustion Institute, 1984.
18. Roshland, C.P. and Bowman, C.T.: Twentieth Symposium (International) on Combsution, 1979, The Combustion Institute, 1984.
19. Chiu, H.H.: "Droplet laws in Spray Combustion Processes" under Preparation, 1990.

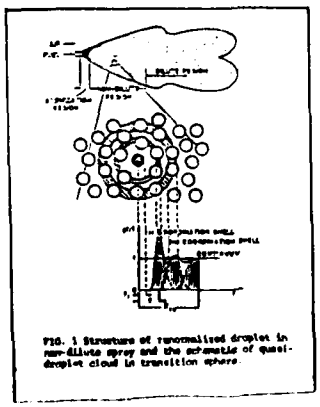

FIG. 1 Structure of renormalized droplet in non-dilute spray and the schematic of quasi-droplet cloud in transition sphere.

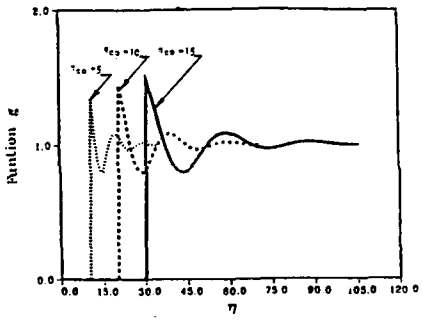

Fig. 2 Pair-distribution function of quasi-droplets in transition sphere for three selected test droplet bubble sizes.

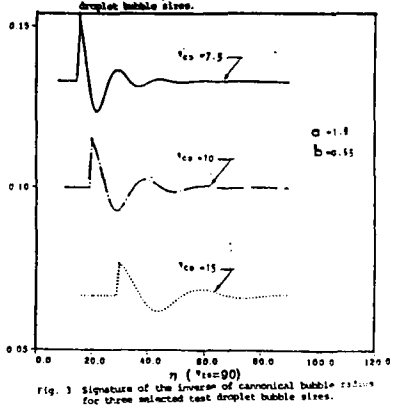

Fig. 3 Signature of the inverse of canonical bubble radius for three selected test droplet bubble sizes.

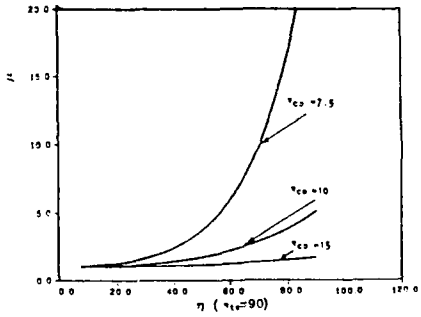

Fig. 4 U-stratification; Vaporization shape factor distribution in transition sphere for three selected test droplet bubble sizes.

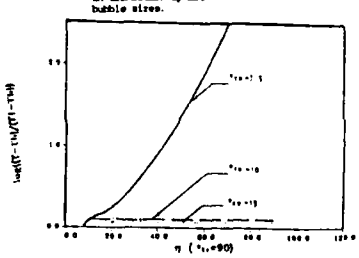

Fig. 5 U-stratification - gas temperature distribution in transition sphere for three selected test droplet bubble sizes.

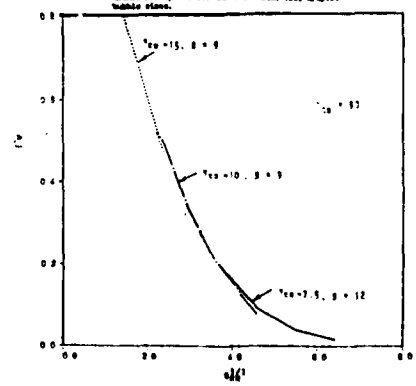

Fig. 6 Correction factor for vaporization rate vs group combustion number for three selected test droplet sizes Exact Solution.

IUTAM Symposium on
Aerothermodynamics in Combustors
June 3-5, 1991, Taipei

Spray with Annular Air Flow in Bluff-Body Combustor

H. J. Sheen* and S. J. Yen**

Institute of Applied Mechanics
National Taiwan University
Taipei 10764, TAIWAN, R.O.C.

ABSTRACT

The objective of this study is to investigate the influences of annular air flow to the hollow cone spray structure and the interactions of liquid droplets and air flow. Under various annular air flow conditions, the hollow-cone shaped spray structures of a cylindrical bluff body combustor have different flow patterns. Three different spray flow patterns are observed and investigated: (I) with no air flow, (II) with annular air flow and spray angle increase slightly, (III) with annular air flow and spray angle expanded significantly. The experimental techniques used in this study include laser-Doppler anemometry (LDA) for gas and droplet phase velocity measurements and phase-Doppler anemometry (PDA) for droplet size and velocity measurements. The major interests are the gas phase mean velocity, velocity fluctuation and Reynolds stress, and the droplet phase mean size, size distribution function, droplet velocity and their relation for three different patterns.

INTRODUCTION

The basic geometry of a bluff body combustor for this study is shown in Figure 1. The liquid spray is injected from the nozzle placed at the center of the end of the cylinder which is coaxial with the outer annular air flow. The end of the cylinder will induce flow separation, which is preferable for both the stabilization of flame and mixing of fuel and air.

There are many previous studies focused on the investigation of flow properties of different kinds of bluff body combustors. Bluff body with different kind of shape, for most of the studies, is placed in the flow to form a recirculation zone which dominate flame stabilization. Davies and Beer [1] studied the flow in the wake of bluff body flame stabilizers. They studied the effects with different blocking ratios, defined as the ratio of bluff body cross section area to the original outlet area, and bluff body shapes to the flow field features. They found that the larger the blocking ratio, the shorter the recirculation zone. Durao and Whitelaw [2] study the velocity characteristics of the flow in the near wake of a disk and also the similar result about the effects of blocking ratio on the length of recirculation zone. Fujii [3, 4] studied a bluff body flame stabilizer in a two dimensional duct. The shape of the cross section of the bluff body is equilateral triangular. He found that the turbulence intensity was reduced and recirculation zone was enlarged in the reacting flow.

Rothe [5] studied the interaction between air and spray. He found that the drag force of liquid phase causes the entrainment of gas phase and entrained gas results in the contract of spray. Yeung [6] proposed a similarity solution of gas-liquid spray systems but an appropriate turbulence viscosity model was needed and some flow characteristics must be given, such as mean droplet size and initial droplet velocity.

The combination of spray and annular air flow behind cylindrical bluff body results in a more complicated problem. The separation of the annular air flow will change the spray characteristics substantially. Tankin [7] studied the cylindrical bluff body combustor with a popet type nozzle. He concluded that the structure of the flow field is dominated by the size of the annular vortices of air. As the annular vortices grow comparable to the size of sheet region and penetrate into the spray, the shape of the spray will be dramatically changed. In order to study the flow structure of a cylindrical bluff-body combustor, the present experiment is conducted.

EXPERIMENTAL SET-UP

Figure 2 shows the general arrangement of the experimental system set-up. The testing chamber, made by casted aluminum alloy, contains the cylindrical shape bluff body combustor, a swirl type nozzle, annular air flow duct and has three observation windows, diameter of $7in$, to be used for laser sheet-lighting flow visualization and LDA and PDA measurements. The whole test chamber is placed on a computer-controlled transversing system. The diameter of the bluff-body cylinder is $31.75mm$ and the dimension ratio of the outer diameter is 1.75 as shown in Figure 1.

* Associate Professor
** Graduate Student

The nozzle used in this experiment is Spraying System Co. Model No. $1/4LN60$ swirl type nozzle, with outlet exit diameter of nozzle $0.016in$. The compressed liquid comes out of the nozzle through two swirl slots and forms a hollow cone spray by centrifugal force and water is used for liquid phase instead of liquid fuel. Water is stored in a pressurized liquid tank, which connected to an air compressor, set at a constant pressure to consistently supply constant liquid flow during the test. The flow rate, which is $60.7cc/min$ for this test, is measured from a calibrated rotameter. A blower is used to supply the annular air flow and honeycomb straightener is placed at the top of the testing chamber. A calibrated orifice flow meter is used to measure the air flow rate. The Validyne pressure transducer, digital multimeter, and computer are used to monitor the air flow during the test. The air flow rate in this test is adjusted in the range from 0 to $1.39m^3/min$.

Laser sheet-lighting technique is employed for flow visualization by using a Coherent 90-3 3-watts Argon-ion laser and a cylindrical mirror to generate a thin light sheet for spray flow structure observation of a cross-section plane. A four beams, two components, on axis forward scattering Tsi 9100-7 laser-Doppler anemometry system is used for velocity measurement of liquid droplets and gas phase through two observation windows. By adding an INVENT phase/Doppler extension to the existing LDA system, the phase Doppler technique is used for the measurements of liquid phase information, droplet size, size distribution, mean and fluctuation velocity, number flux, etc.

RESULTS

Detailed experimental results of the followings will be discussed in the presentation.

(A) Three different spray flow pattern are observed under various annual air flow condition by flow visualization.
(B) Spray structure of droplet and gas phase near the nozzle exit, the location at 20 times of nozzle diameter.
(C) Droplet size probability distribution at various location for different flow pattern. (Figure 3)
(D) Comparison of droplet and gas phase velocity, droplet mean size, Sauter mean diameter, size standard deviation along the central axis.

REFERENCE

[1] Davies, T.W. and Beer, J.M., "Flow in the Wake of Bluff-Body Flame Stabilizers", 13th International Symposium on Combustion, 1971.

[2] Durão D. F. G. and Whitelaw, J. H., "Velocity Characteristics of the Flow in the Near Wake of a Disk", J. Fluid Mech., Vol. 85, p. 369, 1978.

[3] Fujii, S., Gomi, M. and Eguchi, K., "Cold Flow Test of a Bluff-Body Flame Stabilizer", ASME J. Fluids Eng., Vol. 100, p. 323-332, 1978.

[4] Fujii, S. and Eguchi, K., "A Comparison of Cold and Reacting Flows Around a Bluff-Body Flame Stabilizer", ASME J. Fluids Eng., Vol. 103, p. 328, 1981.

[5] Rothe, P.H., and Block, J.A., "Aerodynamic Behavior of Liquid Sprays", Int. J. Multiphase Flow, Vol. 3, p. 263-272.

[6] Yeung, W.S., "Similarity Analysis of Gas-Liquid Spray Systems", J. Applied Mech., Vol. 49, p. 687, 1982.

[7] David, F. and Tankin, R.S., "Spray from a Bluff-Body Combustor in Annular Air Flow", Comust. Sci. & Tech., 1988

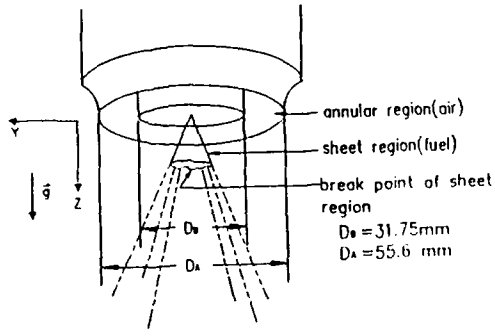

Figure 1. Geometry of a bluff-body combustor.

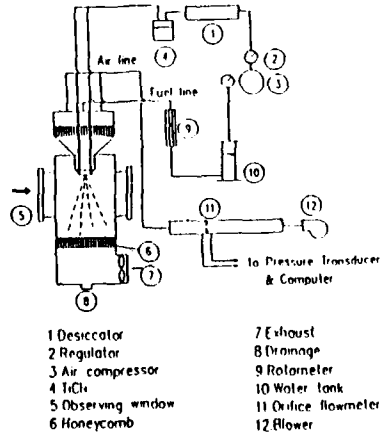

Figure 2. Experimental system set-up.

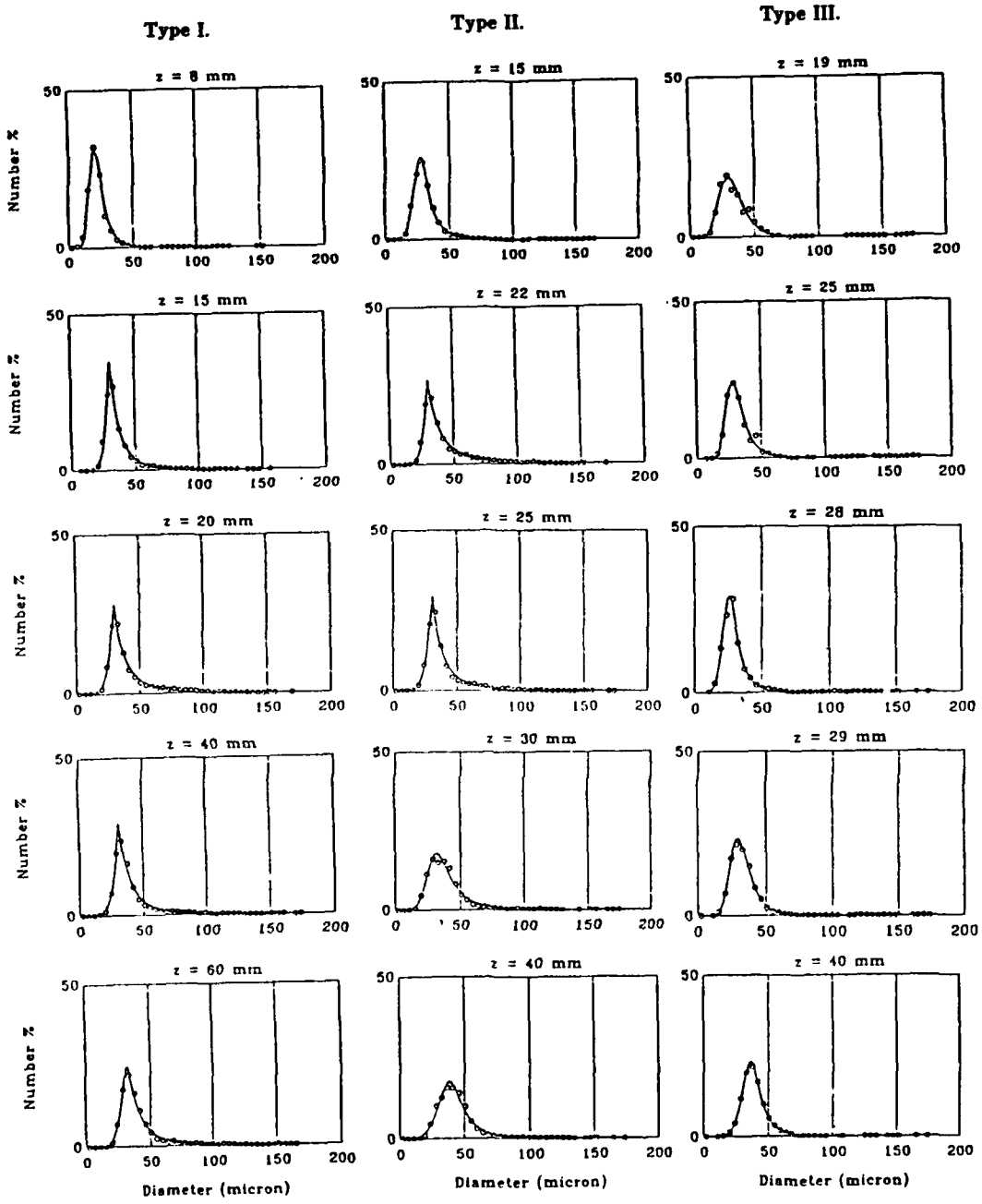

Figure 3. Particle size probability distribution for different flow patterns at various axial location.

IUTAM Symposium on
Aerothermodynamics in Combustors
June 3-5, 1991, Taipei

EXPERIMENTAL INVESTIGATION OF THE REDUCTION OF BURNING RATE DUE TO A FINITE SPACING BETWEEN DROPLETS

N. Roth, K. Anders, A. Frohn

ITLR·Institut für Thermodynamik der Luft- und Raumfahrt
Universität Stuttgart
Pfaffenwaldring 31, 7000 Stuttgart 80

INTRODUCTION

Many combustors in technical applications are supplied with liquid fuel. Usually the fuel is atomized in order to improve the evaporation process. In such fuel sprays the droplet diameter ranges typically from 10 µm up to 500 µm. If the distances between the droplets are small, the mutual interactions of the droplets have to be taken into account for the describtion of the physical and chemical processes in the combustor. Usually it is very difficult to investigate these processes quantitatively in real sprays. To overcome these difficulties monodisperse equally spaced droplets may be applied as a useful tool for studying basic droplet phenomena.

DROPLET SYSTEMS

Monodisperse droplet arrays consisting of one or more parallel droplet streams with defined droplet spacings have been examined. These monodisperse droplet streams have been produced by vibrating orifice droplet generators [1,2]. The initial droplet size d_{To}, velocity v_{To}, and distance between the droplets s_{To} can be chosen in a wide range [3]. A single droplet stream is called a linear droplet array. To obtain planar monodisperse arrays several parallel droplet streams arranged in one plane are used. To study droplet combustion the droplet streams are ignited by a heated coil of filament. After ignition the droplet streams are surrounded by a stationary laminar flame. In Fig. 1 the main parameters characterizing a planar droplet array are explained. All droplets are moving with the velocity v_T in the direction of the droplet streams. By measuring the droplet size d_T and the droplet velocity v_T at different distances from the point of ignition the temporal evolution of size and velocity along each droplet path can be determined. This is possible because the initial conditions of each droplet are the same and each droplet undergoes the same history along a stream.

MEASURING TECHNIQUES

To investigate the interaction between the droplets a very precise sizing method is necessary. At ITLR an interference method was developed for determining droplet sizes with an accuracy of about 2 %. This instrument is independent of the intensity of the incident light. Detailed information about this sizing method has been published elsewhere [2,3]. The droplet velocity is determined simultaneously using a conventional LDV-technique [5].

RESULTS

Linear arrays consisting of one single droplet stream and planar arrays consisting of three or five parallel droplet streams have been studied. In the experiments with the single droplet stream the measurements were performed for different spacings s_T. The burning rate decreases with decreasing droplet spacing s_T. In planar droplet arrays the temporal evolution of droplet size has been measured along each droplet stream. As an example the results of a droplet array consisting of three parallel streams are shown in Fig. 2. It may be shown, that these results are in accordance with the d^2-law. In Fig. 3 results for arrays consisting of two parallel streams are shown for different spacing s_A. In this figure the square of the dimensionless droplet diameter d_T/d_{To} is represented as a function of the dimensionless time $t^* = t\ D/d_{To}^2$. Here t is the time, D the coefficient of diffusion for the fuel against air and d_{To} the initial droplet diameter. Each line represents the mean of both streams in a particular array configuration. For comparison the result of a linear array having the same initial spacing s_{To}, the same initial velocity v_{To} and the same initial droplet diameter d_{To} is plotted in Fig. 3. The slopes c_L of the different lines characterize the burning rate. The values c_L are shown in Fig. 4 as a function of the distance s_A between the streams. The dotted line represents the value of c_L for the linear droplet array, which can be considered as a two stream configuration with infinite distance s_A. Due to symmetrical reasons the result for an array configuration of two droplet streams with zero spacing can be derived from the result of the linear array. This value of c_L is marked on the c_L-axis with a star. Results of planar droplet arrays consisting of three streams are shown in Fig. 5 and 6. Shown is again the slope c_L as a function of the spacing s_A. In both diagrams the dotted line represents results for an infinite spacing s_A like in Fig. 4. In Fig. 5 the results of the edge streams of the configurations are presented. For each configuration the result of the left

and the right edge stream are presented by one common line due to their symmetric position. Figure 6 shows the corresponding results of the center streams. In all cases the initial values of droplet diameter d_{To}, velocity v_{To}, and droplet spacing s_{To} were chosen the same in order to allow comparisons between the results. In addition a droplet configuration consisting of five droplet streams was examined. The spacing between the droplet streams was s_A = 400 µm. In Fig. 7 the slope c_L for each of the five streams is plotted against the distance s_i from the center stream. In all experiments ethanol was used as fuel.

CONCLUSIONS

The diagrams of Figs. 3 to 6 show clearly that for wider spacings s_A between the droplet streams the results approximate the results for a linear array consisting of a single droplet stream. Furthermore the diagrams of Figs. 2 and 7 show, that the burning rate for the droplet streams in or near the center of the configuration is lower. These results show clearly, that the combination of the above mentioned measuring techniques with well defined droplet configurations is a very suitable instrument in the study of basic combustion phenomena. The results obtained may be considered as a experimental basis for improvement of numerical simulations.

REFERENCES

[1] Berglund, R.N., Liu, B.Y.H., (1973), Generation of Monodisperse Aerosol Standards. ENV. SCI. TECH. 7, 147-153.

[2] König, G., Anders, K., Frohn, A., (1986), A New Light Scattering Technique to Measure the Size of Periodically Generated Moving Particles.J.AEROSOL SCI. 17, 157-167.

[3] Roth, N., Anders, K., Frohn, A., (1988), Simultaneous Measurement of Temperature and Size of Droplets in the Micrometer Range. Proc. Int. Conf. Optical Methods in Flow and Particle Diagnostics. LIA Vol.67, 294-304.

[4] Durst, F., Ernst, F. und Völklein, J., (1987), Laser-Doppler-Anemometer-System für lokale Geschwindigkeitsmessungen in Windkanälen, Z. FLugwiss. Weltraumforschung 11, pp.61-70.

ACKNOLEDGEMENT

This work has been sponsored by 'Stiftung Volkswagenwerk'.

FIGURES

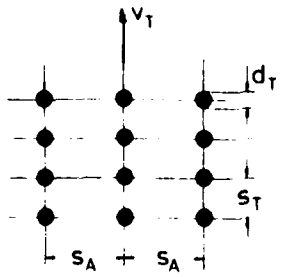

Fig. 1: Sketch of a planar array with configuration parameters.

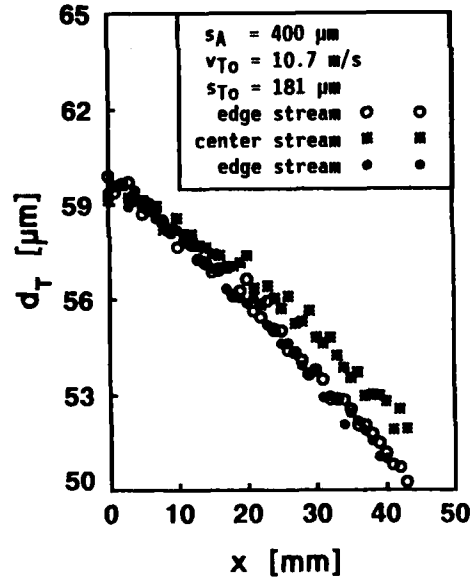

Fig. 2: Droplet diameter d_T as a function of the distance x from the ignition point for droplets of planar droplet array consisting of three droplet streams. The distance between neighbouring streams was s_A = 400 µm. The behaviour of the droplets in the center stream differs significantly from the behaviour in the edge streams.

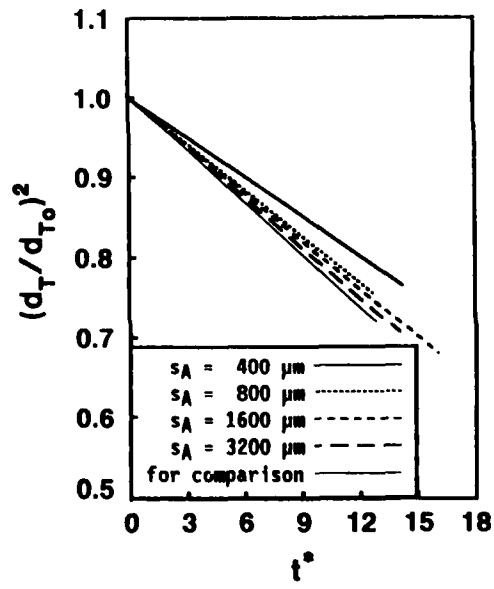

Fig. 3: Square of the dimensionless droplet diameter dT/dTo versus dimensionless burning time t*. The diagram shows results of planar droplet arrays of two droplet streams with different spacing s_A. Results of both streams of a particular array configuration are represented by the mean of the individual streams. Each line represents best fits to the measured data.

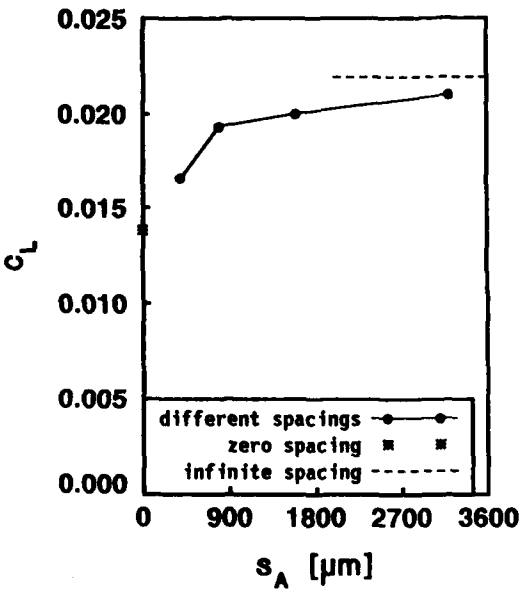

Fig. 4: Slope c_L as a function of the distance s_A between the two droplet streams of the array. The dotted line marks the level of c_L if the spacing is infinite. This level is represented by the results of a single droplet stream. The star on the c_L-axis marks the limit for zero spacing between the streams. This limit is derived from the results of the single stream. The initial droplet diameter was 61 µm.

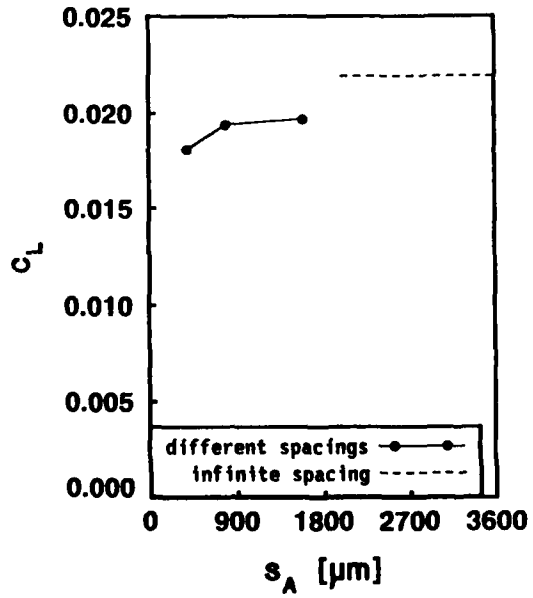

Fig. 5: Slope c_L as a function of the distance s_A between neighbouring droplet streams of a planar array of three streams. Results are shown for droplets of the edge streams. The dotted line marks the level of c_L if the spacing is infinite. This level is represented by the results of a single droplet stream. The initial droplet diameter was 61 µm.

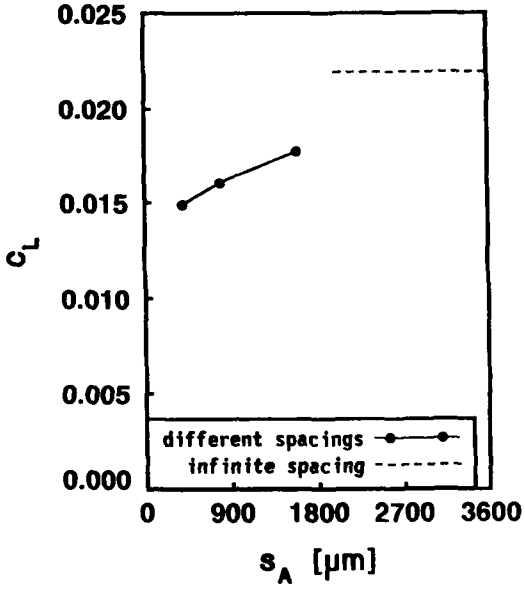

Fig. 6: Slope c_L as a function of the distance s_A between neighbouring droplet streams of planar array configuration consisting of three streams. Results are shown for droplets in the center stream. Their behaviour differs from droplets in the edge streams. The dotted line marks the level of c_L if the spacing is infinite. This level is represented by the results of a linear droplet array consisting of a single droplet stream. The initial droplet diameter was 61 µm.

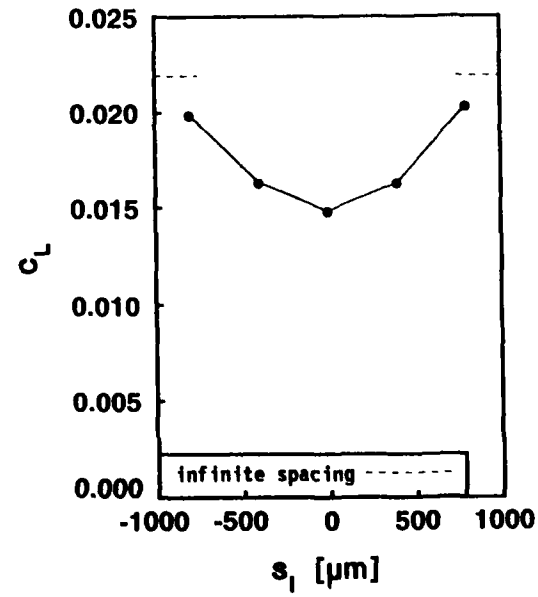

Fig. 7: Slope c_L as a function of the distance s_1 from the center stream of planar droplet array consisting of five droplet streams. The distance s_A between neighbouring droplet streams was 400 µm. The dotted line shows the value of c_L for a single droplet stream.

IUTAM Symposium on
Aerothermodynamics in Combustors
June 3-5, 1991, Taipei

COAL PARTICLE MOVEMENT IN DROP-TUBE FURNACE

Zhang Shaohong, Shi Xuegui and Xu Xuchang

Dept. of Thermal Engineering, Tsinghua University, Beijing, CHINA

The drop-tube furnace (Fig.1) in which the gas flow is purely laminar, is an experiment device for the study on chemical kinetic characteristics of coal particles[1]. The velocity profile of the primary air at the outlet of the coal feeder tube is parabolic. The velocity of the secondary air at the outlet of the honeycomb flow strainer is uniform. Generally, in the experiments to determine the chemical kinetics of pulverized coal with drop-tube furnace, the particles are supposed to move downward along the furnace axis after they are ejected out of the coal feeder tube, until they are cooled down quickly and caught by the sampling probe. With the assumption that every single particle has the same history of movement and reaction in the furnace tube, the results can be figured out from the collected data.

However, it has been discovered that pulverized coal particles may disperse quickly after entering the purely laminar flow reaction zone even though they are entering into the furnace closely to its axis. In order to find out the cause and influence of the dispresion, the multi-pulse laser holographic technology was employed in this experiment and the holographic picture of particle movement at room temperature has been taken. In this paper the cause of particle dispersion in laminar flow is analyzed, and the trajectories and the forces imposed upon coal particles under various conditions are studied. Besides, the trajectory and residence t ime are simulated through calculation.

The double-pulse holographic pictures taken at three different positions away from the feeder tube mouth (0 ~ 11,11 ~ 22,33 ~ 45mm) under the above condition are shown in Fig.2(a), (b), (c). The time interval between the two exposures is $\Delta\tau = 700\mu s$. It is found that in the experiment the mean initial velocity of the primary flow is 1.59m / s and forming a parabolic profile, while the corresponding particle velocity is only 1.13m / s on average. The particles don't drop freely in the coal feeder tube but they collide with each other or with the tube wall so that their kinetic energy is mostly lost and the initial velocity of particle is reduced significantly.

The particles possess different radial component velocities when ejected out of the outlet of the coal feeder, that is, the particle doesn't always enter the reaction zone axially but with various velocity in different directions. Besides, particles themselves are rotating in diffferent rotational directions and rates. Meanwhile, it is found that the directions of rotation do not relative to the radial deviation movements, however the maximum angular displacement shown in the pictures is approximately $\pi / 2$ and the correspondent angular velocity is 2244 1 / s.

After leaving the coal feeder, the rate of rotation of the particle drops quickly and reduces to a very small value at a very short distance from the outlet of the coal feeder tube (Fig. 2(b)). This shows that the collision of the particle with the feeder tube wall is the only important cause of the rotation, while the irregular shapes of partiles or the un-uniform of the velocity field has little effect on the rotation.

Coal particles disperse when dropping down in the laminar flow at room temperature in the drop-tube furnace. The reason of this phenomenon is that, many particles are ejected out of the coal feeder tube with different initial radial component velocities, which is caused by the collision between particles each other or the strike between the particles and the feeder tube wall. Saffman force makes the range of dispersion of particles slightly larger, while Magnus force has nearly no effect on the radial displacement of the particles.

Under the high temperature operating condition, the discrepancy of the residence time of anthracite or char particles, is not great, when moving and dispersing in the laminar flow in the furnace. The residence time of the particles can be calculated according to the real gas velocity distribution with the assumption that the particles along the furnace axis.

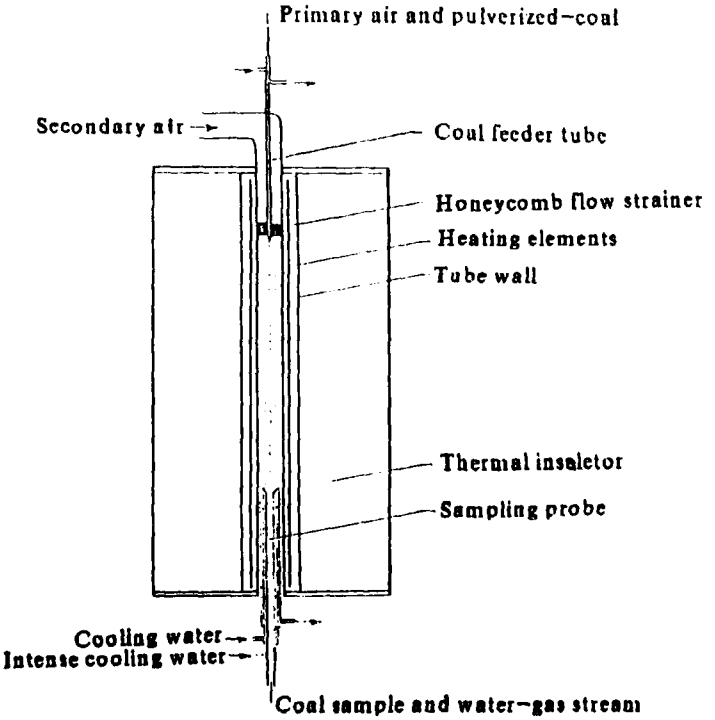

Fig.1 Drop Tube Furnace

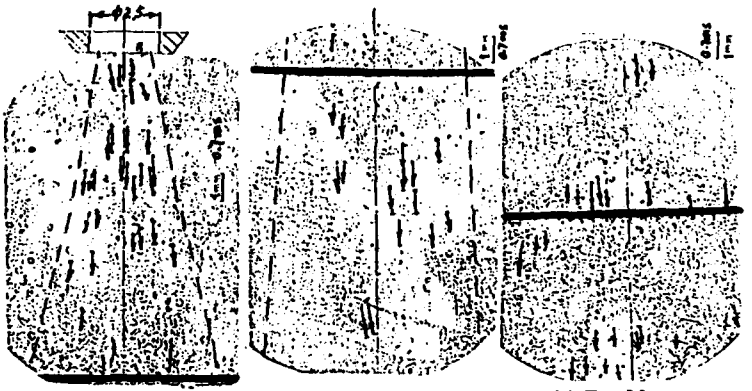

(a) Z = 11mm, (b) Z = 11mm, (c) Z = 39mm.

Fig.2 The Double-Pulse Holographic Pictures of Moving ParticlesThe time interval is 700μs. The remarkable thread is located from th burner mouth at the distance Z.

IUTAM Symposium on
Aerothermodynamics in Combustors
June 3-5, 1991, Taipei

THE EFFECT OF FUEL ATOMIZATION ON SOOT-FREE COMBUSTION IN A PREVAPORIZING COMBUSTOR

Prof. Dr.-Ing. W. Buschulte, VDI

Deutsche Forschungsanstalt für Luft- und Raumfahrt e.V. (DLR)
Institut für Chemische Antriebe und Verfahrenstechnik
D - 7101 Hardthausen-Lampoldshausen, Germany

THE COMBUSTION SYSTEM

In combustor technology soot-free combustion is a general aim, when hydrocarbon fuels are involved. During recent research work a combustor system was developped, which fulfills the demands for stoichiometric soot-free and stable combustion. In domestic oil burners this system is applied in series production.

The combustion system itself applies the technique of prevaporization and premixing by means of a mixing tube, which is located immediately downstream of the fuel nozzle and the air metering port (Fig. 1). By this air flow speed is maintained above flame propagation velocity which does not allow combustion flame to establish itself upstream of the mixing tube exit. Downstream the mixing tube exit the flame stabilizes, because the flow has decelerated by turbulent mixing after the channel is widened past the mixing tube end.

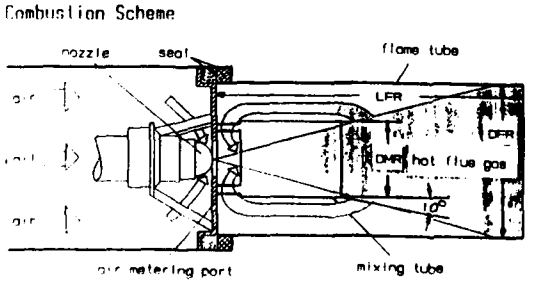

Fig. 1 Blue flame combustor

Inside the mixing tube evaporation takes place as heat is transfered to the air-fuel-stream by recirculation and radiation from the red glowing mixing tube. Recirculation of hot combustion gases from the downstream positioned combustion zone is established by means of windows in the mixing tube wall at its upstream end and through the injector effect of the main air-fuel-stream inside the mixing tube after having passed through the air metering port. The mixing tube is heated by the hot gas flowing backward from the combustion zone to the recirculation windows through the annulus between the mixing tube and flame tube.

An essential for the combustion stability is to prevent cool flue gas to be sucted into the recirculation region. If this occurs the flame starves out and combustion is interrupted. To avoid this the combustion flame is encapsuled by a flame tube which has to have certain length and diameter measures, depending on combustor performance. According to these considerations the flame tube length may be calculated from
LFR > LMR + (DFR - DMR) / 2 / tg 10°.
To guarantee safe operation the flame tube has to have about 10 to 20% overlength.

To achieve optimal spatial mixture distribution inside the combustor the distribution characteristic of the fan spray nozzle was selected so that it met the given conditions of the air flow. This then finally ends up in a combustion which burns soot-free at stoichiometric mixture ratios with almost theoretically low carbon monoxide contents, low NO_x-values and almost free of hydrocarbons (Fig. 2). In the mean-time it has experimentally been proven that this system can also be applied to controllable combustors with a performance ratio of 4:1 at least.

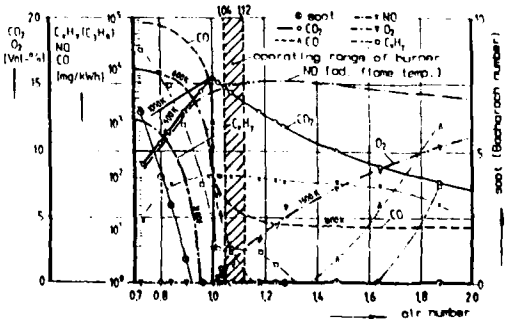

Fig. 2 Flue gas species content versus air/fuel ratio

This combustor concept was developped by computing atomization fineness and evaporation length of the fuel droplet applying a model which before had been proven successful in rocket combustor design. There combustion efficiencies, which mainly depend on evaporation efficiency, could be predicted very accurately and within

narrow tolerances.

COMPUTING MAXIMUM DROPLET SIZE IN SWIRL NOZZLE SPRAY

To compute evaporation length in the combustor maximum droplet size in the spray must be known. The following equations have been applied, which were developped during atomization research and here are specified for swirl nozzles:

$$\frac{D_{max}}{D_j} = 3{,}35 \left(\frac{\sigma}{\rho_j \cdot V_{rel}^2}\right)^{1/3} \left(\frac{K}{D_j^3}\right)^{1/3} \left(\frac{\rho_j}{\rho_g}\right)^{1/6} \cdot A^{1/5} \cdot B^{1/6}$$

$$A = 1 + 2{,}6\,\eta_j \left[\frac{K \cdot \rho_g^4 \cdot V_j^7}{72 \cdot \rho_j^2 \cdot \sigma^5}\right]^{1/3}$$

$$B = 1 + \frac{3 \cdot \eta_j}{\left[\rho_j \cdot \sigma \cdot 0{,}96 \left(\frac{\sigma}{\rho_j \cdot V_{rel}^2}\right)^{1/3} (K/D_j^3)^{1/3} (\rho_j/\rho_g)^{1/6} \cdot A^{1/5}\right]^{1/2}}$$

$$V_{rel} = \frac{\eta \cdot \dot{m}_{Ol} \cdot d_o^2}{\pi \cdot \rho_j \left(1 - (d_i/d_o)^2\right) \cdot \cos \varepsilon/2}$$

$$K = \frac{\pi}{\eta} \left(d_o^2 - d_i^2\right) \cdot \frac{1}{2 \cdot \sin \varepsilon/2}$$

Fig. 3 illustrates the relation between the maximum droplet diameter Dmax in swirl nozzle sprays for $\varepsilon = 60°$, the fuel volume flow $\dot{V}$, the nozzle exit bore diameter d_o and the nozzle pressure drop ΔP.

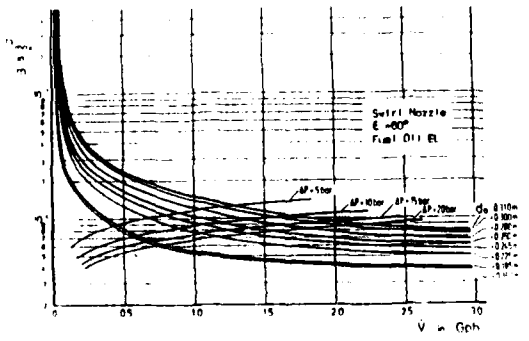

Fig. 3 Maximum droplet diameter in the spray versus throughput and bore diameter

EXPERIMENTAL INVESTIGATIONS ON EFFECT OF FUEL ATOMIZATION ON SOOT-FREE BURNING

The concept of sootfree, blue-flame burning demands that the evaporation of the fuel droplets, and here especially of the biggest ones, must be finished before the flow velocity decreasing by jet mixing with the recirculating flow drops below flame propagation speed. For the working conditions of the investigated burner this means that evaporation must be accomplished within a length of 90 mm downstream of the air metering port. Then the allowable maximum droplet diameter in the spray was computed to be 78 µm. It also showed that this droplet diameter should be a very important parameter, whether sooting yellow-flame combustion occurs or not.

This theoretical result was examined by two different series of experiments.

During the first campaign the fuel type and con dition remained constant. It is a hydrocarbon of 20 cSt viscosity at 293 K and 32 percent share of aromatic compounds. The variation in droplet size was achieved by different nozzle sizes within a combustor performance from 17 to 40 kW, by oil pressure variation, which also varied the air-fuel-ratio, and by changing air metering port area. As Fig. 4 shows, varying air-fuel-ratio finally led to values mainly in the fuel-rich-region, where soot started to raise.

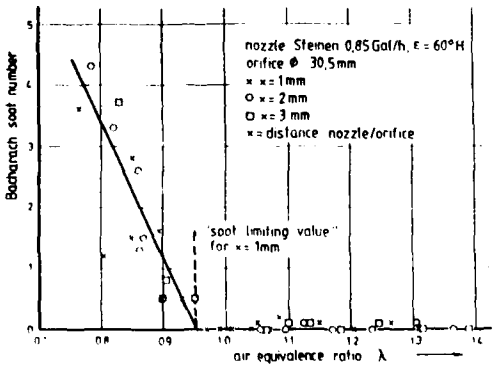

Fig. 4 Soot number of combustor gases versus fuel-air-ratio

This limiting soot value of the fuel air ratio was evaluated and related to the appropriate maximum droplet size, produced by the nozzle under those conditions. From these measurements it was found - as Fig. 5 shows - that the spray fineness must be improved, if the fuel air ratio is moved to wards fuel-rich. And in general, it is shown that the maximum allowable droplet size in the spray for soot free stoichiometric combustion is about 90 µm. This value is somewhat higher than the calculated value of 78 µm. The reason for this difference may be the complexity of the temper ature field, which is generated by mixing of fresh air and recirculating hot gas streams, and/or by the fact, that very small remainders of the biggest droplets of the spray do not produce measurable quantities of soot, if they enter the combustion zone without being evaporated

completely. This evaluation predicted that - applying swirl nozzles - the oil pressure must be considerably increased, if the combustor performance is raised. Experimental work with combustors of about 500 kW have proven this interrelationship.

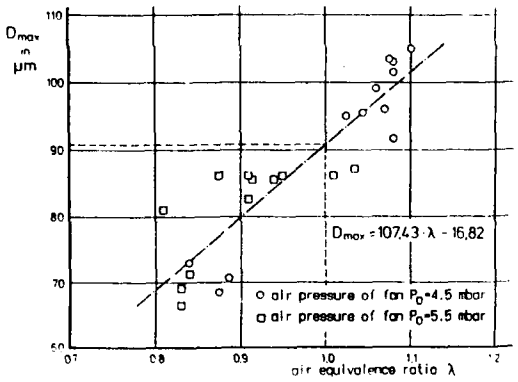

Fig. 5 Maximum allowable droplet sizes for soot-free combustion

In the second campaign combustor and nozzle remained unchanged, but the oil quality has been varied, mainly its viscosity, which defines the droplet size in the spray at a given oil pressure. After basic investigations of the viscosity influence on nozzle characteristics and atomizing capability, the spray fineness was varied by changing the fuel viscosity through varying the fuel temperature by preheating.

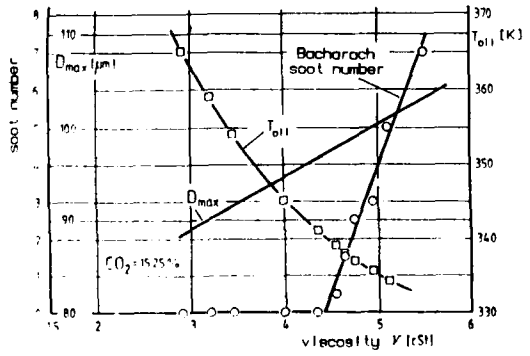

Fig. 6 Soot number of combustor gases versus fuel viscosity and temperature

The combustion experiments showed that soot free combustion could be achieved with high viscosity fuels, if by preheating of the fuel the droplet size is lowered to values in the range of normal viscous fuels. Fig. 6 shows, how by decreasing fuel temperature resp. increasing fuel viscosity the combustor can be controlled from soot free into increasingly sooting combustion. The whole sample of data shows the same dependance of maximum allowable droplet diameter versus fuel air ratio, but at slightly higher droplet size values, which is due to some size changements of the combustor between the first and second campaign. The application of fuel with higher aromatic portions showed the tendency for then lower droplet size limits. But this aspect has not yet fully been investigated.

REFERENCES

/1/ Buschulte, W.: Liquid Propellant Atomization by Injector Elements and its Effect on Combustion Chamber Efficiency. Israel Journal of Technology, Vol. 12, pp. 57 - 68, 1974.

/2/ Buschulte, W.: Process for High Efficiency Fuel Oil Combustion with Low Pollutant Emission. Ger. Chem. Eng. 2 (1979), 293-298, Weinheim, 1979.

/3/ Buschulte, W.: Untersuchungen zur Anwendung höher viskoser Heizöle in einem rußfrei arbeitenden Verbrennungssystem, VDI-Bericht Nr. 423, Flammentag 1981, pp. 181 - 187.

IUTAM Symposium on
Aerothermodynamics in Combustors
June 3-5, 1991, Taipei

Aerodynamic Characteristic of Pulverized Coal Bluff-body Burner with Stabilization Chamber

Caiyuan Han

Huazhong University of Science and Technology, Wuhan, China

INTRODUCTION

The pulverized coal bluff-body burners are widely used in China power boilers[1].The characteristic of flow field in burner outlet and its profile in furnace are shown in Fig.1 and 2. The kinds of burned coal are sub-bituminos coal,anthracite,etc, the boiler capacities are 35-670(t/h).

In order to utilize lower-grade coal and meet the need of stable combustion at low boiler load, a new type pulverized coal burner is developed, which is the bluff-body burner with stabilization chamber.

EXPERIMENT DEVICE AND BURNER MODULES

The characteristic tests of flow field in burner outlet are performed in a wind tunnel, a stationary one dimensional flow with low turbulance intensity can be formed in the outlet.

In experiments, the geometrical shapes and sizes of stabilazing chamber can be changed, with those of the bluff-body maintained unchanged.Three types of stabilizing chamber are shown in Fig.3, whose shapes of cross section are all rectangular.

RESULTS OF COLD FLOW TESTS AND DISCUSSION

1.Effects of geometrical shape of stabilizing chamber on recirculation

The velocity field in centre section is measured after the flow self-modeling zone formed. The sizes of recirculating zone and mass flux rate in three types of stabilizing chamber are obtianed and shown in Fig.4, and the testing results are listed in table 1.

It can be known from Fig.4 and table 1 that the stabilizing chamber makes recirculating zone and mass flux rate behind the bluff-body considerably enlarged. Compared with bluff-body without chamber, the length of recirculating zone is increased 2 times and maximum mass flux rate appoximately 2 times.

2.Fullness of recirculating zone in stabilizing chamber

Through mensuring the condition of recirculating zone along bluff body height, we can find that its size at the middle section is maximum, approaching the two ends of bluff-body, it goes smaller. Obviously, gas will enter the recirculating zone from the two ends of bluff-body because of negative pressure. If stabilizing chamber is used, the upper and lower ends of bluff-body seem to be covered, and air flow can not affect the recirculating zone. Therefore, whole cavity can be more fully filled with the recirculating zone, and the mass flux rate and heat capacity greatly increased. This screen effect can prevent cold air from entering the recirculating zone directely, which are helpful the heating of lower-grade pulverized coal and suitable for stable combustion at lower boiler load. A detail testing results are listed in table 2.

RESULTS OF COMBUSTION TESTS AND DISCUSSION

Pulverized coal combustion tests are performed on the experiment device shown in Fig.5 [2], which can burn pulverized coal 20kg per hour. Fig.6 shows the temperature profile of flame along centreline, from which it can be seen that combustion process is further improved by use of stabilizing chamber, temperature of burned gas in furnance is remarkably increased, about by 60-100 C compared with that without stabilizing chamber.

CONCLUSION

Based on analysing the results of cold flow and combustion tests for the burners in stabilizing chamber, following conclusions can be obtained.

1. Stabilizing chambers can remarkably enlarge the size of recirculating zone behind bluff-body and mass recirculating rate.

2. The fullness of recirculating zone in stabilizing chambers is much better than that of common bluff-body.

3. It is seen from the test results for three different shapes of stabilizing chambers that the shapes have no great influence on recirculation zone. In view of avoiding coking, the stabilizing chamber of type Ⅲ is most reasonable,which is suddenly-extended from two sides and gradually enlarged from two ends.

4.The utilization of chambers is helpful for stability and strengthen of combustion process, and the flame temperature is increased,so that it can be adapted for combustion of lower-grade coal and stable combustion at low boiler load.

REFERENCES

1. Y. Mi and C. Zheng, Pulverized coal bluff-body burner and its mechanism of flame stabilization, Coal Combustion, Beijing, 1988

2. J. Yuan and C. Han, Investigation on flow characteristic and combustion process of the controllable-vortex pulverized coal burner, Coal Combustion, Beijing, 1988

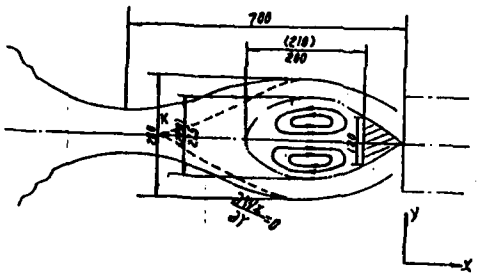

Fig.1.flow field in outlet of burner

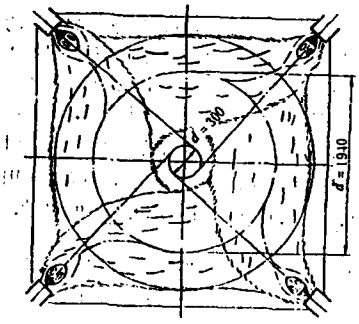

Fig.2. flow field in furnace

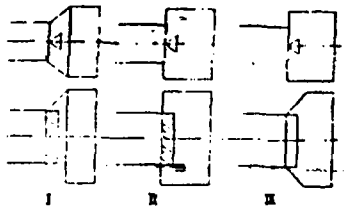

Fig 3

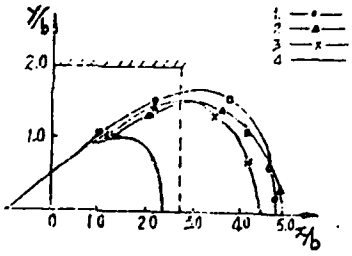

Fig.4(a) size of recirculation zone

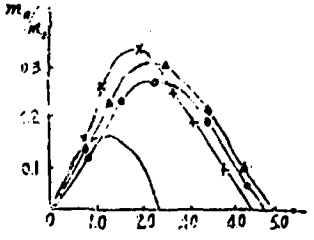

Fig.4(b) mass recirculation rate

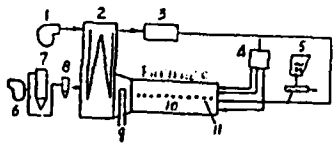

Fig.5. experiment device

1.blast fan 2.air preheater
3.electric heater 4.stabilization pressure box 5.pulverized coal distributor 6.draft fan
7.cloth duster 8.wind duster
9.cooling water 10.combustion chamber 11.holes

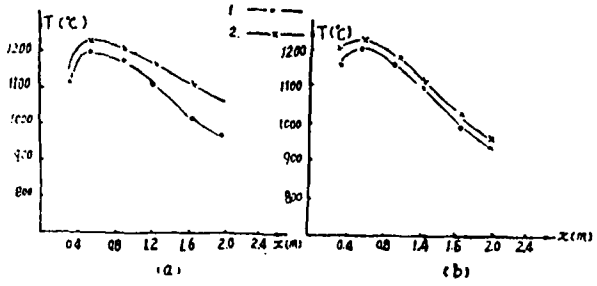

Fig.6.Flame temperature profile in centreline
(a) coal A (b) coal B
--- no stabilizing chamber
-*- with stabilizing chamber

Table 1

Burner Type	L/b	D/b	$(m_R/m_0)_{max}$
Bluff-Body	2.36	2.00	0.17
Type I	4.75	3.42	0.23
Type II	4.78	3.22	0.34
Type III	4.56	3.22	0.35

Table 2

Burner Type	Section	L/b	D/b	$(m_R/m_0)_{max}$
Type I	Z = 0	4.75	3.42	0.23
"	Z = 35mm	4.79	3.56	0.35
"	Z = 80mm	5.04	2.72	0.15
Type II	Z = 0	4.78	3.22	0.34
"	Z = 35mm	4.31	2.78	0.215

IUTAM Symposium on
Aerothermodynamics in Combustors
June 3-5, 1991, Taipei

MATCHING FUEL INJECTION EQUIPMENT TO DIESEL ENGINES

R Ziarati BSc, PhD, FIProdE, MIMechE, C Eng
Dean of External Affairs, Birmingham Polytechnic
Birmingham, United Kingdom

A Veshagh BSc, PhD, MASME, MSAE
Advanced Technology Centre,
University of Warwick
Coventry, United Kingdom

SYNOPSIS

This paper describes the development and validation of two computer models developed for the matching of fuel injection equipment to diesel engines. Both models included mathematical representation of fuel atomisation and ignition delay together with a simple simulation model of engine cycle. The effect of fuel quality was taken into account on a qualitative basis while empirical relationships were employed for the prediction of ignition delay under various operating conditions.

Both models were tested against experimental results including tests using varying quality fuels. All the calculations were carried out on a step-by-step basis to predict engine performance parameters over the whole cycle.

The success of the models were primarily based on the use of a number of empirical coefficients or correlation factors in the formulae used in the models. However, in order to enhance the simulation capabilities of the models, their dependence on such empirical coefficients had to be removed. The two models were therefore merged into a new model combining the "jet mixing" calculation with those of "droplet burning" with a potential for predicting combustion emissions.

The full paper will include the mathematical expressions derived for the earlier models and their enhancements when combined into the new model. The paper will also report on the results of the tests carried out on two engines running on diesel and heavy fuels at different conditions, together with predicted results from the earlier as well as the new model.

INTRODUCTION

In an earlier research project [1] two Diesel simulation programs were developed one based on a "jet mixing" model and the other on a "droplet burning" model for simulating the penetration and combustion of fuel spray. Both models were employed separately to study the effect of various fuel injection equipment (f.i.e.) parameters or fuel spray and also to match the f.i.e. to DI Diesel engine of different types [2]. However, no attempts were made to combine the two models into one comprehensive simulation package such that the combined effect of jet mixing and droplet burning could be taken into consideration.

This paper reports on the recent developments of the simulation models and also the assessment of their individual merits in order to formulate a single combustion model for the medium and small size DI Diesel engines.

THE COMBINED SIMULATION MODEL

The new simulation program is based primarily on "jet mixing model", together with an engine cycle model based on a modified air standard cycle, Fig. 1. The combustion formulation assumes that air entrainment is controlled by an elemental and multizone jet and, after impingement, by an elemental wall jet, Fig. 2. The fuel - air mixing within the jet (micro mixing) is controlled by turbulent diffusion. The jet interaction is determined by the spray envelop geometry and when interaction is detected, the entrained air is assumed to be shared by the sprays using a single 'global' model, Fig 3.

The air entrained by the gas jet at any instant quantifies the larger scale mixing (macro mixing) of injected fuel and air in the chamber. Micro mixing is represented by a simple representation of turbulent diffusion.

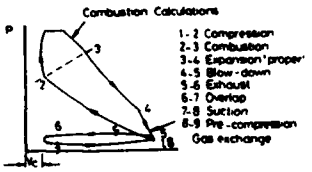

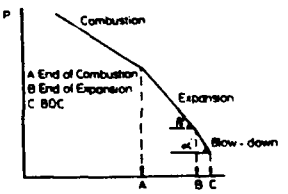

n_e (expansion index) = tan β
n_b (blow-down index) = tan α'

Fig 1 Details of Engine Cycle

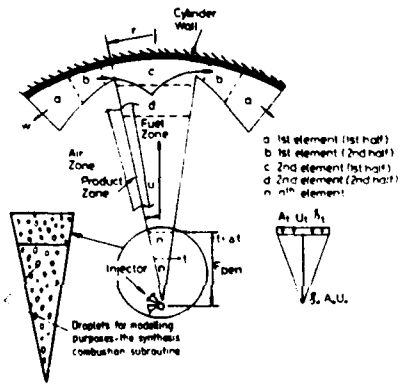

Fig 2 Simplified Presentation of Elemental Free and Wall Jets with No Swirl

The engine cycle is divided into:

i) Close Cycle Calculations
a. Compression period (1-2)
b. Combustion period (2-3)
c. Expansion period (3-4)

ii) Open Cycle Calculations
a. Blowdown period (4-5)
b. Exhaust period (5-6)
c. Overlap period (6-7)
d. Suction period (7-8)
e. Pre-compression (8-9)

The model utilises two types of combustion calculations (A) analysis, (B) synthesis, Fig. 4. Analysis is required to interpret a given cylinder pressure diagram in terms of the release of heat by combustion to account for the known changes in pressure. In this way data relevant to combustion process are obtained from the diagram of cylinder pressure as a function of crank angle measured on a running engine. The heat release diagram obtained from analysis, is checked against the heat release diagram predicted by synthesis. The procedure assumes a single zone approximation i.e. conditions of pressure, temperature and gas composition are taken as uniform throughout the cylinder.

Synthesis is the reverse procedure, the calculation of cylinder pressure and hence engine performance parameters from combustion equations that leads to the calculation of heat release rate.

A computer program called 'Heat Release' is used for the analysis. In this program, the heat release and work output are calculated from the measured values of cylinder pressure together with data on engine geometry and air/fuel ratio.

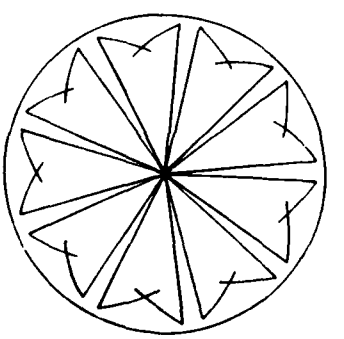

Fig 3 Jet Interaction Model

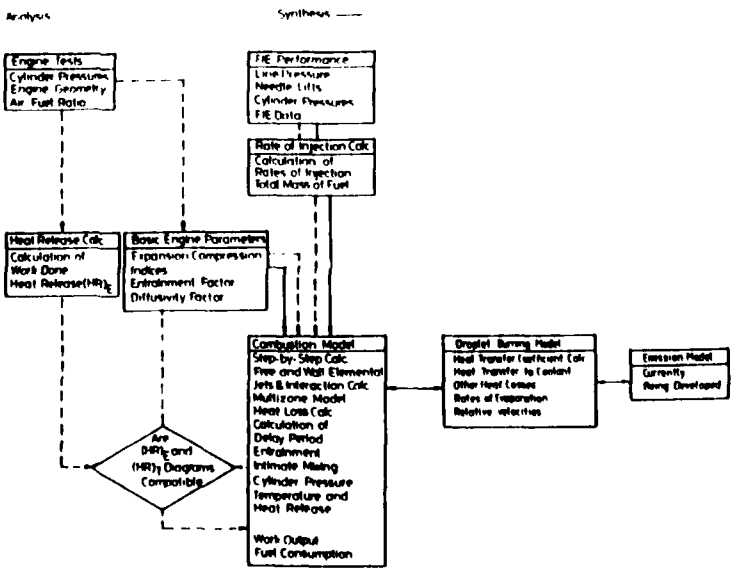

Fig 4 Engine Combustion Model

The basis of the calculations in this program is the application of the first law of thermodynamics to the cylinder contents.

The synthesis is the main program called 'Diesel Engine Simulation'. Here, for a given set of initial conditions and fuel injection rate diagram, the program calculates pressure and temperature values, heat release, power and fuel consumption for one engine cylinder. The model only considers the thermodynamics and fluid mechanics of the combustion process and does not include chemical kinetics.

It should also be noted that the 'Diesel Engine Simulation' program (for quantitative considerations) requires the total mass of fuel injected and the rate of fuel injection as input data. These two parameters are obtained from the line pressure and the needle valve lift diagrams. Here, numerical arrays representing the line pressures and the needle valve lifts are fed into a program called 'Fuel Injection' and the required outputs are obtained for any type of nozzle configuration.

The synthesis calculations are supplemented by a "droplet burning" subroutine [3]. This subroutine is almost entirely confined to the 'closed' period in the cycle and is only used when detailed analysis is required viz when different quality fuels are being tested and/or for emission calculations. It considers the injection of the fuel and its evaporation. The life span of each element of fuel spray and the droplets within the elements are monitored at given time intervals (usually one degree crankangle). The evaporation of the droplets, the mixing of the vapour with air within each element of the jet and their combustion is examined at each step. The heat released by combustion is calculated by a set of differential equations considering heat transfer to engine block and coolant leading to the prediction of cylinder pressure variations during the engine cycle.

This subroutine performs the following calculations:
i) heat transfer coefficient calculation using Woschni formula [4]

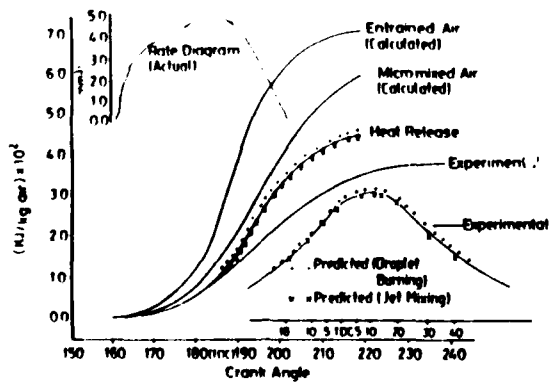

Fig 5 Comparison Between Experimental and Predicted Results

ii) heat transfer to coolant [5] other heat losses [6]
iii) rate of droplet evaporation
iv) relative velocity of fuel droplet

The two pressure variations obtained from the synthesis and the above subroutine can be compared and therefore both 'rate' and 'magnitude' tolerances may be reduced using an iterative technique. Successful matching can then lead to the calculation of engine performance parameters and emissions.

If at least one set of experimental data on the injection characteristics viz line pressure and needle lift diagrams together with an actual engine pressure oscillogram are available, an 'analysis' evaluation can be carried out between experimental and predicted data. Good correlation can lead to quantitative prediction of performance parameters and emissions.

Fig. 5 shows the experimental and predicted results for 210 mm diameter bore engine running on diesel oil. The droplet burning subroutine eliminated the need for estimating a number of empirical coefficients viz the entrainment factor and diffusivity constants.

REFERENCES

1 Ziarati R.
"An Investigation into Fuel Injection Equipment and Combustion Performance of Medium Size Diesel Engines"
IMechE - Seminar on Practical Limits of Efficiency of Engines, Proc. IMechE London, 1986

2. Ziarati R., Veshagh A.
"Mathematical Modelling and Computer Simulation of Medium Size Diesel Engine Running on Varying Quality Fuels"
COMODIA 90 - International Symposium on Diagnostics and Modelling of Combustion in Internal Combustion Engines, Kyoto, Japan, Sept 1990

3. Ziarati R., Veshagh A., Hawksley G.
"Penetration, Interaction and Combustion Modelling"
EC Non-Nuclear Research Programme Report, Jan 1988

4. Woschni, G.
"A Universally Applicable Equation for the Instantaneous Heat Transfer Coefficient in the Internal Combustion Engine"
SAE Paper No 670931, 1967

5 Alcock, J.F.
"Thermal Loading of Diesel Engines"
IMechE., Trans.Vol 77, 1965

6 Annand, W.J.D.
"Heat Transfer in the Cylinder of Reciprocating Internal Combustion Engines"
Proc. IMechE., Vol. 177, No 56, 1963

7 Hirayasu, H., Kadota T.
"Fuel Droplet Size Distribution in Diesel Combustion Chamber"
SAE Paper No 740715, 1974

IUTAM Symposium on
Aerothermodynamics in Combustors
June 3-5, 1991, Taipei

Thermal Decomposition of CH_2Cl_2 in $H_2/O_2/Ar$ mixtures: Implication to Acceleration and Inhibition of Combustion and Pyrolysis by Chlorocarbon

WenPin Ho and Joseph W. Bozzelli

Dept. of Chemical Engineering, Chemistry, and Environmental Science
New Jersey Institute of Technology,
Newark, NJ 07102 U.S.A.

Chlorinated hydrocarbons (ClHC) have been used on a large scale by industry either as raw materials for products or as solvents; with both cases often producing large amounts of these chlorocarbons as wastes. Reasonable methods for effective destruction of these ClHCs include: conversion to HCl and CO_2 (oxidation/incineration) or conversion to HCl and hydrocarbons (pyrolysis in a hydrogen or methane rich atmosphere. There is, therefore, a significant need to develop quantitative insights into the mechanisms of these pyrolysis and oxidation reactions in order to better understand and utlimately to optimize these reaction processes and the conversion of chlorocarbons by incineration. In this paper, we present results from an experimental study on dichloromethane (DCM) reactions in H_2/O_2 atmospheres and a detailed kinetic model based upon fundamental thermochemical principles for the reagent and product concentration profiles versus time and temperature. Sensitivity analysis on the model clearly shows which reactions are important to inhibition and leads to a better understanding of the fundamental combustion process which occur during the incineration of CH_2Cl_2 and similar chlorinated methanes; here we focus on the reactions which cause inhibition in CO burnout and acceleration in fuel rich pyrolysis regimes.

The thermal decomposition of dichloromethane in hydrogen/oxygen mixtures with argon bath was carried out at 1 atmosphere total pressure in tubular flow reactors of varied surface to volume (S/V) ratio. Varying reactor surface to volume ratio helps verify that homogeneous reaction dominates the observations and allows one to decouple the apparent wall and bulk phase decomposition rates. The reactions were analyzed systematically over temperature ranges from 600 to 820 ^0C, with average residence times between 0.1 to 2.0 seconds.

It was found that complete decay (99%) of the dichloromethane at 1 second residence time occurs at about 820^0C for all the reactants ratio sets. The major products for dichloromethane decomposition are methyl chloride, methane, CO, and HCl. The quantity of chlorinated products decrease with increasing temperature and residence time. Oxygen has almost no effect on the decay of dichloromethane when conversion is below 50% (less than 750^0C) and/or the initial oxygen concentration is below 5%. Formation of CH_3Cl as one of the major products from CH_2Cl_2 increases to a maximum when conversion of dichloromethane is at 80%; and this is observed for all reactant ratio sets. CH_3Cl then drops quickly with increasing temperature and/or increased oxygen. The higher the ratio of O_2 to H_2, the lower the temperature needed to observe the formation of CO and CO_2. The major products when conversion is above 90% are HCl and non-chlorinated hydrocarbons : CH_4, C_2H_2, C_2H_4, CO, and CO_2. Minor intermediate products whose concentrations are also monitored include: C_2H_3Cl, $CHClCHCl$, and CH_2CCl_2.

A first order plug flow model was utilized to analyze the overall (global) experimental data on CH_2Cl_2 loss. In addition the homogeneous and wall rate constants were decoupled and separately evaluated. The following Arrhenius rate expressions were found to fit the overall reaction systems studied.

$Ar : O_2 : H_2 : DCM$	k (1/sec)
97 : 1 : 1 : 1	$k = 3.76 \times 10^{14} \times \exp(-69982/RT)$
95 : 2 : 2 : 1	$k = 5.00 \times 10^{12} \times \exp(-60405/RT)$
95 : 3 : 1 : 1	$k = 2.25 \times 10^{15} \times \exp(-72645/RT)$
95 : 1 : 3 : 1	$k = 4.25 \times 10^{13} \times \exp(-61969/RT)$

A detailed kinetic reaction mechanism was developed and used to model results obtained from the experimental reaction system. The kinetic mechanism includes 142 elementary reaction steps involving 67 stable compound and free radical species with the addition, beta scission and recombination type reactions all analyzed by Quantum Rice-Ramsperger-Kassel (QRRK) theory [1][2].

Experimental data are compared with model predictions for reagent decomposition and product distribution between 700^0C and 800^0C. The calculated mole fractions for CH_2Cl_2 are in very good agreement with those determined experimentally. For CO, CH_4, and CH_3Cl, model predictions are also in reasonable accord with the experimental data. The model predicts the mole fraction levels of CO_2 versus time and temperature reasonably well, where it slightly over-predicts CO_2 at higher temperature; when compared to the experiment and it under-predicts chlorinated C_2 products

Sensitivity analysis indicates that the reaction:

$$OH + HCl \longrightarrow H_2O + Cl$$

is a major cause of OH loss and this decrease in OH effectively stops the $OH + CO$ conversion. The reaction of $CO + HO_2$ is now the primary mechanism for CO burnout to CO_2. In chlorocarbon oxidation reactions, the OH reaction with HCl will occur in preference to reaction with CO because of the higher rate constant, when chlorocarbons which lead to HCl levels comparable to those of CO are present.

The reaction of $Cl + HO_2$ part of which goes to $HCl + O_2$ (termination), now becomes an important part of the inhibition process, because decreased CO burnout decreases the temperature. This synergistic effect makes the HO_2 radical even more important, because its unimolecular decomposition is slowed.

The model tells us one more interesting component relating to the effects of chlorocarbon inhibition. The addition of limited quantities of high temperature H_2O to the oxidation system, where Cl or oxygen atoms are present, shifts the reactions of:

$$OH + HCl \longleftrightarrow H_2O + Cl$$

and

$$OH + OH \longleftrightarrow H_2O + O$$

to left increasing the OH concentrations and helping CO conversion.

We also observe that chlorocarbons initiate reaction in fuel rich regions of ClC/HC/O2 mixtures faster than occurs in normal oxidation of hydrocarbons. This results in more pyrolysis or molecular weight growth reactions in the fuel rich zones and increased possibility of soot formation. The reason for the increased HC reactions is again the presence of chlorine. Carbon-chlorine bonds are known to be weaker than carbon - hydrogen, carbon-carbon or carbon-oxygen bonds and thus the C-Cl bond will break (chain-branching) at lower temperature. The Cl atoms generated will rapidly abstract H from the hydrocarbons, (low activation energies and relatively high Arrhenius A factors), thus extending the chain.

The inhibition effect is dominant in the CO burnout regime and significant levels of HCl can dramatically effect conversion.

The authors gratefully acknowledge funding from the New Jersey Institute of Technology NSF Industry/University "Hazardous Substance Management Center".

REFERENCES

1. Dean, A.M., J. Phys. Chem. 89 4600 1985.

2. Westmoreland, P.R. and Dean, A.M. AICHE J. 32 176 1986.

IUTAM Symposium on
Aerothermodynamics in Combustors
June 3-5, 1991, Taipei

MODELLING OF THE DETONABILITY LIMITS IN CHANNELS

A. A. BORISSOV and O. V. SHARYPOV

Institute of Thermophysics
Siberian Branch of USSR Academy of Sciences
Novosibirsk 630090 USSR

ABSTRACT

The paper is devoted to study of wave-kinetic interactions in active medium. The attempt of a new way description of pulsating cellular structure of gas detonation front is undertaken in the paper. The use of self-organization theory methods is non-traditional approach to the modelling of detonations.The developed non-linear model is very convenient for numerical simulation of the processes of detonation wave evolution. In practice detonations often is undesired and dangerous phenomenon. When one designs a furnace, reactor, combustor, engine and so on it needs to take the additional precautions against the detonation regime. A great number of the opposite applied problems also exists. For successful solution of these problems it is necessary to understand in detail the physical factors affecting the detonation process. The great number of experiments shows that gas detonation fronts as a rule have a non-steady three-dimensional structure. Planar stationary (in the model of Ya.B. Zeldovich, W. Doring and J. von Neumann [1]) detonation waves appear to be unstable with respect to small transverse perturbations with wavelength of the same order of magnitude with the induction zone size [2,3]. Infinitesimal disturbances in non-equilibrium medium can increase, their instability deals with the transition of internal energy of the system into the energy of waves. The structures of finite amplitude appear as a result of competition between a dissipative gas-dynamic mechanism and perturbation energy pumping due to reaction thermal release. In practice it is very important to be able to predict the mean size of detonation front inhomogeneities for determination of detonability limits and critical tube diameter.

The initial formulation of the problem involves three-dimensional equations of perfect gas dynamics with one-step chemical reaction (kinetics is of Arrhenius type). One can represent detonations in form of superposition of Zeldovich's planar stationary wave and unsteady three-dimensional perturbations. Initially these perturbations are infinitesimal. The wavelength of transverse perturbations is supposed to be much more than the amplitude of front curvature. Conserving only the terms of the 1st order infinitesimal we'll seek the solution of linearized system (in the vicinity of the shock front) in form of superposition of harmonics. Then for the front surface we'll obtain the equation:

$$x - x_o = F(t,y,z) = f_{mn} \exp(\Omega t + i k_m y + i g_n z)$$

the subscript "o" marks the values of variables at the shock front of stationary detonations. The solutions of unsteady linear problem can be written in the form of superposition of chemical and gas-dynamic wave modes with indefinite coefficients. One can write the conditions of conservation of reactant concentration, mass flux, normal and tangential momentum flux components at the perturbed shock. The condition of compatibility leads to the relation $\Omega(æ)$ [4-6], where æ is two-dimensional wave number:

$$Im(\Omega) = C(D)\, æ \qquad (1)$$

$$Re(\Omega) = -æ + (\alpha+1)\, æ^2 - æ^4 \qquad (2)$$

where $\alpha = (1 - \rho_-/\rho_o)(E/RT_o)$,

$$C(D) = \pm \frac{1}{2}\left\{ \sqrt[3]{b+\sqrt{d}} - \sqrt[3]{b-\sqrt{d}} \right\} \qquad (3)$$

$$b = (18D - 10)/3^{3/2}, \quad d = D^3 + 5D^2 + 3D - 9$$

ρ is the density, T is the temperature, E is the activation energy, R is the universal gas constant, D is the planar detonation wave speed, C is the velocity of transverse waves, ρ_- is the density of unperturbed gas ahead

of the detonation wave. All the variables are normalized using the time and the length of chemical transformation zone, ρ_o and T_o. Linear relation (2) predicts the amplification of weak harmonics with the wavelengths λ from the interval:

$$2\pi \leq \lambda \leq \frac{4\pi\alpha}{\sqrt{4\alpha+1}+1} \qquad (4)$$

The reason of amplification is the pumping of perturbation energy due to the heat release of irreversible reaction. Long wavelenth harmonics are attenuated due to gas-dynamic dissipative mechanism.

If one treats each small part of a weakly distorted shock wave front approximately as a planar wave propagating along the normal at the velocity D, then the velocities of different front sections in the direction of x-axis are different and the curvature decreases. This mechanism is described by the non-linear terms of the evolution equation [7] :

$$\frac{\partial F}{\partial t} = -\frac{D}{2}\left[\left(\frac{\partial F}{\partial y}\right)^2 + \left(\frac{\partial F}{\partial z}\right)^2\right] \qquad (5)$$

The non-linearity can stabilize the solution by redistributing of energy in the spectrum between increasing and subsiding harmonics. In two-dimensional case the solution of equations (2) and (5) both leads to forming of quasi-stationary periodic cellular structure (see Fig.1). Trivial solution is used as initial condition.

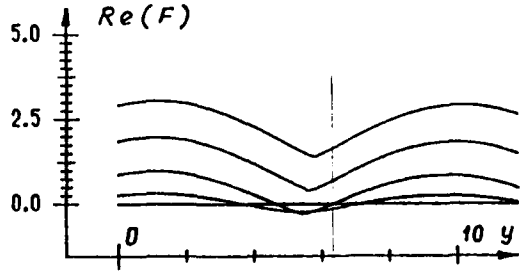

Fig.1 The cellular structure; time: 0; 17.5; 20; 22.5; 25.

For numerical simulation of the solution the spectral method (fast Fourier transform) is used, the non-linearity is calculated with the help of finite-differential scheme.

If one takes into account $Im(\Omega)$ (gas-dynamic oscillatory regime) then the solution turns out to be essentially unsteady. Cyclic motion of transverse waves appears. The picture looks like the natural pulsating detonation front in plane channel (see Fig.2). The velocity of transverse waves is approximately 0.4 D (a velocity of (0.58 ± 0.05) D is found in experiments).

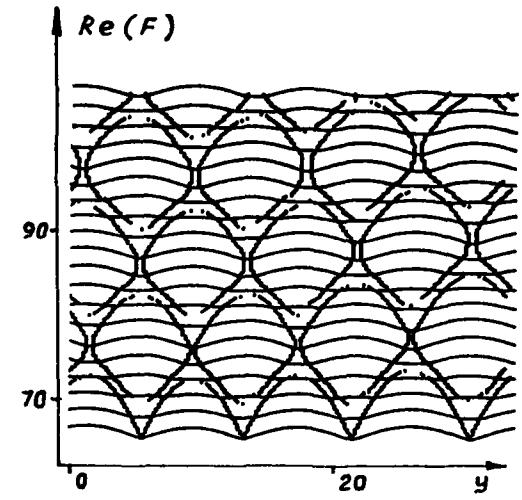

Fig.2 Pulsating regime (α=3, C=.4 D).

If one follows the trajectories of the angled points of the front (see dotted lines in Fig.2) then the scheme reproducing the detonation imprints on the sooty channel wall can be obtained.

The comparison of theoretical results with experimental data shows that this simple quasi-linear evolution model is able to predict certain reliable information. In spite of the existence of large gas parameters' variations behind the natural pulsating detonation front relatively to the stationary values the used quasi-linear approach turns out to be admissible. Apparently the cause is that the deviation of the state of all gas mass from the state in planar stationary detonation wave is in general sufficiently weak. It would be interesting to try to answer with the help of the model some questions which are not clear yet.

The first one: The experiments [8] show that regular cellular structure of detonations is destroyed as the activation energy increases. This is not quantitative effect but one can observe cells of quite different sizes. The regularity also depends on the intensity of detonation wave and adiabatic exponent γ. There is no any theoretical model now to explain this dependence. But it is easily seen from the equation (2) for real part of Ω or equation (4) that the width of the unstable harmonics region in the spectrum is a function of parameter α. So the larger α, the larger quantity of unstable harmonics which present in solution, therefore the regularity of the cellular structure disappears. If one would remind the expression for α one would see that it is proportional to activation energy and depends on the wave intensity and γ. This is very clear physical explanation for the interesting experimental observation. The results of calculations as α = 3, 5, 7 are represented in Fig.2-4 to illustrate this effect.

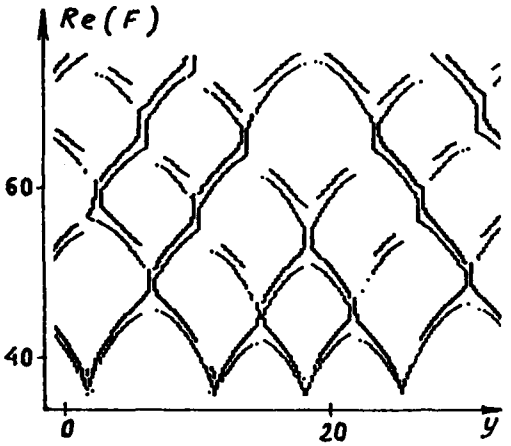

Fig.3 Pulsating regime, $\alpha = 5$.

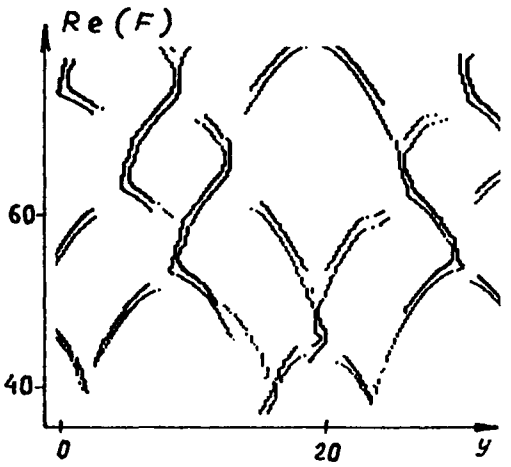

Fig.4 Pulsating regime, $\alpha = 7$.

The second problem is connected with so-called "13 λ - correlation" of critical tube diameter d_c . When the planar detonation wave emerges into a volume or when the detonations propagates in the channel with elastic walls then rarefaction waves can transform it to the deflagration regime. There is the qualitative criterion which states that critical radius of the tube equals to effective thickness of detonation wave Δ_H . This thickness is the distance from the shock front to the equilibrium Chapman-Jouguet plane. But the problem of Chapman-Jouguet plane position is very complicate and isn't solved yet, so in practice this criterion turns out to be useless.

On the basis of the model presented here one could try to formulate a new criterion. First of all there is a certain characteristic time of the process which could be included in new criterion. Namely, it i the time of forming of cellular structure t_f which must be not more than time of rarefaction wave propagation to the tube axis $t_c = d_c/2C$. This criterion notes the competition of two opposite physical mechanisms. The rarefaction waves tend the front to become smooth, but the sharp folds are the origins of fast reaction and without them detonations transforms to deflagration. So the critical condition requires the time of fold forming t_f to be equal to t_c . In other words the time of forming of cell structure must be equal to the time of its destruction. May be there is a certain physical connection between this new criterion and the traditional one.

The experiments [8] show that critical tube diameter can be two times more or less than 13 cell sizes, the criterion $d_c = 13\ \lambda$ is not universal and depends on the kinetics of reaction. Except this the critical diameter is approximately inversely proportional to the wave intensity. The represented model could explain these facts. In calculations the characteristic time of forming of cellular structure t_f grows as α decreases. This is due to proportionality of increment $Re\ (\Omega)$ to α . The larger real part of Ω the less time t_f and the less relation of critical tube diameter per cell size. For α =3 and α =5 the relations d_c/λ differ approximately two times.

Thus the developed approximate mathematical model for the evolution of gas detonation front helps us to explain the physical essence of certain phenomena. Particularly it shows the great significance of parameter α (proportional to activation energy, γ and intensity of shock wave) for description of the dynamics of gas detonations.

REFERENCES

1. Zel'dovich Ya.B., Kompaneyets A.S., 1955 The Theory of Detonations.- Moscow, USSR, Gostekhteorizdat.
2. Zaydel' R.M., 1961 Doklady Akad. Nauk SSSR, **136**, pp. 1142-1145.
3. Pukhnachyov V.V.,1963 Doklady Akad. Nauk SSSR, **149**, pp. 798-801.
4. Borissov A.A., Sharypov O.V., 1989 Intern. Forum on Mathematical Modelling and Computer Simulation of Processes in Energy Systems, Sarayevo, Yugoslavia, March 20-24.
5. Borissov A.A., Sharypov O.V., 1989 3-d Intern. Seminar on Flame Structure, Alma-Ata, USSR, Sept. 18-22.
6. Borissov A.A., Sharypov O.V., 1990 1st Asian-Pacific Intern.Symposium on Combustion and Energy Utilization, Beijing, China, October 15-18.
7. Zel'dovich Ya.B.,1966 Zh. Prikladn. Mekhan.Tekhn.Phys.,No 1,pp.102-107.
8. Vasiliev A.A., Mitrofanov V.V., Topchiyan M.E., 1987 Phys. Goreniya Vzryva, **23**, No 5 , pp. 109-131.

IUTAM Symposium on
Aerothermodynamics in Combustors
June 3-5, 1991, Taipei

FLOW DILATATION EFFECT UNDER CONDITION OF COMBUSTION

STANISLAW ZURKOWSKI

Aviation Institute, Warsaw, Poland

The flow field in a combustion chamber during its operation is often evaluated on the basis of measurements carried out with isothermal flow. To make this evaluations properly it is necessary to know the effect of combustion on deformations of the flow field.

This paper presents a theoretical study of the influence that the chemical reaction, particularly combustion, has on the dilatation of flow. The method based on phenomenological theory of balancing was used to study the dilatation of the substantial region of balancing as well as the componential regions for the case of the gas phase reaction in the steady-state conditions.

The paper proves that the dilatation of the reacting flow can be expressed as a superposition of three phenomena: baroclinic dilatation, thermal dilatation and kinetic dilatation.

Baroclinic dilatation for both types of regions is caused by the pressure gradient in flow mixture.

Thermal dilatation for both types of regions is caused by the thermal gradient which results from the thermal effect of a chemical reaction.

It was demonstrated that the effect of thermal gradient is opposed to the effect of pressure gradient.

Kinetic dilatation of the substantial region is a phenomenon caused by the concentration gradient which results from the conversion of mass.

Kinetic dilatation of the i-th componential region is a phenomenon caused by two factors:

- flow of the i-th mass, which results from the fact that the concentration gradient of this mass does exist;
- flow of the i-th mass through the region with variable concentration of other components.

It is shown that the dilatation of the substantial region is not the algebraic sum of the dilatations of componential regions.

In the case of kinetic combustion the dilatation of every componential region is equal to the dilatation of the substantial region.

In the case of diffusion combustion the kinetic component of the dilatation of the substantial region disappears.

On the basis of solutions obtained for general case of combustion the analysis of flow dilatation in a sector of an annular combustion chamber is presented.

IUTAM Symposium on
Aerothermodynamics in Combustors
June 3-5, 1991, Taipei

ON AEROTHERMODYNAMICS OF ELECTRO-CHEMICAL PULSEJET

STANISLAW WOJCICKI

WASHINGTON STATE UNIVERSITY
PULLMAN, WASHINGTON 99164-2920, USA

GENESIS

Electro-chemical pulsejet combines the pulse combustion technology [1] with electro-chemical effect, that consists in flame acceleration, when the flame is affected by an electric discharge [2].

The development of pulse combustors was initiated in the thirties, when P. Schmidt obtained a German patent on mechanically valved pulsejet (Fig. 1a). The engine consists of a combustion chamber and a long exhaust pipe. The combustion in the chamber promotes a pressure buildup. This in turn starts expansion and then vacuum formation as a result of inertia of the flow. The partial vacuum opens the check valve and begins recharging the combustion chamber with fresh combustible mixture. Interaction between the fresh mixture and the remainder of the combustion products from the previous cycle reignites the mixture and initiates a new cycle.

In the late forties J. Bertin designed a pulsejet equipped with an aerodynamic valve. Operation of the valve is controlled by inertia of the flow in both directions. The design rendered the engine void of any moving parts and its operation is exclusively controlled by the interaction of termofluid effects and the geometry of the engine (Fig. 1b).

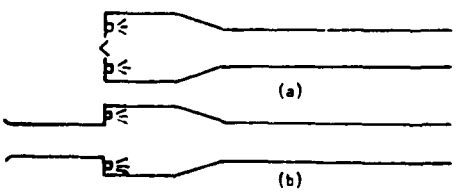

Fig. 1 Mechanically valved pulsejet (a) vs. aerovalved pulsejet (b)

Low efficiency of these engines (resulting from low compression ratio) made it impossible for them to compete with other aircraft and missile engines, and the engines such as turbojets, rockets and ramjets, gained supremacy and the interest in pulsejets declined.

It looks, however, that by application of more intensive combustion (exploiting, for example, the electro-chemical effect), it is possible to increase the compression ratio in the thermodynamic cycle and considerably improve thermal efficiency of the engine.

OPERATION OF THE ELECTRO-CHEMICAL PULSE- JET

A schematic of the electro-chemical pulsejet is presented in Fig. 2. The only difference between this engine and the standard pulsejet consists in making use of the two electrodes which are attached to the combustion chamber, and connected to a high voltage power supply.

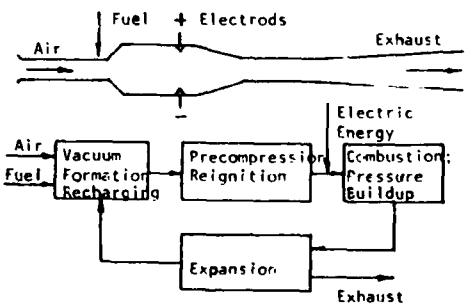

Fig. 2 Electro-chemical pulsejet as an autocyclomaton

The electric discharge is triggered automatically at the instant when the flame occurs between the electrodes.

ELECTRO-CHEMICAL PULSEJET AS AN AUTOCYCLOMATON

The electro-chemical pulsejet may not only raise some interest as an engine that has potential to increase both efficiency and effectiveness of a standard pulsejet but first of all it is particularly in-

teresting as a self-controlled thermal system. The engine is devoid of moving parts and its operation and adaptation to the varying external conditions is based solely on the interactions between the geometry of the system and the multiphenomena processes.

Combustion, which drives the engine, is not only a source of heat that is used to build up the pressure, but also a source of ions that control the injection of electric energy to the system. Expansion not only increases velocity and generates thrust of the engine, but also produces partial vacuum that in turn effects recharging and precompression, and as such is responsible for feedback, which allows the engine to operate on the cyclic mode.

All these attributes permit to include the electro chemical pulsejet into a new emerging class of thermal systems termed autocyclomata.

GASDYNAMICS OF COMBUSTION IN ELECTRO-CHEMICAL PULSEJETS

The mechanism of reignition and combustion in the electro-chemical pulsejet is presented in Fig. 3

At the beginning, the combustion chamber is filled with hot combustion products that interact with the entering jet of combustible mixture, thermally and aerodynamically. In the frontal region of the jet a toroidal vortex is formed and the mixture is ignited at the contact surface with combustion products.

The ignition is transmitted into the vortex, where fast burning and vortex expansion begin. The expansion generates pressure wave that intensifies flame propagation. It also bridges the electrodes by the flame, and provokes electric discharge. The discharge converts fast combustion of the vortex into explosion which strengthens the pressure waves and causes the upstream flame to propagate and to release heat at pressure higher than in conventional pulsejet. This, besides all other effects, should increase the amplitude of pressure variation during the operation of the engine.

EXPERIMENTAL RESULTS

Experiments with a small electro-chemical pulsejet seem to confirm the above conclusion. It was found that the increase in amplitude of pressure pulsations depended on the kind of fuel, shape of the combustion chamber, and the amount of electric energy added.

In one of the experiments an 80% rise in amplitude was caused by only 3% increase in energy input due to electric discharge.

The 3% increase in chemical energy would produce only unnoticeable rise in the amplitude.

REFERENCES

[1] . Putnam, A.A., Belles, F.E. and T.A.C., "Pulse Combustion," Prog. Energy Comb. Sci., 1986, Vol. 12, pp. 43-79.

[2] . Wojcicki, S. "Influence of Electric Discharge on Flame Propagation," Astronautica Acta, Vol., 17, 1972, pp. 827-832.

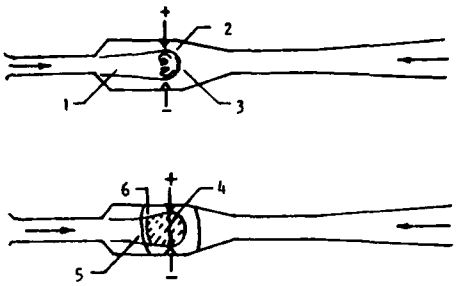

Fig. 3 Combustion in the electro-chemical pulsejet
(1) Entering jet of the combustible mixture
(2) Vortex formation
(3) Reignition
(4) Vortex explosion due to electric discharge
(5) Pressure wave
(6) Upstream Flame

IUTAM Symposium on
Aerothermodynamics in Combustors
June 3-5, 1991, Taipei

COMPUTER SIMULATION OF CHEMICAL VAPOUR DEPOSION TECHNOLOGIES

Khoruzhnikov S.E., Segal A.S., Vasil'yev V.N., Velukhanov V.N., Vorob'yov A.N.

Institute of Precision Mechanics and Optics, Leningrad, USSR

Fokon GMBH, F.R.Germany

Let us consider the general scheme of CVD technologies we are interested in. The starting component mixture flows through the reactor where it is heated up by means of exterior energy sources so that chemical reactions should start. The reactions occurring in the bulk or on the deposition surface provide desired composite material production. It should be noted that in some cases one can observe the formation of the particles (with diameter 100 - 1000 μ m) during the spontaneous condensation because the reaction products are in oversaturated state in the bulk. This particle formation is a necessary condition in some technologies (optical fiber technology) while in others it causes homogeneity changes in deposited layers (material technology for IR optics).

From the brief study of CVD technologies it follows that their mathematical model is to be founded on general equations of flow dynamics with non-equilibrium chemistry and phase transition.

The simplification of starting equation is carried out considering small parameters characteristic of the technologies in question: Mach number, the bulk part of condensate particles, the ratio of characteristic momentum and energy exchange time among phases to characteristic gas dynamic time.

Thus, a set of hyposonic flow equations of chemically reacting gas mixture with spontaneous condensation includes: the equations of mass, momentum and energy conservation of carrier gas mixture; the equations of mass conservation of i-th gaseous component with the sources caused by chemical interaction and phase transition; the equation of pseudogas mass conservation of condensate particles and the chain of Hill moment equations

for condensate particle distribution function depending on sizes. It should be noted that in the latter equations the particle velocity vector is represented as the sum of velocities of the carrier gas and thermophoresis. In spontaneous condensation simulation the cluster formation of critical size is described by classical Frankel-Zel'dovich relations and the particle growth of beyond-critical size is described by Knudsen relations.

This mathematical model was used for numerical study:

- MCVD technology of preform fabrication for optical fiber - here the reactor is the cylindrical fused silica tube (with diameter ~ 0.02 m, length ~ 1 m); the exterior energy source is the traversing oxyhydrogen torch; the starting mixture consists of O_2 , $SiCl_4$, $GeCl_4$; the condensed SiO_2 particles doped with GeO_2 are formed during spontaneous condensation of oxidation products of corresponding chlorides (these reactions occur at T > 1300 K) and deposited on the interior tube wall.

- VAD technology of preform fabrication for optical fiber - in this case the reactor is the cylindrical chamber; the doped condensed SiO_2 particles are formed in flame of oxyhydrogen torch and deposited on rotating susceptor.

- CVD technology of polycrystalline zinc selenide growing - here the starting components are H_2Se, zinc vapour and argon which flow through the heated rectangular reactor under pressure of 5 kPa; the deposition surfaces are reactor walls.

Compute simulation these problems made it possible to study special feature of gas dynamics, heat and mass exchange in these technologies application, the natural convection influence on deposition effectiveness, the dependence of deposited layer thickness upon basic technological parameters.

IUTAM Symposium on
Aerothermodynamics in Combustors
June 3-5, 1991, Taipei

ON COMBUSTION WITH BI-FLAT JETS ATTACHED TO THE WALLS

Wei Jing-Bin*

Instituto Superior Tecnico
Technical University of Lisbon
Department of Mechanics Engineering
Av. Rovisco Pais, 1096 Lisboa Codex
Portugal

ABSTRACT

A new type of combustion method with bi-flat jets was developed following the previous studies on single flat jet combustion (Wei, et al, 1986 and 1990) and presented in this paper.

There are three kinds of elementary jets, that is swirling jet, round jet and flat jet. They are used in verious channel combustors designed with the aims of enhancing combustion effeciency and reducing emissions of NOx, SOx and particles (Gupta,1976, Kelly,1980, Fu,1986, Smart, 1989).

The research on the flat jet is noticeable and interesting. Generally, flat jet might form two dimensional flow with symmetric spread in an unconfined space. But it will become either symmetric flow or asymmetric one in a confined channel. It depends on Re and M numbers based upon the entry conditions and fluid properties (Cherdron, durst and Whitelaw,1978, Cliffe,1982, Sobey, 1986, Richard, 1988).The studies indicated that there were two small symmetric recirculation flow regions behind each step separated from the main flow by shear layers at low Re number. But, when Re number is over critical value with same geometry, the flow mode transformed from symmetry to asymmetry. Durst,Melling and Whitelaw(1974)suggested that the asymmetry of the flow was caused by small disturbances generated in the shear layer between the main flow and reversed flow. The asymmetric flow is a steady structure based on Coanda effect.

The single flat jet combustor was an application of the asymmetric flow. It can stabilize flame using small and large recirculation zones located at both sides of the main flow.

So far, the research performed has only involved a single flat jet as quoted above. Although the combustor had good ability of flame stabilization, but the asymmetric thermal stress might happen between the upper and lower walls, and slagging also might occur in the overheated upper wall near the large recirculation zone with high temperature when burning some sorts of pulverized coal with low ash fusing point.

In order to overcome the drawbacks as pointed out above and provide more intense combustion, lower NOx emissions and no slagging in the wall, the bi-flat jets configuration is proposed as a new type of combustor using reasonable aerodynamics principle. The combustor is a rectangular channel chamber with, through which the two flat inlet jets at the up end, mixture of air and fuel is injected. The aerothermodynamics mechanism of the combustion was studied, including velocity and temperature

*Visiting Associate Professor from Institute of Mechanics, Chinese Academy of Sciences, Beijing 100080, China.

measurements using LDV and thermocouples, respectively in the model combustor.

The following sections present and discuss the most significative results obtained in the studies.

Two flat jets veered to upper and lower walls, respectively. The deflected forward jets attached to the walls at the ahead and middle sections of the combustor. The higher velocity flow layers were near the walls. At the rear the flows came back to the center region. Axial mean velocity, U, is a double-peak distribution on the vertical plane in the combustor. One of most significative features is the existance of a large central recirculation zone. Due to two flat jets entrance from boundaries of the recirculation, therefore reversed flow intensity increased when compared with a single flat jet.

The axial turbulent velocity, u', also is a double-peak distribution, and peak values occur at the locations of the zero mean velocity between forward and reversed flows. The velocity fluctuations are higher using bi-flat jets than a single in the combustor.

The secondary flow is small. This benefits to increase axial momentum and length of the flame from combustor.

Studies indicated that the axial nondimensional mean velocity distribution, local velocity over enter velocity, U/Uin, also is self-simulative as similar as that in single flat jet combustor.

The temperature distribution indicated that it is higher in central recirculation zone than upper and lower. While burning pulverized coal, the particles will not follow the air flow but will largely enter the high temperature recirculation zone, therefore combustion is intensed significantly. Because high temperature zone is away from walls but high velocity layers are near one, therefore ash and slagging were not observed at the walls. Low NOx emission is another significative feature since there were rich-fuel combustion in ahead of the combustor and staged-combustion as second air entered.

REFERENCE

Fu,W.B., Wei,J.B., Zhan,H.Q., Sun,W.C., Chen,Y.L., Han,H.Q., Huang,W.S., Wu,C.K. (1986), 21st Symp. Inter. on Combustion, pp567-574.

Cherdron,W., Durst,F., Whitelaw,J.H. (1987), J. Fluid Mech. 84, 13.

Cliffe,K.A., Greenfield,A.C. (1982), AERE, Report, T.P. 939.

Durst,F., Melling,A., Whitelaw,J.H. (1974), J. Fluid Mech. 64, 111.

Gupta,A.K., Beer,J.M., Swithenbank,J. (1976), 16th Symp. Inter. on Combustion, pp79-91.

Kelly,J.T., Brown,R.A., Wightman,J.B., (1980), 18th Symp. Inter. on Combustion, pp1275-1283.

Richard, M. Fearn (1988), 4th Symp. Inter. on Laser Tech. to Fluid Mech.

Smart, J.P., Weber,R. (1989), J. of the Institute of Energy, pp237-245.

Sobey,I.J., Drazin,P.G. (1986), J. Fluid Mech. 171,263.

Wei,J.B., Wang,H.Y., Li,J., Li,G.D., Wu,C.K. (1986), Patent CN 86106725.

Wei,J.B., Li,J., Gao,L.Z., Zhao,L. (1990), 23rd Symp. Inter. on Combustion.

IUTAM Symposium on
Aerothermodynamics in Combustors
June 3-5, 1991, Taipei

ON A POSSIBILITY OF THERMODYNAMIC MODEL OF PULSATING ENGINE

V.K.Baev, E.V.Perkov

Insttitute of Theoretical and Applied Mechanics
USSR Academy of Sciences, Siberian Division

Of great interest is the problem of modelling of physical processes in pulse combustion chambers because pulse jet engines look out very attractive as one of prospective propulsion systems for high speed flying vehicles. A thermodynamics modeling of internal combustion installations is used as a "zero-approach" in order to discover their main features which do not require detailed processes consideration and to evaluate general efficiency of those installations. In present paper the set of obvious thermodynamic relations is closed by additional thermodynamic hypothesis. The solution allowes to connect all cycle parameters on each stage of operation cycle.

Let chamber V_0 with one open end is filled with combustible mixture at temperature T_1. Initial pressure in chamber is given to be equal to ambient and denoted as p_0. Ambient temperature is equal to T_0 (see figs. 1 and 2).

At definite instant of time a fast explosive burning occurs in chamber at constant volume. Pressure and temperature within burned region become equal to p_{max} and T_{max} respectively. Then very sharp, explosive expansion of burned gas will take place, the final pressure being established less than ambient one: $p_{min} < p_0$. It provides the inflow of fresh gas with parameters (p_0, T_0) on the next stage of cycle. If we accept that after expansion the mass of gas remaining in the chamber is equal to gM_{total} then the mass of inflowing gas must be equal to $(1-g)M_{total}$ and temperature T_1 must establish in the chamber after mixing. In such case cycle of operation would be closed and system may be realized in principle.

The main question is how to define minimal cycle parameters p_{min} and T_{min}? We suggested that the work of burned products over ambient medium during expansion process is equal exactly to the one of ambient medium over products remaining in chamber during backflow of fresh gas. The initial statement (p_0, T_1) is defined by mixing of burned products gM_{total} at T_2 with fresh gas $(1-g)M_{total}$ at T_0 (see fig.2). We also accept the processes of expansion and backflow compression to be adiabatic. Hence we obtained the following set of relations (in dimensionless form):

$$(1 - g) + g\theta_2 = \theta_1 \qquad (1)$$

- equation of mixing at p = const;

$$\frac{\theta_2}{\theta_{max}} = \frac{1}{\pi_{max}^m} \qquad (2)$$

- adiabatic expansion from p_{max} to p_0;

$$\frac{\theta_{min}}{\theta_1} = \theta \qquad (3)$$

- definition of parameter θ;

$$\pi_{max} = \theta \qquad (4)$$

- relation for heating at constant volume;

$$\frac{\theta_{min}}{\theta_1} = \frac{\pi_{min}}{g} \qquad (5)$$

- this relation follows from the fact that volume V_0 does not change during the whole process;

$$\theta_2 - \theta_{min} = (1 - g)(\gamma - 1)\theta_1 \qquad (6)$$

- mathematical formulation of our additional hypothesis;

$$\frac{\theta_{min}}{\theta_2} = \pi_{min}^m \qquad (7)$$

- adiabatic expansion from p_0 to p_{min},

where $\theta_1 = T_1/T_0$; $\theta_2 = T_2/T_0$; $\theta_{max} = T_{max}/T_0$; $\pi_{max} = p_{max}/p_0$; $\pi_{min} = p_{min}/p_0$; $\theta = T_{max}/T_1$; $m=(\gamma-1)/\gamma$.

We obtain 7 equations for 7 variables and 1 parameter. It is more convenient for further experiment to choose $\theta = T_{max}/T_1$ as parameter. In such case all remain values are functions of θ. Some results of solution are given in Table 1.

This model allowed also to evaluate the region of stable operation of model and main

reason of possible instabilities in its operation.

On the second step of our theoretical studies we replace thermodynamic hipothesis (6) by more detailed gasdynamics consideration of wave processes in gas during outflow and inflow. This one makes possible to include factor of inner geometry of chamber. These two models showed good correlation in the case of simple geometry of short tube with end.

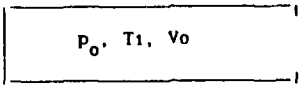

Fig. 1. Model chamber at initial instant of time.

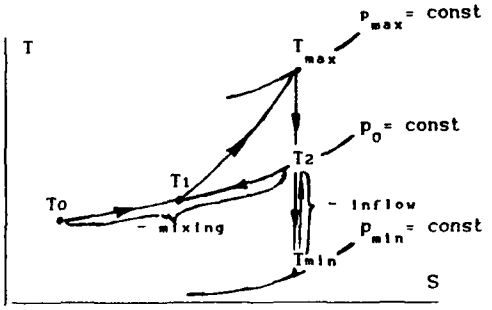

Fig. 2. TS-diagram of thermodynamic cycle to be considered.

$\bar{\theta}$	$\bar{\theta}_1$	$\bar{\theta}_2$	$\bar{\theta}_{max}$	$\bar{\theta}_{min}$	g	π_{min}	π_{max}	$\bar{\pi}$
1.5	1.56	2.09	2.35	1.79	0.51	0.58	1.5	1.04
2	1.85	3.03	3.70	2.60	0.42	0.52	2	1.295
2.5	2.14	4.11	5.35	3.58	0.37	0.61	2.5	1.555
3	2.45	5.36	7.35	4.7	0.33	0.63	3	1.815

Table 1. Some results of cycle calculations.

REFERENCES:

1. J.V. Foa, Elements of Flight Propulsion. J.Wiley & Sons, Inc., N.-Y. and London, 1960, pp. 344-399;

2. G.Markstein, Nonsteady flame propagation, Mir, Moscow, 1968, pp. 407-409.

IUTAM Symposium on
Aerothermodynamics in Combustors
June 3-5, 1991, Taipei.

Velocity and Size Characteristics of Kerosene-fuelled Flames Stabilized by Bluff-body with and without a Quarl

Y. Hardalupas, C.H. Liu and J.H. Whitelaw

Imperial College of Science Technology and Medicine,
Mechanical Engineering Department, Thermofluids Section,
Exhibition Road, London SW7 2BX, U.K.

INTRODUCTION

Flame stability in industrial burners or gas turbine combustors is usually achieved by recirculation generated by swirlers or bluff-bodies downstream of the nozzle (Chen et al, 1990). In liquid-fuel burners spray nozzles are used to atomise the fuel in a wide range of droplet diameters, which have different aerodynamic and combusting characteristics, and the flame is stabilised by similar arrangements.

Knowledge of the behavior of fuel droplets in flames can be important for the improvement of stability and combustion efficiency. Earlier studies of liquid fuel flames included photographic studies (McCreath and Chigier, 1973) and laser Doppler studies (El Banhawy and Whitelaw, 1981) but without detailed information of droplet sizes. Recently, instantaneous velocity and size measurements of fuel droplets have been obtained in non-swirling flames (Kawazoe et al, 1990; McDonell and Samuelsen, 1988) or in swirling flames (Hardalupas et al, 1990; Milosavljevic, 1991) and the results show that the inertia and the burning time of different droplet sizes affects the combustion efficiency. Water sprays at the exit of annular air flow streams had been examined by Li and Tankin (1989) who showed that there is a strong influence of the air flowrate on the spray behavior.

The present work examines the fuel droplet characteristics of two non-swirling flames stabilised by bluff bodies in burner geometries with and without a quarl and measured by phase-Doppler velocimeter. The following sections provide a brief description of the geometry of the burner, the flow conditions and experimental techniques. Results in combusting flow are presented and discussed in the third section, and the summary of the more important findings is given in the final section.

FLOW CONDITIONS AND INSTRUMENTATION

Figure 1 shows the geometry and dimensions of the kerosene-fuelled burner. A constant air mass flow rate of 3.35×10^{-2} kg/s was supplied to the burner through an upstream annular tube with inner and outer diameters of 18 and 50.8 mm, respectively. A 43.8 mm diameter flat disk with blockage ratio of 0.74 was positioned normal to the flow at the exit of the annulus and generated a recirculation zone essential for flame stabilization. The area averaged air velocity was U_a=15.4 m/s in the annulus upstream of the disc and 51 m/s in the annulus at the exit of the disk, resulting in Reynolds numbers of 5.37×10^4 and 1.77×10^5, respectively, based on the outer diameter of the annulus. A quarl of 50.8 mm length and 50° divergence angle was positioned at the end of the annulus. Kerosene, with density 800 kg m^{-3} and kinematic viscosity 1.3×10^{-3} m s^{-1}, was supplied by a pump to an axial spray nozzle (Delavan Type SN 30609-7) at a constant flow rate of 6×10^{-4} kg s^{-1} and

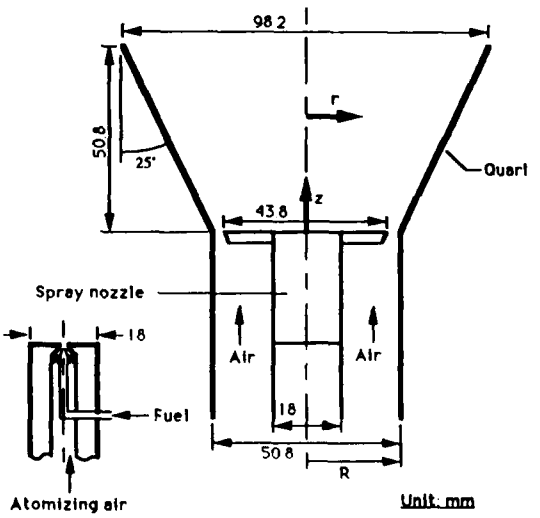

Fig. 1 Dimensions of the kerosene burner.

atomised by an air flowrate of 6.53×10^{-4} kg s^{-1} to produce a 30° solid cone spray. The equivalence ratio based on the atomising air only was 13.6 and 0.26 for the total air flow. Quartz windows on the transmitting and receiving sides of the quarl provided optical access to the flow inside the quarl.

Velocity and size information of the fuel droplets was obtained by a phase-Doppler anemometer described by Hardalupas (1989). The characteristics of the transmitting and receiving optics are summarised in Table. Measurement of volume flux of liquid fuel droplets can also be made by phase-Doppler velocimeter as a function of droplet sizes as has been shown by Bachalo et al (1988) and Hardalupas and Taylor (1989), and was used to quantify the combustion efficiency. The mean diameter measurements were based on 7000 measurements resulting in statistical uncertainties of less than 2%. The accuracy of the sizing measurement was less than 2 μm for droplets larger than 20 μm. The mean velocity is presented for two size ranges of 5-10 and 45-50 μm, which will be referred to as 10 and 50 μm, with uncertainties of less than 1% based on the average sample size of 1000 for each 5 μm size class.

RESULTS AND DISCUSSION

The shaded part of Figure 2 shows the overall equivalence ratios for Reynolds numbers based on the area averaged velocity upstream of the disc and the disc diameter, where the flame is stable with and without the quarl. The presence of the quarl improved the rich limit of the flame by more than three times than that without quarl and the flame

Table: Characteristics of the optical system

Laser	1 W Ar^+ laser (514.8 nm) Operated at 400 mW
Transmission optics	
Beam intersection angle	4.86°
Fringe spacing	6.06 μm
Probe volume dimensions	diameter : 0.084 mm length : 1.9 mm
Receiving optics	
Collection angle	30°
Rectangular collection apertures separation	2.3° and 4.6°
Particle sizing range	0-110 μm
Spatial filter width	200 μm
Effective length of probe volume	0.4 mm

could not be extinguished. However, the presence of the quarl reduced the lean stability limits of the flame by up to four times than that without quarl. The stability limits of the flame were affected by the dispersion of different sizes of fuel droplets, resulting in local equivalence ratios inside the recirculation zone much different than the overall equivalence ratio.

In an effort to explain the stability limits of the flames, local information of velocity and size were obtained with the phase-Doppler velocimeter. The area-averaged air velocity in the annulus upstream of the disc, U_a, was used to normalize the measured velocity values and the outer radius of the annulus, R. Figure 3 shows the radial variation of the axial mean velocity of the 10 and 50 μm droplets at an axial distance from the nozzle of z/R=0.8. It is expected that the 10 μm droplets will follow the mean flow of the continuous phase, since their mean Stokes number, St_m, is 4, while 50 μm droplets will not follow the mean flow for their mean Stokes number of 0.16. The mean Stokes number is defined as

$$St_m = T_f/\tau$$

where T_f is the characteristic mean timescale of the flow (1ms), taken here as the ratio of the outer diameter of the annulus (50.8 mm) to the tip velocity at the exit of the disk (51 m/s) and τ is the relaxation time of the droplets which is 0.25 and 6.2 ms for 10 and 50 μm droplets, respectively. The behavior of the 10 μm droplets in the flame suggests a recirculation zone divided by the central spray. The location of maximum negative mean axial velocity was around r/R= 0.7 in the flame without the quarl, and with the quarl was close to the wall, r/R=1.0, so that the flame was wider and filled the quarl. This observation suggests that the flowrate of air entrained inside the recirculation zone was larger with the quarl resulting in lower local equivalence ratio and this explains why the lean stability limits of Figure 2 were reduced for the quarl flame and emphasises the importance of local fuel droplet characteristics in the flame. In the central region, the mean axial velocity of the 10 μm droplets was always positive, since the initial 10 μm droplets produced by the spray burned quickly (≈0.1ms) and were replaced by larger droplets after evaporation. The 50 μm droplets shared the same tendency but to a lesser extent, since their residence time in the recirculating region of the flame was around 6ms and 2ms with and without quarl, respectively, and their burning time was around 2.5ms. The behavior of the 50 μm droplets in both flames was similar, apart from the region close to the wall where their velocity was higher without the quarl due to unburned fuel droplets dispersed outside the flame zone and carried by the outer shear layer.

The Sauter mean diameter was 25% larger with the quarl, Figure 4, which suggests fewer droplets of diameter less than 20 μm. That the smaller droplets burned faster with the quarl, implies higher local temperatures and this explains the high axial velocity of the 10 μm droplets at the centre in the flame, Figure 3, since the residence time of up to 50 μm droplets was similar to the burning time and low velocity droplets had more chance to burn.

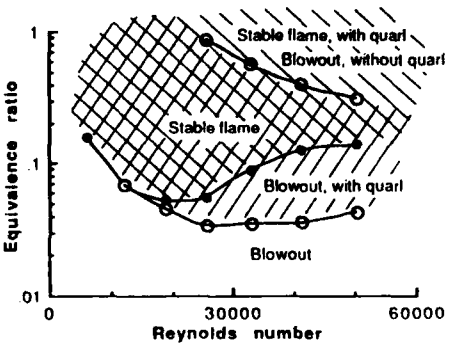

Fig. 2 Stability limit of kerosene flames stabilized by a flat disk.
(O , without quarl; • , with quarl)

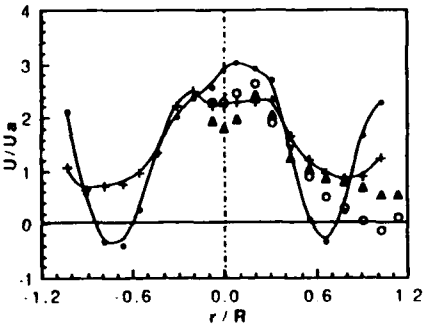

Fig. 3 Radial mean velocity profiles of the fuel droplets at z/R = 0.8.
(—•— , 10 μm droplet without quarl;
—+— , 50 μm droplet without quarl;
o , 10 μm droplet with quarl;
▲ , 50 μm droplet with quarl)

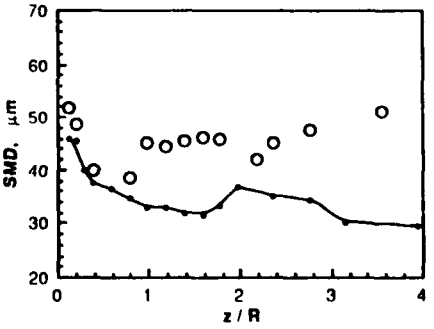

Fig. 4 Sauter mean diameter of fuel droplets on the centreline.
(—•— , without quarl; O , with quarl)

Combustion with the quarl was more intense with the flame filling the full volume of the quarl and extending to z/R=4.7. The flame without quarl was weaker with the major combustion zone downstream and at the outer radii of the disc and so that many unburned fuel droplets escaped downstream. The combustion efficiency can be quantified from the amount of unburned fuel droplets remaining in the flame, provided that the fuel vapour is all burned. Figure 5 shows the total volume flowrate of fuel droplets normalized by the supplied fuel flowrate passing through the radial planes at different axial locations, obtained by integration of the radial profiles of the measured fuel droplet flux. In the flame without quarl, the liquid fuel flowrate in the flame zone (z/R=0.4 to 1.2) remained nearly constant and was less at z/R=2.4. In the flame with the quarl, the fuel flowrate

decreased monotonically by 90% at the exit of the quarl (z/R=2.4) and the measured fuel flowrate was 50% lower than that supplied by the nozzle due to the dense spray and attenuation of the incident laser beams with reduced data rate. However, the results can still quantify the combustion efficiency of each burner at the last measured location (z/R= 2.4) which was found 88% with quarl and 36% without quarl.

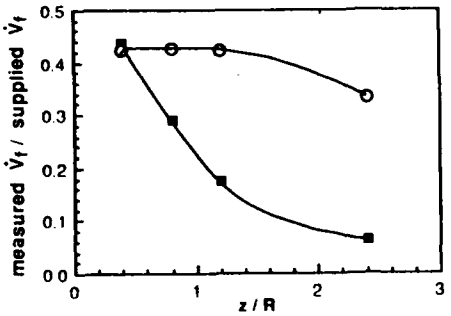

Fig. 5 Fuel droplet flow rate at different radial planes along the axis of the burner.
(o , without quarl; ■ , with quarl)

CONCLUDING REMARKS

Flame stability and fuel droplet characteristics have been measured by phase-Doppler velocimeter in a kerosene non-swirling flame stabilized by a flat disc bluff-body with and without a quarl. In the flame without the quarl, fuel droplets moved faster in the flame zone, the recirculation zone was smaller and the resulting combustion was weaker and incomplete, since the residence time of the droplets was small relative to their evaporation time. The flame with the quarl had a combustion efficiency of 0.88, rather than 0.36, and the rich stability limits were extended due to the larger recirculation zone.

ACKNOWLEDGEMENTS

The authors are grateful to Mr. V. Milosavljevic for his design and construction of the burner. The work was supported by the Commission of European Communities.

REFERENCES

Bachalo, W.D., Rudoff, R.C. and Brena de la Rosa, A. 1988. Mass flux measurements of a high number density spray system using the phase-Doppler particle analyzer. AIAA-paper-88-0236.

Chen, R.H., Driscoll, J.F., Kelly, J., Namazian, M. and Schefer, R.W. 1990. A comparison of bluff-body and swirl-stabilized flame. Comb. Sci. and Tech., vol. 71, pp. 197-217.

El Banhawy, Y. and Whitelaw, J.H. 1981. Experimental study of the interaction between a fuel spray and surrounding combustion air. Comb. and Flame, vol. 42, pp. 253-275.

Hardalupas, Y., Taylor, A.M.K.P. and Whitelaw J.H. 1990. Velocity and size characteristics of liquid-fuelled flames stabilized by a swirl burner. Proc. R. Soc. Lond. A 428, pp. 129-155.

Hardalupas, Y. 1989. Experiments with isothermal two-phase flow. Ph.D. Thesis, University of London.

Hardalupas, Y. and Taylor, A.M.K.P. 1989. On the measurement of particle concentration near a stagnation point. Exp. in Fluids, vol. 8, pp. 113-118.

Kawazoe, H., Ohsawa, K. and Fujikake, K. 1990. LDA measurement of fuel droplet sizes and velocities in a combustion field. Comb. and Flame, vol. 82, pp. 151-162.

Li, X. and Tankin, R.S. 1989. Spray behavior in annular air streams. Comb. Sci and Tech., vol. 64, pp. 141-165

McCreath, C.G. and Chigier, N.A. 1973. Liquid-spray burning in the wake of a stabilizer disk. Proc. 14th Int'l Symp. Comb., pp. 1355-1363.

McDonell, V.G. and Samuelsen, G.S. 1988. Evolution of the two-phase flow in the near field of an air-blast atomizer under reacting and non-reacting condition. Proc. 4th Int'l Symp. on Appl. of Laser Anemometry to Fluid Mechanics, July 1988, Lisbon, Portugal.

Milosavljevic, V. 1991. Ph.D. Thesis, in preparation, University of London.

AUTHOR INDEX